



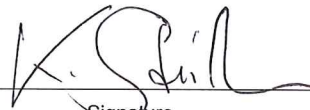
*Überall geht ein frühes Ahnen dem späten Wissen voraus.*  
Alexander von Humboldt (1769-1859)

## AFFIDAVIT

I declare that I have authored this thesis independently, that I have not used other than the declared sources/resources, and that I have explicitly indicated all material which has been quoted either literally or by content from the sources used. The text document uploaded to TUGRAZonline is identical to the present doctoral thesis.

09.03.2017

Date

A handwritten signature in black ink, appearing to be 'K. Schill', written over a horizontal line.

Signature

## Preface

This PhD thesis is submitted for the degree “Doktor der technischen Wissenschaften” at the Faculty of Mechanical Engineering and Economic Sciences at Graz University of Technology. The work was conducted as collaboration between the Research & Development Department, University of Applied Sciences Upper Austria, the voestalpine Stahl GmbH and the Institute of Materials Science and Welding, Graz University of Technology.

Research findings were published in several scientific papers and presented at conferences relevant for the scientific community. The following list assembles the contributions made as author or co-author.

- (a) K. Steineder, R. Schneider, D. Krizan, C. Béal, and C. Sommitsch, Microstructural evolution in 0.1%C5%Mn steel after intercritical annealing depending on temperature and cooling rate, in: Proc. - Eur. Conf. Heat Treat. 21<sup>st</sup> IFHTSE Congr., Munich, 2014: pp. 301–308.
- (b) K. Steineder, R. Schneider, D. Krizan, C. Béal, and C. Sommitsch, Microstructural evolution of two low-carbon steels with a medium manganese content, in: 2<sup>nd</sup> Int. Conf. High Manganese Steel, Aachen, 2014.
- (c) R. Schneider, M. Rahofer, K. Steineder, L. Samek, C. Commenda, and E. Arenholz, Metallographische Untersuchung von Medium-Mn-Stählen, in: Spec. Ed. Pract. Metallogr. 46, Leoben, 2014: pp. 77–82.
- (d) K. Steineder, R. Schneider, D. Krizan, C. Béal, and C. Sommitsch, “Comparative Investigation of Phase Transformation Behavior as a Function of Annealing Temperature and Cooling Rate of Two Medium-Mn Steels,” *Steel Res. Int.*, vol. 86, no. 10, pp.1179–1186, 2015.
- (e) K. Steineder, R. Schneider, D. Krizan, C. Béal, and C. Sommitsch, “Investigation on the Microstructural Evolution in a Medium-Mn steel (X10Mn5) after Intercritical Annealing,” *HTM J. Heat Treat. Mater.*, vol. 70, no. 1, pp.19–25, 2015.
- (f) K. Steineder, M. Dikovits, C. Beal, C. Sommitsch, D. Krizan, and R. Schneider, “Hot Deformation Behavior of a 3<sup>rd</sup> Generation Advanced High Strength Steel with a Medium-Mn Content,” *Key Eng. Mater.*, vol. 651-653, pp.120–125, 2015.
- (g) K. Steineder, R. Schneider, D. Krizan, C. Béal, and C. Sommitsch, Einfluss des Ausgangsgefüges und der Glüh Temperatur auf die Restaustenitstabilität von Medium-Mn Stählen, in: Symp. “12 Jahre MHT” Metallurgie und Härtereitechnik, Wels, 2016: pp. 10–11.
- (h) K. Steineder, D. Krizan, R. Schneider, C. Béal, and C. Sommitsch, “The effects of intercritical annealing temperature and initial microstructure on the stability of retained austenite in a 0.1C-6Mn steel,” *Adv. Mater. Res.*, vol. 879, pp. 1847-1852, 2016.



- (i) K. Steineder, D. Krizan, R. Schneider, C. Béal, and C. Sommitsch, On the micro-scale damage behavior of a 0.1C6Mn Medium-Mn steel, in: 3<sup>rd</sup> Int. Conf. High Manganese Steel, Chengdu, 2016: pp. 415-419.
- (j) R. Schneider, K. Steineder, A. Watanebe, M. Okumiya, D. Krizan, and C. Sommitsch, Determination of a new empirical  $M_s$ -formula suitable for Medium-Mn-steels, in: 24<sup>th</sup> IFHTSE Congr. Eur. Conf. Heat Treat. Surf. Eng., Nice, 2017à submitted

## Acknowledgments

During my PhD thesis I was in the fortunate position that I was surrounded by a lot of friendly, talented and extremely supportive people. I want to thank all of them for their help and kindness.

I want to thank Prof. Dr. Christof Sommitsch for the opportunity to work with his team at the IMAT institute and for his excellent supervision. I would like to express my sincere thanks to Dr. Coline Béal for the great hospitality all the times I traveled to Graz and the many discussions and precise reviews of many manuscripts.

Especially, I want to thank FH-Prof. Dr. Reinhold Schneider, who not only played an integral role during my PhD, but has been there from the very beginning of my University career, inspired and encouraged me and most of all taught me with endless patience.

A good deal of my time I was able to spend at the R&D department of voestalpine Stahl GmbH. Amongst the many great people there I would like to express my sincere thanks to Dr. Andreas Pichler, who enabled the project in the first place and enriched the discussions with his great knowledge and Dr. Thomas Hebesberger for his critical mind and expertise. Special thanks go to Dr. Daniel Krizan for all the time he took for fruitful discussions, most accurate reviews, guidance and encouragement. Moreover, I want to thank the whole “Medium-Mn” team Dr. Johannes Rehrl and Ing. Johannes Staudinger for the pleasant collaboration and the many “Klimmzüge” we managed together.

Furthermore, I want to thank Dipl.-Ing. Reinhold Aichinger for his efforts to provide great SEM micrographs, Dipl.-Ing. Christian Commenda for his excellent work on XRD and EBSD and Mario Panholzer for doing quite a lot of high-quality metallography.

## Abstract

Medium-Mn-steels are considered as one of the future steel alloying concepts to fulfill the demanding requirements of the automotive industry concerning the opposing trends of light weight potential and crash worthiness. This work concentrates on C-Mn alloying concepts suitable for batch annealing routes. Additionally to the influence of the C- and Mn-content on the mechanical properties, the influence of the annealing temperature during intercritical annealing was thoroughly examined. Furthermore, the impact of a full austenitization prior to intercritical annealing was investigated (two-step heat treatment).

By detailed microstructural investigation the development of the mechanical properties could be properly related to the altering amounts and changing chemical composition of the respective microstructural constituents. This could be further supported by thermodynamic modelling of the microstructural development during annealing as well as at room temperature. An existing model for the prediction of retained austenite could be refined by establishing a new empirical  $M_s$ -formula for steels with Mn-contents  $\geq 3.5$  wt-%. The obtained mechanical properties by tensile testing could achieve their target for a 3<sup>rd</sup> generation advanced high strength steel.

An extended yield point elongation, commonly observed with the group of Medium-Mn-steels, depict a potential drawback in application. Therefore, this aspect was examined in detail. It was found that the ultra-fine grained microstructure promotes localized deformation, which resulted in pronounced yield point plateaus. In order to overcome this difficulty, the introduction of metastable retained austenite as well as a two-step heat treatment appeared to be remarkably helpful.

This leads to the next physical aspect which was studied most accurately, *i.e.* the retained austenite stability considered from the viewpoint of the work hardening behavior. Improved work hardening behavior was observed with increasing C- and Mn-content as well as for the two-step heat treatment. Higher alloying with C and Mn resulted in a higher chemical stabilization of the retained austenite against transformation by mechanical deformation, while the retained austenite obtained by the two-step heat treatment was more stable due to grain size and morphology of the austenite and the obtained stronger matrix.

As crash worthiness displays a crucial aspect for application of Medium-Mn-steels, increased attention was paid to the damage response of the material. While Mn and the applied heat treatment schedule showed no significant influence on the postuniform behavior, increased C-contents deteriorated the respective figures. Moreover, the intercritical annealing temperature decisively controlled the damage behavior. It could be stated that for the targeted mechanical properties a reasonable damage response can be assumed.

Overall a detailed examination of the structure-property relationship of Medium-Mn-steels was conducted which clearly emphasized the enormous potential of this steel group for the automotive safety-related applications. But it also highlighted some crucial challenges that have to be considered when bringing the product to industrial scale production and introducing it into the market.

## Kurzfassung

Medium-Mn-Stähle stellen hinsichtlich der Vereinbarkeit der gegensätzlichen Anforderungen an Automobilstähle bezüglich Leichtbaupotential und Crashperformance ein neues vielversprechendes Legierungskonzept dar. Diese Arbeit untersucht C-Mn Legierungen, welche sich für die Produktion über eine Haubenglühroute eignen. Neben dem Einfluss des C- und Mn-Gehaltes auf die mechanischen Eigenschaften, wurde der Einfluss der interkritischen Glühtemperatur genauestens untersucht. Weiters wurden die Auswirkungen einer Voll-austenitisierung vor dem interkritischen Glühen (zweistufige Wärmebehandlung) geprüft.

Mit Hilfe detaillierter Untersuchungen der Mikrostruktur konnte die Entwicklung der mechanischen Eigenschaften mit den sich verändernden Anteilen und chemischen Zusammensetzungen der jeweiligen Gefügebestandteile korreliert werden. Dies konnte durch thermodynamische Modellierung des Gefüges bei interkritischer Glühtemperatur wie auch bei Raumtemperatur, weiters bestätigt werden. Ein aus der Literatur bekanntes Modell zur Vorhersage des Restaustenitanteils wurde durch Ermittlung einer neuen empirischen  $M_s$ -Formel für Stähle mit Mn-Gehalten  $\geq 3.5$  wt-% verbessert. Die erhaltenen mechanischen Eigenschaften konnten die Anforderungen an AHSS Stähle der dritten Generation erfüllen.

Da eine stark ausgeprägte Streckgrenze wiederholt in der Gruppe der Medium-Mn-Stähle beobachtet worden ist und dies einen potentiellen Rückschlag für die technische Anwendung bedeuten könnte, wurde diesem Aspekt besondere Aufmerksamkeit geschenkt. Es stellte sich heraus, dass die Ultrafeinkörnigkeit des Gefüges lokalisierte Verformung fördert und eine stark ausgeprägte Streckgrenze daraus resultiert. Um dieses Problem zu verhindern, erwies sich metastabiler Restaustenit sowie die Anwendung der zweistufigen Wärmebehandlung als besonders wirksam.

Dies führte zum zweiten metallkundlichen Aspekt, der vertiefend untersucht wurde, der Restaustenitstabilität und dem damit verbundenen Kaltverfestigungsverhalten. Durch erhöhtes Legieren mit C und Mn sowie dem Anwenden der zweistufigen Wärmebehandlung, konnte die Kaltverfestigungsrate optimiert werden. Der höhere Legierungsanteil resultierte in einer erhöhten chemischen Stabilisierung des Restaustenits, während die zweistufige Wärmebehandlung die Restaustenitstabilität durch Korngröße und Morphologie des Austenits sowie der umgebenden Matrix verbesserte.

Wie anfangs erwähnt stellt die Crashperformance einen entscheidenden Faktor hinsichtlich der Anwendung von Medium-Mn-Stählen dar. Deshalb wurde auf das Schädigungsverhalten dieses Werkstoffes besonderes Augenmerk gelegt. Während der Mn-Gehalt und die angewendete Glühroute keinen signifikanten Einfluss auf die postuniformen Eigenschaften zeigten, war der Einfluss von C besonders stark und wirkte sich nachteilig aus. Darüber hinaus erwies sich die interkritische Glühtemperatur als entscheidende Stellgröße, welche das Schädigungsverhalten stark beeinflusst. Glücklicherweise erwiesen sich die postuniformen Kennwerte als relativ gut im Bereich der angestrebten exzellenten mechanischen Kennwerte.

Zusammenfassend lässt sich ein detailliertes Bild der Gefüge-Eigenschaftsbeziehung von Medium-Mn-Stählen zeichnen, welches das enorme Potential dieser Werkstoffgruppe für sicherheitsrelevante Bauteile in der Automobilindustrie aufzeigt. Allerdings wurden auch einige entscheidende Herausforderungen aufgezeigt, welche es zu klären gilt, bevor das Produkt großtechnisch erzeugt beziehungsweise auf den Markt eingeführt werden kann.

## Abbreviations and Symbols

Abbreviation	Meaning
AHSS	Advanced high strength steels
ART	Austenite reverse transformation
BA	Batch annealed
BH	Bake hardening
CAL	Continuous annealing line
CP	Complex phase
DP	Dual phase
EBSD	Electron backscattered diffraction
ECD	Equivalent circle diameter
EDX	Energy-dispersive X-ray spectroscopy
FA	Full austenitization
FS	Fracture strength
H-P	Hall-Petch
HSS	High strength steels
HT	Heat treatment
HSLA	High strength low alloy
IA	Intercritical annealing
IF	Interstitial free
IR	Infrared
MP	Measuring point
ODF	Orientation distribution function
Q&P	Quenching and partitioning
RT	Room temperature
SEM	Scanning electron microscopy
SFE	Stacking fault energy
SMM	Saturation magnetization method
TE	Total elongation
TEM	Transmission electron microscopy
TBF	TRIP-assisted Bainitic Ferrite
TRIP	Transformation induced plasticity
TWIP	Twinning induced plasticity
UE	Uniform elongation
UTS	Ultimate tensile strength
WDX	Wave-dispersive X-ray spectroscopy
YP	Yield point
YPE	Yield point elongation

Symbol	Unit	Meaning
$\alpha$		Ferrite
$\alpha_c$		Constant
$\alpha'$		Martensite
$\alpha''$		Tempered martensite
$\beta_c$		Constant
$\gamma$		Austenite
$\gamma_L$		Lath-like retained austenite
$\gamma_G$		Globular retained austenite
$\Delta G_1$	J	Chemical driving force
$\Delta G_2$	J	Mechanical driving force
$\varepsilon$	%	Engineering elongation
$\bar{\varepsilon}$	%	Elongation of the composite
$\varepsilon_3$	%	Thickness strain
$\varepsilon_\alpha$	%	Elongation of material $\alpha$
$\varepsilon_\beta$	%	Elongation of material $\beta$
$\varepsilon_E$		Emission constant
$\varepsilon_{true}$		True elongation
$\theta$		Cementite
$\sigma$	MPa	Engineering stress
$\bar{\sigma}$	MPa	Strength of the composite
$\sigma_0$	MPa	Peierls-Nabarro stress
$\sigma_\alpha$	MPa	Strength of material $\alpha$
$\sigma_\beta$	MPa	Strength of material $\beta$
$\sigma_B$		Stefan-Boltzmann constant
$\sigma_{true}$	MPa	True stress
$\sigma_{YS}$	MPa	Yield stress
$A_0$	m <sup>2</sup>	Initial cross section
$A_f$	m <sup>2</sup>	Cross section after fracture
$A_{c1}$	°C	Temperature of the beginning of the austenite formation during heating
$A_{c3}$	°C	Temperature of the completion of the austenite formation during heating
$B_s$	°C	Bainite start temperature
$d$	m	Grain diameter
$f_\alpha$	vol.-%	Fraction of $\alpha$
$f_\beta$	vol.-%	Fraction of $\beta$
$f_{\alpha'}$	%	Fraction of martensite
$I$	W/m <sup>2</sup>	Intensity
$k$		Material constant
$k_p$		Value for retained austenite stability
$k_{pc}$		Critical value for retained austenite stability

		concerning discontinuous yielding
$M_s$	°C	Martensite start temperature
$M_s^\sigma$	°C	Temperature where the austenite transforms when the applied stress equals the yield stress
$M_d$	°C	Temperature where the austenite is not transformed while plastic deformation
$M_{d30}$	°C	Temperature where at 30% of plastic strain 50% of the existing austenite is transformed
$n$		Work hardening coefficient
$n_i$		Incremental work hardening coefficient
$n_L$		Number of initiated Lüders bands
$p$		Strain exponent corresponding with the autocatalytic effect
$T$	K	Absolute temperature
$T_A$	°C	Austenitization temperature
$t_A$	s	Austenitization time
$T_{AN}$	°C	Annealing temperature
$T_{IA}$	°C	Intercritical annealing temperature
$t_{IA}$	s	Intercritical annealing time
$T_{IAmax}$	°C	Temperature where the maximal amount of retained austenite is achieved
$T_{IH}$	°C	Isothermal holding temperature
$t_{IH}$	s	Isothermal holding time
$U$	J	Additional energy
$V_{\gamma 0}$	vol.-%	Volume fraction of retained austenite at unstrained state
$V_{\gamma 0one-step}$	vol.-%	Volume fraction of retained austenite at unstrained state after one-step heat treatment
$V_{\gamma 0two-step}$	vol.-%	Volume fraction of retained austenite at unstrained state after two-step heat treatment
$v_c$	mm/s	Specimen extension rate
$v_b$	mm/s	Average Lüders band velocity
$Z$	%	Reduction of Area

## Table of content

1.	Introduction .....	1
2.	Objectives .....	2
3.	Literature .....	3
3.1	Recent developments in AHSS .....	3
3.2	Current state of research - Medium-Mn-steels .....	4
3.3	Retained austenite and TRIP-phenomenon.....	9
3.4	Ultra-fine grained steels.....	16
3.5	Damage behavior of multiphase steels .....	19
4.	Experimental procedure .....	24
4.1	Production and chemical composition of the investigated steels.....	24
4.2	Dilatometry .....	25
4.3	Heat treatment .....	27
4.4	Thermodynamic simulations.....	27
4.5	Microstructural investigations.....	27
4.6	Retained austenite measurement .....	29
4.7	Mechanical testing.....	31
5.	Results .....	33
5.1	Influence of C and Mn.....	33
5.1.1	Microstructural evolution .....	33
5.1.2	Mechanical properties .....	43
5.1.3	Yielding behavior.....	46
5.1.4	Work hardening behavior .....	48
5.1.5	Damage behavior .....	51
5.2	Influence of the heat treatment.....	53
5.2.1	Microstructural evolution .....	53
5.2.2	Mechanical properties .....	64
5.2.3	Yielding behavior.....	67
5.2.4	Work hardening behavior .....	67
5.2.5	Damage behavior .....	70
6.	Discussion.....	75
6.1	Microstructural evolution .....	75
6.2	Mechanical properties .....	86
6.3	Yielding behavior.....	95
6.4	Work hardening behavior .....	108
6.5	Damage behavior.....	116



7. Summary and Conclusions .....	121
8. Outlook.....	123
9. References .....	124
10. Appendix .....	132

## 1. Introduction

The persistent demand of the automotive industry on advanced high strength steels (AHSS) due to their lightweight potential, excellent crash behavior, outstanding formability and reasonable pricing compared to non-ferrous material solutions drives the development of new high strength steel grades. Challenging regulations within the EU legislation concerning CO<sub>2</sub> emissions of new passenger cars increase the research and development activities concerning high strength steel grades as potential lightweight materials. [1] Studies show that in the automotive industry the share of high strength steels (HSS) will increase up to 38 % in 2030, which means that the applications will more than double compared to 2010. [2] To meet the demanding requirements of the market the improvement of existing concepts as well as the design of a new generation of AHSS will be necessary.

As this work engages with the further development of the currently applied AHSS a brief overview of those cold rolled sheet steels will be given. The first highlighted steel group will be the conventional HSS, including high strength interstitial free (IF), bake hardening (BH) and microalloyed (HSLA) steels with tensile strengths up to 550 MPa. All of those concepts have a single phase ferritic microstructure using the conventional steel strengthening mechanisms of solid solution, precipitation hardening and grain refinement. In order to achieve higher strength levels it was necessary to introduce a second, harder microstructural constituent. This was accomplished by the development of dual phase (DP) steels in the late 1970's and early 1980's. DP-steels consist besides ferrite of a second, hard martensitic phase. [3,4,5] This led to a significant increase in tensile strength but came along with a substantial loss in elongation and formability. A superior strength-ductility combination was achieved by the development of transformation induced plasticity (TRIP) steels. [6] The introduction of metastable retained austenite, which transforms into martensite during deformation, substantially improved the strain hardening behavior. Despite the excellent mechanical properties of DP- and TRIP-steels in the tensile test their performance concerning stretch-flangeability and bendability is limited. This resulted in the development of complex phase (CP) steels, which mainly consist of hard microstructural phases. Therefore, CP-steels have a more homogeneous hardness distribution obtaining excellent bendability properties. [7] In general DP-, TRIP- and CP-steels are referred to as the 1<sup>st</sup> generation of AHSS. Around the turn of the millennium extensive researching efforts have been made to develop a fully austenitic steel grade affordable for the automotive industry by alloying with Mn (15-30 mass.-%). As these steels deform mainly by the formation of twins, they are called twinning induced plasticity (TWIP) steels. Those austenitic C-Mn steels display remarkable mechanical properties with product of ultimate tensile strength (UTS) multiplied by total elongation (TE) of more than 50.000 MPa%. [8,9,10,11,12] Together with the high C-Mn-Al-alloyed TRIPLEX-steels they represent the 2<sup>nd</sup> generation of AHSS. Due to high alloying costs, challenging manufacturing and delayed hydrogen cracking these steel grades never really succeeded on the market. Currently the development of steel grades which are postulated to be the 3<sup>rd</sup> generation of AHSS is ongoing. Increased research and development efforts have been made to investigate several promising alloying concepts. This work concentrates on the steel grade of so-called Medium-Mn-steels, which are TRIP-assisted steels consisting of a fine-grained ferritic matrix with about 30 vol.-% of retained austenite. The typical chemical composition of this steel group contains between 0.05-0.2 mass-% C and between 4-10 mass-% Mn.

## 2. Objectives

The purpose of the current study was to determine the potential of Medium-Mn-steels (C-Mn concepts) produced *via* batch annealing concerning their mechanical properties compared to 1<sup>st</sup> generation AHSS. Therefore, the influence of C (0.003-0.12 wt-%) and Mn (4.8-6.4 wt-%) was investigated by studying six chemical compositions. Concerning the heat treatment, the influence of the annealing temperature during intercritical annealing was thoroughly examined. Additionally an optional two-step heat treatment, containing a full austenitization prior to the intercritical annealing, was applied.

This work set out to characterize the mechanical properties of Medium-Mn-steels by tensile testing and to clarify the microstructure – property relationship properly. Therefore, tensile testing combined with thermodynamic modelling, detailed microstructural investigations by qualitative and quantitative electron microscopy as well as extensive dilatometric testing was used to characterize this relation. Particular interest was placed on the yield point phenomena observed with this steel group. On the one hand, this aspect was investigated thoroughly in order to obtain a metallurgical explanation in terms of the scientific progress and on the other hand, to find ways to overcome this potential drawback in industrial application. In order to understand the materials behavior, transmission electron microscopy and thermographic investigations during deformation, were performed. A further focus was given to the work hardening behavior of these steels as it substantially contributes to the obtained mechanical properties. Here, the retained austenite stability was highlighted and investigated by interrupted tensile testing combined with the measurement of the retained austenite content. Several analytical techniques to determine the chemical stability (energy-dispersive and wave-dispersive X-ray spectroscopy) and quantitative metallography in order to estimate the influence of the mechanical stabilization were used. The last highlighted topic is represented by the investigated damage response of the steel group. Analysis of the fracture behavior (thickness strain, microscopic and macroscopic fracture appearance) as well as the void appearance contributed to this thematic focus.

The overall objective of the study was to obtain a clear understanding of the microstructural mechanisms controlling the mechanical behavior of Medium-Mn-steels concerning different aspects (yielding, work hardening, damage). As a result a clear validation of the influence of C and Mn as well as the intercritical annealing temperature and applied HT schedule on Medium-Mn-steels should be given.

### 3. Literature

In the following chapter many different sources are cited, all of them applying a different nomenclature for the used materials. In order to obtain a consistent nomination within this work and add information about the material's chemical composition, names consist of the rounded percentage of the main alloying elements in weight-percent.

#### 3.1 Recent developments in AHSS

**Figure 3.1** gives an overview of all the available cold rolled steel grades according to their total elongation and ultimate tensile strength. The blue bubbles represent the mild steels and conventional HSS with tensile strength typically up to 550 MPa. The green bubbles illustrate the currently applied 1<sup>st</sup> generation of AHSS including DP-, CP-, TRIP- and martensitic steels. The orange bubble in the upper left corner shows the outstanding mechanical properties of the 2<sup>nd</sup> generation of AHSS – the fully austenitic steel grades. D. K. Matlock *et al.* [13] addressed the property gap between the available 1<sup>st</sup> generation of AHSS (green) and the 2<sup>nd</sup> generation (orange) as property band for the future 3<sup>rd</sup> generation of AHSS with improved properties compared to the 1<sup>st</sup> generation and reduced costs compared to the 2<sup>nd</sup> generation.

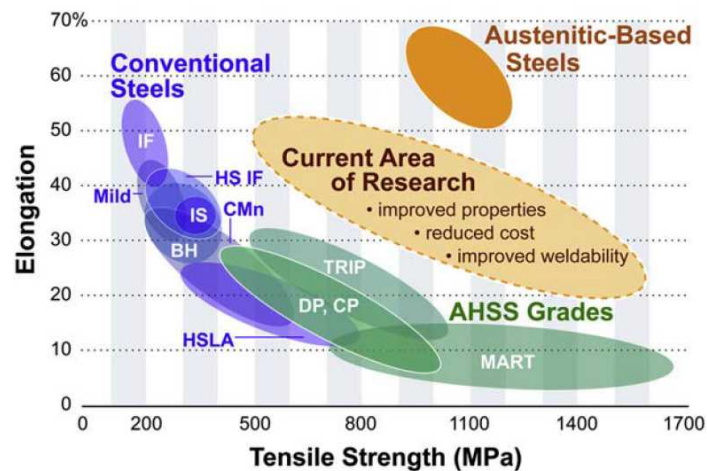


**Figure 3.1:** Tensile strength vs. elongation of available steels grades and targeted properties of the current research work [14]

In order to fulfill the property requirements several promising candidates were presented lately. In **Figure 3.2** a selection of the most interesting reported concepts and their tensile properties (adjusted to ASTM E8 tensile specimen geometry) are shown. The group of Medium-Mn-steels is represented by the work of M. J. Merwin *et al.* [15,16] indicated by the green area. Reported tensile strengths between 800 and 1400 MPa and elongations between 10 and 30 % clearly indicate the great variety of achievable properties. Optimum strength-ductility combinations were obtained at tensile strengths below 1000 MPa, where the combination of UTS\*TE reached about 25.000 MPa%. This clearly fulfills the targeted properties of 3<sup>rd</sup> generation of AHSS. Aside from the group of Medium-Mn-steels, several other to some extent very promising approaches, towards the 3<sup>rd</sup> generation of AHSS were made. The group of modified TRIP- steels in **Figure 3.2** partially obtained very high elongations reported especially by O. Matsumura *et al.* [6]. Unfortunately, these alloying concepts contain up to 0.4 mass-% C, which is not preferred in terms of weldability. A leaner

alloying concept (0.2C-1.5Mn-1.5Si) was suggested by K. Sugimoto *et al.* [17]. TRIP-assisted steels with a fully bainitic matrix instead of a ferritic one (in **Figure 3.2** referred to as “TRIP Type Bainite”) so called TRIP-assisted Bainitic Ferrite (TBF) steels, can obtain UTS of 900 MPa and TE of up to 16 %. The steel group of bainitic steels in **Figure 3.2** represents one further steel concept based on a bainitic microstructure. All these concepts achieve very high UTS of  $\geq 1400$  MPa. Some approaches as of H. K. D. H. Bhadeshia and D. V. Edmonds [18] (0.4C-3Mn-2Si) reached extraordinary mechanical properties but the bainitic transformation took place within several days which limits its industrial use. Efforts have been made to design leaner alloying systems and more industrial applicable processing times. [19,20] Another material concept using the TRIP-effect was introduced by E. De Moor *et al.* [21,22] the so called Quenching and Partitioning (Q&P) steels. Q&P-steels consist of a martensitic matrix and therefore UTS between 800 and 1600 MPa and corresponding TE between 10 and 25 % can be achieved.

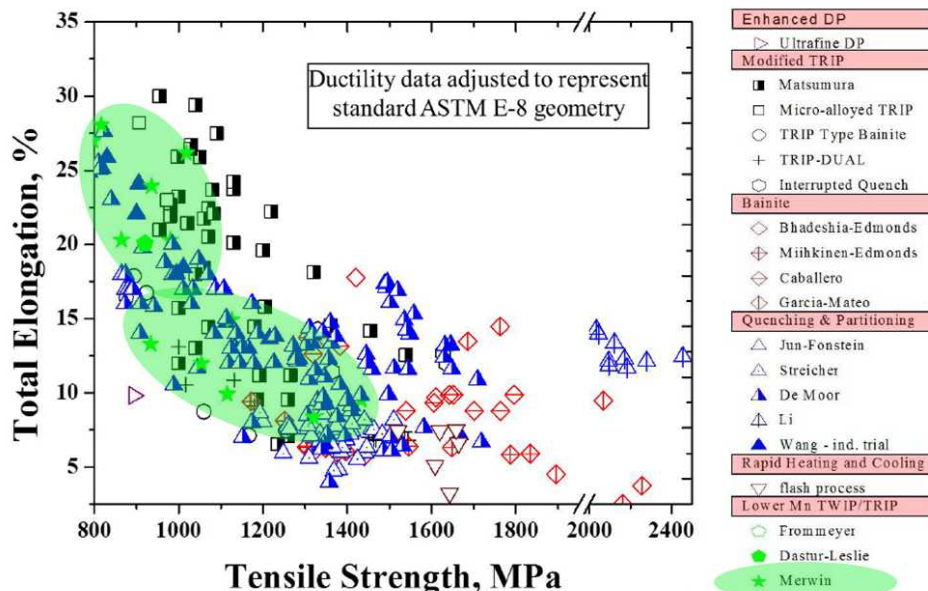


**Figure 3.2:** Overview of reported mechanical properties on potential 3<sup>rd</sup> generation of AHSS adjusted to ASTM E-8 geometry [23]

### 3.2 Current state of research - Medium-Mn-steels

First research work concerning the development of Medium-Mn-steels goes back to R. L. Miller [24] in 1972. In his work he suggested intercritical annealing of high alloyed Ni (9-21 %) steels and a 6 %-Mn steel for holding times within the range of hours to obtain remarkable mechanical properties. At that time this alloying concept did not meet the requests of the industry. In 2007 M. J. Merwin [15] readopted the alloying design and proposed a simple C-Mn chemical composition containing 0.1 %C and 5-7 %Mn for intercritical annealing in batch furnaces. Compared to the 1970's, the requirements of the automotive industry have radically changed and the alloying concept of Medium-Mn-steels has currently found rising attention. The alloying concept is proposed as one of the most promising candidates to fulfil the property requirements of the 3<sup>rd</sup> generation of AHSS. Up to now, concepts for a production route via batch annealing (BA), which involves annealing an entire

coil in a large furnace for several hours, and continuous annealing lines (CAL), where the typical annealing times is within the range of minutes, exist.

**Mechanical properties.** Figure 3.3 shows a selection of the reported values of UTS vs. TE of Medium-Mn-steels in literature. [15,16,21,24-38] To improve comparability the total elongations are normalized to a gauge length of 80 mm. Sorted according to the applied heat treatment (HT), (Figure 3.3a) displays the mechanical properties for BA concepts. The reported tensile strengths range between 550 and 1150 MPa, while total elongations from 15 to 41 % can be stated. The CAL concepts (Figure 3.3 b) generally offer higher tensile strengths (750-1600 MPa) and lower total elongations (7-27 %). From the great variety of mechanical properties reported in literature it can be seen that Medium-Mn-steels are a highly interesting candidate for 3<sup>rd</sup> generation AHSS as they could be potentially used in many automotive applications.

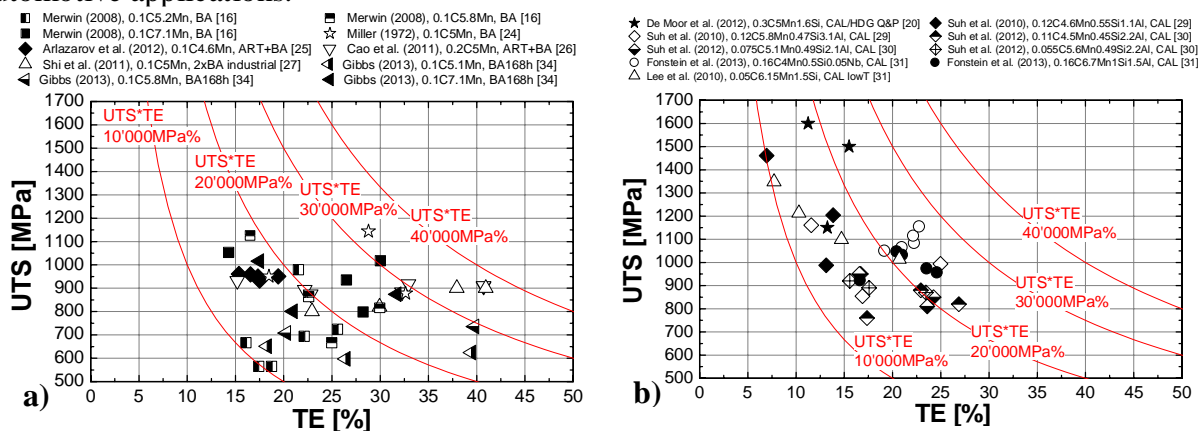


Figure 3.3: Literature review – mechanical properties of Medium-Mn-steels reported for a) batch annealing (BA) and for b) continuous annealing lines (CAL) [16,21,24-27,29-32,34]

Furthermore, the variation of mechanical properties within one chemical composition, based on the respective intercritical annealing temperature ( $T_{IA}$ ) is also very high. As Figure 3.4 shows for a 0.1C7Mn altering the  $T_{IA}$  and therefore the respective phase fraction of ferrite, retained austenite and martensite leads to changing UTS between 800 to 1400 MPa and TE from 12 to more than 40 %. Despite the great potential in the application of the material and the new possibilities of designing automotive components, this figure also reveals the great challenge in manufacturing these steel grades concerning process stability as small variations in the process temperature have huge effects on the properties.

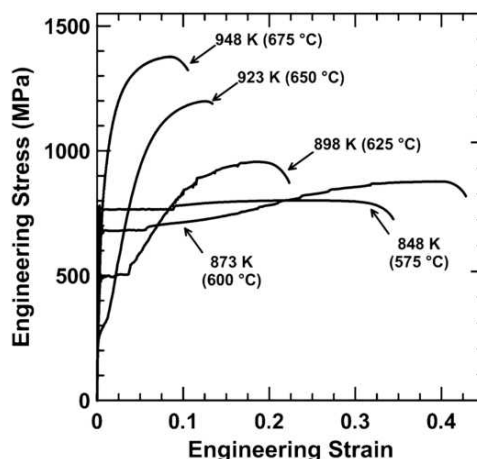
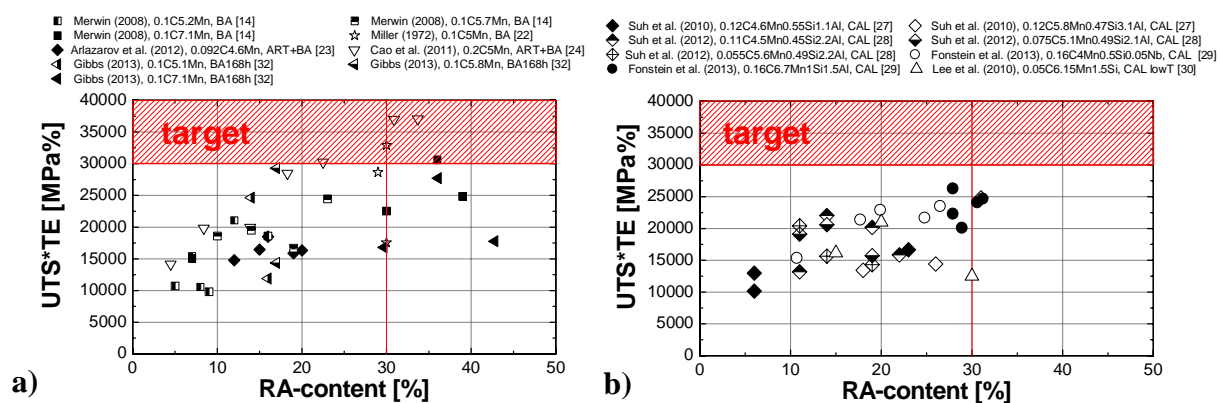


Figure 3.4: Tensile stress-strain curves of 0.1C7Mn annealed for 1 week at  $T_{IA} = 575 - 675$  °C [34]

**Alloying concepts.** Depending on the selected production route (batch or continuous annealing) the alloying concept has to be adapted. For the batch annealing route simple C-Mn concepts are suitable. The current research work concentrates on C-contents from 0.05-0.2 wt % and Mn-contents from 4-7 wt-%. [15,32,34] Both elements are austenite stabilizers and lower the  $A_{c1}$ - and  $A_{c3}$ -temperature. As the batch annealing route provides long annealing times in the range of hours and days respectively, the  $T_{IA}$  can be rather low. The relatively low diffusion rates of Mn at low  $T_{IA}$  are compensated by the annealing time.

For continuous annealing lines the boundary conditions are different. Here time definitively is a limiting factor. Thus, it is necessary to enhance the diffusion rate by annealing at elevated  $T_{IA}$ . As Al is known to increase the  $A_{c1}$ - and  $A_{c3}$ -temperature, Medium-Mn-alloying concepts for continuous annealing additionally contain between 1-3 % Al. [29] Furthermore, the addition of Si between 2-3 % on top of Al alloying has also been reported. [39,40]

**Microstructure.** The general idea of Medium-Mn-steels is to produce a duplex microstructure consisting of ferrite and retained austenite. Referring to a very straightforward prediction of mechanical properties based on microstructural components, proposed by D.K. Matlock and J.G. Speer [41], more than 30 vol.-% of ideally stabilized retained austenite is necessary to meet the targeted properties for a third generation AHSS. **Figure 3.5** shows reported  $UTS*TE$  as a function of the retained austenite. [16,21,24-32] For BA as well as CAL concepts the trend indicates that increasing the retained austenite content in general results in better mechanical properties. But it is important to notice that this is not valid for all the data. Especially for high amounts of retained austenite  $\geq 35$  % generally very poor mechanical properties are reported. This indicates a very unstable retained austenite which cannot fully contribute to improving the mechanical properties. Moreover, it can be seen that in order to accomplish  $UTS*TE > 30.000$  MPa% for BA a smaller amount of retained austenite is sufficient than for CAL. Again this can be referred to the retained austenite stability, which is assumed to be higher for BA. The highest products of  $UTS*TE$  are reported for BA concepts.



**Figure 3.5:** Literature review –  $UTS*TE$  as a function of the retained austenite (by XRD) –content for **a)** batch annealing (BA) and for **b)** continuous annealing lines (CAL) with the shaded area representing the targeted  $UTS*TE > 30.000$  MPa% [16,24-26,29-32,34]

A. Arlazarov *et al.* [42] studied the microstructural evolution of a Medium-Mn-steel during intercritical annealing with initial undeformed and deformed martensitic microstructure respectively. **Figure 3.6** illustrates the schematic process of austenite formation during



intercritical annealing. The initial martensitic microstructure, as obtained after hot rolling or prior full austenitization and quenching, first underwent a precipitation of cementite along the laths of the martensite and the grain boundaries. Hence, austenite nucleation and growth occurred lath-like along the martensite laths and globular at the high-angle grain boundaries of prior austenite grains. Consequently this resulted in a double morphology of lath-like retained austenite  $\gamma_L$  and a globular one  $\gamma_G$  especially at the triple points of the former austenite. In contrary, in the case of the initially deformed microstructure (*e.g.*: after cold rolling), restoration and recrystallization preceded the austenite formation. Therefore, the obtained retained austenite morphology after the heat treatment was globular  $\gamma_G$ .

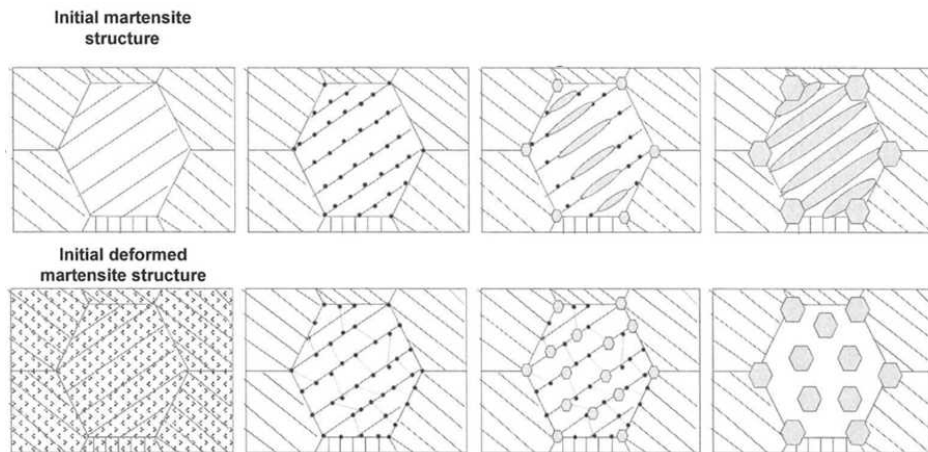


**Figure 3.6:** Schematic illustration of austenite formation during intercritical annealing (grey areas – austenite) [42]

A further crucial microstructural aspect of Medium-Mn-steels, which contributes significantly to their mechanical behavior, is the very small grain size that is mainly below 1  $\mu\text{m}$ . [24,43]

**Heat treatment schedules.** The main heat treatment step in the producing of Medium-Mn-steels is an intercritical annealing step. Depending on which production route is chosen the holding time at  $T_{IA}$  ranges between several minutes (continuous annealing) or several hours (batch annealing). In both cases, it has to be ensured that the intercritically formed austenite is stabilized to room temperature. Therefore, a sufficient chemical as well as mechanical stabilization is essential.

The  $T_{IA}$  has proven to be the dominant influencing factor on the amount of intercritically formed austenite. The dilatometric curves of 0.15C4Mn [37] (**Figure 3.7**) during intercritical annealing clearly indicate that the amount of intercritical austenite increases with increasing  $T_{IA}$ . Furthermore, **Figure 3.7** reveals the decreasing stability of the formed austenite. While annealing at 650 and 675  $^{\circ}\text{C}$  respectively did not cause any transformation during cooling, annealing at  $T_{IA} \geq 700$   $^{\circ}\text{C}$  provoked a martensitic transformation, indicated by the black arrows. The higher the  $T_{IA}$  the higher was the resulting  $M_s$ -temperature of the intercritical austenite. This indicated a lower stabilization of the austenite. The  $T_{IA}$  for Medium-Mn-steels should be selected such that no martensitic transformation occurs during cooling.



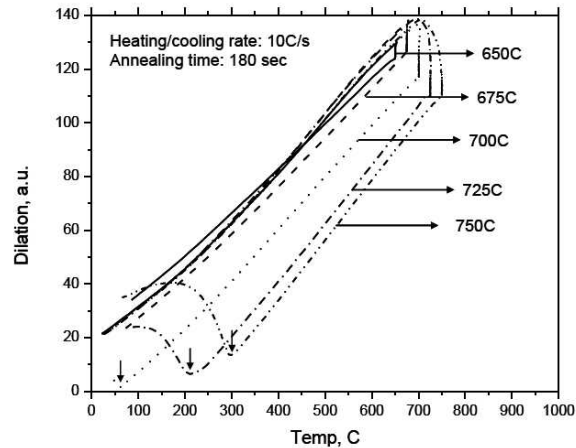


**Figure 3.7:** Dilatometric curves of 0.15C4Mn during intercritical annealing [37]

Furthermore, the  $T_{IA}$  determines the diffusion rate and solubility of alloying elements in ferrite and austenite as well as the amount of these two constituents in the microstructure. **Figure 3.8** shows that intercritical annealing at altering  $T_{IA}$  for 60 h results in Mn-contents up to 12 % Mn in the austenite while the Mn-content in ferrite stays rather low.

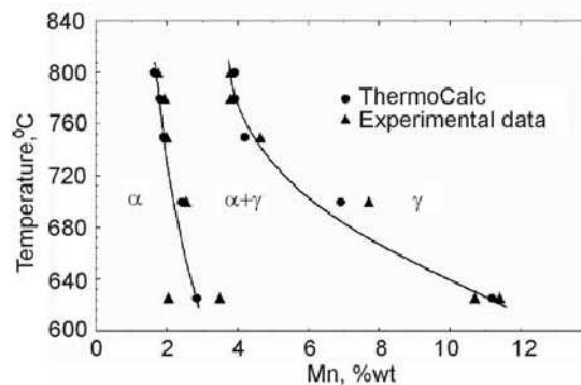


**Figure 3.8:** Mn-distribution in ferrite and austenite depending on annealing temperature for 0.05C4Mn  $t_{IA} = 60$  h [44]

As shown in several studies on Medium-Mn-steels the retained austenite stability was ensured, besides C-partitioning and the small grain size, by a significant Mn-enrichment of the austenite. [25,43,45] **Figure 3.9 a)** illustrates the Mn-content in the initial cold rolled martensitic material, where the Mn is evenly distributed. After annealing at  $T_{IA} = 680$  °C for 180 s the martensite was tempered and a significant amount of austenite was formed. After the HT the Mn-content in the austenite was significantly higher with about 8 mass-% than in the ferrite with about 4 mass-%. A clear diffusion profile was detected on the phase boundary of the recrystallized ferrite. After annealing at  $T_{IA} = 680$  °C for 24 h and cooling to RT (**Figure 3.9 b)** no retained austenite was found. The intercritical formed austenite fully transformed into martensite during cooling. Although the Mn-content in the present martensite was about 8 mass-%, which corresponded with the enrichment of the stable austenite after annealing for 180 s, the stability decreased due to grain growth of the austenite and provoked the martensite formation. Nevertheless, substantial Mn-diffusion from ferrite to austenite took place during the intercritical annealing. [43]

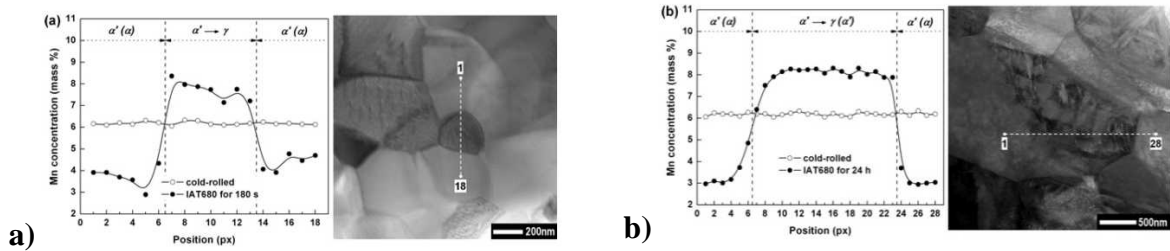


**Figure 3.9:** Mn-distribution and corresponding microstructure in TEM of 0.05C6Mn1.4Si before and after intercritical annealing at  $T_{IA}= 680\text{ }^{\circ}\text{C}$  for **a)** 180 s and **b)** 24 h [43]

**Figure 3.10** shows that besides the one-step intercritical annealing, there is one further existing HT concept, which includes a full austenitization prior to the intercritical HT step. [25,25,45, 46 ] This two-step HT concept is often referred to as austenite reverse transformation (ART) annealing. [25,45] Furthermore, **Figure 3.10** reveals the microstructural development during the HT. The initial microstructure for the one-step HT consists of heavily cold worked martensite (and bainite). Depending on the selected  $T_{IA}$  this deformed microstructure recrystallizes during heating or intercritical annealing. Corresponding to the applied  $T_{IA}$  a certain amount of austenite is formed and enriched in C and Mn. By sufficient stabilization of the austenite this HT results in a globular shaped ferritic/austenitic microstructure at RT. The two-step HT additionally consists of a full austenitization prior to intercritical annealing (**Figure 3.10 b**) in order to establish an undeformed martensitic microstructure. The same effect can be achieved by providing a sufficient cooling rate after the hot rolling process. This martensitic microstructure is then strongly tempered during heating to  $T_{IA}$  and annealing. Alike to the one-step HT, austenite is formed and enriched in Mn and C. Finally, the resulting microstructure at RT differs mainly in its shape, which is dominantly lath-like.

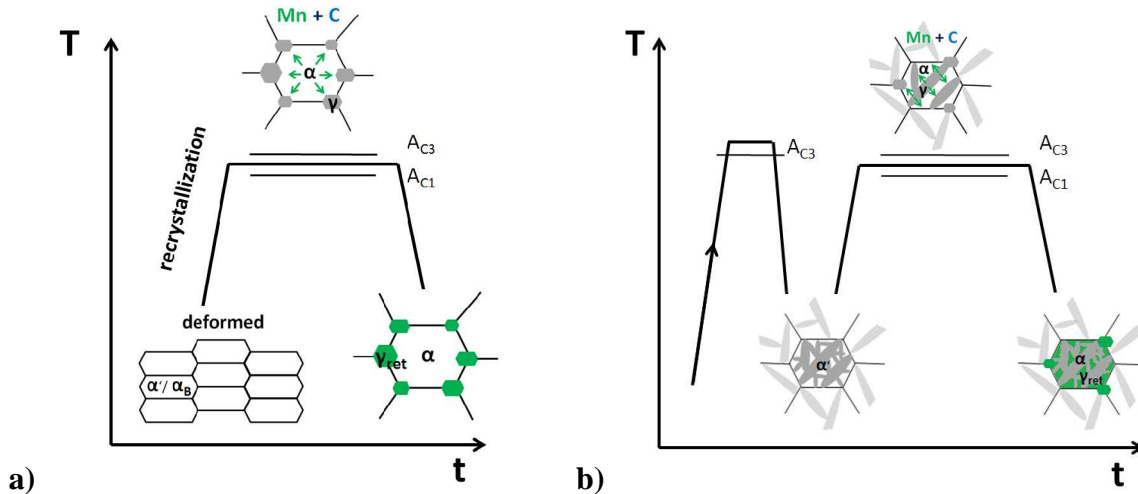


**Figure 3.10:** Time-temperature schedule and microstructural development during **a)** one-step HT and **b)** two-step HT according to [47]

### 3.3 Retained austenite and TRIP-phenomenon

In pure iron austenite is referred to as a high temperature phase. Nevertheless, there are certain conditions that can stabilize austenite to room temperature. For example austenite can be retained as a result of an incomplete martensitic transformation after hardening of steel with  $\geq 0.5\text{ \% C}$ . [48] In this case the retained austenite represents an inauspicious

microstructural component which can cause poor dimensional stability of the end-product. [49] On the other hand great effort is put into retaining austenite to room temperature in order to obtain the so called Transformation Induced Plasticity (TRIP) effect. Most commonly the TRIP-effect is used in high strength cold rolled sheet steels to obtain improved ductility by the transformation of austenite into martensite. This phenomenon was first described by V.F. Zackay *et al.* [50] in 1967 observed in a high alloyed Cr-Ni steel. An important step towards industrial application was made by O. Matsumura *et al.* [6] in 1987 by showing that via intercritical annealing and subsequent isothermal holding in the bainitic transformation region, often referred to as “austempering”, substantial amounts of dispersed retained austenite can be stabilized in a low alloyed 0.4C1.5Si0.8Mn steel. The improvement of the combination of strength and ductility in TRIP-assisted steels can be explained by the increased strength of  $\alpha'$  compared to  $\gamma$  and the simultaneous local strengthening of the matrix caused by the volume expansion due to the  $\gamma$  to  $\alpha'$  formation. As a consequence, the resulting high strain hardening coefficient leads to a delayed necking of the material as can be derived from **Equation 3.1** the Considère instability criterion:

$$\sigma_{true} = \frac{d\sigma_{true}}{d\varepsilon_{true}}. \tag{3.1}$$

Here  $\sigma_{true}$  is the true stress and  $\varepsilon_{true}$  the true strain.

In order to achieve high uniform elongations, a steady and moderate hardening is required. Therefore, the amount and also stability of the retained austenite plays a major role in order to obtain excellent mechanical properties. [51] It is necessary that the stability of retained austenite is not too low – meaning that the entire  $\gamma$  to  $\alpha'$  transformation occurs at small strains – but also not too high – meaning that no or only little  $\gamma$  to  $\alpha'$  transformation occurs. Consequently adjusting the optimal retained austenite stability is one of the main keys to achieve excellent mechanical properties. **Figure 3.11** shows that at temperatures below  $M_s$  the chemical driving force  $\Delta G_1$  is large and the  $\gamma$  to  $\alpha'$  transformation starts without additional external forces. At temperatures above  $M_s$  an additional energy of the magnitude  $U$  is necessary to form martensite. This energy can be introduced by applying external stresses which adds as mechanical driving force to the available chemical driving force  $\Delta G_2$  (**Equation 3.2**).

$$U = \Delta G_1 - \Delta G_2. \tag{3.2}$$

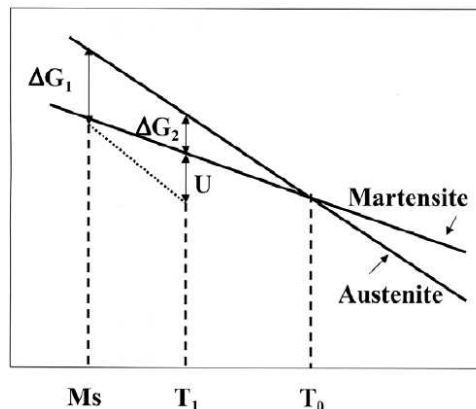


**Figure 3.11:** Compensation of shortfall in chemical driving force compensated by mechanical driving force [52]

**Figure 3.12** illustrates the dominant deformation mechanisms of austenite depending on the deformation temperature. [56] In the temperature range between  $M_s$  and  $M_s^\sigma$  the austenite rapidly transforms to martensite initiated by elastic stresses. The mechanical driving force needed for  $\gamma$  to  $\alpha'$  transformation is rather small. At  $M_s^\sigma$  the austenite transforms when the applied stress equals the yield stress. Above this temperature the austenite transformation changes from stress-induced to strain-induced martensitic transformation. The austenite is plastically deformed and it is assumed by G.B. Olsen *et al.* [53] that shear band intersections are most likely the nucleation site for martensitic transformation. This shear bands can be mechanical twins, stacking faults or  $\epsilon$ -martensite plates. [54,55] Increasing the deformation temperature above  $M_d$  austenite is not transformed while plastic deformation. In practice  $M_{d30}$  – indicating the temperature where at 30% of plastic strain 50% of the existing austenite is transformed – is rather used instead of  $M_d$ . In order to obtain superior mechanical properties compared to other steel grades the stability of the retained austenite should be adjusted so that  $M_s^\sigma$  is below room temperature and  $M_{d30}$  is above room temperature.

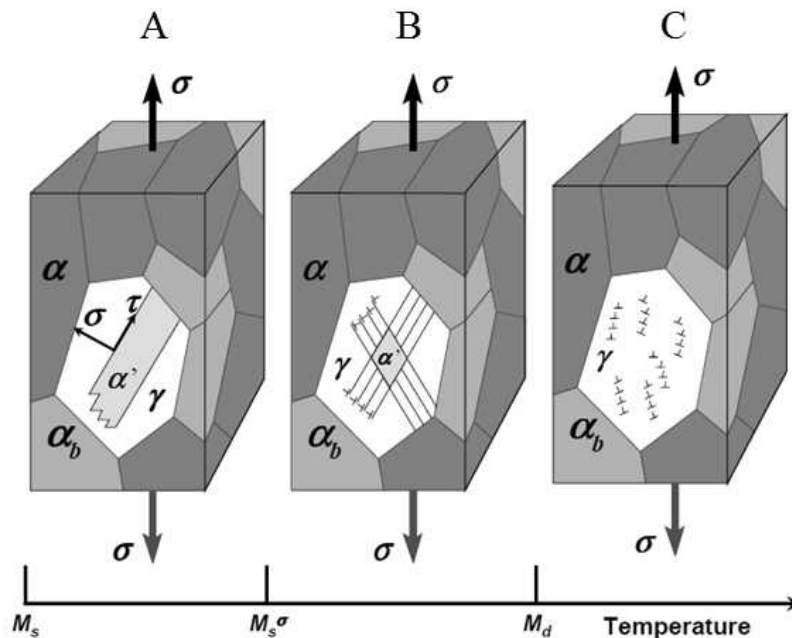


**Figure 3.12:** Schematic illustration of the dominant deformation mechanisms of austenite in different temperature ranges A – stress-induced plasticity, B – strain-induced plasticity and C- dislocation glide plasticity [56]

**Figure 3.13 a)** illustrates the influence of the C- and Mn-content on the phase fractions of austenite,  $\alpha'$ - and  $\epsilon$ -martensite at RT. The increase of both elements leads to a stabilization of austenite. Furthermore, the dominant deformation mechanism, determined by the stacking fault energy (SFE) of the material, is altered by its chemical composition (**Figure 3.13 b**). [8,10,57] With increasing C- and Mn-content the deformation mechanism changes from  $\alpha'$ / $\epsilon$ -martensite formation to mechanical twinning at  $SFE > 20 \text{ mJ/m}^2$ .

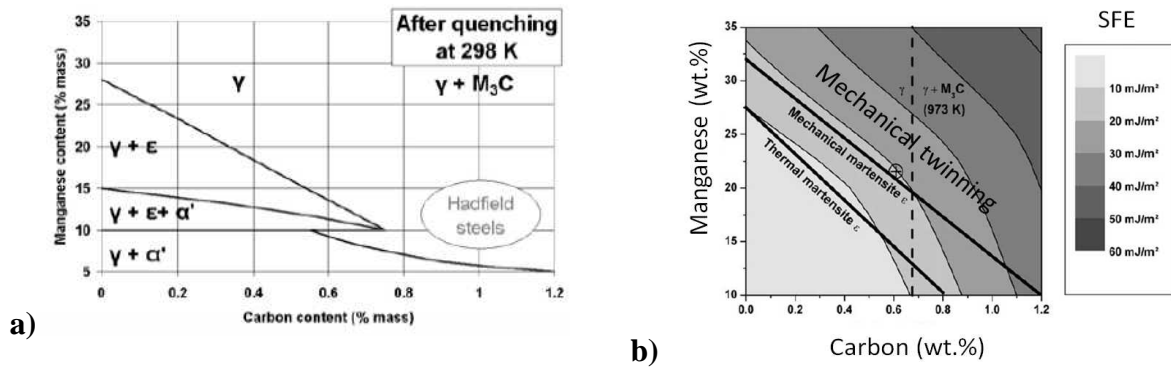


**Figure 3.13:** Formation of phases austenite,  $\alpha'$ - and  $\epsilon$ -martensite as a function of C- and Mn-content after **a)** heat treatment [57] and **b)** deformation [10]

The stability of austenite is determined by a number of influencing factors on the chemical and mechanical stability. The C-content, which lowers the  $M_s$ -temperature drastically, strongly increases the chemical stability. Typical C-concentration in the retained austenite of TRIP-assisted steels are reported mostly between 0.5-1.5 mass-% C. [51,58,59] Furthermore, also Mn significantly increases the chemical stability of retained austenite. Austenite stabilization through Mn is not a key feature in conventional TRIP-steels but for Medium-Mn-steels it is one of the main influencing factors as pointed out in detail in **Chapter 3.2**. [25,43,45] Regarding the mechanical stabilization of retained austenite, the grain size is the most decisive influencing factor. Smaller retained austenite grains lower the  $M_s$ -temperature [60,61] (**Figure 3.14**) as they offer less potential nucleation sites for the martensitic transformation and therefore a higher driving force is required. [62] Grain sizes between 0.01 and 1  $\mu\text{m}$  have been suggested to ideally contribute to the TRIP-effect. Larger grains tend to transform already before yielding or at a very early stage of straining while grains smaller than 0.01  $\mu\text{m}$  have been reported to not transform at all. [63]

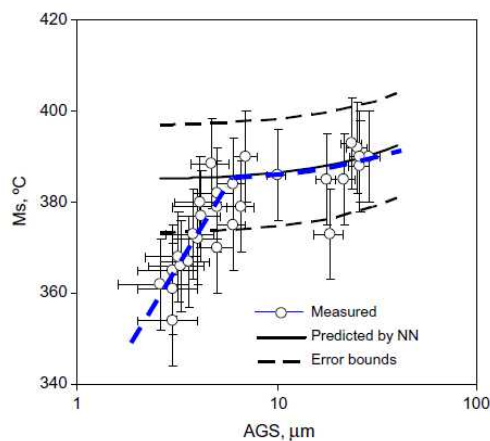


**Figure 3.14:** Comparison of experimentally determined  $M_s$  from different austenite grain sizes and  $M_s$  calculated from neural network (NN) model [60]

Further influencing factors of the mechanical stability of retained austenite are the morphology and the surrounding matrix. Generally it can be stated that lath-like formed retained austenite grains  $\gamma_L$  are more stable than globular ones  $\gamma_G$  [17,64,65] and that a surrounding phase *e.g.* bainite which is harder compared to the austenite enhances its stability. This is explained by a shielding effect of the harder phase whereby more stress is partitioned

into the harder phase, resulting in a more slowly transformation of the austenite. [64,65,66] On the other hand if the surrounding matrix is softer *e.g.* ferrite load is transferred to the retained austenite which than transforms more quickly. [67,68,69] In conventional TRIP-steels these two influencing factors, morphology and surrounding matrix, are connected to each other as the lath-like austenite forms within the hard bainite. Therefore, the impact of each influencing factor on its own is challenging to determine precisely. **Figure 3.15 a)** clearly exhibits the different strain hardening behavior of two microstructures containing dominantly globular retained austenite  $\gamma_G$  and lath-like retained austenite  $\gamma_L$  respectively in a 0.17C2.2Mn1.6Al steel. While the globular retained austenite shows an increasing strain hardening exponent between 0.01 and about 0.03 of true strain, which steadily decreased at higher strains, the microstructure containing the lath-like retained austenite behaves just oppositely. The strain exponent tends to increase up to 0.06 of true strain and then stays constant. This strain hardening behavior of the lamellar austenite results in delayed necking and therefor a higher total elongation.

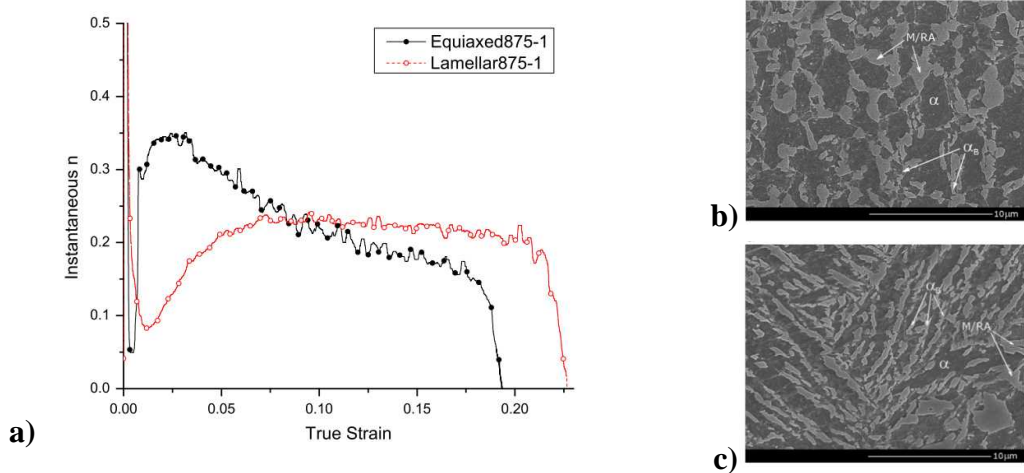


**Figure 3.15: a)** Incremental strain hardening exponent vs. true strain of dominantly globular (black line) and dominantly lath-like (red line) retained austenite containing steel, micrographs of the microstructures containing **b)** globular retained austenite and **c)** lath-like retained austenite [65]

The mechanical stabilization of retained austenite is also influenced by the crystallographic orientation of the grains with respect to the loading direction. [68,70] The {200} planes of the austenite orientated with their normal plane parallel to the loading direction showed the lowest stability. R. Blondé *et al.* [68] argued that the {200} planes experience the highest Schmid factor  $m$  of all planes while K. Asoo *et al.* [70] stressed the fact that the {200} planes bear the highest stresses because they are harder compared to the {111} planes. D. De Knijf *et al.* [71] ranked the influencing factors on the mechanical stability by their importance with the most important being the grain size, second morphology and last crystallographic orientation.

**Kinetics of strain-induced martensitic transformation.** Several approaches describing the kinetics of the strain-induced martensitic transformation have been made so far. [72,73,74] Here the approach of D. C. Ludwigson and J. A. Berger [74] modeled based on an austenitic stainless steel will be discussed in detail. **Equation 3.3** determines the amount of retaining austenite as a function of true strain:

$$\frac{1}{V_\gamma} - \frac{1}{V_{\gamma 0}} = \frac{k_p}{p} \varepsilon^p. \quad 3.3$$

Here  $V_\gamma$  is the volume fraction of retained austenite at a corresponding strain,  $V_{\gamma 0}$  is the volume fraction of retained austenite in the unstrained state,  $k_p$  is the stability constant and  $p$  is a strain exponent corresponding with the autocatalytic effect. Due to the volume expansion during martensite formation internal stresses are introduced which increase the mechanical driving force for the martensite formation and accelerate the strain-induced martensitic transformation. According to O. Matsumura *et al.* [6]  $p$  can be considered as 1 for TRIP-steels because the retained austenite islands are isolated from each other as they are located within the bainitic ferrite. L. Samek *et al.* [75] confirmed this assumption but showed that for higher deformation temperatures the autocatalytic effect cannot be neglected due to a lower yield strength of the austenite. **Figure 3.16** adapted from D. Krizan and B.C. De Cooman [76] shows some reported data of the retained austenite stability of TRIP-steels investigated by the Ludwigson-Berger approach. The  $k_p$ -values varied in a range between 20 and 388. A low  $k_p$ -value corresponds with a high stability. As represented in **Figure 3.16** within the reported data a lower  $k_p$ -value resulted in a higher elongation.

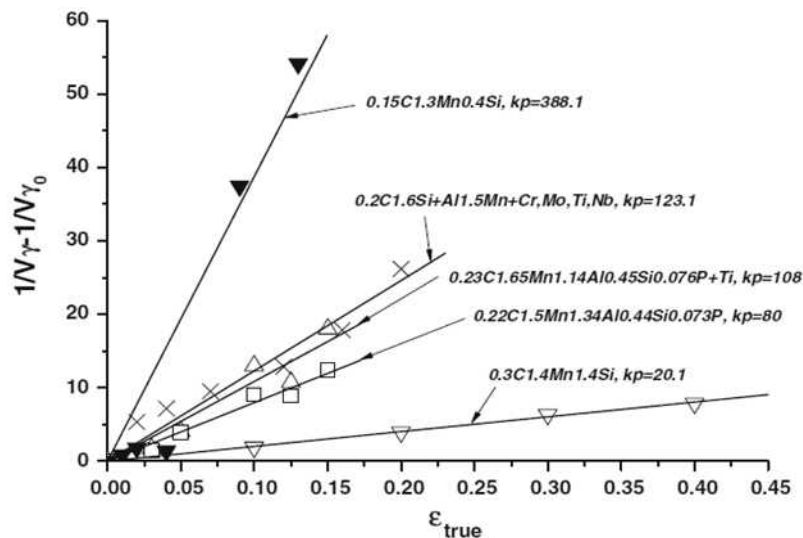


**Figure 3.16:** Comparison of retained austenite stability of reported data of a variety of TRIP-steels [76]

**Modeling of the chemical  $\gamma_R$  stabilization of Medium-Mn-steels.** E. De Moor *et al.* [77] proposed a model for the prediction of the retained austenite content as a function of the  $T_{IA}$  for Medium-Mn-steels. It consists of the following steps:

- The calculation of the equilibrium phase fractions of austenite as a function of temperature
- The calculation of the equilibrium chemical composition of austenite as a function of temperature
- The incorporation of martensite formation during cooling assuming that diffusional transformations are suppressed

The kinetics of the martensite formation were calculated by **Equation 3.4** proposed by D. P. Koistinen and R. E. Marburger [78].

$$f_{\alpha'} = 1 - \exp[-\alpha_c(M_s - RT)^{\beta_c}]. \quad 3.4$$

Here  $f_{\alpha'}$  is the amount of martensite,  $M_s$  is the martensite start temperature, RT is room temperature, and  $\alpha_c$  and  $\beta_c$  are constants. E. De Moor *et al.* [77] suggested  $\alpha_c = 0.011$  and  $\beta_c = 1$ . The  $M_s$  is calculated by **Equation 3.5** proposed by J. Mahieu *et al.* [79].

$$M_s = 539 - 423C - 30.4Mn - 7.5Si + 30Al. \quad 3.5$$

**Figure 3.17 a)** shows an exemplary model prediction of the retained austenite content as a function of the  $T_{IA}$ . As long as no martensite formation occurs during cooling the retained austenite equals the austenite fraction at  $T_{IA}$ , which steadily increases. At the onset of martensite formation the retained austenite decreased. Therefore, a maximum amount of retained austenite exists. In **Figure 3.17 b)** the model prediction is compared with experimental data from [24], which shows besides a shift of the experimental data to higher temperatures, a good accordance.

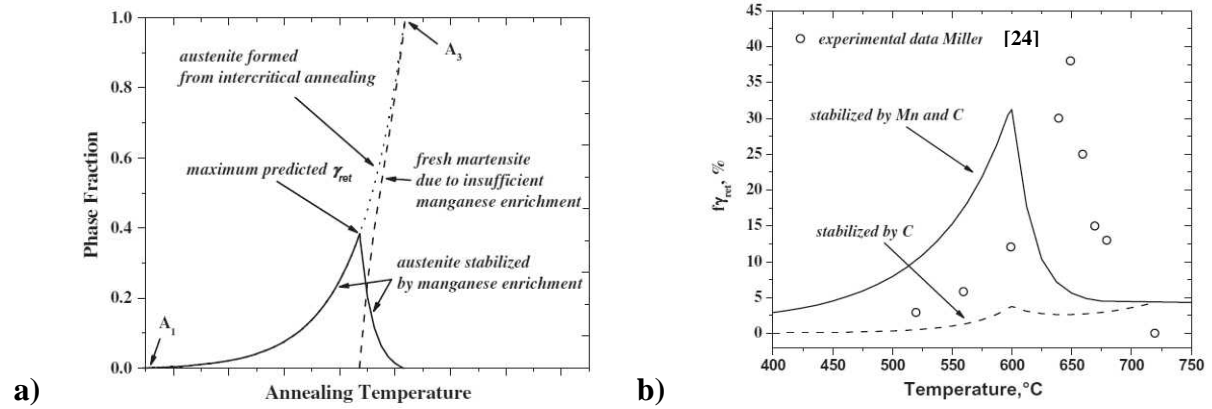


**Figure 3.17:** a) Schematic illustration of predictive model of retained austenite content and b) predicted austenite content by model compared to experimental data [24] after 1 h of annealing [77]

S.-J. Lee *et al.* [80] further developed the model by introducing the constants  $\alpha_c$  and  $\beta_c$  as dependent on the chemical composition of the intercritically formed austenite (**Equation 3.6** and **3.7**). Both constants take into account that higher C as well as Mn-contents retard the martensite transformation.

$$\alpha_c = 0.0076 - 0.0182C + 0.00014Mn. \quad 3.6$$

$$\beta_c = 1.4609 + 0.4483C - 0.0545Mn. \quad 3.7$$

Introducing a value for  $\beta_c$ , which is different from 1, respects the fact that the transformation kinetics of martensite are not a linear function of the temperature. Thus, it is considered that the transformation is related to the temperature-dependence of  $\Delta S^{\gamma \rightarrow \alpha'}$  and therefore **Equation 3.4** is gaining in physical significance.

Furthermore, the model proposed by S.-J. Lee *et al.* [80] pays respect to the ultra-fine grained (UFG) microstructure and its influence on the  $M_s$ -temperature as well as the kinetics of martensite formation. In order to introduce the aforementioned effect of decreasing  $M_s$ -temperature with decreasing grain size **Equation 3.8**, including the effective grain volume  $V/\gamma$ , was incorporated.



$$M_s = 545 - 423C - 30.4Mn - 60.5V_\gamma^{-1/3}. \quad 3.8$$

With decreasing grain size S.-J. Lee *et al.* [80] found that the martensite formation kinetics accelerated. In the past this effect was also reported for various other steels. [81,82] Therefore, the transformation acceleration coefficient  $k_g$  was additionally introduced to the formula proposed by D. P. Koistinen and R. E. Marburger [78], describing the martensite formation kinetics (**Equation 3.9**).

$$f_{\alpha'} = 1 - \exp[-k_g \cdot \alpha_c (M_s - RT)^{\beta_c}]. \quad 3.9$$

### 3.4 Ultra-fine grained steels

One decisive characteristic of Medium-Mn-steels is definitely the ultra-fine grained (UFG) microstructure achieved through intercritical annealing. In the following chapter, steels with an average grain size of less than 1  $\mu\text{m}$  are considered as UFG steels.

Grain size is known to strongly influence a lot of mechanical properties. Grain refinement is one of the strengthening mechanisms of steels expressed by the Hall-Petch relationship (**Equation 3.10**):

$$\sigma_{YS} = \sigma_0 + k \cdot d^{-\frac{1}{2}}. \quad 3.10$$

Here,  $\sigma_{YS}$  is the yield stress,  $\sigma_0$  is the Peierls-Nabarro stress, which is necessary to move a dislocation within a defect free lattice,  $k$  is an experimentally determined, materials depending constant and  $d$  is the grain diameter. The empirical **Equation 3.10** was originally established for grain sizes larger than 10  $\mu\text{m}$ . [83] Several studies of different materials such as Cu and Au [84,85] showed that the Hall-Petch (H-P) relationship is restricted by a certain minimal grain size, where a further decreasing the grain size results in a reduced slope (represented by the constant  $k$ ) of the H-P relationship. Moreover, it is reported that the slope becomes negative when the grain size undergoes a certain lower limit – meaning that grain size softening occurs. This phenomenon is often referred to as inverse Hall-Petch (IH-P) relationship. [86] For most metals a critical grain size for the breakdown was reported for  $d < 30 \text{ nm}$ . [87,88] The classical explanation for the mechanism behind the increase of yield strength with decreasing grain size is that pile-ups in smaller grains contain fewer dislocations. Therefore, the stress at the tip of the pile-up decreases and thus, a higher stress to generate new dislocations in the adjacent grain is required. In very small grains this mechanism is not working anymore as the grains are too small to accommodate dislocation pile-ups or deformation cells. [86,89,90,91] The debate on the mechanisms of IH-P is ongoing and attributed amongst others to diffusional grain boundary sliding (*e.g.*: Coble creep) at temperatures where it is normally restricted [92] and increased absorption of dislocations by grain boundaries [86] respectively.

Furthermore, many other mechanical properties, besides strength, are influenced by the grain size. Most of them are generally improved or at worst not affected with the exception of high-temperature strength and uniform elongation. **Figure 3.18** shows different stress-strain

behavior transitioning from Type I to IV with increasing grain size. Mainly Type I and II are associated with ultra-fine grained steels and aluminum. [24,93-96]

N. Tsuchida *et al.* [96] described the characteristics of the stress-strain behavior as following:

- Type I: continuous yielding; yield point becomes maximum loading point, afterwards load decreases until rupture occurs, no work hardening
- Type II: discontinuous yielding; no detectable yield point elongation (YPE), yield point drop after maximal load, afterwards load decreases until rupture occurs, no work hardening – according to [24,93] Lüders deformation is initiated and necking occurs during the propagation of the band
- Type III: discontinuous yielding, Lüders deformation after yield drop and constant load, subsequent work hardening until load maximum, then load decreases until rupture
- Type IV: continuous yielding, no yield point drop, work hardening until maximal load, then load decreases until rupture

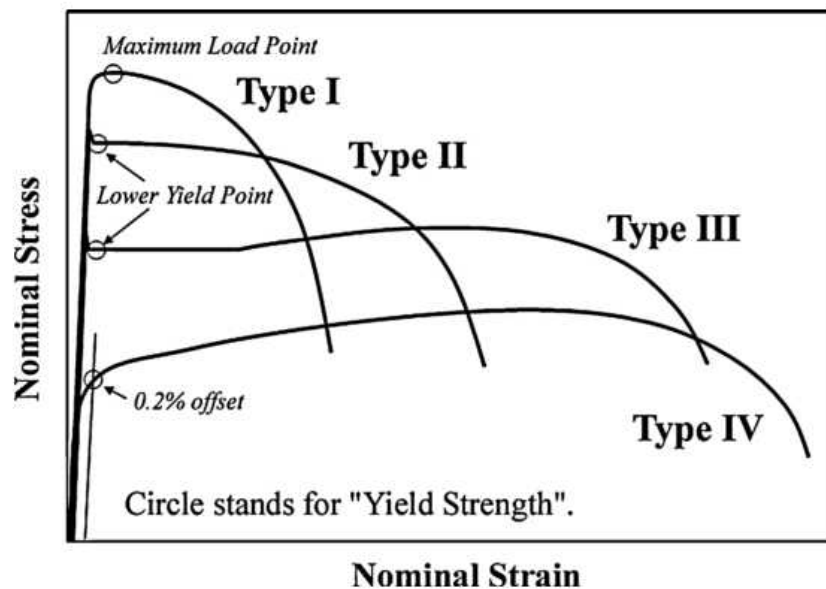


**Figure 3.18:** Schematic illustration of different stress-strain curves [96]

In general UFG materials exhibit very little strain hardening (Type I and II) and extensive Lüders deformation. [97,98] During Lüders band propagation the deformation is localized in the band. For tensile testing the band usually is initiated at the grips and propagates through the entire gauge length at constant stress. J. Butler [97] proposed **Equation 3.11**, where the YPE is assumed to be linearly dependent to the specimen extension rate  $v_c$ , the number of initiated Lüders bands  $n_L$  and the average band velocity  $v_b$ :

$$YPE = \frac{v_c}{n_L \cdot v_b}. \quad \mathbf{3.11}$$

According to B. Jaoul and D. Gonzales [99] large YPE is favored by high yield strength, few active slip systems and low work hardening. Recently, N. Tsuchida *et al.* [98] proposed that YPE is a function of the work hardening rate as the lower yield strength (LYS) (**Figure 3.19**)

for various ferritic steels is independent of different grain size or C-content respectively. The YPE increased exponentially at low work hardening rates.

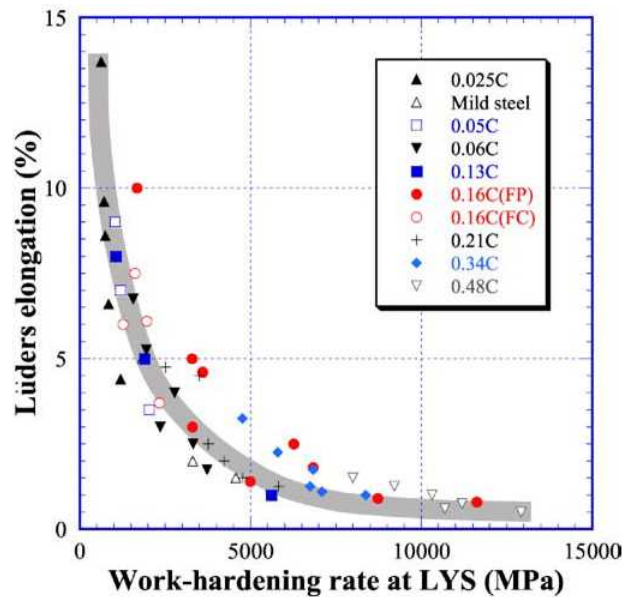


**Figure 3.19:** YPE (here indicated as Lüders elongation) as function of work hardening rate at lower yield strength [98]

Besides localized deformation, the loss of uniform elongation is associated with the limited strain hardenability as expressed by **Equation 3.1** the Considère instability criterion (see **Chapter 3.3**). In the majority of published research work the absence of strain hardening in UFG steels is explained by dynamic recovery. This implies, that with decreasing grain size an increasing amount of dislocations is trapped in grain boundaries. [86,100,101] C. Carlton and P. Ferreira [86] proposed a model assuming that the nature of grain boundaries is not scale dependent but with increasing the amount of grain boundaries in UFG materials the probability of dislocation absorption is steadily increased. The interactions between dislocations and grain boundaries determine important aspects of the materials strength and ductility. The importance of this interaction successively increases with grain refinement and finally dominates at the nano-scaled grain size regime. Grain boundaries represent obstacles to dislocation motion as dislocations generally do not have the proper Burgers vector nor slip plane to glide into the next grain. Thus, in coarse sized grains dislocations tend to pile up and accumulate at grain boundaries and strain hardening is enabled. [102] If dislocations are absorbed by the grain boundaries the strain hardenability is restricted.

A further interesting aspect concerning UFG materials are the reported high elongations during necking (postuniform) which suggest high resistance against micro-crack initiation and growth. As necking occurs, the strain rate increases in the postuniform deformed area. Consequently, an increased stress is required to deform a strain rate sensitive material. Considering the reported increased strain rate sensitivity  $m$  of fine grained materials [103,104] according to A. Vinogradov [102] this enhances the strain hardening in the neck and delays fracture.

In order to overcome the limitation of UFG steels the work hardening rate has to be increased to increase total elongation. Successful strategies that have been reported are the introduction

of a bimodal grain size distribution [89] or of a second, hard phase [105]. Especially UFG steels containing metastable retained austenite transforming into martensite by straining has proven to effectively enhance the uniform elongation. [70,106,107] A further strategy to overcome the drawbacks of UFG materials was reported to be deformation at low temperature as well as high strain rates. Both measures have shown to be an effective way to increase uniform elongation. [91] Both parameters suppress dynamic recovery (annihilation of dislocations at grain boundaries). Therefore, the grains can store a higher dislocations density and the strain hardenability is increased.

### 3.5 Damage behavior of multiphase steels

Ductile fracture in metals is characterized by void initiation, void growth and void coalescence. [108] As shown in **Figure 3.20** voids generally generate at grain boundaries or second phases as non-metallic inclusions, precipitates or grain boundaries of a second phase. Voids form typically at the interface of soft to hard phase or in the soft phase preferable perpendicular to the loading direction.

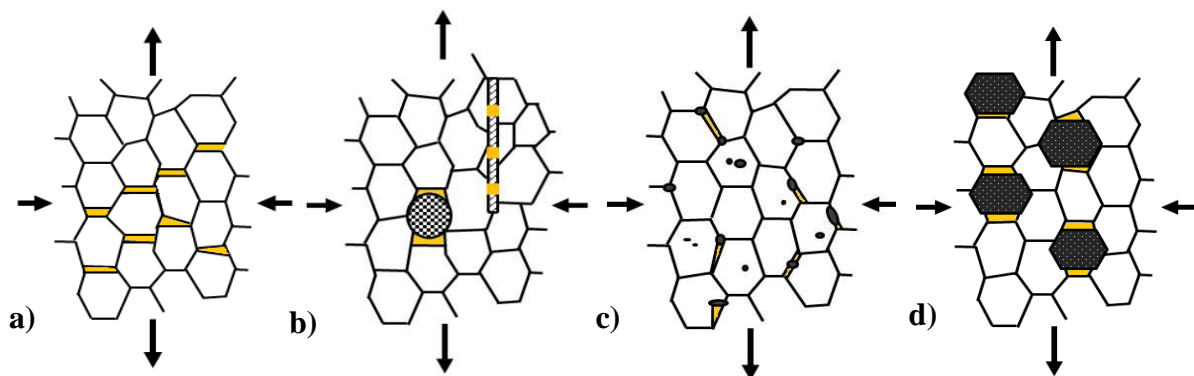


**Figure 3.20:** Schematic illustration of void formation at **a)** grain boundaries, **b)** non-metallic inclusions, **c)** precipitates or **d)** grain boundaries of a second phase

In general voids are easily formed under triaxial stress states. For multiphase steels, with their various microstructural constituents, it has to be distinguished between global and local triaxial stresses. High global triaxial stresses occur *e.g.*: during bending. Local triaxial stresses are provoked by great differences in hardness or formability of the respective phases *e.g.*: between ferrite and martensite. [109,110] It is assumed that global and local triaxial stresses sum up. Therefore, the worst case scenario is *e.g.*: forming sharp edges, which provokes high global triaxial stresses, with a DP-steel, which innately bears high local triaxial stresses due to its microstructure.

M. Kapp *et al.* [111] comparatively investigated the micro-strain deformation behavior of a DP-steel and a CP-steel by tensile testing and digital image correlation. **Figure 3.21** shows the local axial strain distribution, which significantly differs for the two steel grades. Both steels developed bands of high deformation, similarly reported by X. Sun *et al.* [112], oriented in  $35 - 55^\circ$  with respect to the loading direction and building a netlike array intersecting with each other under  $70 - 110^\circ$ . With higher deformation degrees the density of the bands increased. Both steel types showed additionally areas with nearly no deformation (blue). While the DP-steel exhibits about 34 area-% of more or less undeformed area, for the CP-steel only 16 area-% remained weakly deformed. For multiphase steels in general,

deformation is distributed very heterogeneously on a microscopic level while being macroscopically uniform.

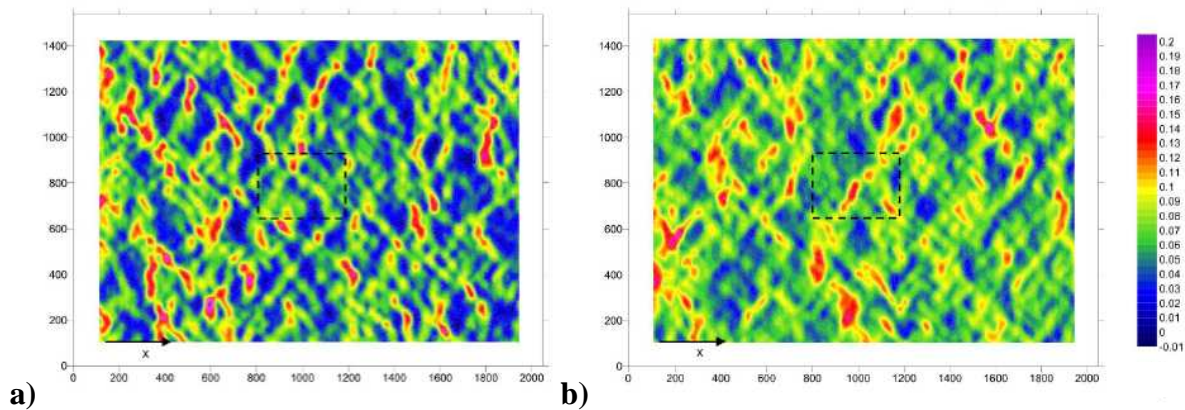


**Figure 3.21:** Local strain distribution (loading direction in x-axis) in **a)** DP-steel and **b)** CP-steel (scan 120 x 90  $\mu\text{m}$ ) [111]

The different behavior in the strain distribution of CP- and DP-steels can be attributed to their different microstructural constituents. In DP-steels the hardness is very unevenly distributed on a microstructural level between soft ferrite and hard martensite. It was shown that during deformation ferrite bore the majority of strain while martensite underwent minimal straining. [113,114,115] The lower the difference in hardness of two phases the sooner the second phase started to deform as well. [116] In DP-steels the strain especially concentrated in narrow ferrite channels situated between martensite grains. [111] For CP-steels straining cannot be attributed to one single phase due to the more homogenous hardness distribution in the respective phases of ferrite, bainite, tempered martensite and martensite. Therefore, CP-steels distribute the strain more diffusely and bear higher local strains resulting in a generally higher damage tolerance and better bendability and stretch-flangeability. [111] Void formation in DP-steels is reported to be microstructure controlled while for CP-steels it is controlled by defects such as non-metallic inclusion.

For DP-steels the hardness of the martensite plays a decisive role for the formation of the local triaxial stresses. **Figure 3.22 a)** displays the influence of the martensite hardness represented by its C-content on the void density at constant strain. The harder the martensite, the higher was the density of existing voids. [117] This indicates that not the amount of martensite but the difference in hardness between the soft and the hard phase is the crucial factor for void formation. **Figure 3.22 b)** and **c)** displays the two typical types of voids observed in a DP-steel. The first type is represented by the decohesion between the ferrite and martensite interface. The **Figure 3.22 b)** displays the void formation at a narrow ferrite channel between two hard martensite grains as described before. The second type of voids that is commonly found in DP-steels occurs by cracking of the hard martensite. The resulting voids appear penny-shaped and very small (**Figure 3.22 c)**). [113,118] Furthermore, network-like martensitic structures in DP-steels have proven to be detrimental for postuniform deformation as the martensite joints are preferred places for void formation. [119]

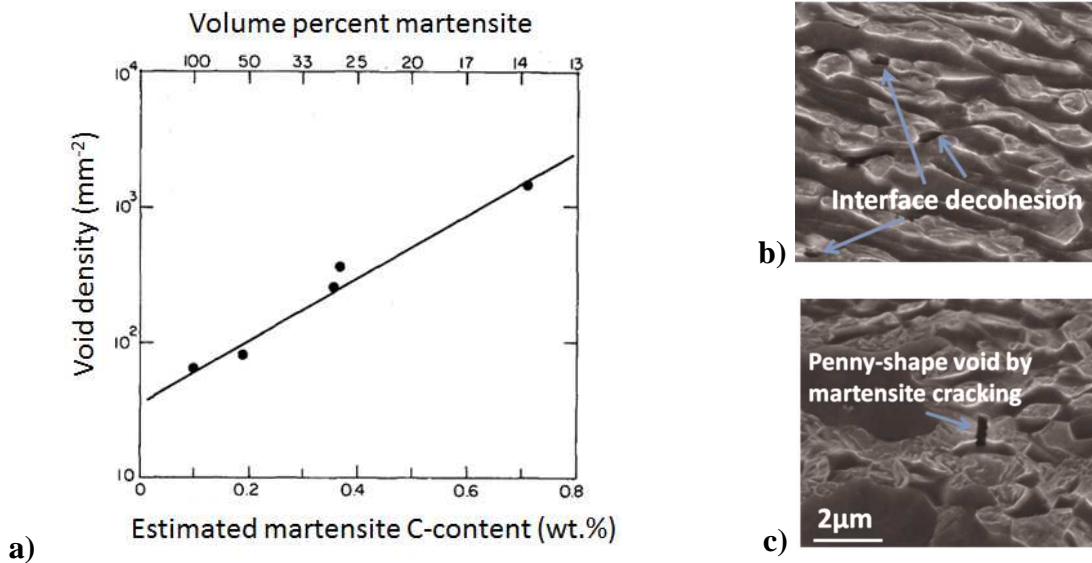


**Figure 3.22:** a) Variation of void density with estimated C-content of martensite at a constant strain of 3.6% [117] b) voids in DP-steel at interface ferrite/martensite and c) voids introduced by martensite cracking [118]

Due to the excellent strain distribution of CP-steels they are reported to be less sensitive to early void formation. Therefore, when comparing the performance of DP- and CP-steels in hole expansion testing (HET) (**Figure 3.23**), which causes increased global triaxial stresses, CP-steels exhibits higher values for the hole expansion ratio (HER). [120] **Figure 3.23** additionally illustrates the influence of different edge conditions during HET: Punching and drilling of the hole introduces a substantial amount of work hardening. Thus, the HER is significantly reduced.

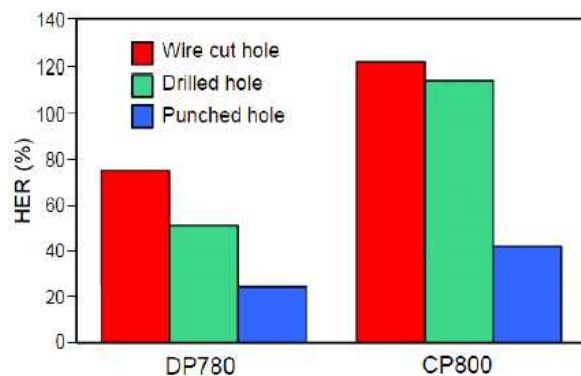


**Figure 3.23:** Hole expansion ratio (HER) of DP- vs. CP-steel with the same tensile strength for different edge conditions [120]

Concerning damage behavior TRIP-steels illustrate a mixed type of DP- and CP-steels characteristics. G. Lacroix *et al.* [121] described the damage behavior as illustrated in **Figure 3.24 a)**. The hardness of the microstructure before deformation is evenly distributed by consisting of ferrite, bainite and retained austenite. While deformation strain-induced martensitic transformation occurred and the austenite transformed to hard martensite accompanied by a volume expansion. This led to a blunting of the pre-crack. Further deformation provoked void formation at the ferrite/martensite interface, comparable to the behavior in DP-steels, which then initiated void growth, coalescence and finally crack initiation. This process is strongly influenced by the stability of retained austenite. As damage is associated with the appearance of martensite, increasing the stability of retained austenite



and retarding its transformation postponed the void formation. On the contrary high carbon contents of the austenite, which ensure the high stability, result in high strength martensite which increases strain incompatibilities. Similar to DP-steels network-like structures of austenite/martensite should be avoided in order to obtain reasonably good damage behavior. [122] The typical void formation is also alike to DP-steels and took place at the ferrite/martensite interface as well as by decohesion of two martensite grains (Figure 3.24 b and c).

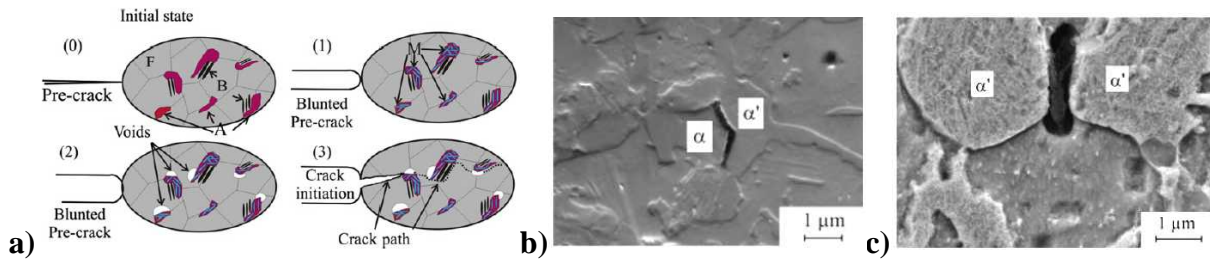


**Figure 3.24:** a) Schematic illustration of damage and fracture process in TRIP-steels (F – ferrite, B – bainite, A – austenite, M – martensite) 0) initial state, 1) crack tip blunting and martensite formation, 2) void formation and 3) void growth, coalescence and crack initiation, b) decohesion between ferrite and martensite and c) decohesion between two martensite grains [121]

Generally it can be stated that grain refinement [118,123] and an evenly distributed hardness increase the materials tolerance against void formation. [109,110]

**Postuniform deformation.** As the damage behavior is controlled by triaxial stress states the behavior of the material during tensile testing in the necking area becomes very interesting. In order to characterize the postuniform deformation several characteristic values are in use. **Figure 3.25 a)** shows the different stages during the elongation of a tensile specimen. At the beginning of the deformation the specimen deforms uniformly until a neck is formed and the entire deformations is limited to a small area. Due to the necking the elongation is unequally distributed along the gauge length as illustrated in **Figure 3.25 b).**

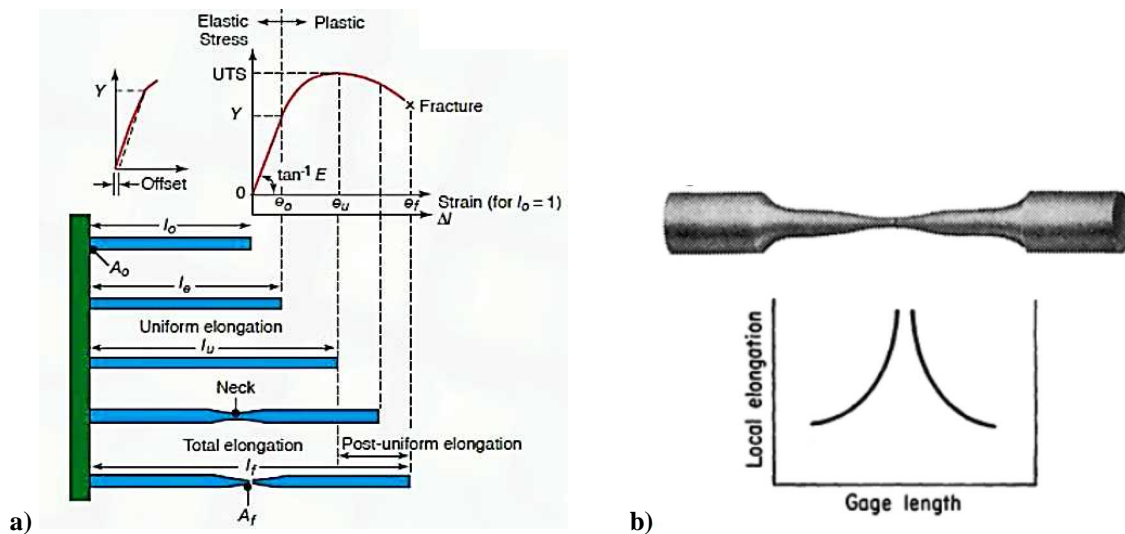


**Figure 3.25:** a) Different stages in the elongation of a tensile specimen [124] b) local elongation with position along the gauge length of the specimen [125]

Therefore, the specimen size plays a decisive role in the obtained total elongation. For smaller samples higher total elongations are achieved as the amount of postuniform elongations is getting more important. On the contrary this means that for rather large sample sizes the uniform elongation is the determining factor and this is triggered by the strain hardenability. In order to characterize the postuniform part of the deformation the reduction of area  $Z$  has shown to be a useful figure (**Equation 3.12**).

$$Z = \frac{A_0 - A_f}{A_0} \cdot 100\% \tag{3.12}$$

Here,  $A_0$  is the initial cross section and  $A_f$  is the cross section after fracture.

As the reduction of area is majorly influenced by complex stress states, the correlation with bending and hole expansion behavior is improved compared to the total elongation (**Figure 3.26**). [126,127]

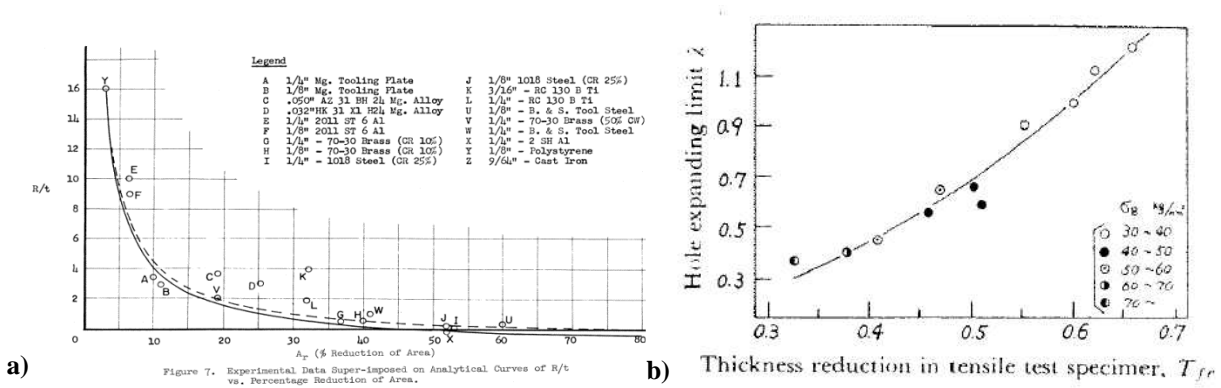


**Figure 3.26:** Reduction of area and thickness reduction respectively show good correlation with a) bending figures ( $R/t$  = bending radius/sample thickness) [126] and b) hole expansion testing [127]



## 4. Experimental procedure

### 4.1 Production and chemical composition of the investigated steels

In this work, Medium-Mn-steels with varying C-contents from 0.003 to 0.12 wt-% and Mn-contents from 4.8 to 6.4 wt-% were investigated, since for batch annealing alloying concepts these are the crucial alloying elements. Therefore, seven heats were cast under laboratory conditions in a medium frequency furnace into ingots of 80 kg (400 x 150 x 150 mm<sup>3</sup>). The chemical compositions are given in **Table 4.1**. To investigate the influence of C the Mn-content has been kept constant at 6 wt-%, while for the Mn-variation a C-content of 0.1 wt-% was the base composition. Al was alloyed to a maximum of 280 ppm in order to deoxidize the steel. The other elements can be considered to be trace elements as their amount was kept as low as possible.

**Table 4.1:** Chemical composition of the investigated steels in wt-%

	steel	C	Mn	Si	Al	Cr	S	N	P
C-variation	0.003C6Mn	0.003	6.09	0.028	0.011	0.014	0.002	0.020	0.005
	0.056C6Mn	0.056	6.02	0.024	0.010	0.014	0.002	0.017	0.006
	0.12C6Mn	0.120	6.02	0.020	0.009	0.014	0.002	0.017	0.006
Mn-variation	0.1C4.8Mn	0.102	4.81	0.011	0.008	0.012	0.007	0.011	0.006
	0.1C5.7Mn	0.099	5.72	0.012	0.009	0.013	0.006	0.010	0.005
	0.1C5.9Mn	0.092	5.91	0.017	0.028	0.015	0.006	0.010	0.006
	0.1C6.4Mn	0.100	6.38	0.011	0.009	0.013	0.005	0.010	0.006

Subsequent to casting, the ingots were hot rolled in a two-step rolling process in a laboratory rolling mill. First the material was hot rolled to a pre-strip of a thickness of 34 mm. After sectioning this pre-strip into three parts the material was reheated and hot rolled to a final thickness of about 4 mm. The final rolling temperature was about 780 °C. The hot rolled sheet was cooled by air to 500 °C and subsequently coiling was simulated with a cooling rate of 0.007 K/s to 300 °C. Final cooling to room temperature was again conducted by air. Independent of the chemical composition or the exact hot rolling conditions the material's microstructure after hot rolling was primarily consisting of martensite and therefore tensile strengths of 950 to 1550 MPa were obtained. In order to provide optimal cold rollability within the given possibilities, tensile strength had to be limited to 1000 MPa. Thus, the martensitic material was tempered in a batch annealing-like furnace under nitrogen atmosphere for 8 or 16 h at temperatures adjusted for each alloying system. The annealing conditions are given in **Table 4.2**. Afterwards, the material was cold rolled to a thickness of 1 mm.

**Table 4.2:** Annealing conditions for tempering step prior to cold rolling

	temperature [°C]	time [h]
C-variations	600	16
Mn-variations	500	8

Furthermore, in order to evaluate the applicability of existing  $M_s$ -formulas on Medium-Mn-steels, seven additional steels were cast and hot rolled under the same conditions

mentioned. The determination of the  $M_s$ -temperatures was performed on the hot rolled material. The chemical compositions are listed in **Table 4.3**.

**Table 4.3:** Chemical composition of the steels used for the  $M_s$ -temperature evaluation in wt-%

	steel	C	Mn	Si	Al	Cr	N
<b>Mn-variation</b>	<b>0.1C3.5Mn</b>	0.106	<b>3.53</b>	0.33	0.01	0.014	0.010
<b>Al-Si-Cr- variations</b>	<b>0.1C6Mn1Al</b>	0.102	6.01	0.03	<b>0.96</b>	0.014	0.018
	<b>0.1C6Mn1.5Al</b>	0.108	6.10	0.05	<b>1.45</b>	0.015	0.017
	<b>0.1C6Mn1.4Si</b>	0.099	5.95	<b>1.38</b>	0.05	0.014	0.020
	<b>0.1C6Mn1.4Si1Al</b>	0.112	6.08	<b>1.39</b>	<b>1.05</b>	0.015	0.017
	<b>0.1C6Mn1.6Al1Cr</b>	0.105	5.91	0.07	<b>1.60</b>	<b>1.02</b>	0.010
	<b>0.1C6Mn1.6Al1.2Si1Cr</b>	0.110	5.80	<b>1.24</b>	<b>1.55</b>	<b>1.00</b>	0.011

## 4.2 Dilatometry

In order to characterize the transformation behavior of the steels listed in **Table 4.1**, intercritical annealing HT was conducted on a Bähr DIL 805 A/D dilatometer. The specimens ( $1 \times 3.5 \times 10 \text{ mm}^3$ ) were produced by wire electrical discharge machining of the cold rolled sheet material. Tempered martensite that was heavily cold rolled represented the initial microstructure for the HT. Basically two different HT regimes were applied, which include one or two HT steps respectively. In the following these two HT regimes are referred to as one-step and two-step HT.

As displayed in **Figure 4.1 a)** for the two-step HT first a full austenitization with a heating rate of  $3.4 \text{ K/s}$  at  $T_A = 810 \text{ °C}$  for  $t_A = 125 \text{ s}$  was performed. The austenitization was followed by quenching at a cooling rate of  $36 \text{ K/s}$  to an isothermal holding temperature of  $T_{IH} = 500 \text{ °C}$  with a holding time of  $t_{IH} = 370 \text{ s}$ . The parameters of this first optional HT were selected in order to simulate a simplified industrial continuous annealing line. The second annealing step (**Figure 4.1 b)** obligatory for both HT regimes represented an industrial batch annealing cycle. The heating as well as the cooling were performed at  $1 \text{ K/s}$ . Intercritical annealing temperatures  $T_{IA}$  between  $580$  and  $700 \text{ °C}$  in steps of  $20 \text{ °C}$  were chosen to adjust the amount of intercritically formed austenite. The annealing time was held constant at  $t_{IA} = 8 \text{ h}$  for all applied HT cycles.

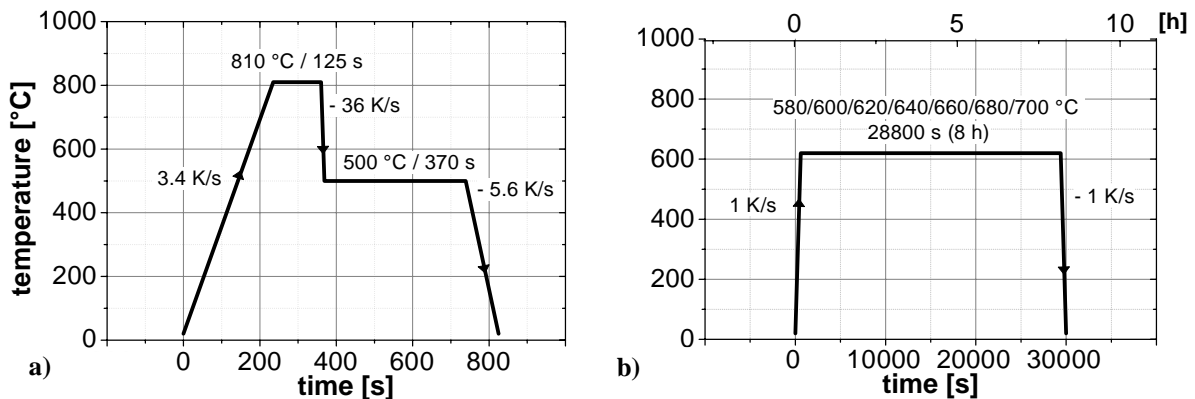


**Figure 4.1:** Time-temperature schedule of **a)** full austenitization and **b)** intercritical annealing

Additionally for all chemical compositions listed in **Table 4.1** and **Table 4.3** the  $M_s$ -temperature was determined on hot rolled samples ( $3.5 \times 3.5 \times 10 \text{ mm}^3$ ). Beforehand, the  $A_{c3}$ -temperature of each steel was investigated in order to achieve comparable austenitizing conditions. The heat treatment schedules were conducted with a heating rate of  $3.4 \text{ K/s}$  to  $T_A$ . The applied  $T_A$  was defined as the experimentally determined  $A_{c3}$ -temperature plus additional  $30 \text{ }^\circ\text{C}$  (**Table 4.4**). In order to achieve a homogenous temperature distribution during cooling a moderate cooling rate of  $10 \text{ K/s}$  was chosen to ensure a full martensitic transformation and to limit possible vibrations due to rapid cooling. The only exception was made for the  $0.1\text{C} \ 3.5\text{Mn}$  steel, as a cooling rate of  $50 \text{ K/s}$  was necessary to prevent any diffusional transformations during cooling.

**Table 4.4:** Investigated steels and corresponding  $T_A$

	steel	$T_A$ [ $^\circ\text{C}$ ]
<b>C-variations</b>	<b>0.003C6Mn</b>	820
	<b>0.056C6Mn</b>	820
	<b>0.12C6Mn</b>	820
<b>Mn-variations</b>	<b>0.1C3.5Mn</b>	830
	<b>0.1C4.8Mn</b>	810
	<b>0.1C5.7Mn</b>	795
	<b>0.1C5.9Mn</b>	810
	<b>0.1C6.4Mn</b>	790
<b>Al-Si-Cr-variations</b>	<b>0.1C6Mn1.4SiAl</b>	885
	<b>0.1C6Mn1Al</b>	900
	<b>0.1C6Mn1.5Al</b>	950
	<b>0.1C6Mn1.4Si1Al</b>	985
	<b>0.1C6Mn1.6Al1Cr</b>	955
	<b>0.1C6Mn1.2Si1.6Al1Cr</b>	1030

For each steel the characteristic transformation temperatures  $A_{c1}$ -,  $A_{c3}$ - and the  $M_s$ -temperature were evaluated using the tangent method to distinguish the start and finishing point of the respective transformation (**Figure 4.2**). Therefore, one micrometer of deviation from the linear elongation due to thermal expansion was set as detection onset of the respective transformation.

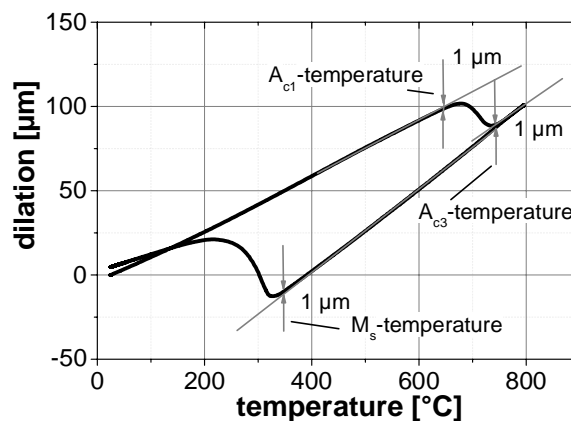


**Figure 4.2:** Dilatometric curve - elongation as a function of temperature – indication of transformation points  $A_{c1}$ -,  $A_{c3}$ - and  $M_s$ -temperature

### 4.3 Heat treatment

The cold rolled sheet material, required for detailed microstructural investigations and mechanical testing, was heat treated with comparable parameters as conducted in the dilatometer. For the austenitization step of the two-step HT a Multipurpose Annealing Simulator was used to heat the cold rolled sheets by conductive resistance heating. The temperature control was ensured by five thermocouples welded to the sheet (1 x 150 x 450 mm<sup>3</sup>). Cooling rates were regulated by adjustable gas jets using compressed air for cooling. The conducted heat treatment cycle was identical to that used within the dilatometric testing (**Figure 4.1 a**). The intercritical annealing was carried out in a laboratory scale batch annealing furnace. The parameters were slightly changed compared to the dilatometric testing as can be seen in **Figure 4.3**. In order to improve the comparability with the industrial aggregates heating was performed with 0.017 K/s to 550°C followed by 0.0056 K/s until T<sub>IA</sub> was reached. The soaking time was identically to the dilatometric testing with t<sub>IA</sub> = 8 h. However, the cooling rate to RT was reduced to about 0.01 K/s. To prevent the material from surface-reactions (*e.g.* decarburization) the annealing was executed under Argon-atmosphere.

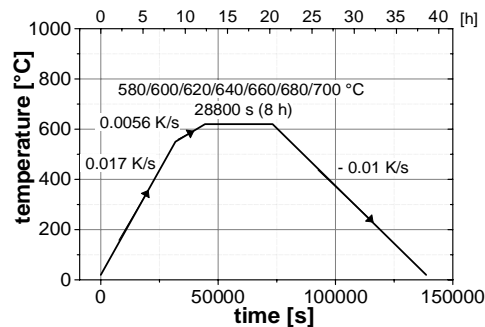


**Figure 4.3:** HT schedule of intercritical batch annealing in laboratory furnace

### 4.4 Thermodynamic simulations

All thermodynamic calculations were performed using Thermo-Calc<sup>®</sup>-software (database: TCFE6). The calculations included the simulation of the amount and the development of the chemical composition of the respective phases as function of temperature. This data was used to apply the thermodynamic model for the prediction of the amount of retained austenite at RT as described by S. J. Lee *et al.* [80]. The model is described in detail in **Chapter 3.3**.

### 4.5 Microstructural investigations

**Scanning electron microscopy.** For high resolution images SEM investigations (Zeiss SUPRA 35) were carried out on selected samples. The samples were electrochemically polished, whereby a topography correlating with the respective phases, was generated. This topography contrast can be detected by SEM. Each phase is differently attacked during electropolishing depending on its crystallography, chemical composition *etc.* Furthermore, defects as grain boundaries, phase boundaries, dislocations *etc.* in the microstructure generally underwent a higher material abrasion than the matrix. Therefore, martensite can be easily differentiated from ferrite, which appears elevated, as well as precipitates can be distinguished from the surrounding matrix. [128] In conventional TRIP-steels retained austenite appeared as smooth and elevated area. [59,129] As Medium-Mn-steels contain highly Mn and C enriched

retained austenite, it responded differently to electropolishing compared to conventional TRIP-steels. A comparative study of SEM and EBSD was performed (see **Figure 4.4**) and revealed that ferrite (bcc-blue) appeared as smooth and elevated areas mainly without any surface structure, while austenite (fcc-green) formed rather deep cavities. As parts of the austenite were dissolved by the etching, there appeared areas where no sufficient pattern information was obtained by EBSD (black). Due to their morphology and location next to the areas of austenite, it was still reasonable to identify them as retained austenite.

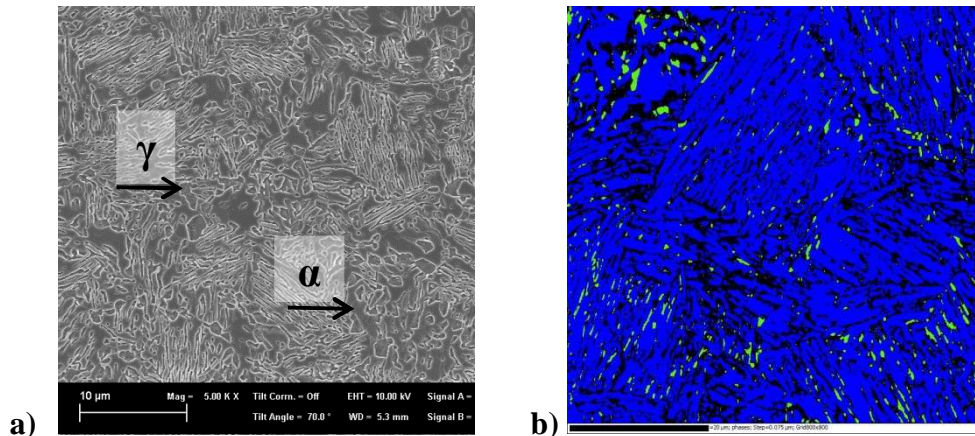


**Figure 4.4:** a) SEM micrograph and b) corresponding EBSD measurement indicating bcc phases blue and fcc phases green

In addition to the micrographs obtained by SEM, the chemical composition (Mn distribution) of the respective phases was investigated by energy-dispersive X-ray spectroscopy (EDX).

**Microprobe.** The microprobe investigations presented were conducted by the Eugen F. Stumpfl Electron Microprobe Laboratory at the Montanuniversität Leoben using a JEOL JXA-8200 with a voltage of 15 kV and a beam current of 10 nA. The diffraction crystal for Mn detection was a LIFH using the  $K_{\alpha}$  emission lines for the analysis.

**Transmission electron microscopy.** Even higher resolution than for SEM can be achieved using TEM. Very thin foils (about 200 nm) of the material were prepared in order to enable electron transmission through the material. This was accomplished by mechanical grinding followed by an electrochemical thinning of the specimen. The foils were taken from one-quarter of the sheet thickness. TEM examinations were carried out on a high resolution TEM Tecnai F20 with a voltage of 200 kV at Montanuniversität Leoben, Alloy Development Group. Besides the advantage of higher resolution than SEM, TEM offers additional information about dislocation structure in the material. For characterization of the chemical composition of individual microstructural compounds EDX was used.

**Fracture surface and void analysis.** The examination of the fracture surface as well as qualitative and quantitative void analysis has been carried out using Zeiss SUPRA 35. For the void analysis tested tensile specimens were cut and examined close to the center line of the cross section of the fracture surface. The microstructure was prepared by electropolishing identically as for microstructural investigations in SEM. For quantitative void analysis the software ImageJ was used to determine the number of voids.

**ECD and circularity.** For characterization of the retained austenite, SEM images were analyzed using the software ImageJ. The grain size was expressed by the equivalent circle

diameter (ECD). Therefore, the retained austenite was highlighted and the grain area was determined using the particle analyzer tool integrated in ImageJ. The ECD was calculated from **Equation 4.1**:

$$ECD = \sqrt{\frac{4A_\gamma}{\pi}}. \quad 4.1$$

Here  $A_\gamma$  is the area of the retained austenite. An average of 180 grains was studied per HT condition.

As the morphology of the retained austenite has proven to have great influence on its stability a form factor was introduced (**Equation 4.2**)

$$circularity = 4\pi \cdot \frac{A_\gamma}{P_\gamma^2}. \quad 4.2$$

Here  $A_\gamma$  is the area and  $P_\gamma$  is the perimeter of the retained austenite respectively. The circularity factor can vary from 0 to 1. A circularity of 1 means that the particle is perfectly spherical. The circularity factor was determined for an average of 120 grains per HT condition.

**Metallographic determination of phase fraction.** The phase fractions of ferrite and martensite respectively were determined by providing five SEM images in adjusted magnification for each selected HT condition. A grid (20 x 20 domains) was applied to the SEM images and the intersections with the respective phase were counted concluding in a phase fraction in area-%.

**Texture analysis by XRD.** The development of the texture of the ferritic and austenitic phase was determined by X-Ray diffraction (XRD). The investigations were conducted on a PANalytical XPert Pro using a Co-source with a wavelength of  $\lambda = 0.179$  nm. An area of  $5 \times 5$  mm<sup>2</sup> was scanned using a current of 45 mA and a voltage of 35 kV. In order to receive textural information the specimen was rotated (0-360°, 5° steps) and tilted (0-90°, 5° steps).

**Infrared-camera.** Thermography was used in order to study the deformation behavior of selected samples during tensile testing. Plastic deformation causes an increase in temperature on the specimen. This can be detected by using an IR-camera (IRCAM Equus 81k M Pro) during tensile testing (constant testing velocity  $v_c = 0.025$  mm/s). The applied sampling rate was 50 Hz.

## 4.6 Retained austenite measurement

The amount of retained austenite was measured by means of the saturation magnetization method. Thereby, the fact that a significant difference in magnetizability of ferromagnetic phase components *e.g.*: ferrite compared to the paramagnetic austenite exists, is used to determine the amount of retained austenite. The measuring setup is given in **Figure 4.5**.

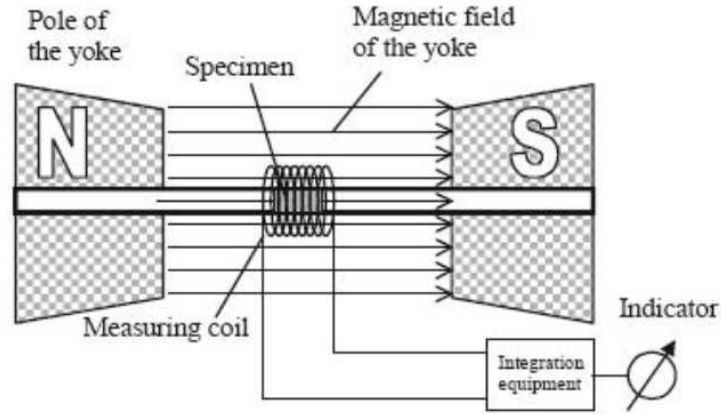


**Figure 4.5:** Measurement setup for saturation magnetization method [130]

The specimen is pushed through a measuring coil and induces a voltage  $U_{ind}$  in the coil. The saturation magnetization  $J$  of the specimen can now be calculated from **Equation 4.3**:

$$J = \frac{\int U_{ind} dt}{\frac{N}{l} V} \tag{4.3}$$

Here  $U_{ind}$  is the induced voltage,  $t$  is the time,  $N$  is a device and calibration constant,  $l$  is the length of the measurement coil and  $V$  is the volume of the specimen.

To determine the actual amount of retained austenite of the specimen the saturation magnetization of a reference material, in this case pure iron  $J_{Fe}$ , is required. As alloying elements alter the saturation magnification they are considered by application of **Equation 4.4**:

$$J_{ref} = J_{Fe} - \sum \alpha_i \cdot A_i \tag{4.4}$$

Here  $J_{ref}$  is the theoretical saturation magnification,  $\alpha_i$  is the reduction factor of element  $i$  given in **Table 4.5** and  $A_i$  is the element content in percent.

**Table 4.5:** Austenite reduction factors  $\alpha_i$  in T/% for the calculation of the reference magnetization

Alloying element	C	Mn	Si	Al	Cr	Mo
Reduction factor $\alpha_i$	0.15	0.0244	0.048	0.057	0.0305	0.6

The amount of retained austenite  $f_y$  can be estimated from the difference of the theoretical saturation magnification  $J_{ref}$  and the saturation magnification of the specimen  $J$  (**Equation 4.5**).

$$f_y = \frac{J_{ref} - J}{J_{ref}} \cdot 100\% \tag{4.5}$$

Further reducing influencing factors on the theoretical saturation magnification  $J_{ref}$  are nano-scale microstructural defects as inclusions, voids, point defects, microstresses and/or crystal anisotropy as well as the presence of cementite. [131] As the amount of cementite at low  $T_{IA}$  is rather small and at optimal  $T_{IA}$  no cementite is present the issue is limited to the higher  $T_{IA}$  range, where greater amounts of tempered martensite are present. Since at this temperature

range retained austenite is not the determining influencing factor on the mechanical properties the potential error in the determination of the retained austenite is considered to be negligible in the interpretation of the results. In this  $T_{IA}$  range the amount of retained austenite is generally very low and its stability is also limited.

#### 4.7 Mechanical testing

**Tensile testing.** Test on flat tensile specimens according to “EN 10002 part 1” have been performed in order to characterize the dependence of the quasistatic mechanical properties on chemical composition and the applied HT schedule. Due to the limited amount of laboratory material a down scaled tensile specimen geometry according to „ASTM E 517, Specimen A, alternative“, as illustrated in **Figure 4.6**, was used. If not indicated otherwise, all tensile tests were performed on longitudinal samples (parallel to rolling direction). For each chemical composition and HT condition two samples were tested. In this manner the characteristic values for yield strength (YS), ultimate tensile strength (UTS), yield point elongation (YPE), uniform elongation (UE) and total elongation (TE) could be obtained. The sample dimensions are listed in **Table 4.6**.

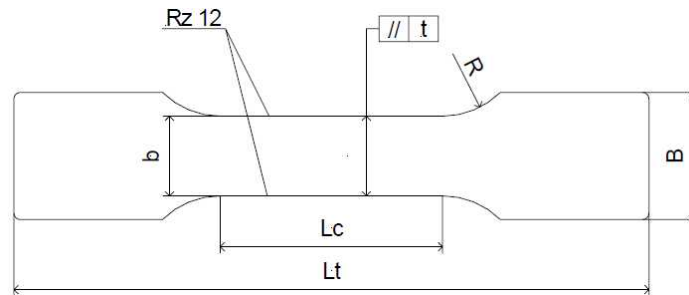


**Figure 4.6:** Flat tensile specimen according to „ASTM E 517, Specimen A, alternative“ [132]

**Table 4.6:** Flat tensile geometry according to [132]

notation	Dimension [mm]	Tolerance [mm]
<b>Sample thickness t</b>	0.3 - ≤ 3	
<b>Sample width b</b>	12.5	± 0.025
<b>Gripping head width B</b>	20	± 0.5
<b>Radius R</b>	13	± 0.5
<b>Gauge length Lc</b>	25	± 0.5
<b>Sample length Lt</b>	100	± 1

For selected specimens the incremental work hardening exponent  $n_i$  (**Equation 4.6**) was determined.

$$n_i = \frac{d \ln \sigma}{d \ln \varepsilon} - \frac{\sigma}{E} \quad 4.6$$

Here,  $\sigma$  is the true stress,  $\varepsilon$  is the true plastic strain and  $E$  the Young’s modulus.

Furthermore, for selected tensile specimens the thinning of the cross section after fracture  $\varepsilon_3$  (thickness strain) was measured on five positions using light optical microscopy. **Figure 4.7**



shows a schematic illustration of the cross section and the measuring points (MP). **Equation 4.7** was used to calculate the thickness strain  $\varepsilon_3$ .

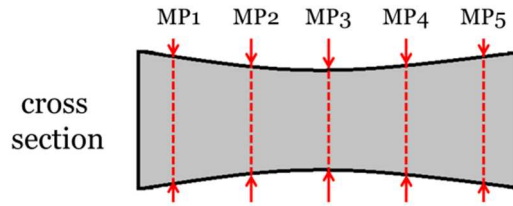


**Figure 4.7:** Cross section of the fractured tensile specimen (schematic) and position of MP

$$\varepsilon_3 = \frac{\sum_{k=1}^5 th_{MPk}}{5 \cdot th_0} \cdot 100\%. \quad 4.7$$

Here,  $th_{MPk}$  is the thickness of the cross section at  $MP_k$ ,  $th_0$  is the initial thickness of the cold rolled material and  $\varepsilon_3$  thickness strain. Subsequently, the given values of the thickness strain  $\varepsilon_3$  always represent the mean value of two tested tensile.

For selected samples the thickness strain  $\varepsilon_3$  was divided into an uniform and a post-uniform fraction. Therefore, the thickness of the tested tensile sample was determined before and after necking (**Figure 4.8**). The thinning of the cross section during uniform deformation is represented by the uniform thickness strain  $\varepsilon_{3\text{uniform}}$  (**Equation 4.8**), while the thinning after necking (post-uniform) is represented by the post-uniform thickness strain  $\varepsilon_{3\text{post-uniform}}$  (**Equation 4.9**).

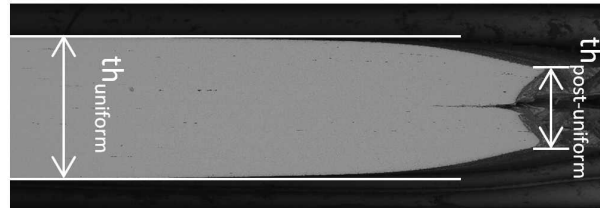


**Figure 4.8:** Determination of the uniform and postuniform fraction of the thickness strain  $\varepsilon_3$

$$\varepsilon_{3\text{ uniform}} = \frac{th_{\text{uniform}}}{th_0} \cdot 100\%. \quad 4.8$$

Here,  $th_{\text{uniform}}$  is the thickness of the cross section before necking,  $th_0$  is the initial thickness of the cold rolled material and  $\varepsilon_{3\text{uniform}}$  the uniform thickness strain.

$$\varepsilon_{3\text{ post-uniform}} = \frac{(th_{\text{uniform}} - th_{\text{post-uniform}})}{th_0} \cdot 100\%. \quad 4.9$$

Here,  $th_{\text{uniform}}$  is the thickness of the cross section before necking,  $th_{\text{post-uniform}}$  is the thickness of the cross section after fracture,  $th_0$  is the initial thickness of the cold rolled material and  $\varepsilon_{3\text{post-uniform}}$  the postuniform uniform thickness strain.

**Interrupted tensile testing.** In order to determine the amount of retained austenite transforming into martensite during straining, interrupted tensile tests combined with saturation magnetization method were carried out. Flat tensile specimens, as displayed in **Figure 4.6**, were strained in x % steps up to the end of uniform elongation. After testing a retained austenite sample was machined by wire electrical discharge machining from the middle of the gauge length of the specimen.

## 5. Results

### 5.1 Influence of C and Mn

The following chapter presents the influence of the C- and Mn-content respectively on the microstructural evolution and the resulting mechanical properties as well as selected aspects of the yielding, work hardening and damage behavior. The C-content was varied between 0.003 and 0.12 wt-% and the Mn-content between 4.8 and 6.4 wt-%. The influence of the intercritical annealing temperature ( $T_{IA}$ ) or the heat treatment (HT) schedule will be apparent to some extent in the figures of this chapter, but it is not included and described here. However, **Chapter 5.2** fully concentrates on the effects of the HT and the results are displayed in detail.

#### 5.1.1 Microstructural evolution

**Thermodynamic simulation.** Thermodynamic simulation of the equilibrium phase fractions and the chemical composition of the austenite as a function of temperature were performed in order to estimate the microstructural development during the heat treatment. As the soaking time at  $T_{IA}$  was 8 h, conditions that converge towards the equilibrium state can be expected. **Figure 5.1 a)** shows the equilibrium phase fractions of ferrite, austenite and cementite as a function of temperature for the C-variations. An increasing C-content decreased the  $A_{c3}$ -temperatures of about 15 °C comparing 0.003C6Mn with 0.12C6Mn. Furthermore, the amount of cementite was increased with a higher content of C in the steel. For 0.003C6Mn no cementite at all was present in the microstructure at any temperature. With the increase of the C-content not only the amount but also the dissolution temperature of the cementite increased. The kinetics of the austenite and ferrite formation were not significantly influenced by the C-content. The C- and Mn-content of the austenite as a function of temperature considerably altered as displayed in **Figure 5.1 b)** and **c)**, respectively. For all three chemical compositions, a drastic increase in the Mn-content with decreasing temperature was calculated. Linked to the decreasing phase fraction of the austenite with decreasing temperature the Mn-content steadily increased from 6 wt-% by full austenitization to 20 wt-% at 520 °C with ~10 vol.-% of austenite. Above the  $A_{c3}$ -temperature the Mn-content was stable at the steel's nominal composition. For all three steels the same trend could be observed. The variation of the C-content showed a different behavior. Below the  $A_{c3}$ -temperature the C-content constantly increased up to a maximum concentration. The temperature, where this maximum occurred corresponds with the beginning of the cementite formation. Therefore, a further decrease of the temperature resulted in a decrease of solute C in the austenite. For the cementite free 0.003C6Mn this trend was not found. Instead the C-content linearly increased below the  $A_{c3}$ -temperature.

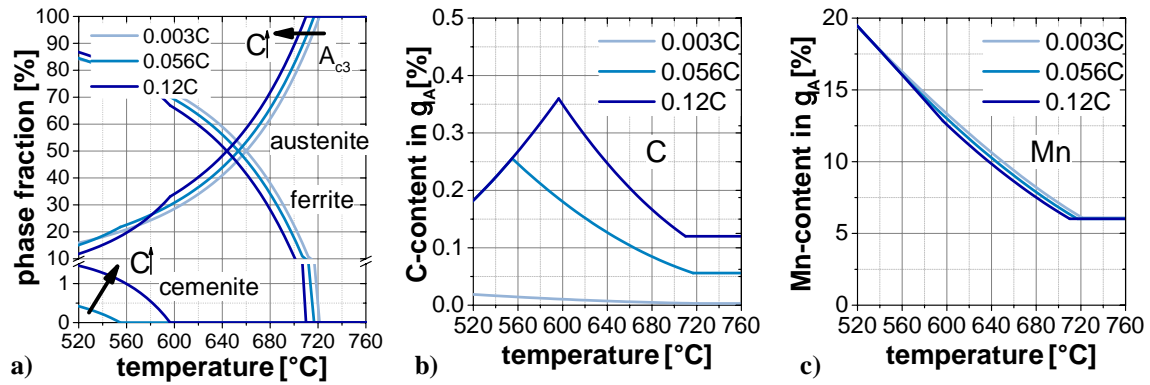


**Figure 5.1:** Thermodynamic calculations of **a)** phase fractions of ferrite, austenite and cementite, **b)** the C-content and **c)** the Mn-content of austenite as a function of temperature (C-variation, 6 wt-%Mn)

The thermodynamic calculations presented in **Figure 5.2 a)** comprise the phase fractions of ferrite, austenite and cementite as a function of temperature for the Mn-variations. A strong influence of the increasing Mn-content on the  $A_{c3}$ -temperatures was found. Comparing the steel 0.1C4.8Mn to 0.1C6.4Mn the  $A_{c3}$ -temperature decreased by more than 30 °C from ca. 735 to 705 °C. The cementite dissolution was as well shifted towards lower temperatures with increasing Mn-content. Similar to the calculations of the C-variations no considerable influence on the characteristics of the austenite or ferrite formation was found. The chemical composition of the austenite (**Figure 5.2 b** and **c**) showed a strong dependency on the temperature. The Mn-content exhibited, equally to the calculations of the C-variations, an almost linear increase below the  $A_{c3}$ -temperature. On the contrary the C-content increased until the cementite formation started. For 0.1C4.8Mn cementite formed at the highest temperature compared to the steel with a higher Mn-content. Hence, 0.1C4.8Mn exhibited its maximum C-concentration at the highest temperature of about 610 °C. Furthermore, this steel inhibited the highest maximum C-concentration in the austenite.

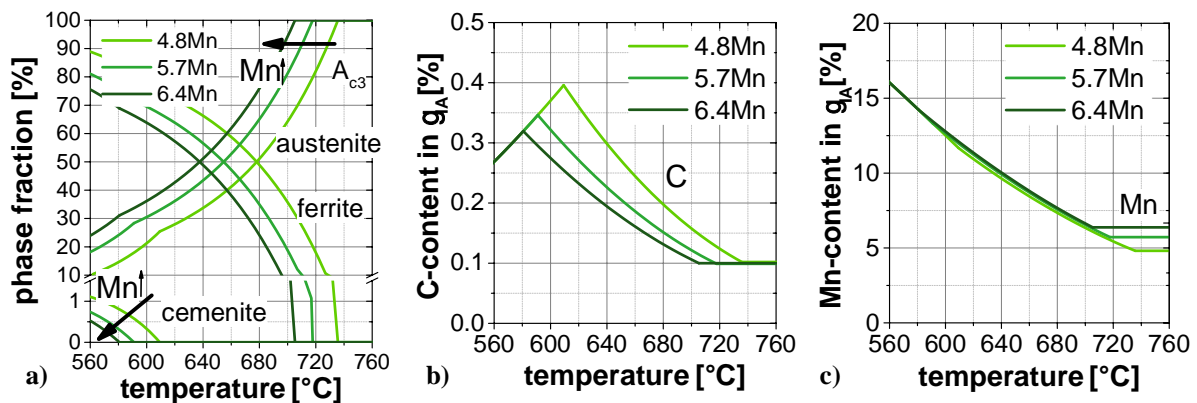


**Figure 5.2:** Thermodynamic calculations of **a)** phase fractions of ferrite, austenite and cementite, **b)** the C-content and **c)** the Mn-content of austenite as a function of temperature (Mn-variation, 0.1 wt-%C)

For all investigated steels of the C- and Mn-variation, a model based on thermodynamic calculations to predict the amount of retained austenite at RT as a function of the  $T_{IA}$  was applied according to S.-J. Lee *et al.* [80]. Therefore, the above presented thermodynamic data of phase fraction and chemical composition of the austenite was used to calculate a  $M_s$ -temperature (J. Mahieu *et al.* [79]) which subsequently was integrated in a modified Koistinen-Marburger equation predicting the martensite formation kinetics. A detailed

description of the model can be found in **Chapter 3.3**. **Figure 5.3 a) – c)** shows the results of the modelling for the C-variation steels, where the formation of the intercritical austenite (black) is displayed. The red line symbolizes the fractions of martensite which was formed during cooling. Due to an altering chemical composition of the intercritical austenite the martensite fractions decreased with decreasing  $T_{IA}$  until the chemical enrichment was high enough to retain the complete amount of intercritically formed austenite to RT. The lines shaded in different blue tones indicated the amount of retained austenite that resulted as the difference between intercritical austenite and martensite. The retained austenite developed a maximum which roughly corresponded with the highest  $T_{IA}$ , where no martensite was formed during cooling and cementite was dissolved completely. Comparing the three steels with altering C-content, it can be noted that the maximal amount of retained austenite considerably increases with higher C-content. The  $T_{IA}$ , where this maximum is obtained (referred to as  $T_{IAmax}$ ), shows no significant link to the C-content. However, it could be observed that the peak became steeper and restricted to a more narrow temperature window with higher C-content.

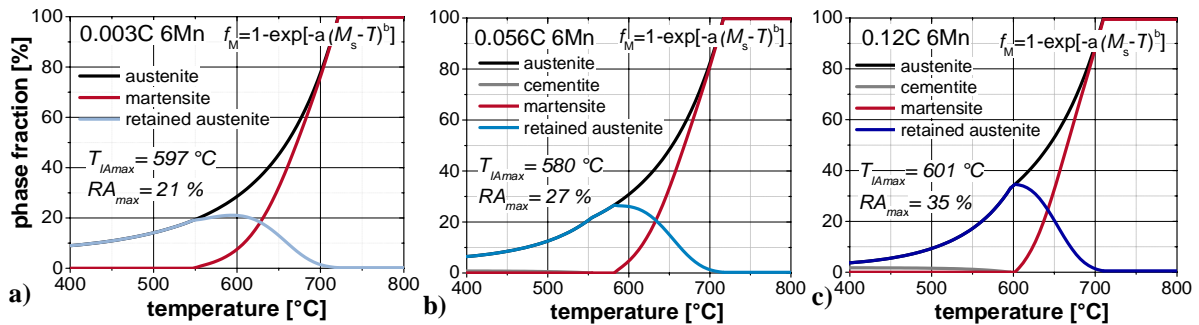


**Figure 5.3:** Application of retained austenite model proposed by S.-J. Lee *et al.* [80] for the chemical composition of a) 0.003C6Mn, b) 0.056C6Mn and c) 0.12C6Mn

The influence of the Mn-content on the predicted retained austenite content at RT is displayed in **Figure 5.4 a) – c)**. Two significant consequences of an increasing Mn-content are shown: first the  $T_{IAmax}$  slightly declined and secondly the amount of retained austenite considerably rose from 25 to 34 %. The influence of the Mn-content on the shape of the retained austenite peak seemed to be opposed to that observed by increasing C-content. With rising Mn-content the peak tended to broaden and thus, the possible processing window increased.

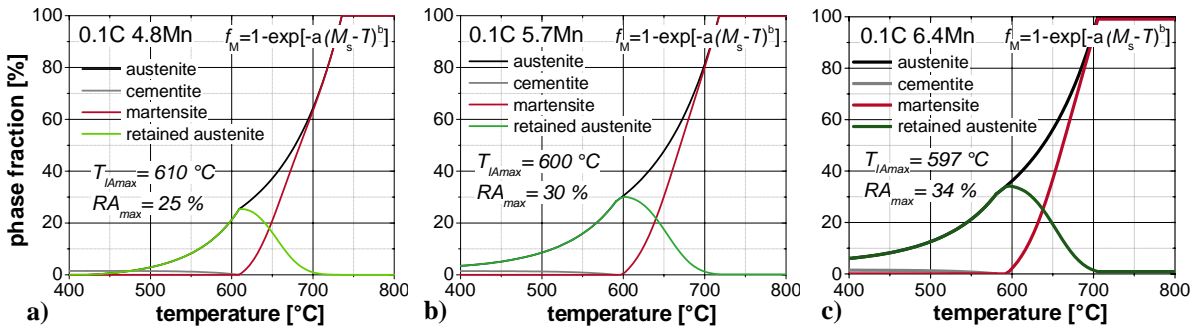


**Figure 5.4:** Application of retained austenite model proposed by S.-J. Lee *et al.* [80] for the chemical composition of a) 0.1C4.8Mn, b) 0.1C5.7Mn and c) 0.1C6.4Mn

**Dilatometry.** The  $M_s$ -temperatures of the respective steels presented in the following chapter were determined after full austenitization for 8 h at  $A_{c3}$ -temperature calculated by Thermo-

Calc®-software plus additional 50 °C to ensure homogenous austenitization. Furthermore, a variation of selected  $T_{IA}$  was additionally investigated to detect microstructural transformations during cooling. These investigations should represent conditions that are closely related to the industrial process. **Figure 5.5 a) - c)** shows the dilatation of the steels with varying C-content during cooling from full austenitization and from selected  $T_{IA}$ . All three steels showed the same trend of decreasing  $M_s$ -temperature with declining annealing temperature. At the respected cooling rate of 1 K/s no diffusional transformation could be observed during cooling. After annealing at  $T_{IA}$  of 640 °C none of the three investigated steels indicated any phase transformation while cooling to RT. This implies that the ferritic-austenitic microstructure which developed during the intercritical annealing fully retained to RT.

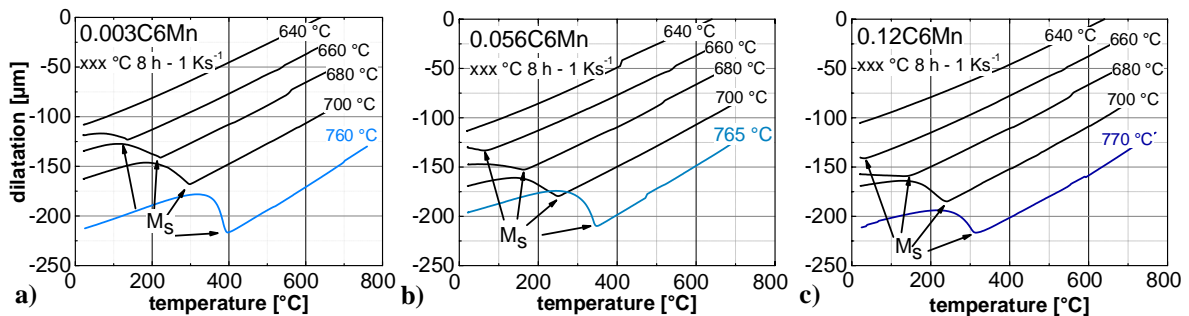


**Figure 5.5:** Dilatometric curves of the cooling phase after intercritical annealing for 8 h of a) 0.003C6Mn, b) 0.056C6Mn and c) 0.12C6Mn

The development of the  $M_s$ -temperature as a function of the C-content is represented in **Figure 5.6 a)**. A clear trend of declining  $M_s$ -temperature with the steel's nominal C-content can be noted for all investigated annealing temperature. **Figure 5.6 b)** displays the influence of the C-content on the  $A_{c1}$  and  $A_{c3}$ -temperature of the investigated steels. While the  $A_{c3}$ -temperature slightly decreased the  $A_{c1}$ -temperature showed a significant rise resulting in a considerable reduction of the temperature window of the intercritical region with increasing C-content.

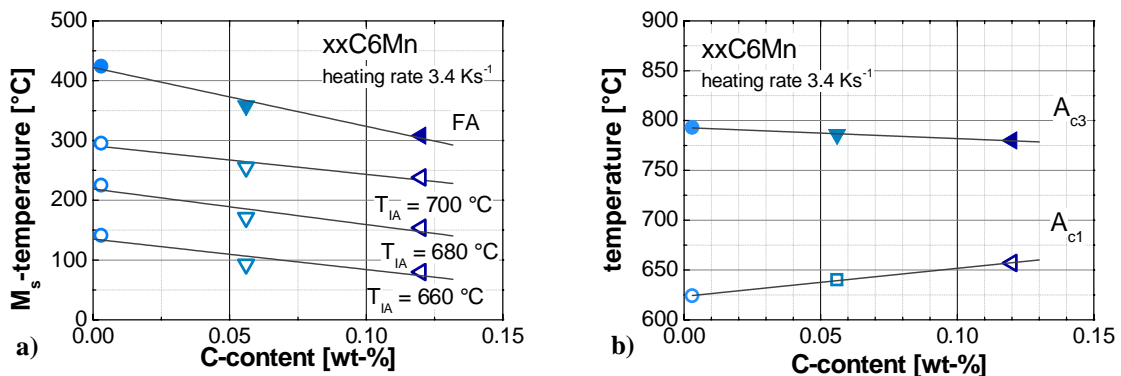


**Figure 5.6:** Development of the a)  $M_s$ -temperature as a function of the annealing temperature and b)  $A_{c1}/A_{c3}$ -temperatures as a function of the C-content

**Figure 5.7 a) – c)** presents the results of the dilatometric investigations with respect to the transformation behavior during cooling for different Mn-contents. The determined  $M_s$ -temperatures after annealing at selected annealing temperature exhibited the same trend as for

the investigated C-variations. With decreasing annealing temperature the  $M_s$ -temperatures strongly declined and for  $T_{IA} \leq 660$  °C no phase transformation occurred during cooling.

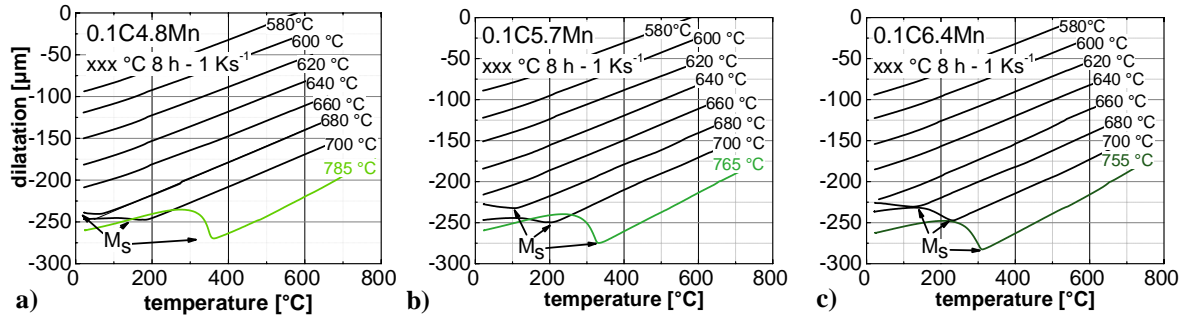


**Figure 5.7:** Dilatometric curves of the cooling phase after intercritical annealing for 8 h of a) 0.1C4.8Mn, b) 0.1C5.7Mn and c) 0.1C6.4Mn

**Figure 5.8 a)** displays the influence of the steel’s nominal Mn-content on the  $M_s$ -temperature after annealing at selected annealing temperatures. After FA an increasing Mn-content led to a significant decline of the determined  $M_s$ -temperature. On the contrary after annealing at the same  $T_{IA}$  the  $M_s$ -temperature strongly increased with elevated Mn-content. **Figure 5.8 b)** shows that the characteristic transformation temperatures  $A_{c1}$  and  $A_{c3}$  both declined with increasing Mn-content. The temperature range of the intercritical region was not significantly influenced by the Mn-content.

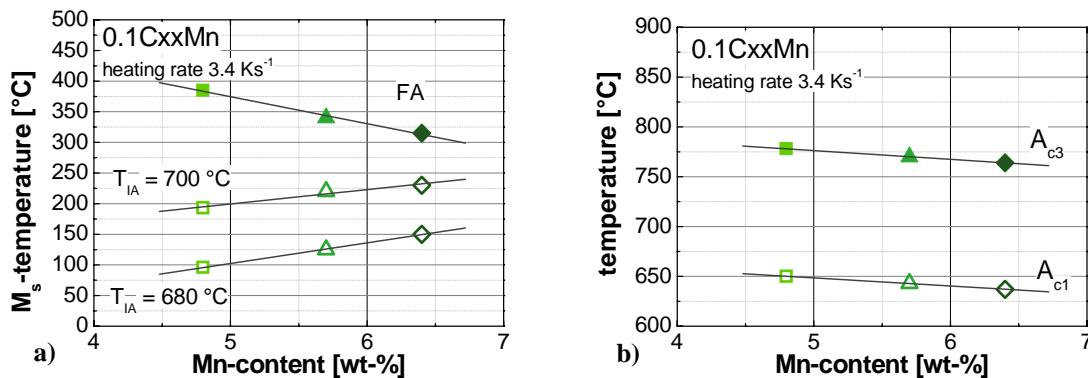


**Figure 5.8:** Development of the a)  $M_s$ -temperature as a function of the annealing temperature and b)  $A_{c1}/A_{c3}$ -temperatures as a function of the Mn-content

Additionally to the above presented dilatometric experiments an extended selection of steels (see **Table 4.3**) with alloying of Al, Si and Cr were investigated in order to verify the validity of common  $M_s$ -formulas for low C-steels for the application to Medium-Mn-steels. **Figure 5.9** displays the results of variation of C, Mn and Al. C and Mn clearly show a linear relationship concerning the  $M_s$ -temperature. The addition of both elements decreased the  $M_s$ -temperature significantly. The effect of Al was found to be rather small compared to C and Mn and opposed to those elements it slightly increased the  $M_s$ -temperature.

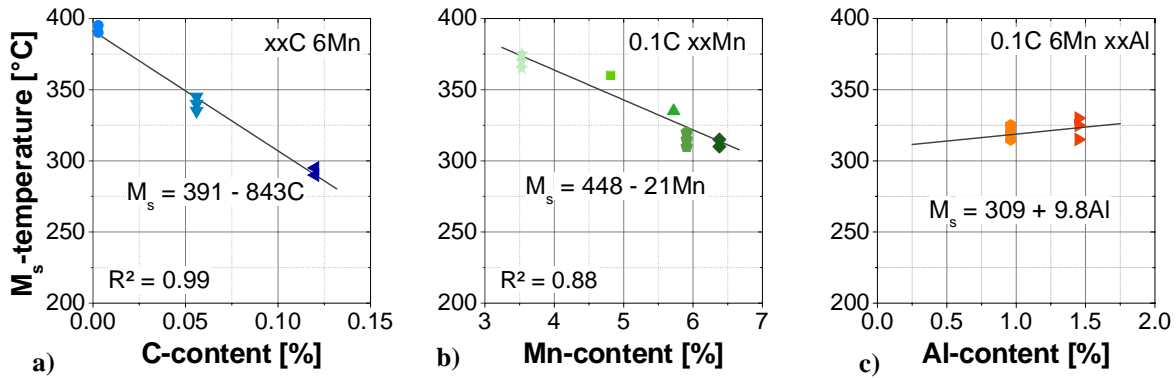


**Figure 5.9:**  $M_s$ -temperature determined by dilatometry as a function of a) C-content, b) Mn-content and c) Al-content

The  $M_s$ -temperatures of the further investigated steels are represented in **Figure 5.10**. The addition of Si decreased the  $M_s$ -temperature compared to plain C-Mn concepts. Comparing the four steels with each other additional Al tended to increase the  $M_s$ -temperature significantly while Cr seemed to have no evident influence.

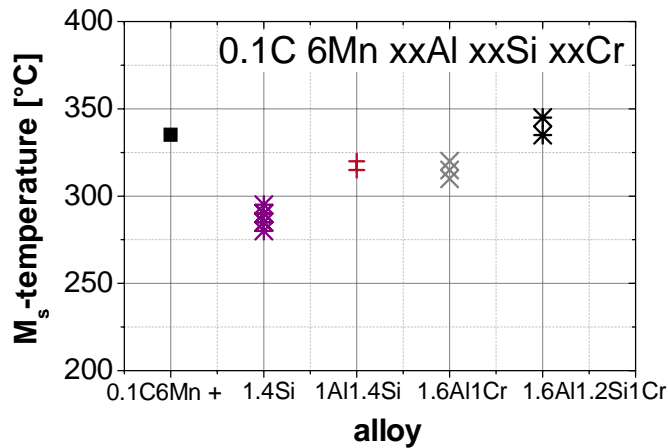


**Figure 5.10:**  $M_s$ -temperature determined by dilatometry as a function of alloying content

**Retained austenite content.** Retained austenite plays an important role on providing excellent mechanical properties of Medium-Mn-steels. Thus, this microstructural constituent was given particular attention. **Figure 5.11** displays the retained austenite content as a function of the C- and the Mn-content after full austenitization and isothermal holding at  $T_{IH} = 500 \text{ }^\circ\text{C}$  as first step of the two-step HT. While the C-content caused a significant rise in the resulting retained austenite content from less than 1 to 6 vol.-% the influence of Mn was comparatively small and lays almost within the scatter band of the testing method.



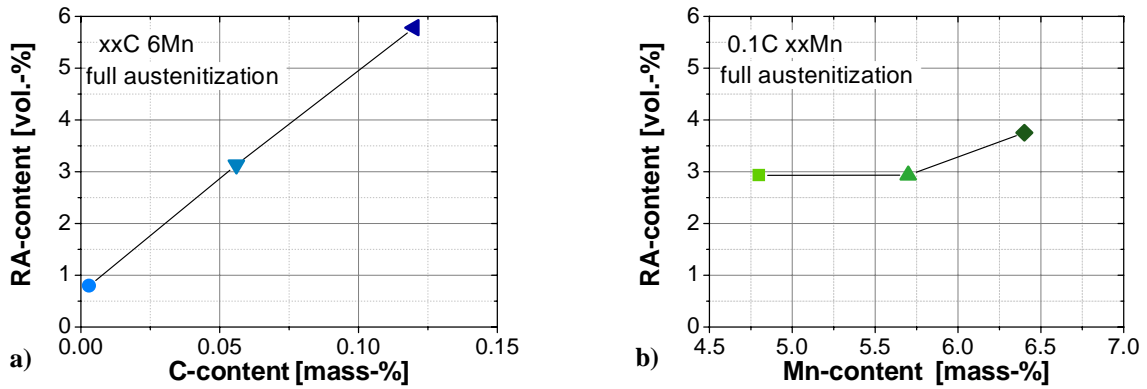


**Figure 5.11:** Retained austenite content as a function **a)** C-content and **b)** Mn-content after FA (first step of two-step HT)

**Figure 5.12** displays the retained austenite content after the intercritical annealing for one-step and two-step HT for the steels with varying C-content. For all investigated steels the same overall trend was observed. Starting at the lowest  $T_{IA}$  the retained austenite content linearly increased up to a maximum. Further increase of the  $T_{IA}$  led to a sharp decrease of the retained austenite content. Besides the strong influence on the  $T_{IA}$  the retained austenite content was strongly dependent on the C-content of the steel. Especially the maximum retained austenite content was elevated by a higher C-content. Furthermore, a higher C-content shifted the maximum retained austenite content to higher  $T_{IA}$ . Subsequently, the temperature, where the maximum amount of austenite is retained will be referred to as  $T_{IAmax}$ .

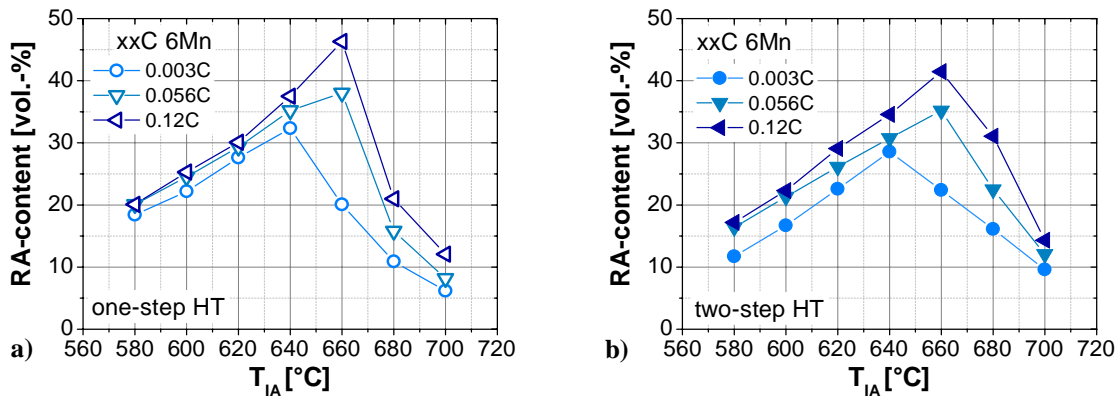


**Figure 5.12:** Retained austenite content as a function of  $T_{IA}$  for **a)** one-step HT and **b)** two-step HT (C-variation, 6 wt-%Mn)

**Figure 5.13** shows the influence of Mn-content on the retained austenite content for one-step and two-step HT. Similar to the steels with the C-variation, the retained austenite content steadily increased to a maximum followed by a sharp drop and further decrease with increasing  $T_{IA}$ . Increasing of the Mn-content not only strongly increased the maximum amount of retained austenite stabilized to room temperature but also the amount stabilized at annealing temperatures lower than  $T_{IAmax}$ . Opposed to the influence of the C-content an increase in Mn provoked a slightly decreasing  $T_{IAmax}$ .



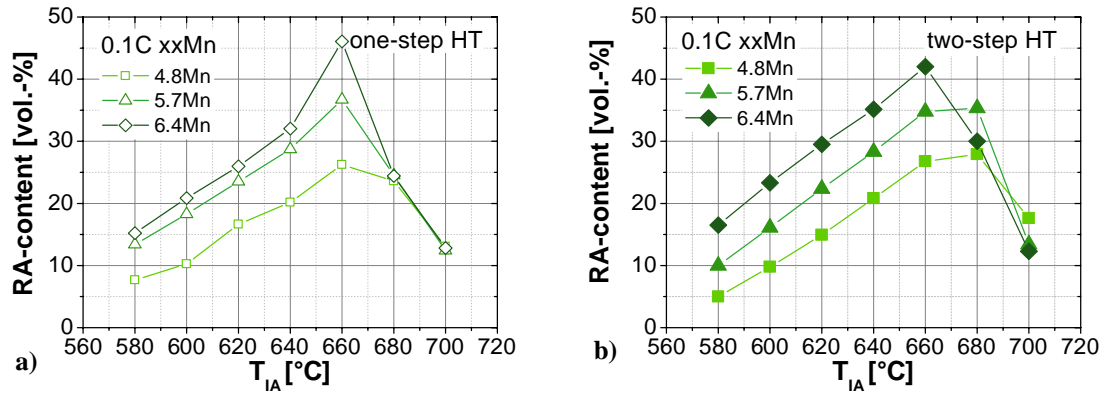


**Figure 5.13:** Retained austenite content as a function of  $T_{IA}$  for **a)** one-step HT and **b)** two-step HT (Mn-variation, 0.1 wt-%C)

**Scanning electron microscopy.** Due to the extreme fine-grained microstructure (grain size < 1  $\mu\text{m}$ ) SEM investigations were necessary to characterize the microstructure in detail. The samples for SEM investigations were grounded, polished and electrochemically etched. This resulted in smooth, elevated areas associated with ferrite and shallow cavities representing retained austenite (see **Chapter 4.5**). Pearlite and martensite were differentiated by their characteristic surficial reliefs. The following section covers the influence of C and Mn on the microstructural constituents present after one-step HT. The results for two-step HT are not presented individually since the trends are the same as for one-step HT. The influence of the HT schedule (one-step vs. two-step HT) is discussed in **Chapter 5.2.1**. The individual microstructural constituents are indicated as followed:  $\alpha$ -ferrite,  $\alpha'$ -martensite,  $\alpha'$ -tempered martensite,  $\gamma$ -austenite and  $\theta$ -cementite. In **Figure 5.14 a) – c)** the microstructures at RT of steels with varying C-content intercritically annealed at 580  $^{\circ}\text{C}$  are displayed. The microstructures consisted of homogenously distributed globular ferrite and austenite. A significant difference in the amount of the present phases due to the C-content could not be observed. The steel 0.12C6Mn additionally contained small amounts of cementite.

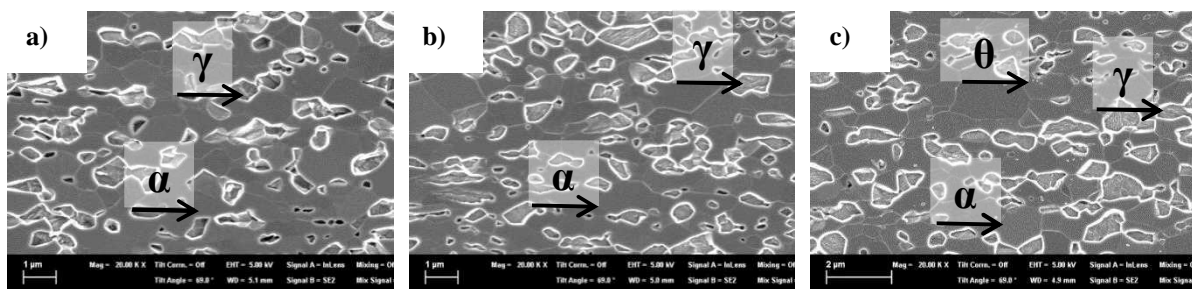


**Figure 5.14:** Microstructure after one-step HT  $T_{IA} = 580^{\circ}\text{C}$  of **a)** 0.003C6Mn, **b)** 0.056C6Mn and **c)** 0.12C6Mn (SEM)

**Figure 5.15 a) – c)** presents the microstructures after annealing at 640  $^{\circ}\text{C}$ . With increasing  $T_{IA}$  the amount of austenite consistently increased. All three steels revealed a duplex microstructure consisting of globular ferrite and retained austenite. Cementite, which was found occasionally at lower  $T_{IA}$ , completely dissolved.

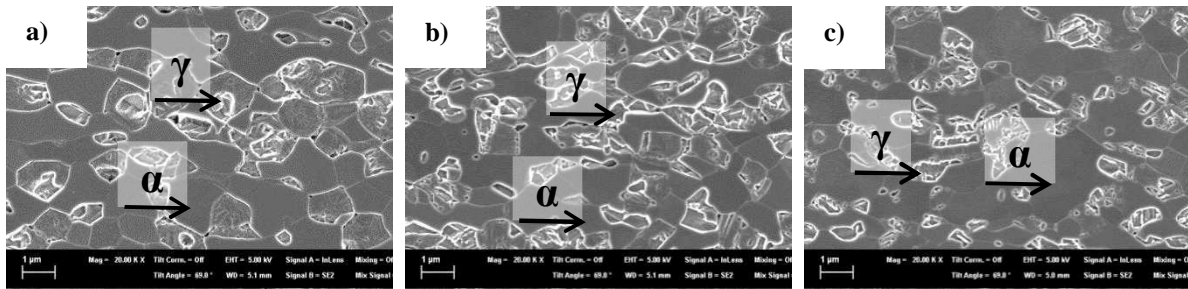


**Figure 5.15:** Microstructure after one-step HT  $T_{IA} = 640\text{ }^{\circ}\text{C}$  of a) 0.003C6Mn, b) 0.056C6Mn and c) 0.12C6Mn (SEM)

After intercritical annealing at  $T_{IA}$  of  $680\text{ }^{\circ}\text{C}$  the microstructures contained besides ferrite and austenite considerable amounts of martensite (**Figure 5.16**). In this case, it could not be reliably differentiated between martensite and austenite and therefore both phases are marked as austenite/martensite constituents. Most probably the structured surface presents the martensite and the cavities the retained austenite. Significant differences in the phase fractions present due to the altering C-content cannot be determined based on the SEM micrographs.

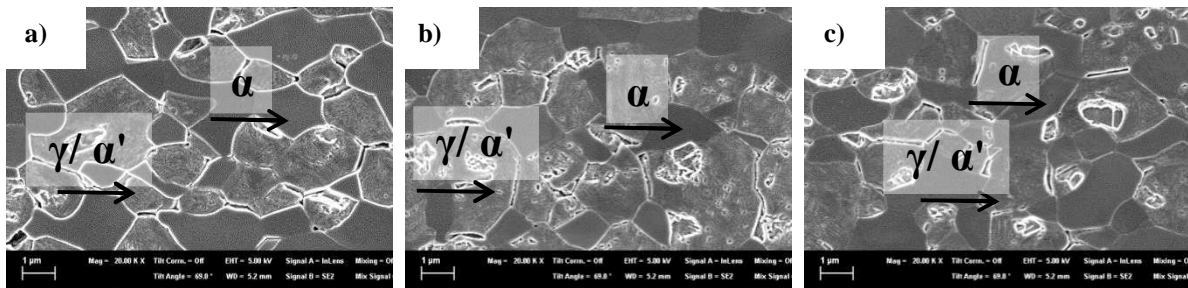


**Figure 5.16:** Microstructure after one-step HT  $T_{IA} = 680\text{ }^{\circ}\text{C}$  of a) 0.003C6Mn, b) 0.056C6Mn and c) 0.12C6Mn (SEM)

The microstructures after annealing at  $700\text{ }^{\circ}\text{C}$  are represented in **Figure 5.17**. As the amount of ferrite was steadily reduced, martensite became the dominant phase in the microstructure. For 0.056C6Mn and 0.12C6Mn self-tempered martensite, indicated by carbide precipitation, was present besides the fresh one. For the almost C-free steel 0.003C6Mn naturally no carbides were observed. The fraction of retained austenite was reduced to a small amount.

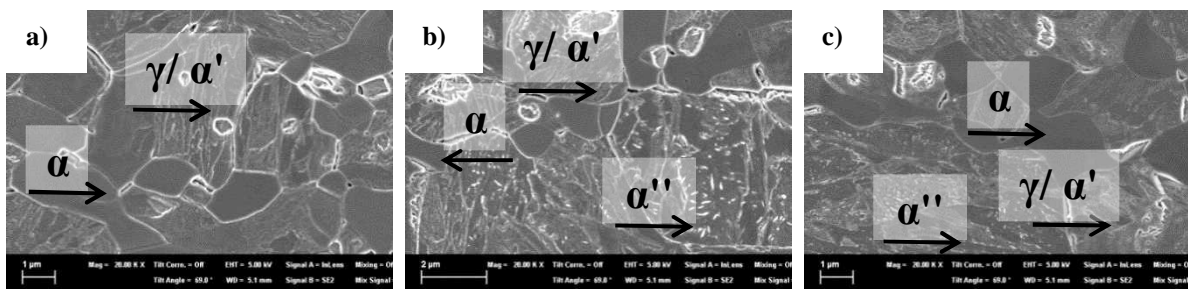


**Figure 5.17:** Microstructure after one-step HT  $T_{IA} = 700\text{ }^{\circ}\text{C}$  of a) 0.003C6Mn, b) 0.056C6Mn and c) 0.12C6Mn (SEM)

The influence of Mn on the microstructure at  $T_{IA} = 580\text{ }^{\circ}\text{C}$  is clearly displayed in **Figure 5.18 a) – c)**. With increasing Mn-content the amount of austenite increased at the expense of ferrite. The amount of cementite on the other hand decreased with increasing Mn-content.

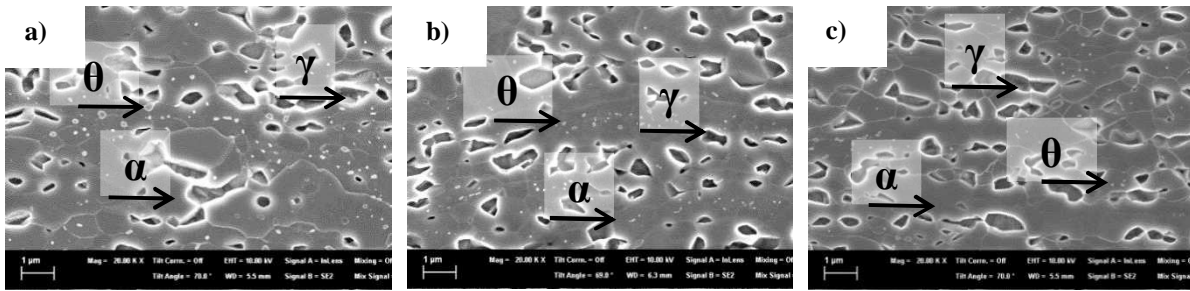


**Figure 5.18:** Microstructure after one-step HT  $T_{IA} = 580\text{ }^{\circ}\text{C}$  of **a)** 0.1C4.8Mn, **b)** 0.1C5.7Mn and **c)** 0.1C6.4Mn (SEM)

Annealing at  $T_{IA} = 640\text{ }^{\circ}\text{C}$  resulted in the desired duplex microstructure consisting of ferrite as matrix and retained austenite inclusions for 0.1C6.4Mn (**Figure 5.19 c**). Neither objectionable cementite precipitates nor hard phases stemming from the cooling process could be identified. However, for 0.1C4.8Mn and 0.1C5.7Mn considerable amounts of pearlite were found (**Figure 5.19 a and b**).

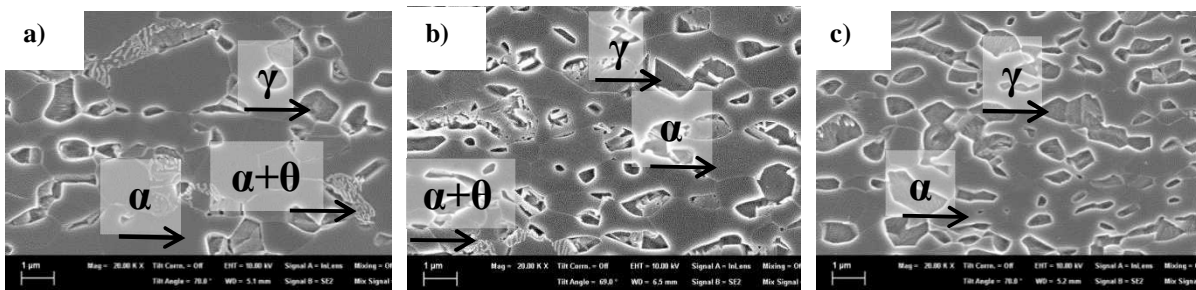


**Figure 5.19:** Microstructure after one-step HT  $T_{IA} = 640\text{ }^{\circ}\text{C}$  of **a)** 0.1C4.8Mn, **b)** 0.1C5.7Mn and **c)** 0.1C6.4Mn (SEM)

The microstructure displayed in **Figure 5.20 a) – c)** resulted from annealing at  $T_{IA} = 680\text{ }^{\circ}\text{C}$ . It consisted of ferrite, retained austenite and significant amounts of martensite that formed during cooling. The steel 0.1C4.8Mn additionally contained small amount of pearlite. Generally, it can be stated that at a constant  $T_{IA}$  an increasing amount of Mn caused the amount of martensite to rise.

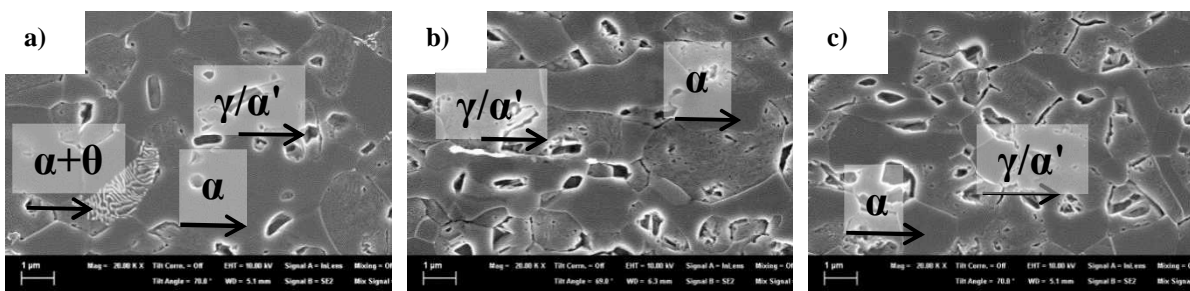


**Figure 5.20:** Microstructure after one-step HT  $T_{IA} = 680\text{ }^{\circ}\text{C}$  of **a)** 0.1C4.8Mn, **b)** 0.1C5.7Mn and **c)** 0.1C6.4Mn (SEM)

In **Figure 5.21 a) – c)** the microstructure after annealing at  $T_{IA} = 700\text{ }^{\circ}\text{C}$  is presented. The rise in the  $T_{IA}$  provoked further martensite formation and decreased the amount of retained austenite. For 0.1C5.7Mn and 0.1C6.4Mn considerable amounts of the martensite were self-tempered and lath-like carbide precipitates were clearly present.

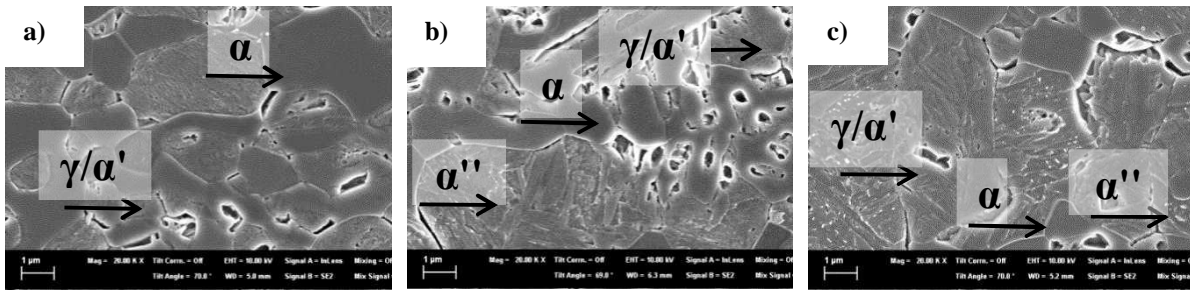


**Figure 5.21:** Microstructure after one-step HT  $T_{IA} = 700\text{ °C}$  of a) 0.1C4.8Mn, b) 0.1C5.7Mn and c) 0.1C6.4Mn (SEM)

### 5.1.2 Mechanical properties

The mechanical properties obtained by tensile testing and their dependence on the chemical composition are presented in the following chapter. The influence of the applied  $T_{IA}$  and the respective HT schedule is discussed in **Chapter 5.2.2**. First of all stress-strain curves after FA (first step during the two-step HT) of the C- and Mn-variations of the investigated steels are illustrated in **Figure 5.22**. An increase in the C- as well as Mn-content clearly increased YS, UTS, UE and TE. However, the variation in C (0.003 - 0.12 wt-%) showed a much higher impact on the mechanical properties than the variation in Mn with YS improving from 825 to 1095 MPa, UTS from 1015 to 1512 MPa, UE from 2.6 to 6.1 % and TE from 6.8 to 10.3 %. The increase in Mn from 4.8 to 6.4 wt-% resulted in an increase of YS from 1003 to 1055 MPa, UTS from 1347 to 1425 MPa, UE from 4.5 to 5.7 % and TE from 8.8 to 10.5 %. The mechanical properties of the mostly martensitic microstructure significantly improved by alloying with C and Mn.

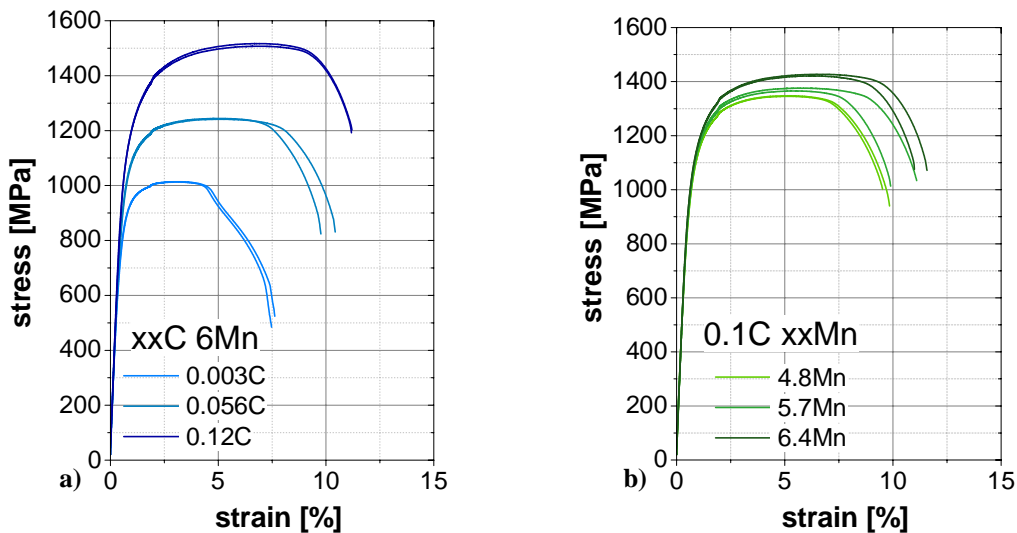


**Figure 5.22:** Engineering stress-strain curves of a) C-variation, 6 wt-%Mn and b) Mn-variation, 0.1 wt-%C after FA (first step during the two-step HT)

**Figure 5.23** shows the influence of the C-content on one-step heat treated samples for selected  $T_{IA}$ . The influence on two-step heat treated samples was basically the same. Therefore, those stress-strain curves are shown in the appendix (**Chapter 10.1**). Generally it can be noted that an increase in C elevated both YS and UTS for all investigated  $T_{IA}$ . At the same time an overall trend to enhanced UE and TE with higher C-contents was provided, with the exception at  $T_{IA} = 680\text{ °C}$ , where 0.12C6Mn displayed the lowest values for UE and TE.

Furthermore, it can be stated that the YPE strongly decreased with increasing  $T_{IA}$  and at  $T_{IA}$  660 and 680 °C respectively finally disappeared. Overall, an increased C-content strongly improved the product of UTS\*TE. From this perspective an increased C-content can be considered as highly favorable.

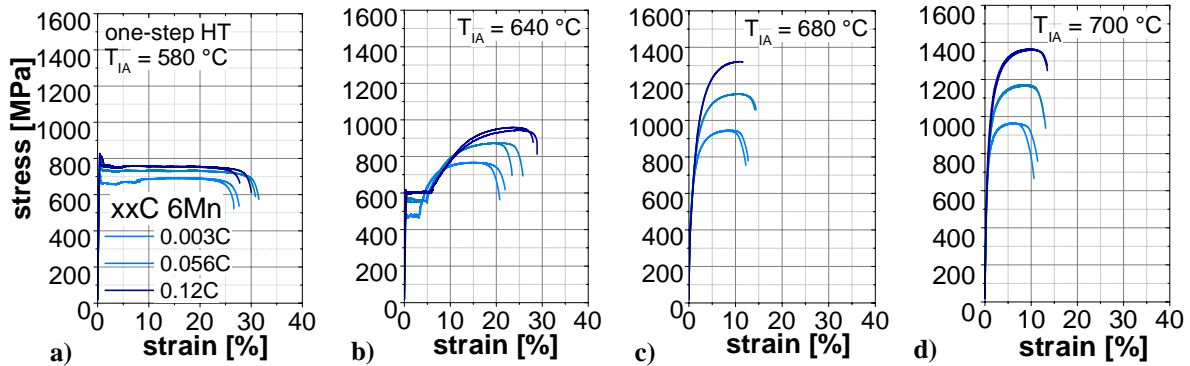


**Figure 5.23:** Engineering stress-strain curves for a  $T_{IA}$  of a) 580 °C, b) 640 °C, c) 680 °C and d) 700 °C for one-step HT (C-variation, 6 wt-%Mn)

The influence of the second investigated alloying element Mn is displayed in **Figure 5.24 a) – d)** representative for one-step HT. Since the influence on the two-step heat treated samples was basically the same the stress-strain curves can be found in the appendix (**Chapter 10.1**). The overall trends of Mn can be compared to those of C. An increase of the Mn-content improved as well YS, UTS, UE and TE, which resulted in an increase of UTS\*TE. However, for  $T_{IA}$  of 680 and 700 °C the trend concerning UE and TE reversed and 0.1C4.8Mn exhibited the highest values for TE and UE although at a lower strength level than for the higher Mn-bearing steels. It can be observed that YPE strongly decreased with increasing  $T_{IA}$  until it finally disappeared at  $T_{IA} = 680$  °C.

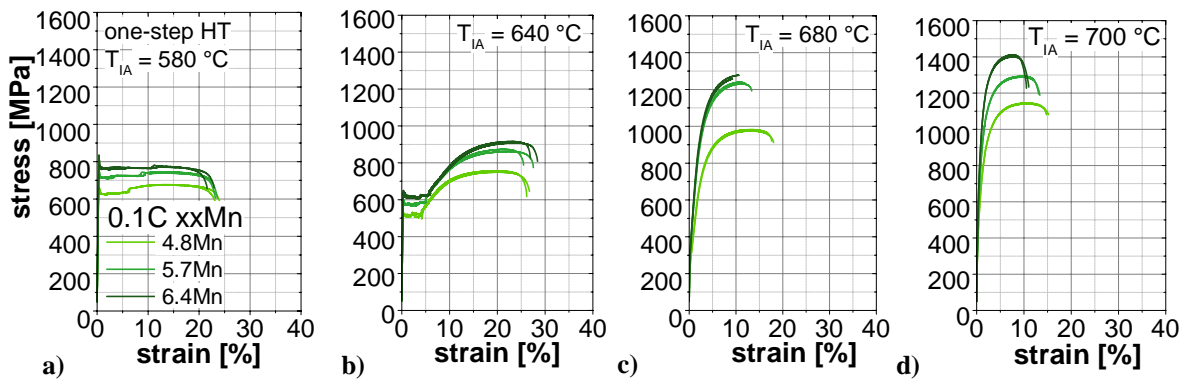


**Figure 5.24:** Engineering stress-strain curves for a  $T_{IA}$  of a) 580 °C, b) 640 °C, c) 680 °C and d) 700 °C for one-step HT (Mn-variation, 0.1 wt-%C)

As shown in **Figure 5.25 a)** for all steels with varying C-content that underwent one-step HT, UTS constantly increased with higher  $T_{IA}$ , while YS initially decreased upon a  $T_{IA}$  of 660 °C and then altered its trend and rose with further increase of the  $T_{IA}$ . A higher C-content of the steel significantly raised both YS and UTS over the whole range of tested  $T_{IA}$ . For YS the impact of the C-content was stronger at the lower range of investigated  $T_{IA}$ , while for UTS the influence appeared to be enhanced at higher  $T_{IA}$ . The evolution of UE and TE is exhibited in **Figure 5.25 b)**. For all investigated steels, UE and TE showed a maximum value at  $T_{IA} = 600$  °C. The higher the steel's C-content the higher were the obtained maxima of both values.



Annealing at  $T_{IA}$  higher than 600 °C resulted in a constant decrease of both values, UE and TE.

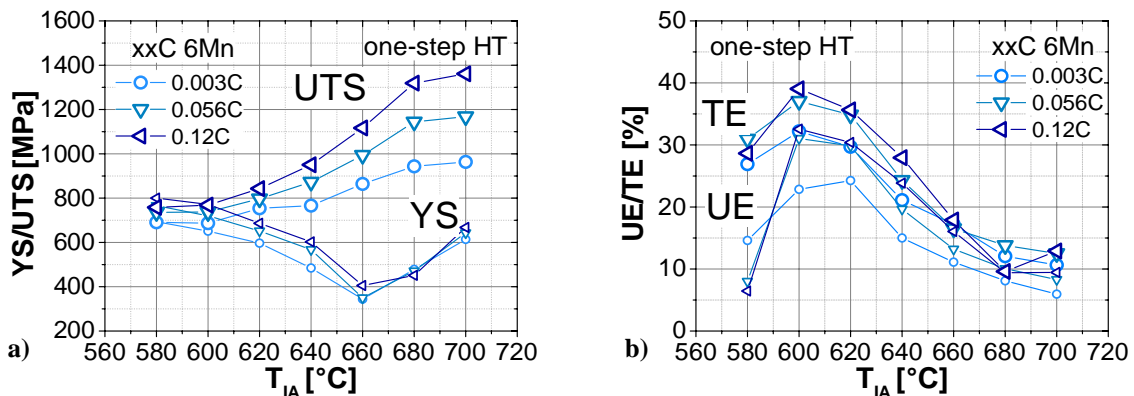


**Figure 5.25:** a) YS and UTS and b) UE and TE as a function of  $T_{IA}$  for one-step HT (C-variation, 6 wt-%Mn)

The influence of the C-content on the mechanical properties of steels that underwent a two-step HT is displayed in **Figure 5.26**. Similar trends to the one-step HT can be observed. UTS strongly increased with raising  $T_{IA}$ , whereas YS continuously dropped until a  $T_{IA}$  of 680 °C. Further increase in  $T_{IA}$  provoked an increase of YS. A higher C-content clearly increased both YS and UTS. For all steels, UE and TE (**Figure 5.26 b**) exhibited a clear maximum at  $T_{IA} = 620$  °C. By increasing the C-content a strong gain in UE and TE could be obtained.

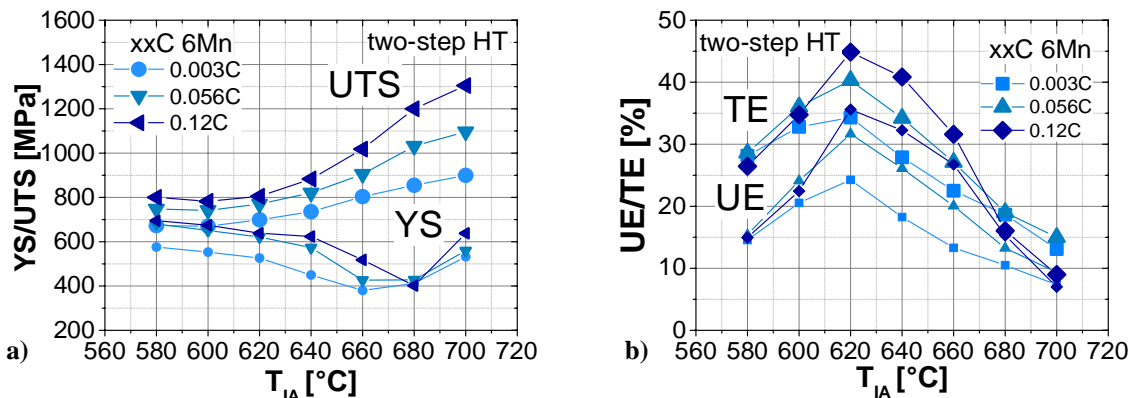


**Figure 5.26:** a) YS and UTS and b) UE and TE as a function of  $T_{IA}$  for two-step HT (C-variation, 6 wt-%Mn)

The influence of the Mn-content on the mechanical properties of the investigated steels with 0.1 wt-% C heat treated by one-step HT is displayed in **Figure 5.27**. Similar to the steels with varying C-content, UTS constantly increased with increasing  $T_{IA}$ . YS dropped to a minimum at  $T_{IA} = 680$  °C and strongly increased by further increase of  $T_{IA}$ . Mn significantly enhanced YS and UTS. The development of UE and TE showed a maximum at  $T_{IA} = 620$  °C for 0.1C4.8Mn and at  $T_{IA} = 600$  °C 0.1C5.7Mn and 0.1C6.4Mn respectively. For the steel with the lowest Mn-content 0.1C4.8Mn the maximum elongation that could be obtained was considerably smaller than for the two other steels. 0.1C5.7Mn and 0.1C6.4Mn did not significantly differ in the maximum elongation obtained. At  $T_{IA} \geq 660$  °C a lower Mn-content seemed to be beneficial in order to obtain higher elongations.

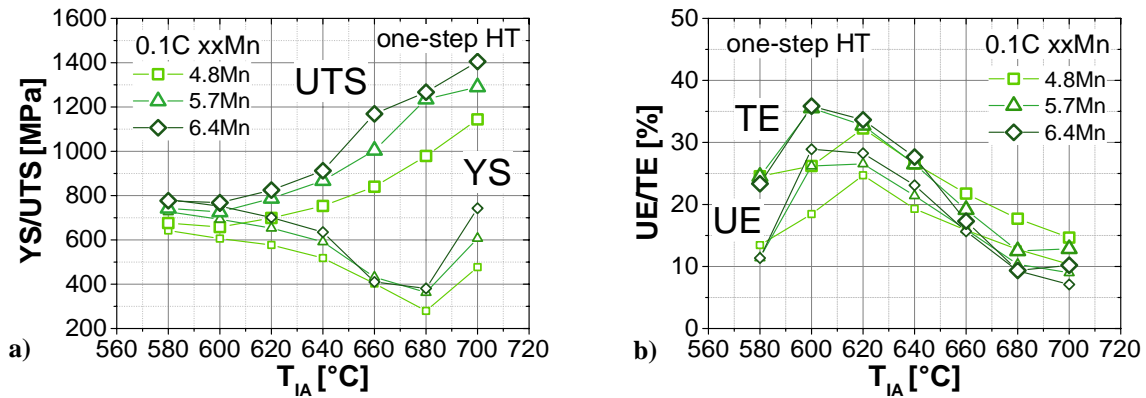


Figure 5.27: a) YS and UTS and b) UE and TE as a function of  $T_{IA}$  for one-step HT (Mn-variation, 0.1 wt-%C)

The mechanical properties of the Mn-variations that underwent two-step HT are represented in **Figure 5.28**. The development of YS and UTS of the two-step HT with altering  $T_{IA}$  (**Figure 5.28 a**) showed the same trend as for one-step HT. A significant rise of UTS and a steady decline of the YS upon a minimum value at  $T_{IA} = 680$  °C can be observed. Annealing at 700 °C further increased the UTS but also resulted in a higher value for YS. By increasing the Mn-content both higher YS and UTS can be gained. **Figure 5.28 b**) displays the evolution of the UE and TE. Both values obtain a maximum at  $T_{IA} = 620$  °C for all three investigated steels. The maximum TE could be increased by increasing the Mn-content from 4.8 to 5.7 wt-%. The difference in the maximal obtained TE between 0.1C5.7Mn and 0.1C6.4Mn lay within the scatter band. For  $T_{IA} \leq 640$  °C a higher Mn-content appeared to be efficient to enhance elongations, whereas for  $T_{IA} \geq 640$  °C lower Mn-contents were beneficial.

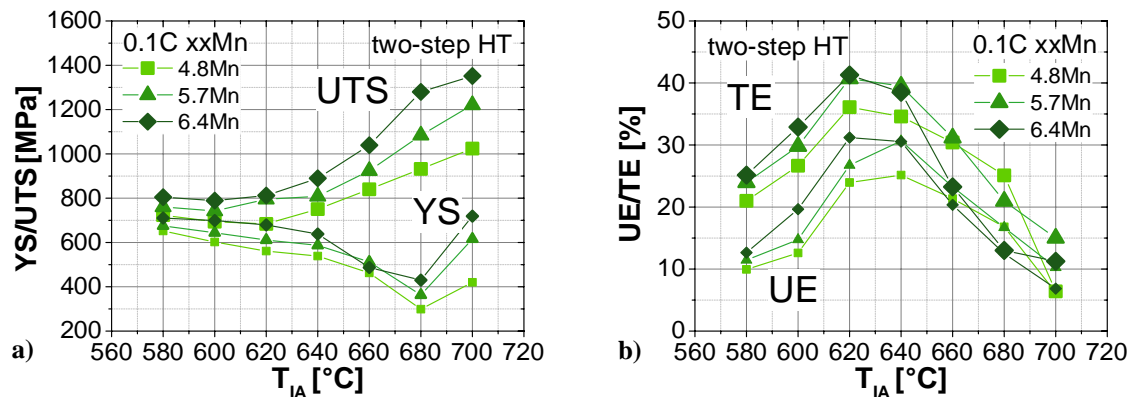


Figure 5.28: a) YS and UTS and b) UE and TE as a function of  $T_{IA}$  for two-step HT (Mn-variation, 0.1 wt-%C)

### 5.1.3 Yielding behavior

The investigated steels showed pronounced discontinuous yielding after certain heat treatment conditions. Especially after annealing in the low range of investigated  $T_{IA}$  large yield point elongations (YPE) and high differences between the upper yield strength (UYS) and the lower yield strength (LYS) were observed. Selected tensile curves are displayed in **Chapter 5.1.2** and **5.2.2**. Therefore the following chapter presents the influence of the chemical composition on these characteristics. In **Figure 5.29** the YPE and the difference between UYS and LYS are plotted as a function of the  $T_{IA}$  for the steels of the C-variation. For the one-step HT a clear trend of declining UYS-LYS and YPE with increasing  $T_{IA}$  was obvious, whereas an influence of C on these parameters cannot clearly be indicated. Despite the overall trend, the

YPE at a  $T_{IA}$  of 580 °C was decreased compared to 600 °C for all three chemical compositions. Depending on the C-content, annealing at 660 and 680 °C respectively resulted in continuous yielding. Tensile curves of samples heat treated with higher  $T_{IA}$  yielded without exception continuously. It should be noted that enormous YPE up to 15 % were observed. For the two-step HT basically the same trends were found. However, the YPE as well as the UYS-LYS were considerably smaller than for the one-step HT. A significant influence of the C-content on the parameters could not be found.

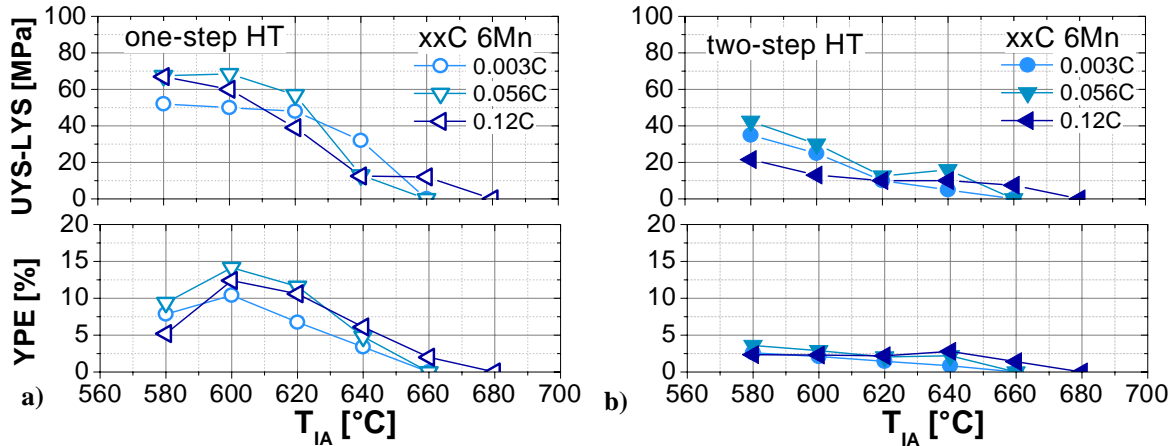


Figure 5.29: YPE and UYS-LYS as a function of the  $T_{IA}$  for a) one-step HT and b) two-step HT (C-variation, 6 wt-%Mn)

The yielding behavior of the Mn-variations showed the same overall trends presented in Figure 5.30 as for the variation for the C-content. For the one-step as well as for the two-step HT, YPE and UYS-LYS decreased considerably with increasing  $T_{IA}$ . Similar to the C-variation a significant influence of the Mn-content on the yielding behavior of the two-step HT could not be observed. However, for the one-step HT a trend of increasing YPE as well as UYS-LYS with increasing Mn-content seems to exist. Annealing at a  $T_{IA}$  of 680 °C led to continuous yielding for all steels and HT schedules.

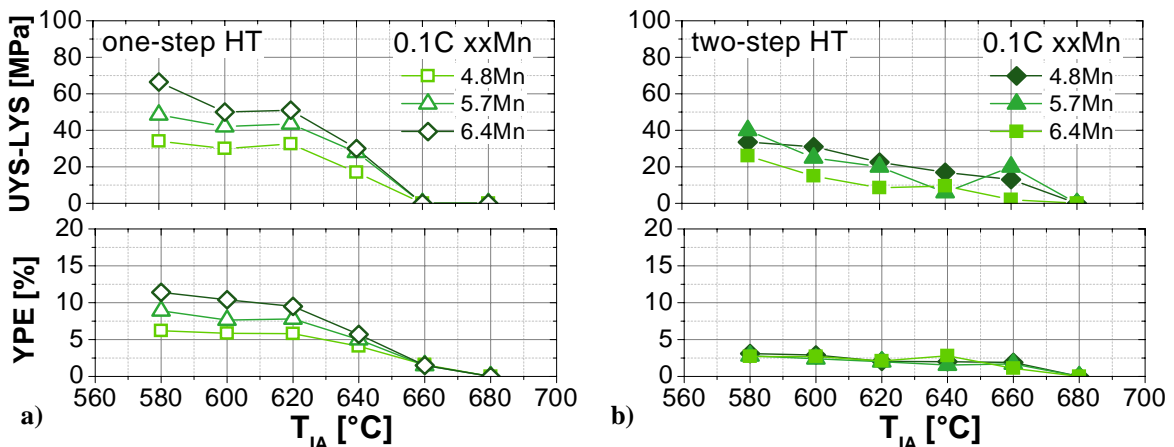
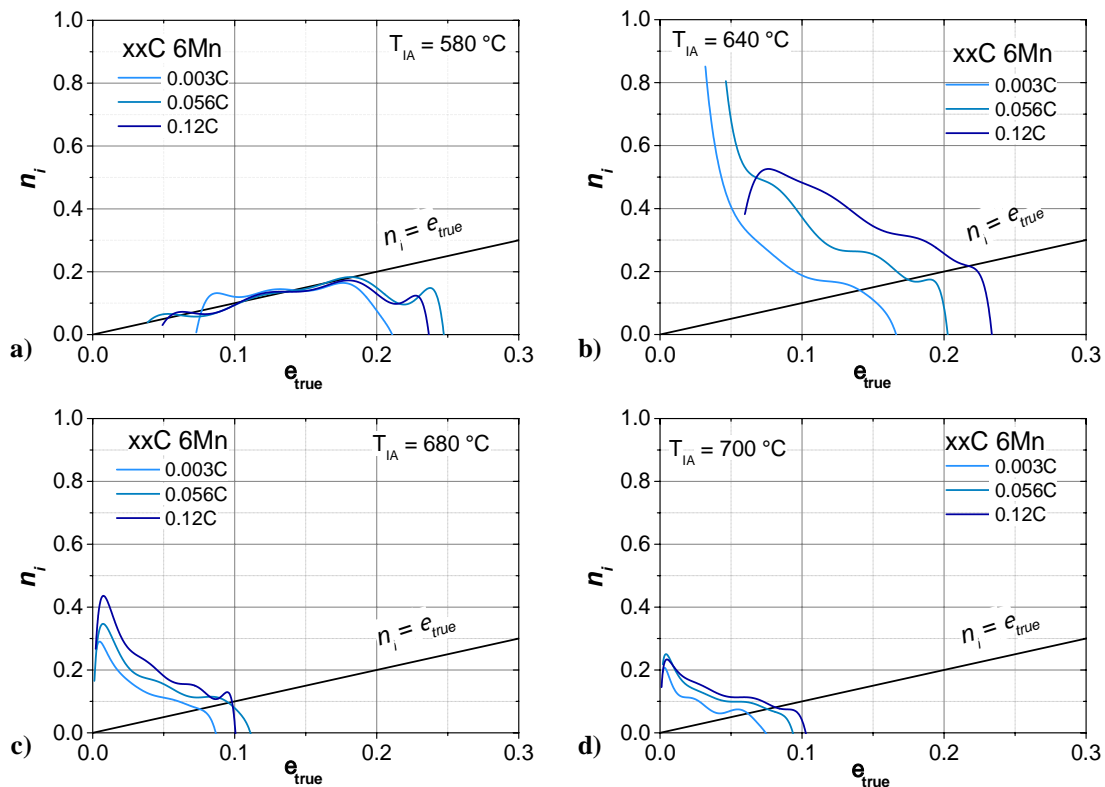


Figure 5.30: YPE and UYS-LYS as a function of the  $T_{IA}$  for a) one-step HT and b) two-step HT (Mn-variation, 0.1 wt-%C)



### 5.1.4 Work hardening behavior

**Incremental n-value.** Figure 5.31 represents the incremental work hardening coefficient  $n_i$  as a function of the true strain  $\varepsilon_{true}$  (calculated between the end of the YPE and fracture) for selected  $T_{IA}$  displaying the investigated steels with altering C-content. Considering the Considère instability criterion the deformation proceeds uniformly as long as  $n_i$  is higher than  $\varepsilon_{true}$ . As soon as those two values become equal the uniform elongation is reached and is followed by necking and localized deformation until fracture, where the Considère instability criterion is not valid anymore. Figure 5.31 a) shows the development of  $n_i$  for  $T_{IA} = 580$  °C. Here,  $n_i$  oscillated around the line representing  $n_i = \varepsilon_{true}$  and therefore, it was not possible to determine the uniform elongation. The progress of  $n_i$  did not show the expected and well-known work hardening and necking behavior. Further, no significant trends correlating with the C-content could be found. Different behavior was found for  $T_{IA}$  of 640 °C (Figure 5.31 b). For this temperature  $n_i$  showed the expected work hardening characteristics. The steels 0.003C6Mn and 0.056C6Mn exhibited very high  $n_i$ -values at small  $\varepsilon_{true}$  which decreased rapidly with increasing strain. The steel with the highest C-content 0.12C6Mn first showed a steep increase in  $n_i$  followed by a decrease at higher  $\varepsilon_{true}$ . The higher the C-content the smaller was the slope of the decreasing  $n_i$ -value which resulted in higher uniform elongations. Examining the development of the  $n_i$ -value for  $T_{IA}$  of 680 and 700 °C (Figure 5.31 c and d) it can be observed that all steels showed a similar behavior as described before with a sharp increase of the  $n_i$ -value at the beginning of the deformation, followed by a decrease towards the  $n_i = \varepsilon_{true}$  intersection. Increasing the C-content led to a moderate decrease of  $n_i$ . Therefore, higher uniform elongations could be reached for higher C-containing steels.



**Figure 5.31:** Incremental n-value  $n_i$  as a function of the true strain for one-step HT for a  $T_{IA}$  of a) 580 °C, b) 640 °C, c) 680 °C and d) 700 °C (C-variation, 6 wt-%Mn)

The influence of the steels' Mn-content on the  $n_i$ -value is presented in **Figure 5.32**. For a low  $T_{IA}$  of 580 °C the development of the  $n_i$ -value started surprisingly with values below  $\varepsilon_{true}$ . For 0.1C4.8Mn and 0.1C5.7Mn the values increased and exceeded  $\varepsilon_{true}$  at some point followed by their deterioration later on. The  $n_i$ -value of 0.1C6.4Mn, on the other hand, remained below  $\varepsilon_{true}$  over the entire tested strain range. All three investigated steels did neither follow the expected work hardening behavior nor fulfil the Considère instability criterion. Nevertheless rather high total elongation could be achieved by tensile testing. With increasing  $T_{IA}$  the work hardening behavior altered. For  $T_{IA} = 640$  °C the  $n_i$ -value right after YPE started from a moderate level up to a maximum value. Further increase in strain resulted in its decrease. For a  $T_{IA}$  of 640 °C the maximum  $n_i$ -value was achieved for the highest Mn-containing steel, which also showed the highest uniform elongation. At  $T_{IA} = 680$  °C the three steels behaved rather similar with the high maximum  $n_i$ -value occurring at very low strains resulting in decreased uniform elongations. The highest investigated  $T_{IA}$  of 700 °C showed slightly reduced  $n_i$ -value stronger pronounced with increasing Mn-content. Therefore, the highest uniform elongation was achieved by 0.1C4.8Mn.

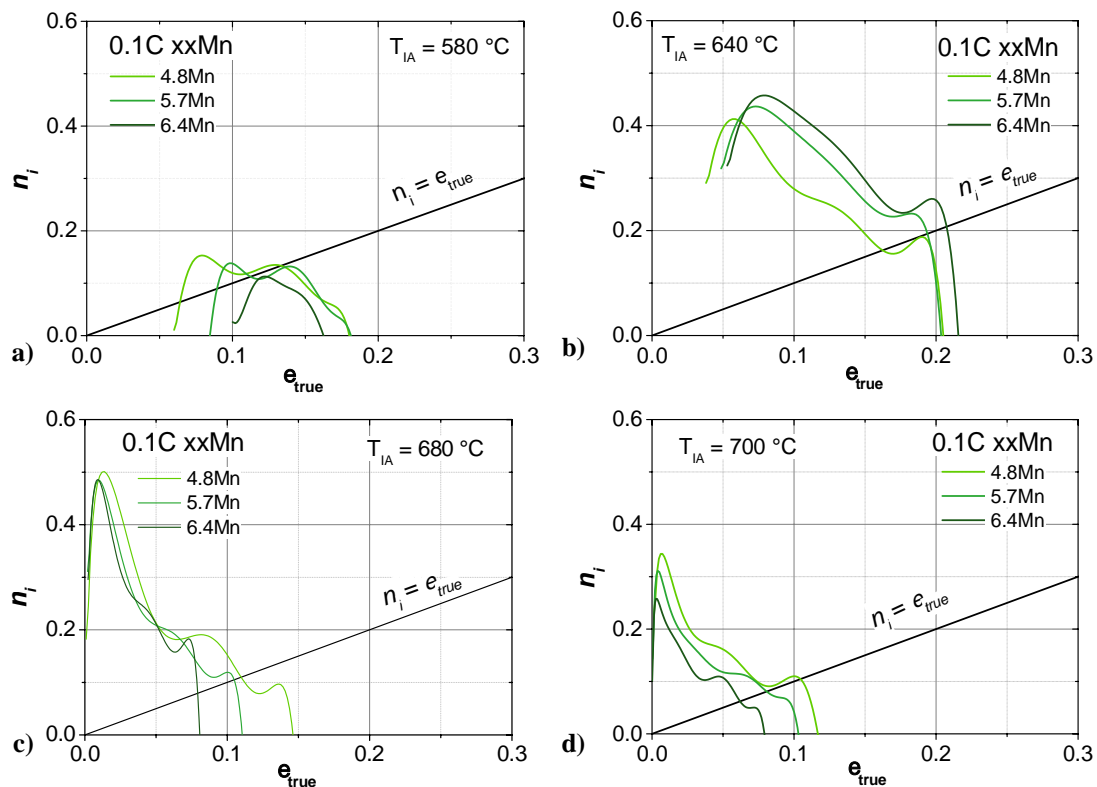


**Figure 5.32:** Incremental n-value  $n_i$  as a function of the true strain for one-step HT for a  $T_{IA}$  of a) 580 °C, b) 640 °C, c) 680 °C and d) 700 °C (Mn-variation, 0.1 wt-%C)

**Retained austenite stability.** In order to determine the stability of the retained austenite interrupted tensile tests were performed and the retained austenite content was measured at several strain levels. **Figure 5.33 a) – c)** displays the retained austenite content as a function of the strain for the steels with C-variation for three different  $T_{IA}$ . In general it can be observed that with increasing strain the amount of retained austenite decreased. Higher C-contents of the steel increased the initial retained austenite fraction before straining. On the basis of the given illustrations in **Figure 5.33** a valid quantifiable conclusion concerning the stability of the retained austenite at constant  $T_{IA}$  and varying C-content could not be made.

But it could be observed that with increasing  $T_{IA}$  the retained austenite became less stable as it transformed at significant lower strains.

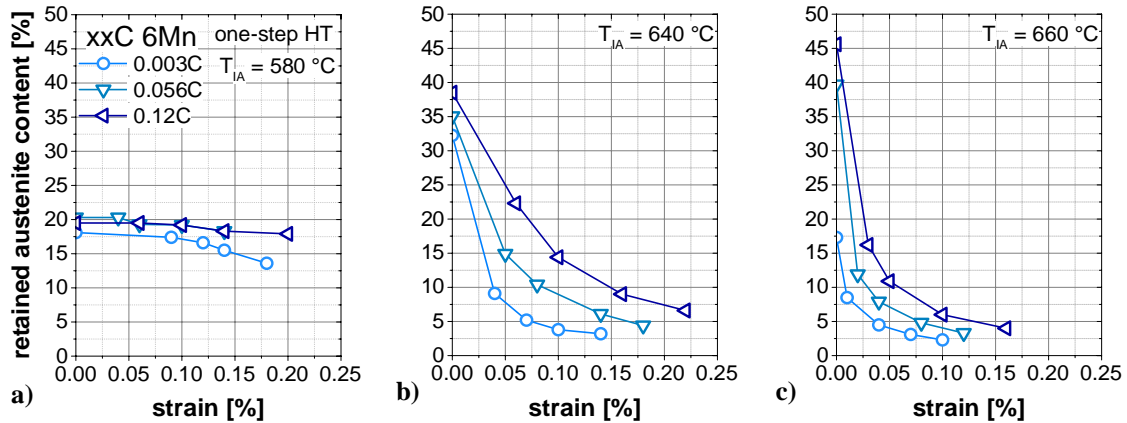


**Figure 5.33:** Retained austenite content as a function of strain for  $T_{IA}$  of **a)** 580 °C, **b)** 640 °C and **c)** 660 °C for one-step HT (C-variation, 6 wt-%Mn)

To enable a convenient comparison of the retained austenite stability depending on the steel's C-content the amount of transformed austenite is displayed as a function of true strain in **Figure 5.34 a) – c)**. The resulting correlations followed a strict linear trend over all investigated steels and  $T_{IA}$ . Thus, the slope of the linear correlation  $k_p$  provided a valid basis to compare the stability of the retained austenite.

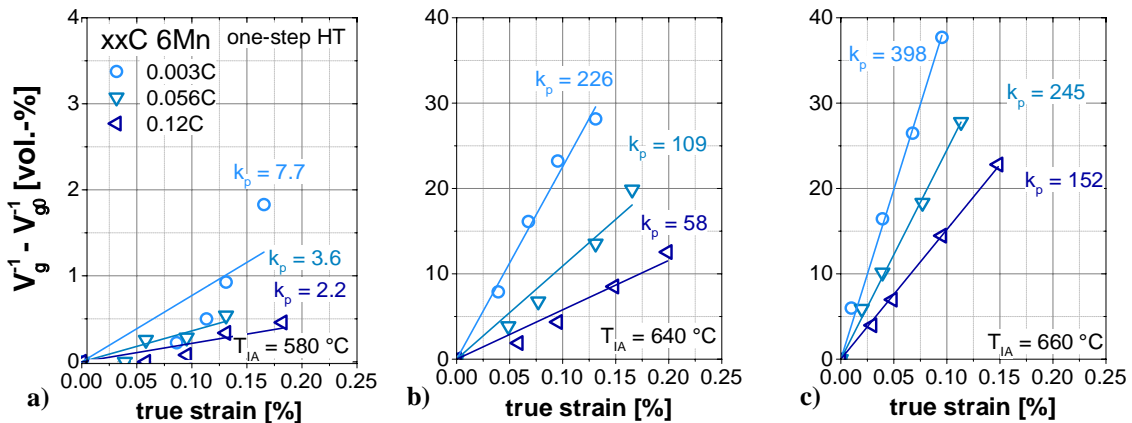


**Figure 5.34:** Transformed retained austenite as a function of true strain for  $T_{IA}$  of **a)** 580 °C, **b)** 640 °C and **c)** 660 °C for one-step HT (C-variation, 6 wt-%Mn)

Therefore, the  $k_p$ -values for the respective steels and  $T_{IA}$  are shown in **Figure 5.35 a)** and **b)**. This illustration reveals the strong influence of the steel's C-content on the retained austenite stability, whereby higher  $k_p$ -values represent lower retained austenite stability. A clear trend of decreasing retained austenite stability with increasing  $T_{IA}$  could be observed. Besides the dominating effect of the  $T_{IA}$  on the retained austenite stability, an increase in C-content significantly enhanced the retained austenite stability and delayed the transformation to martensite to higher true strains or even prevented the transformation totally. This trend could be observed for one-step as well as for two-step HT even though there was a large difference in the retained austenite stability between the two HT schedules, which is described in detail in **Chapter 5.2.4**.

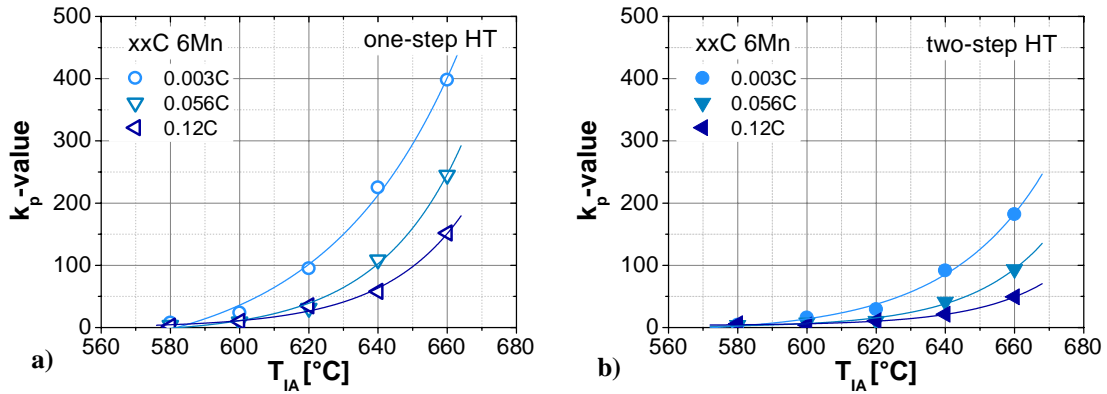


Figure 5.35:  $k_p$ -value as a function of  $T_{IA}$  for a) one-step HT and b) two-step HT (C-variation, 6 wt-%Mn)

Interrupted tensile testing was also performed on two steels containing altering amounts of Mn (0.1C4.8Mn and 0.1C5.9Mn). The testing procedure was identical to the above presented results of the C-variation. The results presented in **Figure 5.36** show the  $k_p$ -values obtained from the linearization of the transformed retained austenite content as a function of the true strain. The retained austenite contents and corresponding strains can be found in the appendix (**Chapter 10.2**). It is clearly shown that within the two investigated steels a higher overall Mn-content of the steel leads to increased retained austenite stability for both HT schedules. The applied  $T_{IA}$  again dominantly influenced the retained austenite stability. Annealing at higher  $T_{IA}$  resulted in substantially higher  $k_p$ -values and therefore, in a lower stability of the retained austenite.

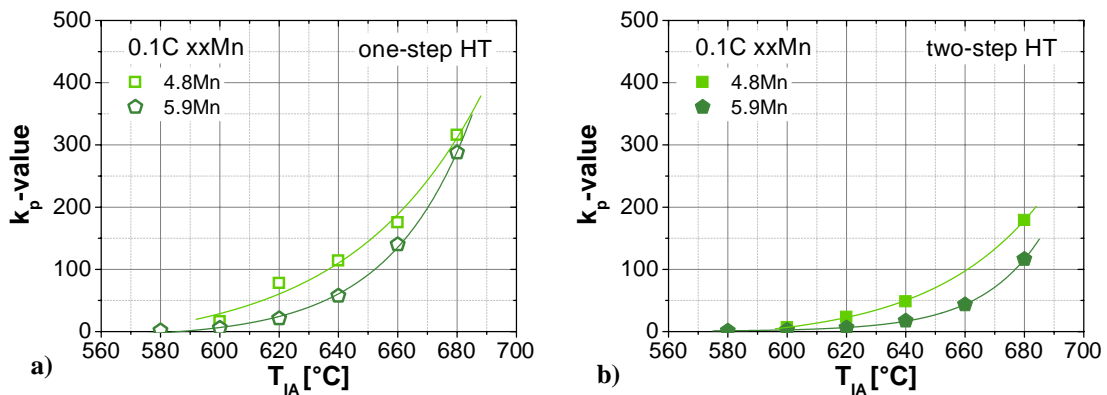
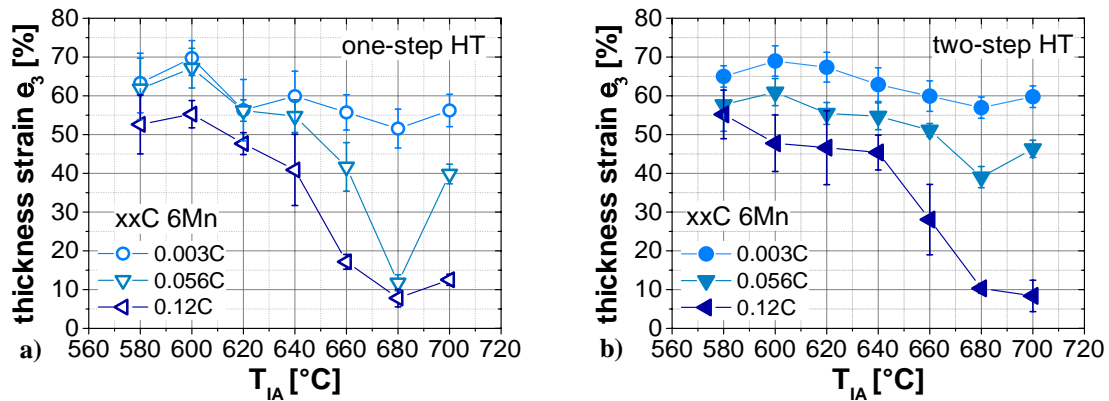


Figure 5.36:  $k_p$ -value as a function of  $T_{IA}$  for a) one-step HT and b) two-step HT (Mn-variation, 0.1 wt-%C)

### 5.1.5 Damage behavior

**Postuniform behavior.** The thickness strain  $\epsilon_3$  after fracture was measured as a criterion for postuniform behavior of the steel. The higher the thickness strain  $\epsilon_3$  is the higher the supposed resistance against crack growth and failure. **Figure 5.37** represents the values of the thickness strain for the C-variation after one-step and two-step HT respectively as a function of the  $T_{IA}$ . The same overall trend was observed for all alloying systems and HT schedules. Starting from a high value at low  $T_{IA}$  the thickness strain  $\epsilon_3$  constantly decreased until a minimum value was reached. A further increase in the  $T_{IA}$  led to a rise in the thickness strain  $\epsilon_3$ . A lower C-content significantly elevated the values of the thickness strain  $\epsilon_3$ , while the most pronounced effect in this respect can be noted at the minimum values: as the steel 0.003C6Mn did not develop a pronounced drop in the thickness strain, it was strongly featured by higher C-containing

steels. A precise look on the data revealed that at the lowest  $T_{IA} = 580\text{ °C}$  a slight drop of the thickness strain  $\epsilon_3$  could be observed except for 0.12C6Mn two-step HT.



**Figure 5.37:** Thickness strain  $\epsilon_3$  as a function of  $T_{IA}$  for **a)** one-step HT and **b)** two-step HT (C-variation, 6 wt-%Mn)

**Figure 5.38** shows the influence of Mn-content on the thickness strain  $\epsilon_3$ . The general trend was similar to the C-variation - with high  $\epsilon_3$ -values at low  $T_{IA}$ , which decreased until a minimum value was reached. For 0.1C4.8Mn one-step HT and 0.1C6.4Mn one-step and two-step HT a rise in the  $\epsilon_3$ -value could be observed with further increase of the  $T_{IA}$ . Higher Mn-contents decreased the thickness strain  $\epsilon_3$  to a small extend. Moreover, compared to the effect of the C-content, Mn affected the thickness strain  $\epsilon_3$  only moderately. Besides decreasing the value of the thickness strain an increased Mn-content shifted the  $T_{IA}$ , where the minimum occurred, to lower temperatures.

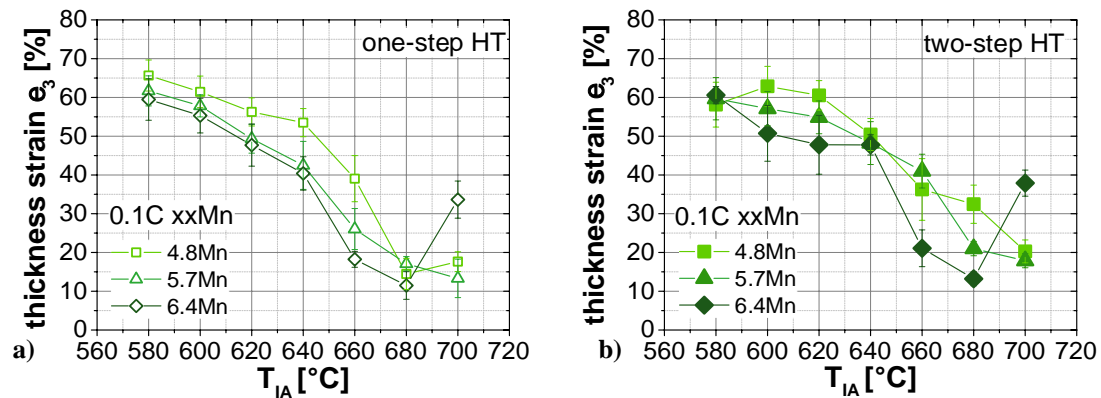


**Figure 5.38:** Thickness strain  $\epsilon_3$  as a function of  $T_{IA}$  for **a)** one-step HT and **b)** two-step HT (Mn-variation, 0.1 wt-%C)

## 5.2 Influence of the heat treatment

The following chapter describes the substantial influence of the heat treatment on the microstructure and the resulting mechanical behavior including a variation of  $T_{IA}$  and especially focusing on the differences induced by one-step and two-step HT respectively.

### 5.2.1 Microstructural evolution

**Dilatometry.** In order to determine the influence of the applied HT on the microstructural evolution dilatometric testing was carried out. In **Figure 5.39** the time-temperature schedule of the FA (first step during the two-step HT) is displayed combined with the dilatation during the HT. All six steels showed the same behavior of expansion during heating to  $T_A$  until the austenite formation started, characterized by shrinking of the sample. Once a fully austenitic microstructure was reached the dilatometric sample expanded again due to thermal expansion. During holding at  $T_A$  no change in the sample dimension could be detected. Quenching to  $T_{IH}$  led to linear reduction in sample size simply due to temperature reduction. During isothermal holding at  $T_{IH}$  of 500 °C none of the steels showed a change in dilatation indicating a phase transformation. Thus, all steels showed a pronounced martensitic transformation during cooling to RT.

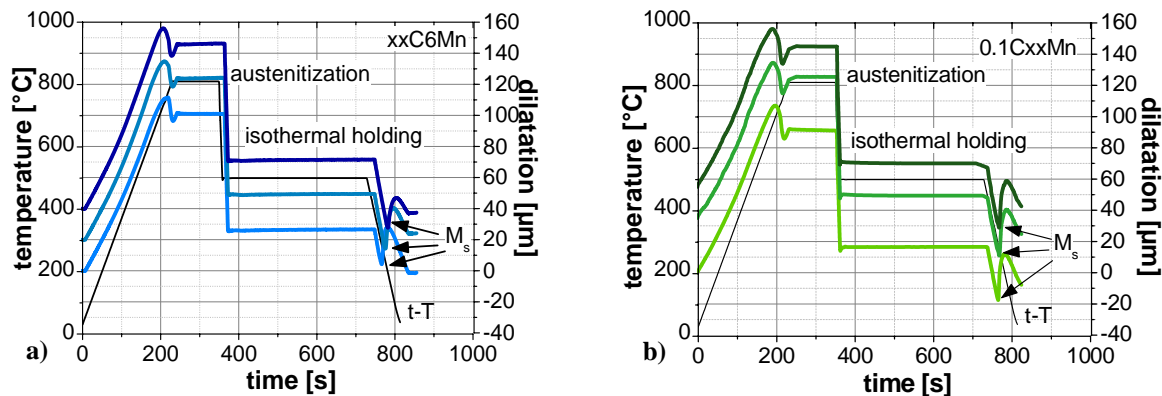


**Figure 5.39:** Time-temperature schedule and elongations of the FA step of the two-step HT for the a) C-variation, 6 wt-%Mn and b) Mn-variation 0.1 wt-%C

**Figure 5.40** shows the dilatometric curves during cooling from  $T_{IA}$  for one-step and two-step HT on the example of the C-variation. By precise evaluation of the transformation temperatures it could be found that the  $M_s$ -temperatures varied depending on the applied HT schedule. Throughout all investigated  $T_{IA}$  and chemical compositions the one-step HT showed a more pronounced martensitic transformation at lower temperatures than the two-step heat treated samples. A closer look on the experimental data revealed that the one-step HT samples exhibited a slight deviation from the linear shrinking at higher temperatures prior to the temperatures where the martensite kinetics started to accelerate. At certain  $T_{IA}$  those indications of phase transformations occurred at temperatures associated with bainite formation and therefore they are denominated with  $B_s$  (bainite start). It has to be mentioned that the observed bainite formation was limited to a very small amount of bainite, which was too low to detect *via* SEM.



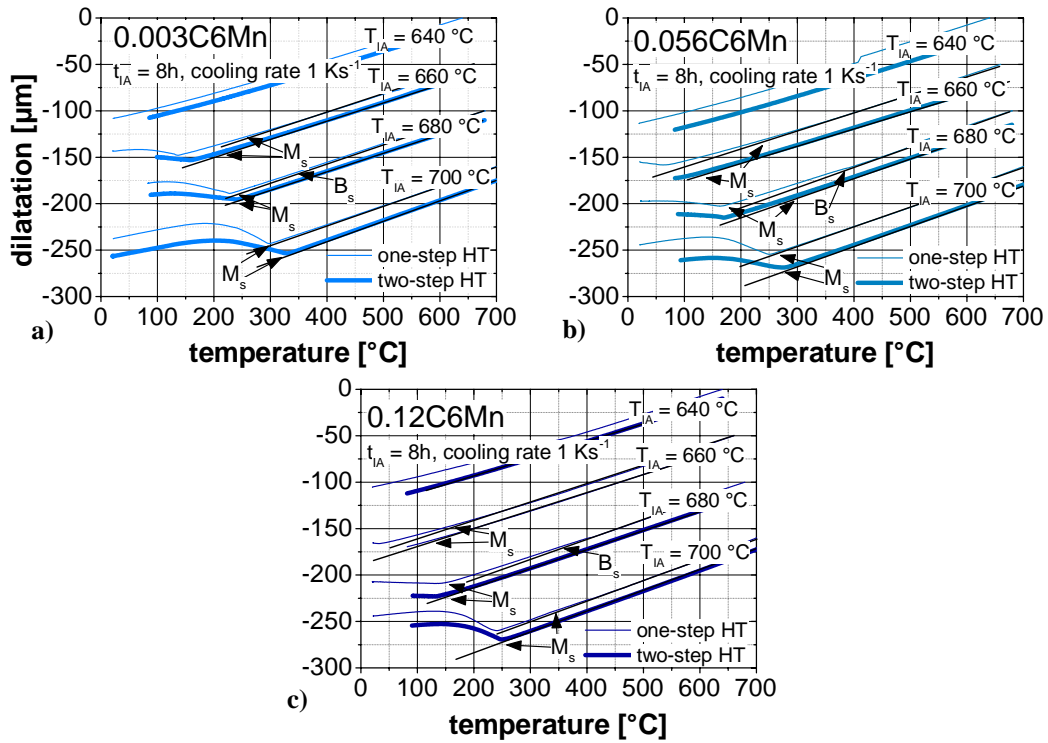


**Figure 5.40:** Comparison of the dilatometric curves of the cooling phase after intercritical annealing for 8 h and cooling rate of 1K s-1 of a) 0.003C6Mn, b) 0.056C6Mn and c) 0.12C6Mn for one-step and two-step HT

The same trends could also be found for the Mn-variation (**Figure 5.41**). Here, the one-step HT again showed slight deviation from the linear shrinking preceding the pronounced martensitic transformation. This means that comparing one-step with two-step HT, throughout all investigated steels phase transformations during cooling started at higher temperatures for the one-step heat treated samples.

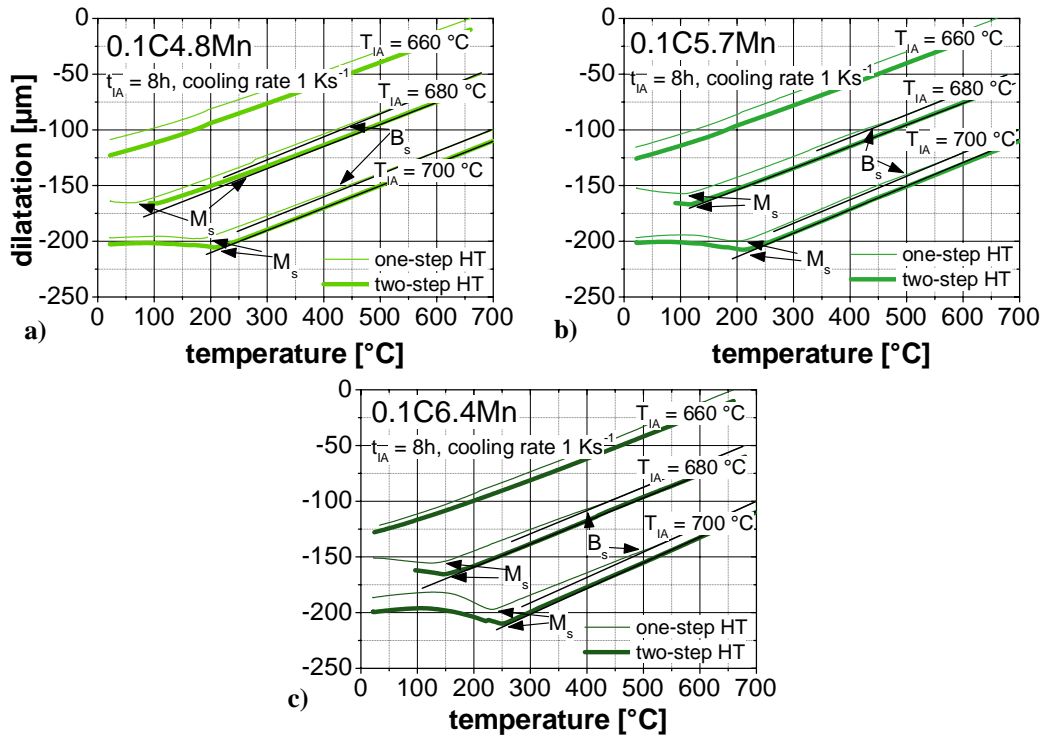


**Figure 5.41:** Comparison of the dilatometric curves of the cooling phase after intercritical annealing for 8 h and cooling rate of 1K s-1 of a) 0.1C4.8Mn, b) 0.1C5.7Mn and c) 0.1C6.4Mn for one-step and two-step HT

**Scanning electron microscopy.** In the following chapter, selected SEM micrographs display the development of the microstructure depending on the applied HT. The individual microstructural constituents are indicated as followed:  $\alpha$ -ferrite,  $\alpha'$ -martensite,  $\alpha'$ -tempered martensite,  $\gamma_G$ - globular austenite,  $\gamma_L$ - lath-like austenite and  $\theta$ -cementite. The microstructural evolution was strongly influenced by the  $T_{IA}$  and the application of one-step or two-step HT respectively. As indicated by thermodynamic calculations as well as dilatometric investigations it is also shown by SEM investigations that with increasing  $T_{IA}$  the amount of ferrite steadily decreased while the amount of retained austenite increased and at higher  $T_{IA}$  also the fraction of martensite raised (**Figure 5.42** and **Figure 5.43**). Exemplarily for the influence of the  $T_{IA}$  and the HT schedule on the development of the microstructure the steel 0.1C6.4Mn is presented in the following. **Figure 5.42 a)** and **b)** displays the microstructure after annealing at  $T_{IA} = 580$  °C. For one-step as well as two-step HT it consisted of a ferritic matrix with a substantial amount of retained austenite. Moreover, a significant amount of cementite/ $M_3C$  was present in the microstructure. Comparing one-step with two-step HT, it was clearly visible that the different HT influences the morphology of all the respective phases. The globular shape of ferrite and austenite after one-step HT was modified to a lath-like shape after two-step HT. While the ferritic matrix was then exclusively lath-shaped, the retained austenite displayed still a small amount of globular shaped grains after two-step HT. The present cementite was homogenously distributed and appeared globular after one-step HT and as small rods after two-step HT. Increasing the  $T_{IA}$  to 640 °C the amount of retained austenite increased at the expense of ferrite (**Figure 5.42 c** and **d**). The cementite was fully dissolved for both HT schedules. The difference in morphology between one-step and two-step HT was increasingly pronounced.

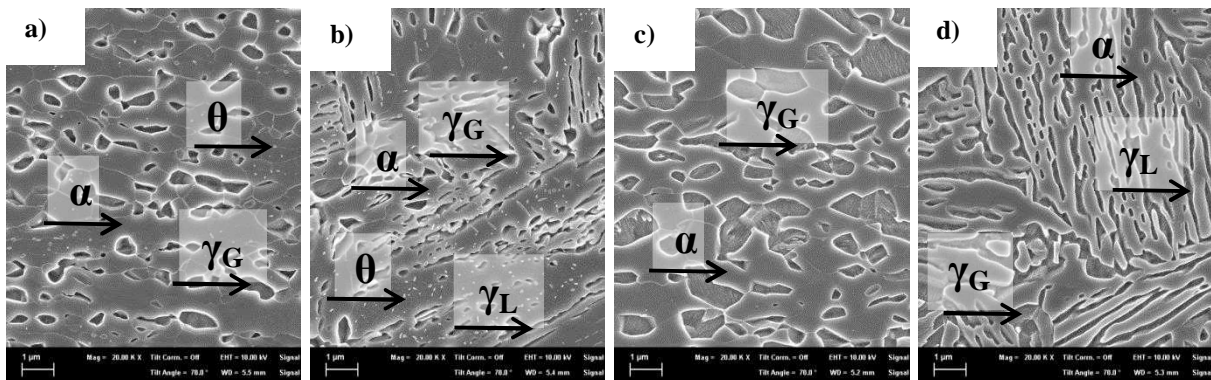


**Figure 5.42:** 0.1C6.4Mn - Microstructure after annealing at  $T_{IA} = 580$  °C for **a)** one-step HT, **b)** two-step HT and at  $T_{IA} = 640$  °C for **c)** one-step HT and **d)** two-step HT (SEM)

Annealing at  $T_{IA} = 680$  °C provoked martensite formation during cooling to RT. Therefore, not only the amount of ferrite but also the retained austenite content decreased (**Figure 5.43 a** and **b**). The differentiation between martensite and austenite became fairly hard due to their similar chemistry. Therefore, the two phases are marked with one arrow. The different morphology of the microstructure still appeared after applying the two different HT cycles. Further increasing the  $T_{IA}$  to 700 °C (**Figure 5.43 c** and **d**), which led almost to a full austenitization of the steel, strongly encouraged martensitic transformation upon cooling. Some of the martensite was even self-tempered, as it was presumably formed at high temperatures ( $> 200$  °C) and a lower cooling rate (0.01 K/s) to RT. The differentiation between one-step and two-step HT by the morphology of the phases was not possible



anymore after annealing at 700 °C. This is most likely due to the high degree of austenitization.

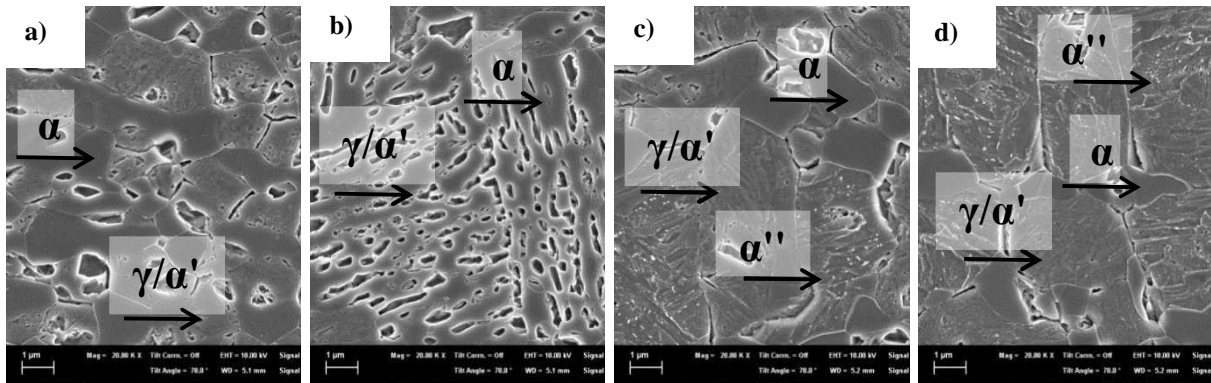


**Figure 5.43:** 0.1C6.4Mn - Microstructure after annealing at  $T_{IA} = 680$  °C for **a)** one-step HT, **b)** two-step HT and at  $T_{IA} = 700$  °C for **c)** one-step HT and **d)** two-step HT (SEM)

**Transmission electron microscopy.** Selected HT conditions were investigated using TEM in order to obtain in-depth understanding of the steel sub- and microstructure. **Figure 5.44** shows the observed microstructure after intercritical annealing at 580 °C for one-step and two-step heat treated samples. The one-step HT resulted in an exclusively globular grained microstructure consisting of ferrite and austenite. The phase and size distribution of the respective phases was dominantly homogeneous apart from some banded areas with a high density of globular Mn-enriched cementite. In these banded areas the grains were extremely fine (**Figure 5.44 a**). Moreover, the microstructure displayed a very low density of dislocations. The two-step HT provoked a lath-like shaped microstructure of ferrite and austenite. The existing cementite was rod-shaped and evenly distributed. As **Figure 5.44 b**) clearly displays that the dislocation density was considerably higher compared to one-step HT.

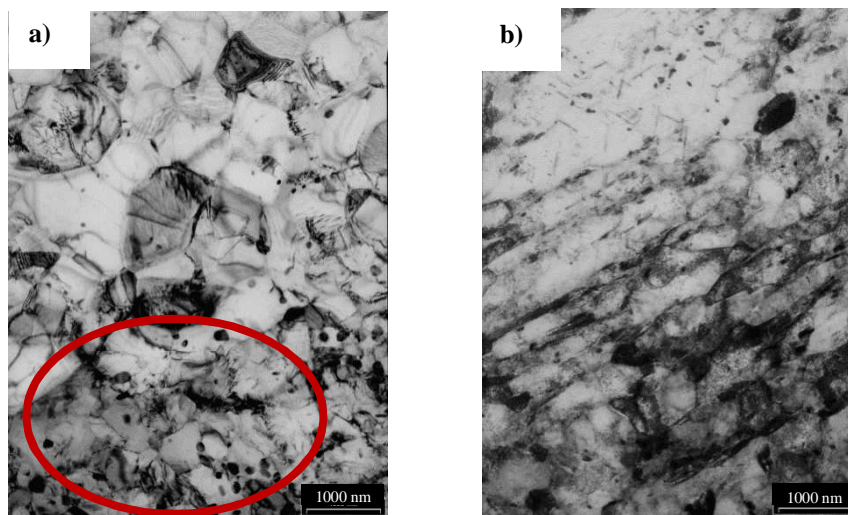


**Figure 5.44:** 0.1C5.9Mn – Microstructure after annealing at  $T_{IA} = 580$  °C for **a)** one-step HT (red circle indicating fine grained areas with precipitates) and **b)** two-step HT (TEM)

Furthermore, the microstructure after annealing at 620 °C for one-step HT and 640 °C for two-step HT respectively were investigated (**Figure 5.45**) using TEM, as annealing at these  $T_{IA}$  resulted in the best mechanical properties. The microstructures after one-step and two-step HT both contained ferrite and a considerable amount of austenite. Both HT schedules

promoted a homogenous distribution of the phases as well as of the grain size. Furthermore, the present microstructures contained a very low density of dislocations. A significant difference between one-step and two-step HT was detectable concerning the shape of the phases. Identical to the observations at lower  $T_{IA}$  one-step HT resulted in globular grains while the two-step HT provoked lath-like structures.

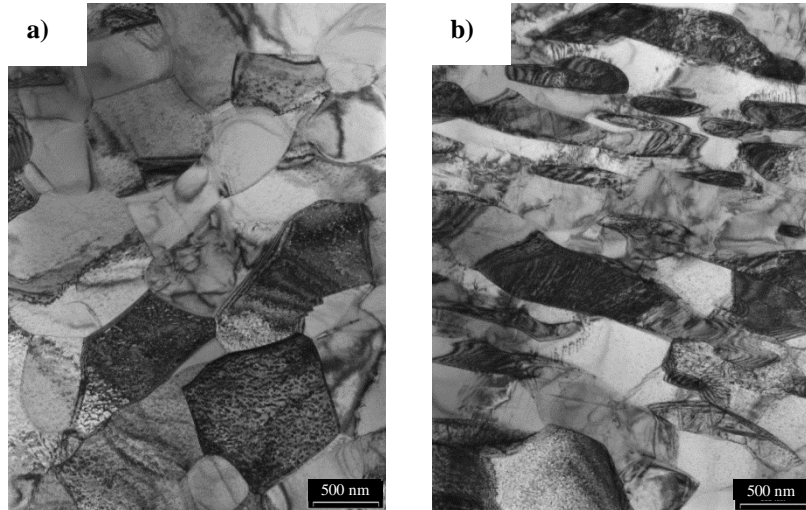


**Figure 5.45:** 0.1C5.9Mn – Microstructure after annealing at **a)**  $T_{IA} = 620\text{ °C}$  one-step HT and **b)**  $T_{IA} = 640\text{ °C}$  two-step HT (TEM)

**Texture analysis.** As texture significantly influences mechanical properties, as for example deep drawability, it was thoroughly investigated depending on the  $T_{IA}$  and the applied HT schedule. The measurements were conducted by XRD and the results are presented as ODF plots. Textures for bcc materials are often displayed compactly by plotting the section  $\phi_2 = 45^\circ$  as the most important texture features can be found there. [133] Hence, **Figure 5.46** shows the ODF for the ferritic phase of one-step heat treated samples for selected  $T_{IA}$  at  $\phi_2 = 45^\circ$ . A strong texture fiber could be noted at  $\Phi = 55^\circ$ . Such fiber textures often produced by axially symmetric deformation (*e.g.* cold rolling). By rotation about the fiber axis  $\langle uvw \rangle$  the components belonging to the fiber texture can be obtained. The present texture was identified as  $\gamma$ -fiber (running from  $\{111\}\langle 110 \rangle$  to  $\{111\}\langle 112 \rangle$  along  $\langle 111 \rangle \parallel ND$ ). [134,135,136] The given color scales for the intensity indicated a very strong texturing of the microstructure, which was becoming less pronounced with higher  $T_{IA}$  as the maximum value of the scale decreased.

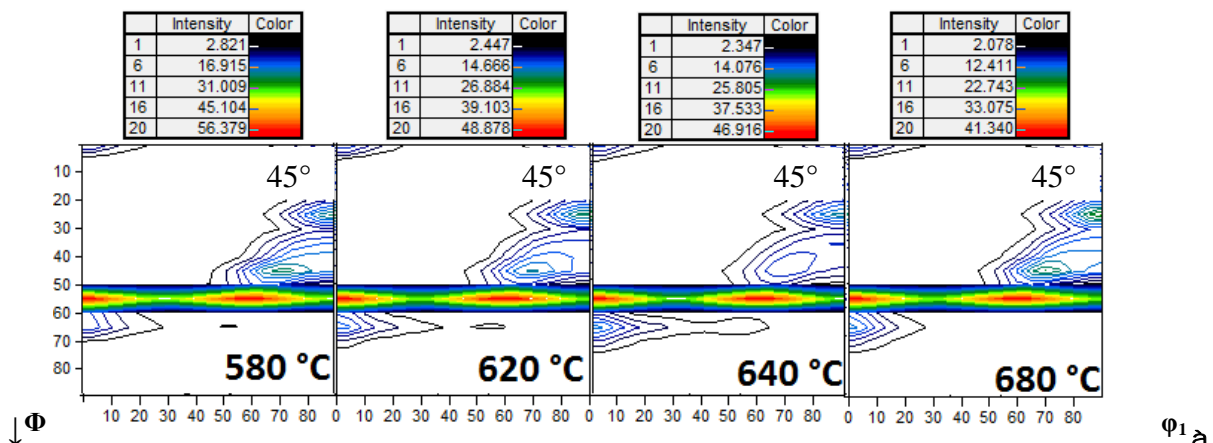


**Figure 5.46:** ODF for the ferritic phase after one-step HT for the respective  $T_{IA}$  ( $\phi_2 = 45^\circ$ )

The ferritic phase of the two-step heat treated samples (**Figure 5.47**) exhibited a similar  $\gamma$ -fiber but the texture was significantly weaker compared to the one-step HT. This was concluded by the fact that the maximal measured intensities were approximately half of those measured for the one-step HT. A trend correlating with  $T_{IA}$  was not observed.

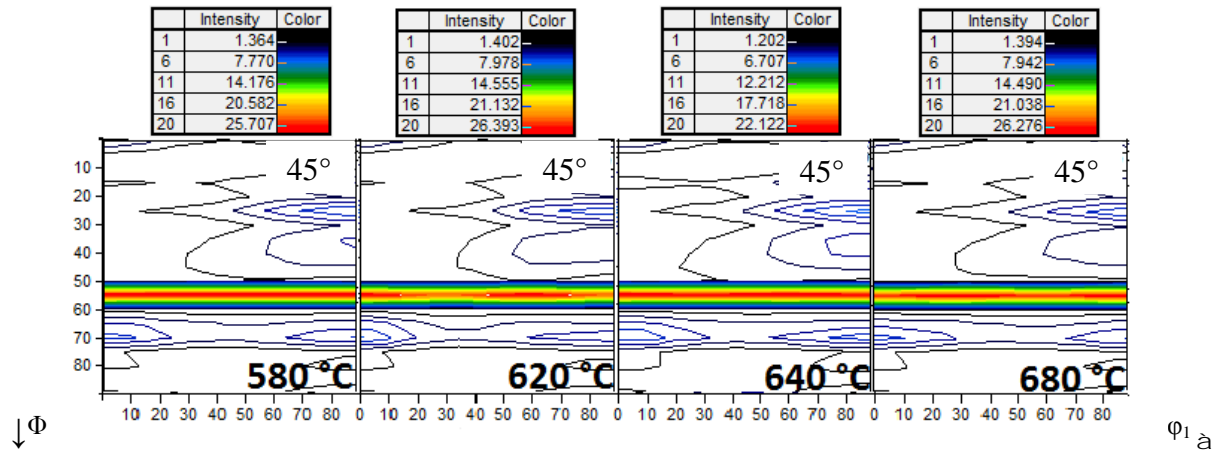


**Figure 5.47:** ODF for the ferritic phase after two-step HT for the respective  $T_{IA}$  ( $\phi_2 = 45^\circ$ )

Texture analyses of fcc metals are normally conducted on aluminum, copper or nickel and their alloys. Studies on steel involve high alloyed austenitic stainless steels. [137] In **Figure 5.48** the texture analysis of the austenitic phase after one-step HT is presented. Similar to the ferritic fraction of the one-step heat treated microstructure the austenite showed a preferred orientation. A fiber type texture could be observed at  $\phi_2 = 5^\circ$  and  $85^\circ$ ,  $\Phi = 50^\circ$ . It could be identified as similar to an  $\alpha$ -fiber texture (running from Goss orientation  $\{110\}\langle 001\rangle$  to brass orientation  $\{110\}\langle 112\rangle$  along  $\langle 110\rangle \parallel ND$ ). [134,138] The  $T_{IA}$  showed no significant influence on the texture development.

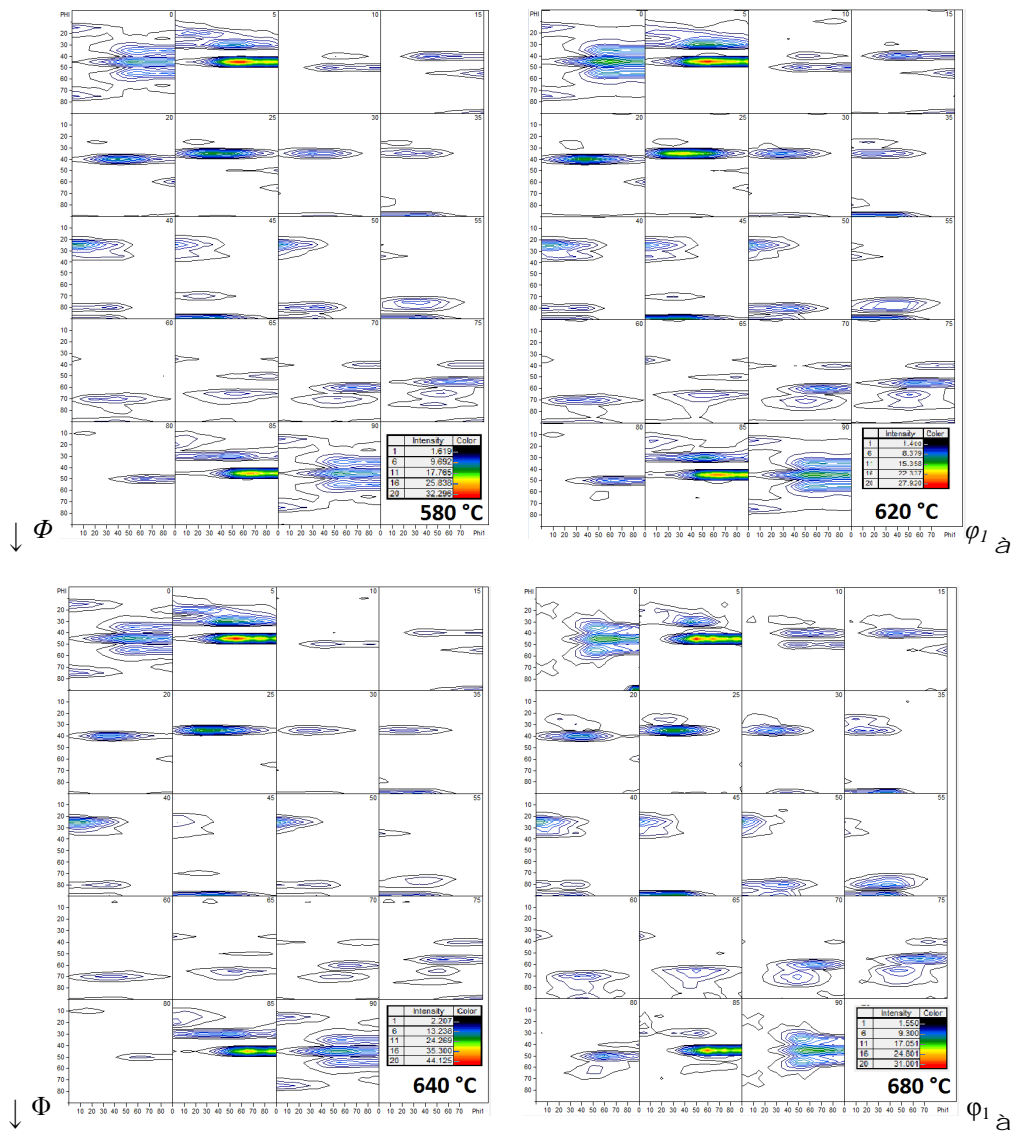


**Figure 5.48:** ODF for the austenitic phase after one-step HT for the respective  $T_{IA}$  ( $\phi_2= 0-90^\circ$ ,  $\Delta= 5^\circ$ )

The texture development of the austenitic phase after two-step HT for selected  $T_{IA}$  is displayed in **Figure 5.49**. For  $T_{IA}$  between 580 and 640 °C the measured maximal intensities were very low and the orientation of the austenite seems to be rather randomized. For  $T_{IA} = 680$  °C the intensities increased and a rather weak component of  $\alpha$ -fiber ( $\langle 110 \rangle \parallel ND$ ) texture was apparent.



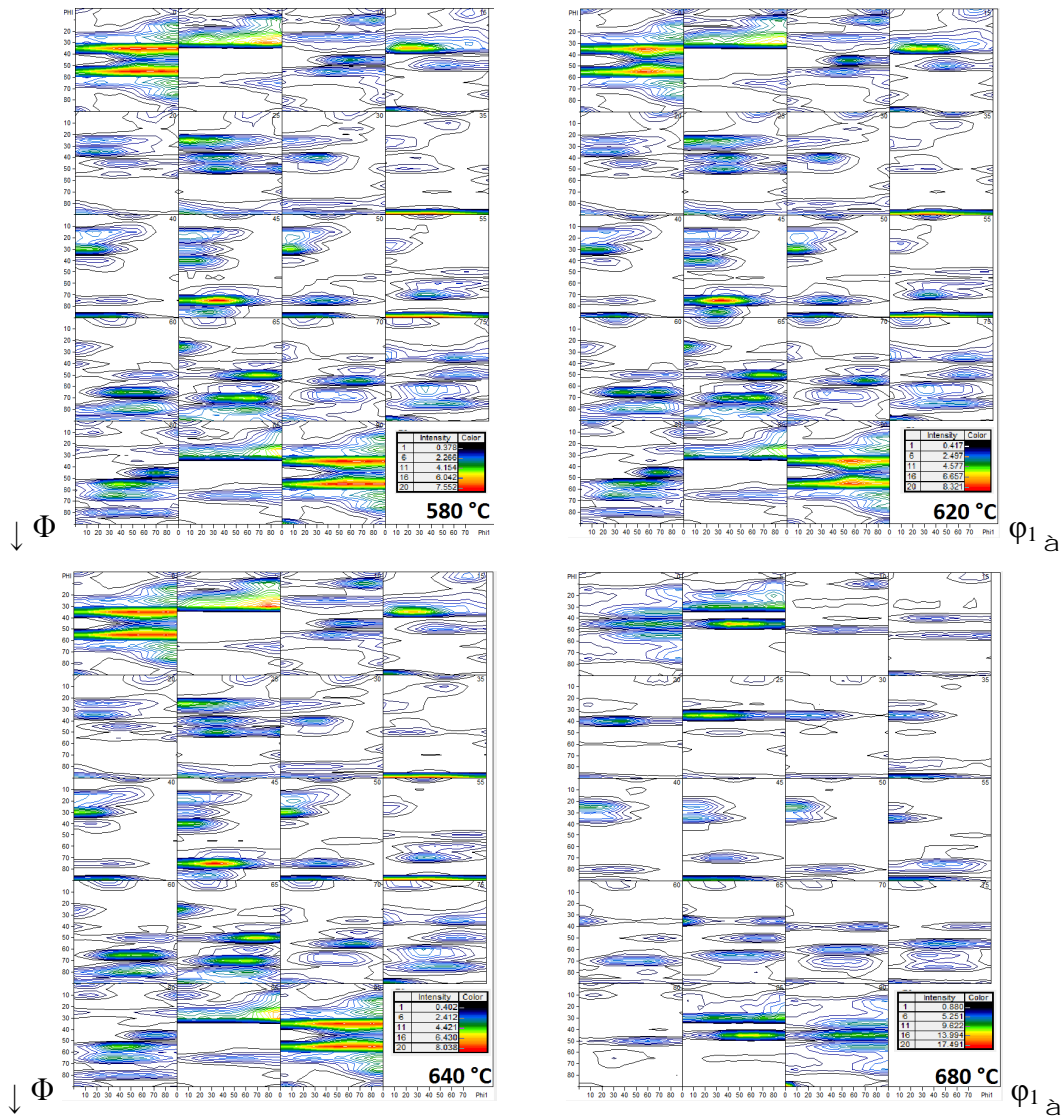


**Figure 5.49:** ODF for the austenitic phase after two-step HT for the respective  $T_{IA}$  ( $\phi_2= 0\text{-}90^\circ$ ,  $\Delta= 5^\circ$ )

**Grain size and morphology.** In order to characterize the grain size development of the retained austenite the ECD was determined for the steel 0.1C6.4Mn. **Figure 5.50 a)** shows the difference in grains size depending on the applied HT. Over the whole investigated  $T_{IA}$  range, the ECD of the two-step HT was considerably smaller than after one-step HT. For both HT schedules, the ECD started to increase slightly at  $T_{IA} \leq 640^\circ\text{C}$ . While the increase in grain size remained almost linear for two-step HT, the grain growth for one-step HT strongly accelerated at higher  $T_{IA}$ . Hence, the difference in ECD strongly increased at  $T_{IA} > 640^\circ\text{C}$  depending on the HT schedule. As the retained austenite for the two-step HT consisted of two modifications of retained austenite morphology **Figure 5.50 b)** displays the development of the ECD after two-step HT split up into lath-like  $\gamma_L$  and globular retained austenite  $\gamma_G$ . It can be observed that the  $\gamma_L$  showed a steady linear increase in ECD while the fraction of  $\gamma_G$  revealed the same accelerated grain growth at  $T_{IA} > 640^\circ\text{C}$  as the one-step HT. This is fairly reasonable as the retained austenite of the one-step heat treated microstructure was exclusively globular. Furthermore, it was observed that the ECD of  $\gamma_G$  after two-step HT was significantly larger than the one-step heat treated. It was found that  $78 \text{ area-\%} \pm 7.5 \text{ area-\%}$  of

the austenite after two-step HT had a lath like structure. This proportional relationship between  $\gamma_G$  and  $\gamma_L$  was not altered by  $T_{IA}$ .

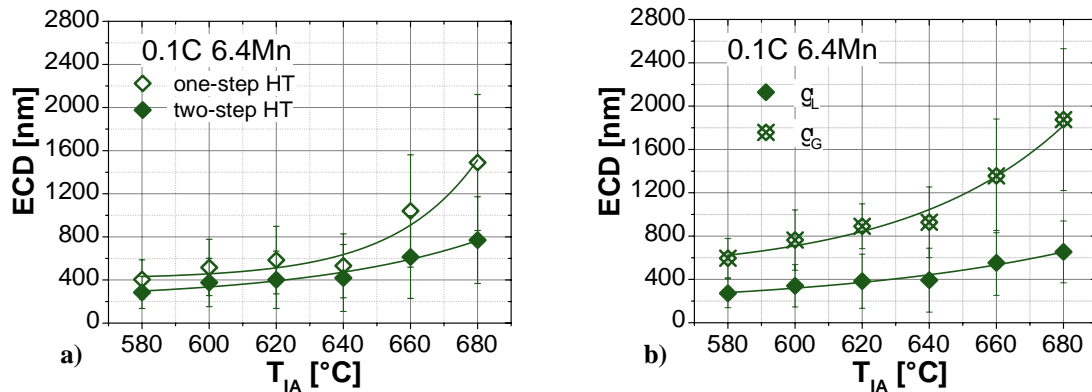


**Figure 5.50:** 0.1C6.4Mn - ECD of retained austenite as a function of  $T_{IA}$  for a) one-step and two-step HT and b)  $\gamma_L$  and  $\gamma_G$  of two-step HT

A further important feature that characterizes the retained austenite was its morphology. The comparative SEM and TEM investigations on one-step and two-step heat treated steels already revealed a qualitative difference in the shape. With the help of a circularity factor it was possible to introduce a quantitative parameter to describe the morphology. A circularity factor of 1 means that the shape of the austenite can be considered as perfectly spherical. **Figure 5.51 a)** shows that as expected the circularity of the one-step heat treated austenite was significantly higher than for the two-step HT. Furthermore, it is important to mention that the difference in shape of the austenite remained up to  $T_{IA} = 680$  °C. At a  $T_{IA}$  of 700 °C the analysis could not be conducted as the etching behavior had substantially changed. In **Figure 5.51 b)** the analysis of the circularity after two-step HT for  $\gamma_G$  and  $\gamma_L$  is displayed. A clear difference in the circularity between the two populations of retained austenite can be detected. The circularity of  $\gamma_G$  is significantly higher. Comparing the  $\gamma_G$  after two-step HT with that after one-step HT, it can be seen that the two-step heat treated is slightly more globular.

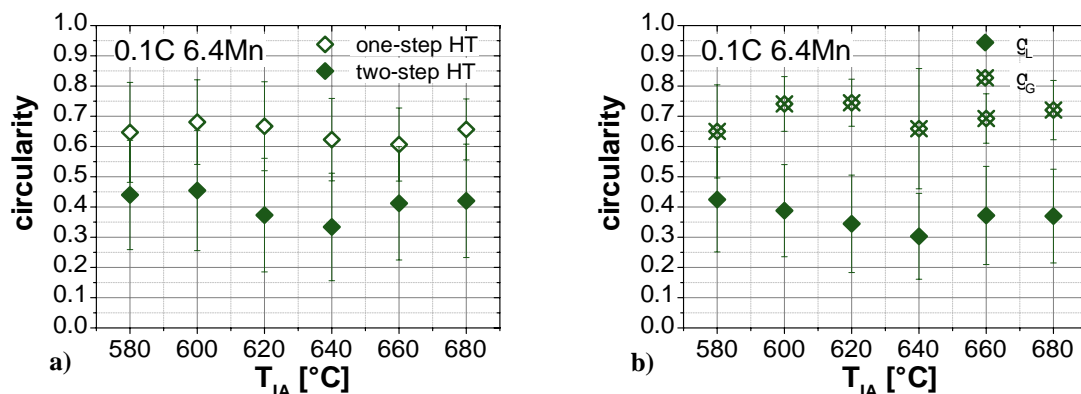


**Figure 5.51:** 0.1C6.4Mn - Circularity of retained austenite as a function of  $T_{IA}$  for a) one-step and two-step HT and b)  $\gamma_L$  and  $\gamma_G$  of two-step HT

**Retained austenite content.** As **Figure 5.52 a) – c)** clearly displays, the  $T_{IA}$  has a determining influence on the retained austenite content. For all investigated steels the same overall trend could be observed. Starting at the lowest investigated  $T_{IA}$  the retained austenite content increased linearly until a maximum was reached. Higher  $T_{IA}$  led to an abrupt decline of the retained austenite content. For the C- variation an interesting effect concerning the

applied HT schedule could be noted. For  $T_{IA}$  lower than  $T_{IAmax}$  one-step HT led to a considerable higher amount of retained austenite. This phenomenon was slightly more pronounced the lower the steel's C-content was. For  $T_{IA}$  higher than  $T_{IAmax}$ , the trend seemed to be reversed and two-step HT generally exhibited higher amounts of retained austenite.

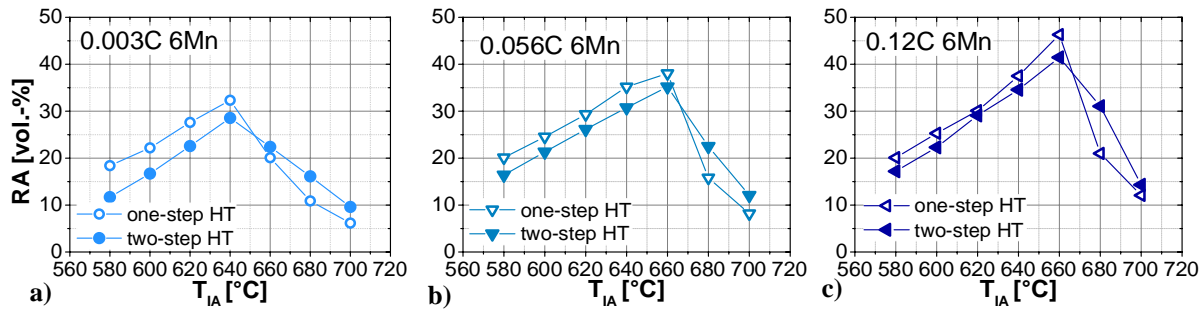


**Figure 5.52:** Retained austenite content as a function of  $T_{IA}$  for a) 0.003C6Mn, b) 0.056C6Mn and c) 0.12C6Mn for one-step and two-step HT

**Figure 5.53** represents the results of the development of the retained austenite content as a function of  $T_{IA}$  for the Mn-variation. In principal the same correlation as for the C-variation could be found. The development was characterized by an increase of the retained austenite content up to a maximum followed by a steep decrease. Concentrating on the effect of the applied HT the trend was not entirely the same. For temperatures higher than  $T_{IAmax}$  two-step HT stabilized higher amounts of retained austenite to RT similarly to the C-variation results. However, no significant difference in the retained austenite content between the HT schedules at  $T_{IA} < T_{IAmax}$  could be observed.

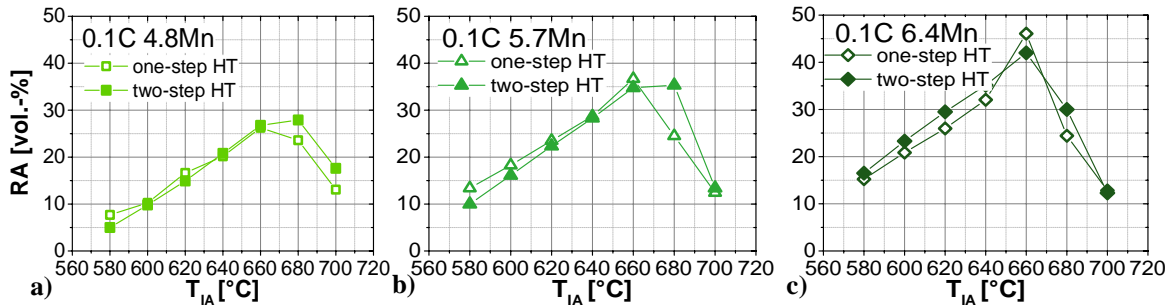


**Figure 5.53:** Retained austenite content as a function of  $T_{IA}$  for a) 0.1C4.8Mn, b) 0.1C5.7Mn and c) 0.1C6.4Mn for one-step and two-step HT

**Chemical composition of the microstructural constituents.** The Mn-contents of the respective microstructural phases of ferrite, austenite and martensite were detected by means of EDX and are represented in **Figure 5.54** as a function of  $T_{IA}$ . For both investigated steels, the Mn-content in the ferrite varied between a minimum of 2 to about 5 wt-%, obeying a decreasing tendency with increasing  $T_{IA}$ . The austenite also showed a declining Mn-content with increasing  $T_{IA}$  until the formation of martensite came into play. However, Mn-levels were significantly higher in the austenite compared to the ferrite varying from 10-14 wt-%. With the formation of martensite the detected Mn-levels in the austenite increased again. For 0.1C4.8Mn martensite formation was detected after annealing at 680 °C while for 0.1C6.4Mn martensite was already present after annealing at 660 °C. The martensite exhibited Mn-contents that follow the continuous trend of the austenite prior to the martensite formation. The black lines represent the equilibrium Mn-contents of the respective phases calculated by

Thermo-Calc<sup>®</sup>. The measured values corresponded remarkably well with these calculated Mn-contents.

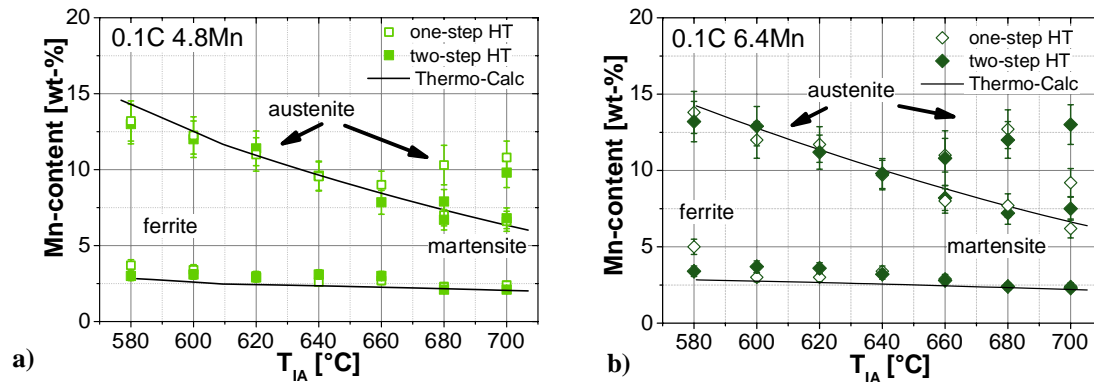


**Figure 5.54:** Mn-content of the respective microstructural phases ferrite, austenite and martensite as a function of  $T_{IA}$  for **a)** 0.1C4.8Mn and **b)** 0.1C6.4Mn

**Phase fraction diagrams.** The present fraction of the respective phases is of great importance if it comes to the evaluation of the mechanical properties. Therefore, the combination of results based on of saturation magnetization method, SEM and thermodynamic calculations was used to quantify the phases. It has to be mentioned at this point that the experimental evaluation of the phase fractions *via* dilatometry was not applicable in this case as the prolonged  $t_A$  led to artefacts during the soaking period that could not be overcome. Thus, the retained austenite was determined by saturation magnetization method and combined with the analysis of SEM micrographs, by which the fraction of martensite was evaluated. Summing up those two values the intercritically formed austenite could be estimated. The fraction of cementite was calculated by thermodynamic modelling. The fraction of ferrite resulted in turn as the residual value. **Figure 5.55 a)** and **b)** shows the development of the respective phases cementite, ferrite, austenite and martensite for 0.1C6.4Mn one-step HT as a function of the  $T_{IA}$  at annealing temperature and at RT respectively. At  $T_{IA} \leq 600$  °C the microstructure consisted of austenite, ferrite and cementite at  $T_{IA}$  as well as at RT. At higher  $T_{IA}$  the cementite dissolved and a duplex microstructure consisting of ferrite and austenite was established. With increasing temperature, the amount of austenite increased on the expense of ferrite. As no transformations appeared during cooling, the microstructure at  $T_{IA}$  and RT was identical. This finally changed at a  $T_{IA}$  of 680 °C where martensite was formed during cooling. While at  $T_{IA}$  the austenite fraction continuously raised, it decreased at RT as martensite formed during cooling.

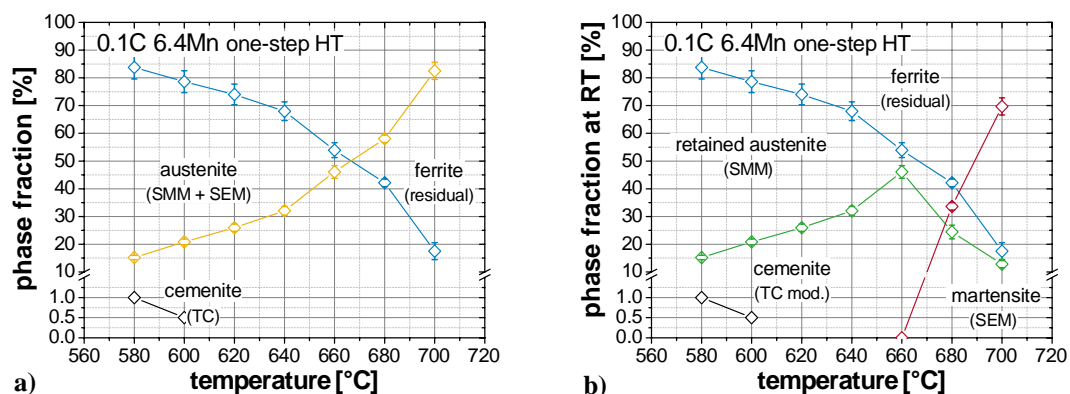


**Figure 5.55:** 0.1C6.4Mn – Phase fraction diagram as a function of  $T_{IA}$  at **a)** annealing temperature and **b)** room temperature (one-step HT)



The same diagrams for 0.1C6.4Mn two-step HT are shown in **Figure 5.56**. Similar trends can be noted. At the lower range of investigated  $T_{IA}$  the microstructure consisted of ferrite, austenite and cementite, which completely dissolved at 620 °C. At  $T_{IA}$  the amount of intercritical austenite constantly increased while the ferrite decreased. At RT martensite was present for  $T_{IA} \geq 680^\circ\text{C}$ .

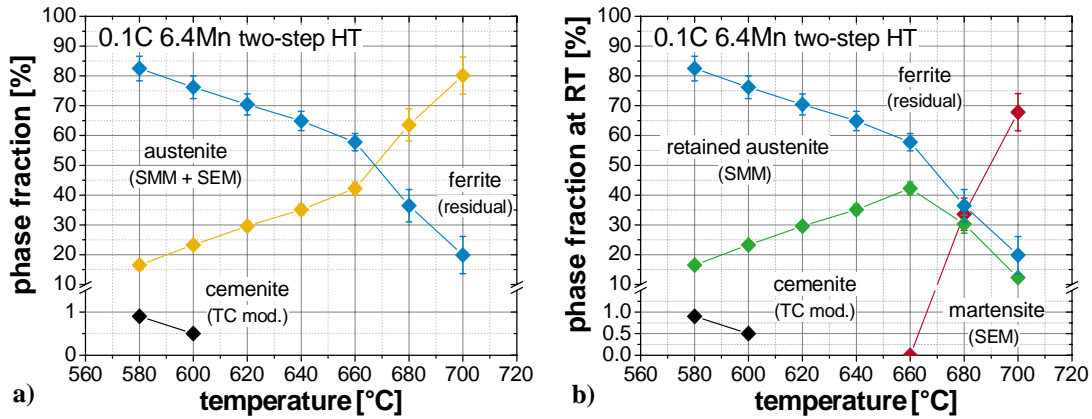


**Figure 5.56:** 0.1C6.4Mn – Phase fraction diagram as a function of temperature at **a)** annealing temperature and **b)** room temperature (two-step HT)

### 5.2.2 Mechanical properties

As the impact of the heat treatment on the mechanical properties is crucial the following chapter concentrates on this specific aspect. First the aspect of the  $T_{IA}$  will be highlighted followed by the influence of the applied HT schedule. As the trends are basically the same for all investigated alloys only selected stress-strain curves are presented. The entire set of curves can be found in the appendix (**Chapter 10.1**). **Figure 5.57 a)** and **b)** display the engineering stress-strain curves of 0.1C6.4Mn for altering  $T_{IA}$  and one-step and two-step HT respectively. Concentrating on the aspect of  $T_{IA}$  it can be seen that a very strong dependence of the mechanical properties on this particular parameter exists. For low  $T_{IA}$  high YS was achieved followed by a low work hardening rate which resulted in rather low UTS combined with moderate TE. With increasing  $T_{IA}$  YS decreased and the work hardening behavior was improved. Therefore, the desired mechanical properties with high UTS combined with excellent TE were achieved. For the one-step HT the highest UTS\*TE were gained at a  $T_{IA}$  of 620 °C, whereas for the two-step HT this maximum was achieved at 640 °C. Further increasing the  $T_{IA}$  strongly increased the UTS but at the same time reduced the TE.

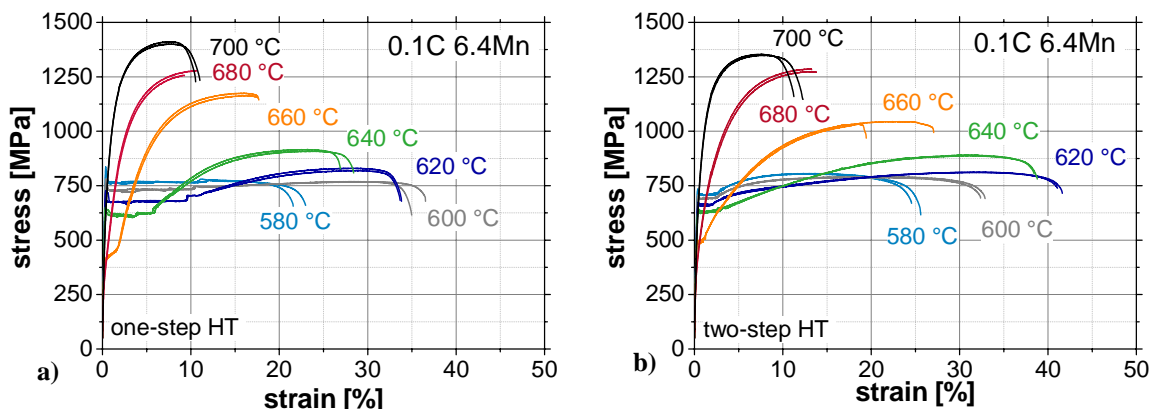


**Figure 5.57:** Engineering stress-strain curves of 0.1C6.4Mn for **a)** one-step HT and **b)** two-step HT ( $T_{IA}$ -variation)

The influence of the two different HT schedules (one-step vs. two-step) on the tensile curves is displayed in detail in **Figure 5.58 a) – d)** for the alloy 0.1C6.4Mn exemplarily for all investigated alloys. At low  $T_{IA}$  the one-step heat treated samples exhibited a higher YS compared to the two-step HT. The stress-strain curves of one-step HT showed nearly no work hardening behavior. Therefore, the resulting UTS was rather low. Two-step HT on the other hand exhibited moderate work hardening resulting in a higher UTS compared to one-step HT. **Figure 5.58 b)** illustrates the influence of the HT schedule at a  $T_{IA}$  of 640 °C. At this intermediate  $T_{IA}$  the samples generally yielded at rather comparable stresses. One-step heat treated samples typically showed a considerably larger YPE than the two-step heat treated ones. Furthermore, the achieved UTS were usually similar but for two-step HT higher elongations could be obtained. For higher annealing temperatures the mechanical properties exhibited a similar behavior independent from the HT (**Figure 5.58 c and d)**. One-step HT tended to achieve higher UTS while *via* two-step HT higher elongations were obtained. These trends could generally be found for all investigated chemical compositions.

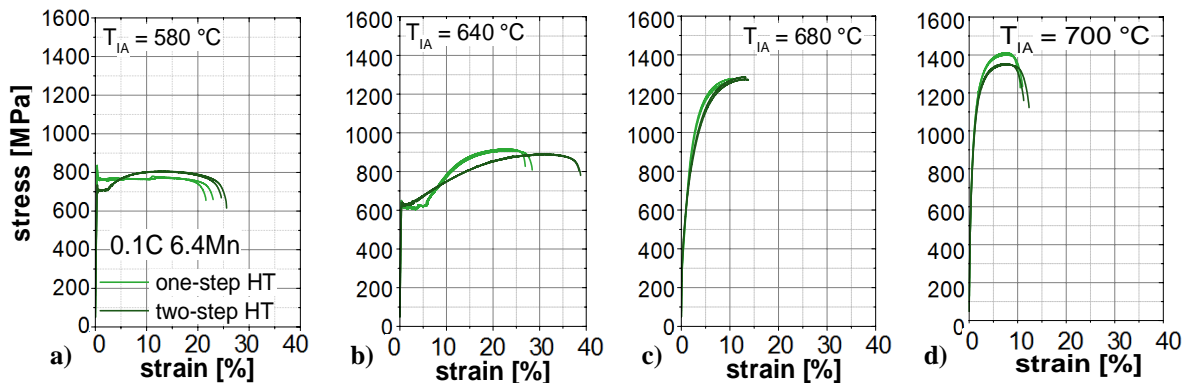


**Figure 5.58:** Engineering stress-strain curves of 0.1C6.4Mn for a  $T_{IA}$  of a) 580 °C, b) 640 °C, c) 680 °C and d) 700 °C for one-step and two-step HT

**Figure 5.59** displays the development of YS and UTS for the C-variation comparing one-step and two-step HT. Concerning YS one-step HT generally exhibited higher values except for the case of the lowest obtained YS at  $T_{IA}$  of 660 °C. There, YS after two-step HT revealed to be higher. UTS was alike till  $T_{IA} = 620$  °C between both HT schedules. At  $T_{IA} \geq 620$  °C higher UTS was achieved for one-step HT compared to two-step one.

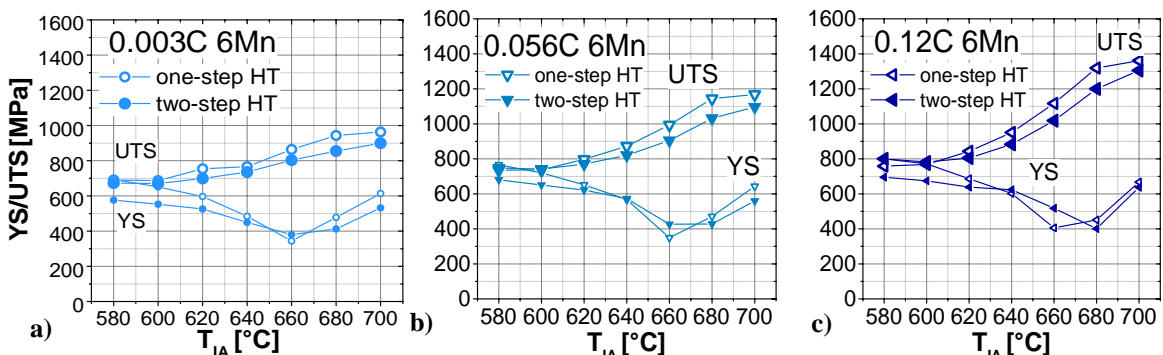


**Figure 5.59:** YS and UTS as a function of  $T_{IA}$  for a) 0.003C6Mn, b) 0.056C6Mn and c) 0.12C6Mn for one-step and two-step HT

The elongations were also substantially influenced by the applied HT schedule. As shown in **Figure 5.60** two-step HT resulted in higher UE as well as TE except for the lower range of

the investigated  $T_{IA}$  ( $T_{IA} = 580 - 600$  °C). At this low temperature range, the achieved elongations were nearly the same or occasionally even better for one-step HT.

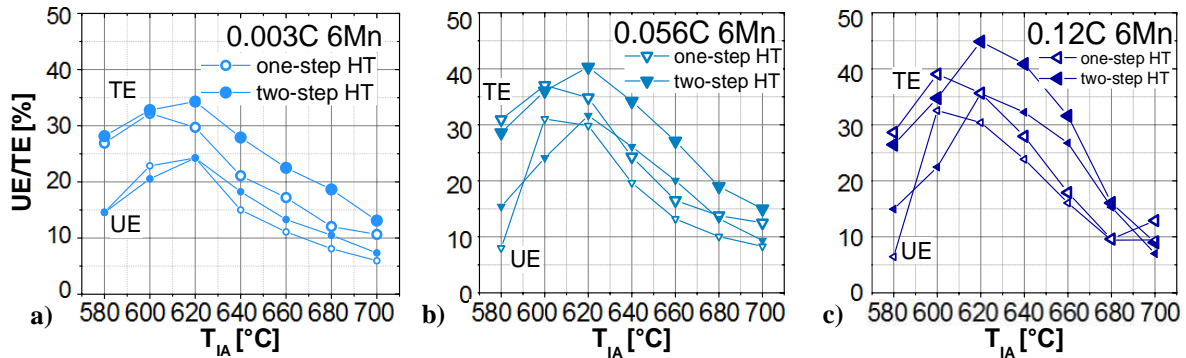


**Figure 5.60:** UE and TE as a function of  $T_{IA}$  for a) 0.003C6Mn, b) 0.056C6Mn and c) 0.12C6Mn for one-step and two-step HT

The influence of the HT schedule on YS and UTS for the steels with Mn-variation is exhibited in **Figure 5.61**. Similarly to the results of the C-variation, one-step HT tended to achieve higher UTS after annealing at higher  $T_{IA}$ . YS was also found to be higher for one-step HT especially for the lower range of investigated  $T_{IA}$ . With increasing  $T_{IA}$  YS of two-step HT tended to be higher compared to one-step HT.

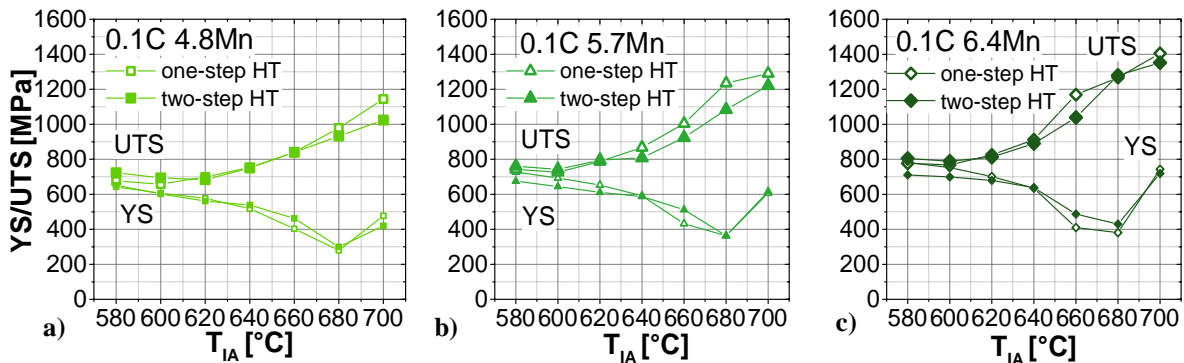


**Figure 5.61:** YS and UTS as a function of  $T_{IA}$  for a) 0.1C4.8Mn, b) 0.1C5.7Mn and c) 0.1C6.4Mn for one-step and two-step HT

Finally the comparison of the two HT schedules influencing the UE and TE of Mn-variation are displayed in **Figure 5.62**. At lower  $T_{IA}$  ( $< 600$  °C) the achieved UE and TE were similar for both HT regimes. With increasing  $T_{IA}$  this trend changed and UE and TE obtained after two-step HT were significantly higher compared to one-step HT.

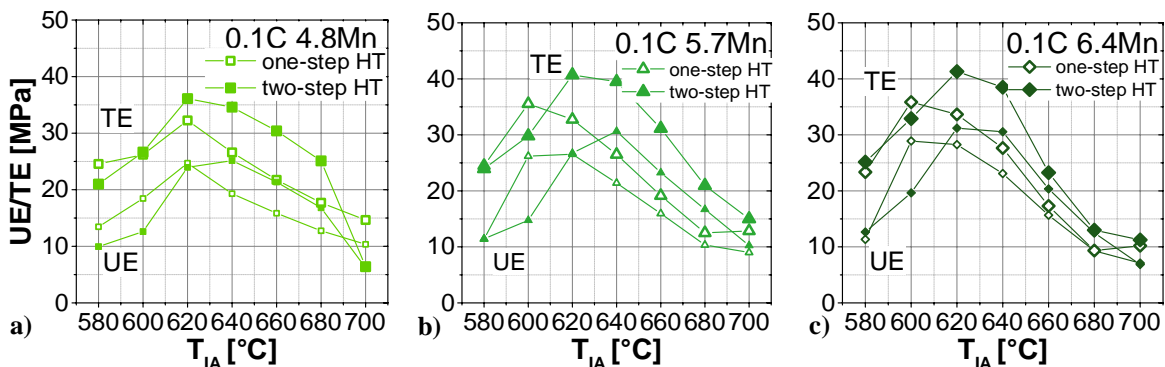


**Figure 5.62:** UE and TE as a function of  $T_{IA}$  for a) 0.1C4.8Mn, b) 0.1C5.7Mn and c) 0.1C6.4Mn for one-step and two-step HT

### 5.2.3 Yielding behavior

The exceptional yielding behavior observed by these steels and by Medium-Mn-steels in general was also investigated concerning the influence of the different HT schedules. As shown in **Figure 5.63** the HT had quite a large influence on the YPE characteristics and the difference between UYS and LYS. For the steels with the C-variation the one-step HT clearly resulted in significantly higher YPE as well as higher values for UYS-LYS. The influence of the  $T_{IA}$  was also pronounced and showed a decreasing YPE and UYS-LYS with increasing  $T_{IA}$ .

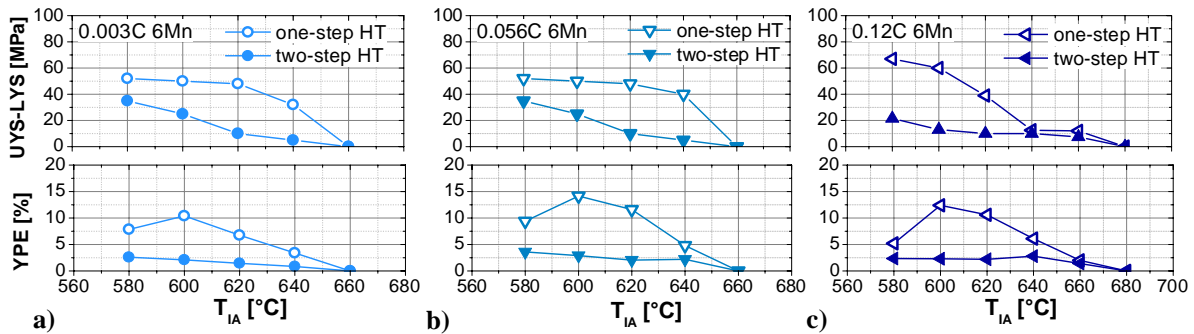


**Figure 5.63:** YPE and UYS-LYS as a function of  $T_{IA}$  for **a)** 0.003C6Mn, **b)** 0.056C6Mn and **c)** 0.12C6Mn for one-step and two-step HT

The influence of the HT schedule on YPE and UYS-LYS on the steels with the Mn-variation is shown in **Figure 5.68**. As indicated before for the C-variation an increase in  $T_{IA}$  strongly decreased YPE and UYS-LYS. Besides that, one-step and two-step HT considerably altered the yielding behavior. The use of a two-step instead of a one-step HT tremendously decreased the resulting YPE. With higher Mn-content this effect got even more remarkable. A similar dependence was found for UYS-LYS. For 0.1C4.8Mn the value was nearly the same for one-step and two-step HT respectively. With increasing Mn-content the two-step HT clearly showed a smaller difference between UYS and LYS. Furthermore, for 0.1C4.8Mn and 0.1C5.7Mn the overall trend reversed at  $T_{IA}$  of 660 °C. Here, the two-step HT exhibited a higher value for UYS-LYS compared to the one-step HT.

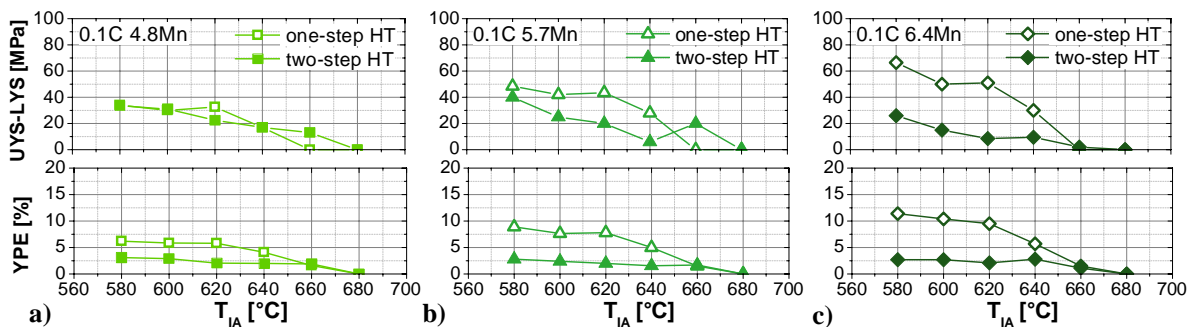


**Figure 5.64:** YPE and UYS-LYS as a function of  $T_{IA}$  for **a)** 0.1C4.8Mn, **b)** 0.1C5.7Mn and **c)** 0.1C6.4Mn for one-step and two-step HT

### 5.2.4 Work hardening behavior

**Incremental n-value.** The incremental work hardening coefficient  $n_i$  as function of the true strain  $\epsilon_{true}$  for different  $T_{IA}$  is displayed in **Figure 5.65** for one-step and two-step HT. It can be clearly seen that the  $T_{IA}$  has a significant impact on the  $n_i$ -value. Starting with one-step HT in

**Figure 5.65 a)** it is apparent that for the lowest investigated  $T_{IA}$  of 580 °C the  $n_i$ -value was smaller than the  $n_i = \epsilon_{true}$  line until rupture. This confirms that the sample did not at all deform uniformly. The one-step heat treated specimen annealed at a  $T_{IA}$  of 580 °C was the only one that exhibited this specific behavior. Increasing the  $T_{IA}$  to 600 °C the  $n_i$ -value displayed the expected behavior whereby with increasing  $\epsilon_{true}$  the  $n_i$ -value steadily increased but remained at a rather low level. However, the highest uniform elongation indicated by  $n_i = \epsilon_{true}$  can be reached after applying this  $T_{IA}$ . All further investigated  $T_{IA} \geq 620$  °C showed a different trend, which started with an increase of the  $n_i$ -value at rather small  $\epsilon_{true}$  up to a maximum value followed by a steady decrease. Comparing the peak value of  $n_i$  for the respective  $T_{IA}$  it can be observed that it steadily increased with increasing  $T_{IA}$  except for a  $T_{IA}$  of 680 °C where the maximum  $n_i$ -value decreased. Excluding the sample heat treated at  $T_{IA}$  of 580 °C, which did not exhibit a uniform elongation, an increase in  $T_{IA}$  was generally accompanied by a loss of uniform elongation. Comparing the  $n_i$ -values of one-step and two-step HT it can be seen that the two-step HT generally revealed lower  $n_i$ -value over the whole range of investigated  $T_{IA}$ . As illustrated in **Figure 5.65 b)** all  $T_{IA}$  exhibited  $n_i$ -values higher than the  $n_i = \epsilon_{true}$ -line until necking and therefore fulfilling the Considère instability criterion. Considering the lower range of investigated  $T_{IA} \leq 640$  °C of two-step heat treated samples the  $n_i$ -value as well as the uniform elongation increased with increasing  $T_{IA}$ . The shape of the  $n_i$ -value development changed as well with  $T_{IA}$ . At low  $T_{IA}$  the  $n_i$ -value steadily increased until  $n_i = \epsilon_{true}$ -line was reached, while for  $T_{IA} \geq 620$  °C it first increased up a peak value, followed by its further decrease. With increasing  $T_{IA}$  the strain where this peak appeared became smaller. For  $T_{IA}$  of 640, 660 and 680 °C the peak  $n_i$ -values were nearly the same but the maxima appeared at smaller strains with increasing  $T_{IA}$  and the following decrease was sharper which resulted in a significant loss of uniform elongation. Comparing the  $n_i$ -values after one-step and two-step HT it can be generally observed, that at the same  $T_{IA}$  the maximum  $n_i$ -value was significantly higher for one-step HT.

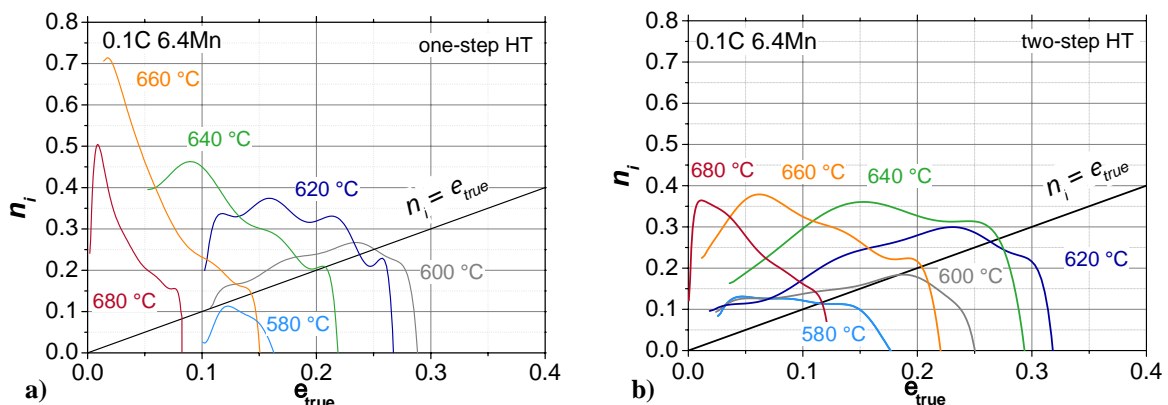


**Figure 5.65:** Incremental n-value  $n_i$  as a function of true strain for 0.1C6.4Mn for **a)** one-step HT and **b)** two-step HT ( $T_{IA}$ -variation)

**Retained austenite stability.** Interrupted tensile tests between YPE and UE were performed and the retained austenite fraction was measured at various strain levels. **Figure 5.66 a)** and **b)** displays the development of the retained austenite content as a function of the strain exemplarily for 0.1C5.9Mn. . The retained austenite contents and corresponding strain values for all investigated steels can be found in the appendix (**Chapter 10.2**). It was clearly observed that except a  $T_{IA}$  of 580 °C all heat treatment conditions led to transformation of the



austenite. Starting at varying initial retained austenite contents the kinetics of the transformation were significantly different for altering  $T_{IA}$ . The transformation of austenite accelerated with higher applied  $T_{IA}$ . A comparative differentiation between the transformation behavior of one-step and two-step HT was not possible by this analysis of the results.

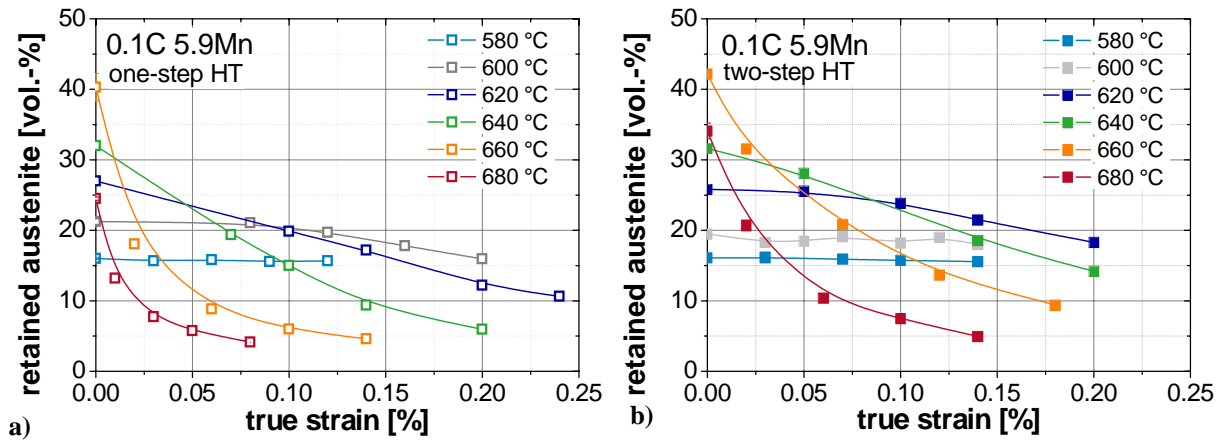


**Figure 5.66:** 0.1C5.9Mn - retained austenite content as a function of true strain for a) one-step HT and b) two-step HT ( $T_{IA}$ -variation)

Therefore, the transformed amount of retained austenite was plotted against the true strain and as displayed in **Figure 5.67** a linear relation could be established. The slope of the linear trend  $k_p$  represents a valid parameter for the retained austenite stability. A high value of  $k_p$  indicates a low stability of the retained austenite.

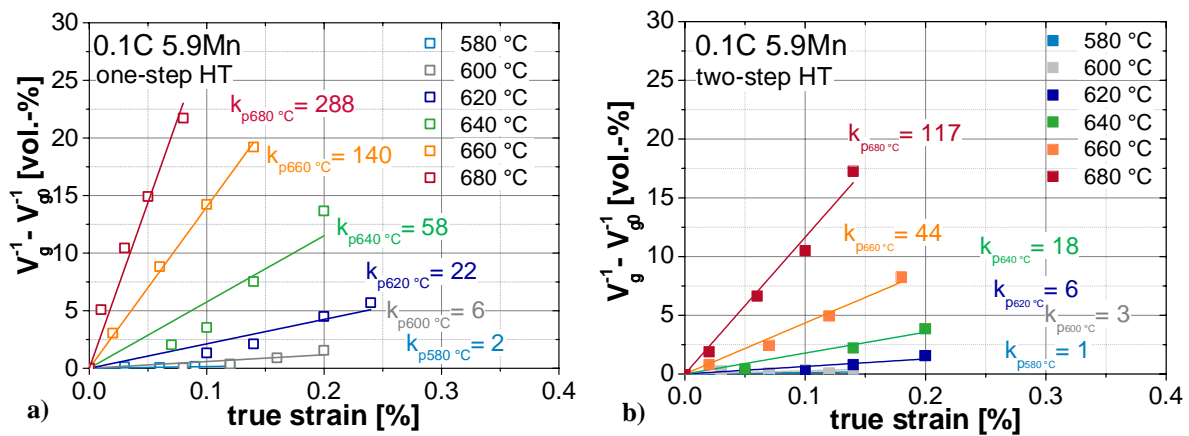


**Figure 5.67:** Transformed retained austenite as a function of true strain for 0.1C5.9Mn for a) one-step HT and b) two-step HT ( $T_{IA}$ -variation)

The determined  $k_p$ -values for the steels with C-variation are illustrated in **Figure 5.68 a) – c)**. The higher the C-content the higher was the retained austenite stability. Furthermore, the strong increase of the  $k_p$ -value by increasing  $T_{IA}$  is obvious. Elevating the  $T_{IA}$  resulted in an exponential rise of the  $k_p$ -value. Yet another rather strong influencing factor was revealed by the analysis of the  $k_p$ -value. A significant increase of the retained austenite stability by applying the two-step HT could also be noted.

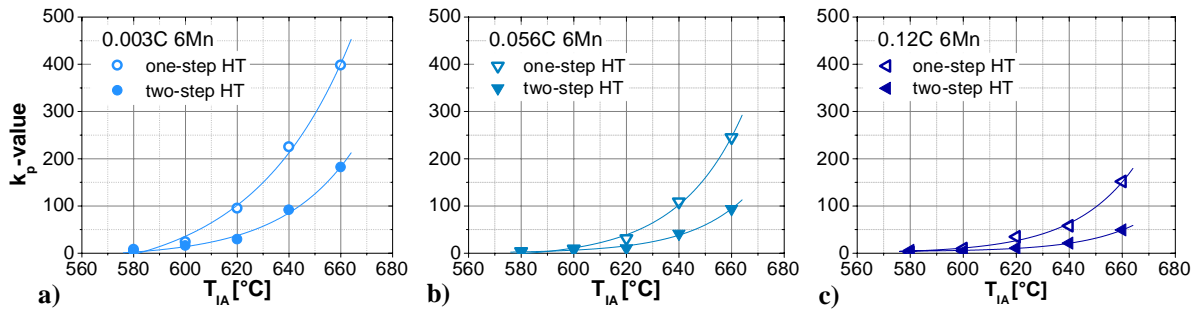


**Figure 5.68:**  $k_p$ -value as a function of  $T_{IA}$  for a) 0.003C6Mn, b) 0.056C6Mn and c) 0.12C6Mn for one-step and two-step HT

The analysis of the  $k_p$ -value was also applied for the Mn-variation (**Figure 5.69**). A slight increase of the retained austenite stability with increasing Mn-content is displayed. Furthermore, the influence of the  $T_{IA}$  and the applied HT was significantly stronger than that of chemistry. While an increase of  $T_{IA}$  drastically increased the  $k_p$ -value, the applications of the two-step HT resulted in an enhancement of the retained austenite stability.

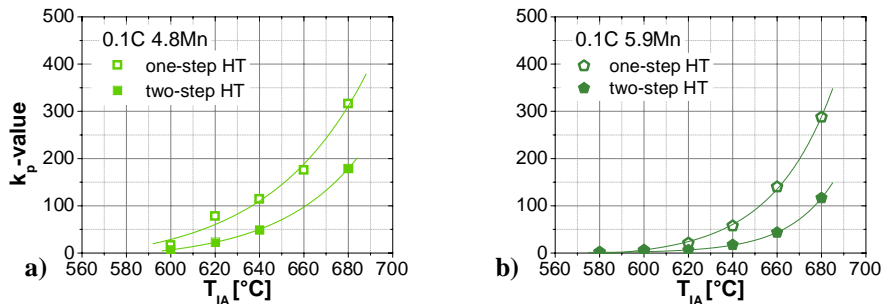


**Figure 5.69:**  $k_p$ -value as a function of  $T_{IA}$  for a) 0.1C4.8Mn and b) 0.1C5.9Mn for one-step and two-step HT

### 5.2.5 Damage behavior

**Postuniform behavior.** The thickness strain  $\varepsilon_3$  can be subdivided in a uniform and a post-uniform part. The uniform  $\varepsilon_3$  represents the thickness strain that forms until uniform elongation, whereas the postuniform  $\varepsilon_3$  is formed after the beginning of necking. **Figure 5.70** shows the analysis of the uniform and postuniform thickness strain  $\varepsilon_3$  for 0.1C6.4Mn after annealing at selected  $T_{IA}$ . A strong influence of the  $T_{IA}$  on the thickness strain  $\varepsilon_3$  was revealed by this investigation. For both HT schedules the same trends were observed. For the lowest selected  $T_{IA}$  the highest values of  $\varepsilon_3$  could be obtained. For these samples it was not possible to detect a uniform fraction of  $\varepsilon_3$  as the Considère instability criterion was not fulfilled (see **Chapter 5.2.4**). Therefore, the entire thickness strain was considered as postuniform  $\varepsilon_3$ . As no uniform  $\varepsilon_3$  could be determined the term non-uniform would correspond better than post-uniform. Increasing the  $T_{IA}$  to 620 and 640 °C respectively resulted in a decrease of the total thickness strain. Here, a uniform amount of the thickness strain  $\varepsilon_3$  could clearly be detected and achieved values nearly up to 20 %. The postuniform part was still the dominant part by causing more than 30 % of thickness reduction. For a  $T_{IA}$  of 680 °C a minimum in  $\varepsilon_3$  occurred with a strong decline in both uniform and postuniform  $\varepsilon_3$ . Although the uniform  $\varepsilon_3$  even decreased compared to  $T_{IA} = 680$  °C, a further increase in  $T_{IA}$  to 700 °C strongly increased the total  $\varepsilon_3$  caused by a tremendous increase in postuniform  $\varepsilon_3$ .

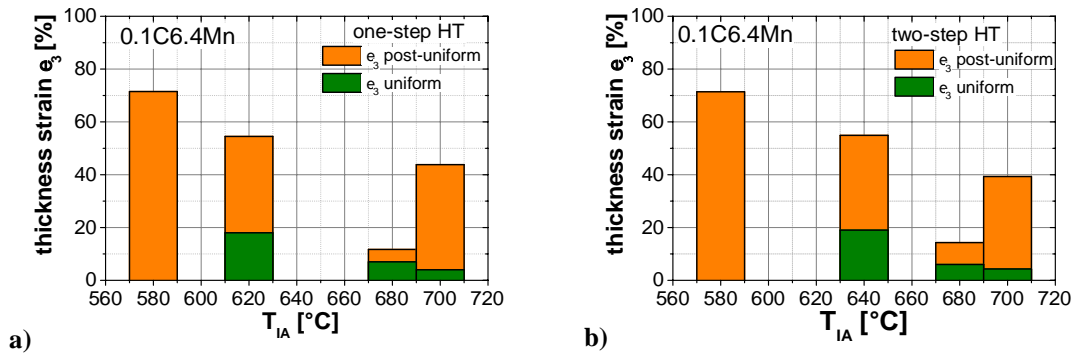


**Figure 5.70:** Uniform and post-uniform thickness strain  $\epsilon_3$  as a function of  $T_{IA}$  for 0.1C6.4Mn after a) one-step HT and b) two-step HT

**Macroscopic fracture appearance.** Figure 5.71 illustrates the fracture appearance of one-step heat treated samples in SEM for altering  $T_{IA}$ , where its strong influence on the fracture behavior is apparent. For a  $T_{IA}$  of 580 °C, the sample was strongly thinned and elongated. The failure mode was a cup-cone shaped fracture. For a  $T_{IA}$  of 620 °C, the sample fractured under about 45° and the whole fracture surface formed a large shear lip. The fracture appearance significantly changed after annealing at  $T_{IA}$  = 680 °C. Only very small shear lips formed at the edge of the sample (about 15% of the whole fracture surface). The amount of brittle fracture was dominant. The material underwent no visible necking opposite to other  $T_{IA}$ . After annealing at  $T_{IA}$  = 700 °C the fracture mode returned to a cup-cone behavior. Necking at this  $T_{IA}$  was not that pronounced compared to  $T_{IA}$  = 580 °C.

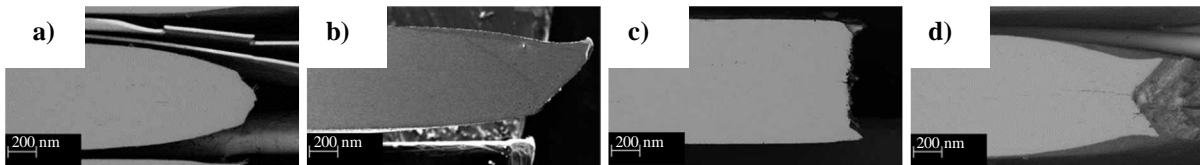


**Figure 5.71:** 0.1C6.4Mn - Macroscopic fracture appearance for  $T_{IA}$  of a) 580 °C, b) 620 °C, c) 680 °C and d) 700 °C (one-step HT)

The fracture modi of the two-step heat treated samples generally exhibited the same trend (Figure 5.72). The only difference appeared in the fracture mode at  $T_{IA}$  of 640 °C, which fractured in cup-cone shape and not as a single shear lip as observed for  $T_{IA}$  = 620 °C for one-step HT. A further remarkable aspect of the fracture behavior of the two-step HT was that a crack was repeatedly initiated in the middle of the fracture surface.

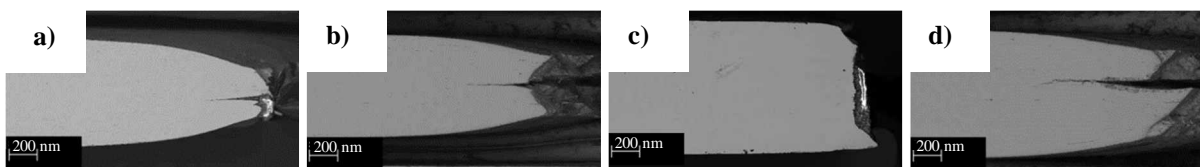


**Figure 5.72:** 0.1C6.4Mn - Macroscopic fracture appearance for  $T_{IA}$  of a) 580 °C, b) 640 °C, c) 680 °C and d) 700 °C (two-step HT)

**Microscopic fracture appearance.** Besides the macroscopic examination of the fracture behavior Figure 5.73 shows the microscopic appearance of the fracture surface for one-step HT after annealing at selected  $T_{IA}$  by SEM. Generally, the displayed figures show the fracture appearance at the edges of the shear lips except for  $T_{IA}$  = 680 °C where the image was taken at the dominant residual fracture surface. All displayed fracture surfaces exhibited characteristics of ductile fracture represented by dimples. These dimples varied in size and



depth. The size of the dimples generally increased with increasing  $T_{IA}$ . For a  $T_{IA}$  of 580 °C the dimples were very shallow and small. For  $T_{IA} = 620$  °C the dimples appeared very fine structured and significantly more extended than for the lower  $T_{IA}$ . **Figure 5.73 c)** displays the fracture surface after annealing at a  $T_{IA}$  of 680 °C. In addition to some dimples smooth areas with no sign of ductile fracture dominate the fracture appearance. Annealing at a  $T_{IA}$  of 700 °C resulted in very large and elongated dimples.

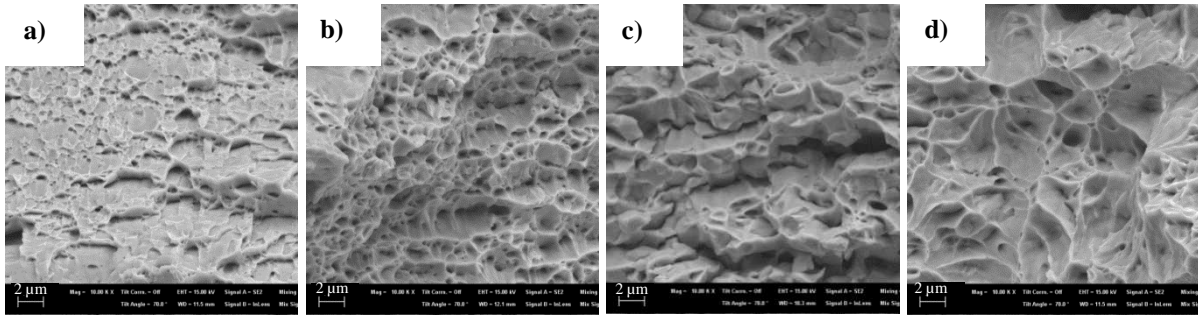


**Figure 5.73:** 0.1C6.4Mn - Fracture surface for  $T_{IA}$  of **a)** 580 °C, **b)** 620 °C, **c)** 680 °C and **d)** 700 °C (one-step HT)

**Figure 5.74** illustrates the microscopic fracture appearance of the two-step heat treated samples. Compared with one-step HT no significant differences were apparent. Accordingly the dimple size increased with rising  $T_{IA}$ . At all  $T_{IA}$  with the exception of 680 °C dimples dominated the fracture surface. At  $T_{IA} = 680$  °C a substantial amount of smooth areas with brittle fracture appearance existed.

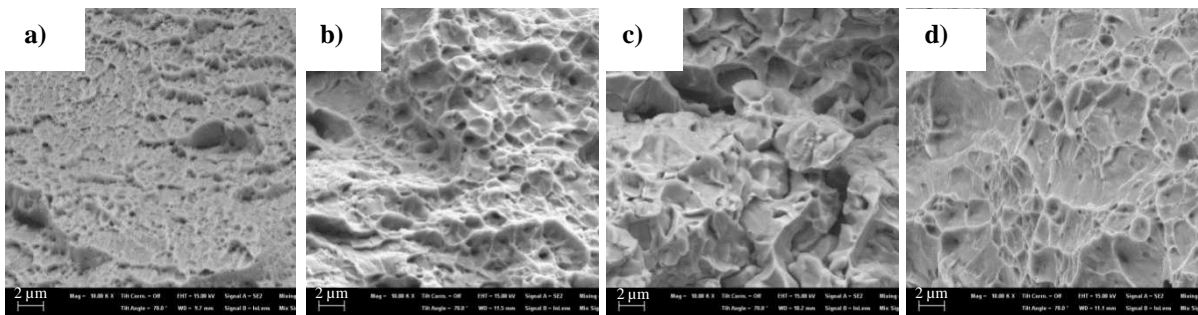


**Figure 5.74:** 0.1C6.4Mn - Fracture surface for  $T_{IA}$  of **a)** 580 °C, **b)** 620 °C, **c)** 680 °C and **d)** 700 °C (two-step HT)

**Qualitative void analysis.** The following section presents the results of SEM investigations on fractured tensile specimens locating the preferred sites for void formation within the microstructure indicated by the white arrows. Void appearance at non-metallic inclusions was found for all tested samples but was not included in this analysis as it was not a representative characteristic for a certain HT schedule. **Figure 5.75 a)** illustrates the heavily deformed microstructure for the sample annealed at  $T_{IA} = 580$  °C. As shown in **Chapter 5.2.1** the microstructure consisted of ferrite and austenite which cannot be differentiated in this figure due to the high degree of deformation. Besides those two phases a considerable amount of cementite was present. The cementite interface showed to be the preferred location for the void formation. The voids appeared highly elongated in rolling direction and rather slim in transversal direction. After annealing at a  $T_{IA}$  of 620 °C (**Figure 5.75 b)** the ferritic/austenitic microstructure underwent a significant austenite to martensite transformation (see **Chapter 5.2.4**). The interfaces between two newly formed martensite grains were preferential locations

for voids. The martensite can be distinguished from the other phases as its grains were less deformed due to its superior strength. Additionally, voids tended to form near to pearlite, which was found in the microstructure in a small amount. Similar to  $T_{IA} = 580\text{ }^{\circ}\text{C}$  the voids were rather elongated in rolling direction than in transversal one. **Figure 5.75 c)** displays the microstructure after annealing at a  $T_{IA}$  of  $680\text{ }^{\circ}\text{C}$  consisting of ferrite, martensite and retained austenite that was apparently much less deformed than after annealing at lower  $T_{IA}$ . The present voids appeared nearly exclusively at the interfaces between two martensitic grains. They were dominantly penny-shaped and oriented transversal to the rolling direction. In **Figure 5.75 d)** the deformed microstructure after annealing at  $T_{IA} = 700\text{ }^{\circ}\text{C}$  is illustrated. The microstructure consisted of martensite, tempered martensite, ferrite and small amounts of retained austenite. The voids initiated preferentially at the martensite/martensite interfaces. But compared to a  $T_{IA}$  of  $680\text{ }^{\circ}\text{C}$ , in this case the voids were much larger and more equiaxed.

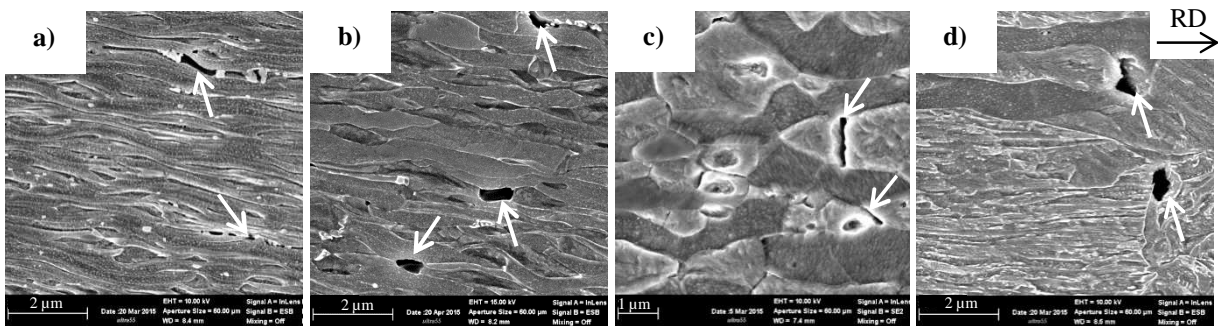


**Figure 5.75:** 0.1C6.4Mn - Void formation for  $T_{IA}$  of **a)**  $580\text{ }^{\circ}\text{C}$ , **b)**  $620\text{ }^{\circ}\text{C}$ , **c)**  $680\text{ }^{\circ}\text{C}$  and **d)**  $700\text{ }^{\circ}\text{C}$  (one-step HT)

**Figure 5.76 a) – d)** represents the same investigations for two-step HT with similar outcome. For a  $T_{IA}$  of  $580\text{ }^{\circ}\text{C}$  the preferred location for the void formation was the interface between ferrite/austenite and cementite. The voids were rather small and elongated in rolling direction. For a  $T_{IA}$  of  $640\text{ }^{\circ}\text{C}$  the voids formed along the interface with the martensite that was formed by strain-induced martensitic transformation during deformation. The voids appeared again elongated in rolling direction. Annealing at  $T_{IA} = 680\text{ }^{\circ}\text{C}$  resulted in a microstructure consisting of considerable amounts of fresh martensite within a ferritic/austenitic matrix. Voids formed at the interfaces of this fresh martensite and appeared small and transversally orientated to the rolling direction. At a  $T_{IA}$  of  $700\text{ }^{\circ}\text{C}$  the present voids formed identically to  $T_{IA} = 680\text{ }^{\circ}\text{C}$  at the interfaces of the martensite. Opposed to the lower annealing temperature the voids appeared much larger and elongated in rolling direction.

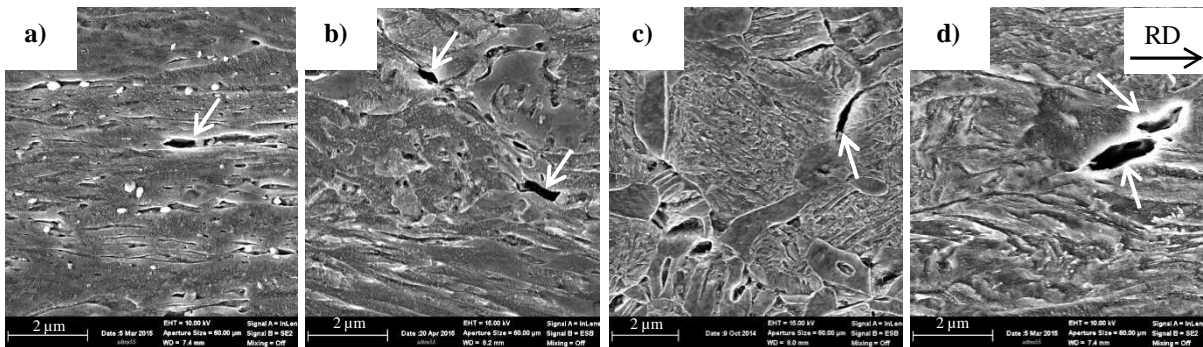


**Figure 5.76:** 0.1C6.4Mn - Void formation for  $T_{IA}$  of **a)**  $580\text{ }^{\circ}\text{C}$ , **b)**  $640\text{ }^{\circ}\text{C}$ , **c)**  $680\text{ }^{\circ}\text{C}$  and **d)**  $700\text{ }^{\circ}\text{C}$  (two-step HT)

**Quantitative void analysis.** Besides the qualitative description of the voids a quantitative analysis of the number of voids as a function of the postuniform thickness strain was carried out. As **Figure 5.70** shows, the number of voids strongly increased with the postuniform strain. For a low  $T_{IA}$  of 580 °C the analysis of one-step as well as two-step HT revealed that the number of detected voids was rather small and increased moderately until up to the fracture surface. Annealing at a  $T_{IA}$  of 620, 640 and 700 °C resulted in a significantly steeper rise of the number of voids up to the fracture surface. One-step HT tended to show a generally higher number of voids.  $T_{IA} = 680$  °C, which generally exhibited very little postuniform deformation, only had voids right next to the fracture surface. For one-step HT the number of voids was very small while for two-step HT a rather high number of voids formed.

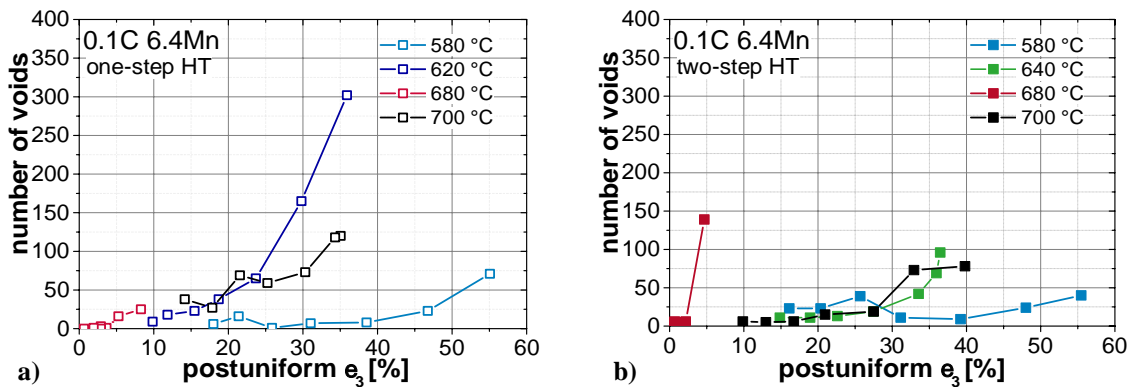


**Figure 5.77:** 0.1C6.4Mn - Number of voids as a function of the post-uniform thickness strain after **a)** one-step HT and **b)** two-step HT

## 6. Discussion

### 6.1 Microstructural evolution

As the microstructure is determining the resulting mechanical properties, a detailed understanding of its phase fractions and their origin is essential. Therefore, a combined discussion of all performed experimental work concerning the microstructural constituents is given in this chapter. First of all, in **Figure 6.1** a validation of the phase fraction diagrams obtained by thermodynamic simulation by comparison with experimentally determined phase fractions is given. Here, exemplarily for all investigated steels, the calculated and experimental phase fractions of 0.1C6.4Mn are compared with each other. The development of the phase fractions of the microstructural constituents of austenite, ferrite and cementite showed the same trends but the experimental data was shifted to higher temperatures. This was found for one-step as well as for two-step HT. This shift seems reasonable as the thermodynamic simulation assumes equilibrium conditions. The applied holding time during the intercritical annealing was quite long with 8 h but potentially not long enough in order to reach full equilibrium. By the precise evaluation of the data it can be noted that with increasing  $T_{IA}$  the deviation between calculation and experiment was significantly reduced from  $\Delta T$  of about 60 to less than 20 °C. As higher temperature accelerates diffusional processes this supports the theory of an insufficient holding time to obtain full equilibrium conditions after the intercritical annealing.

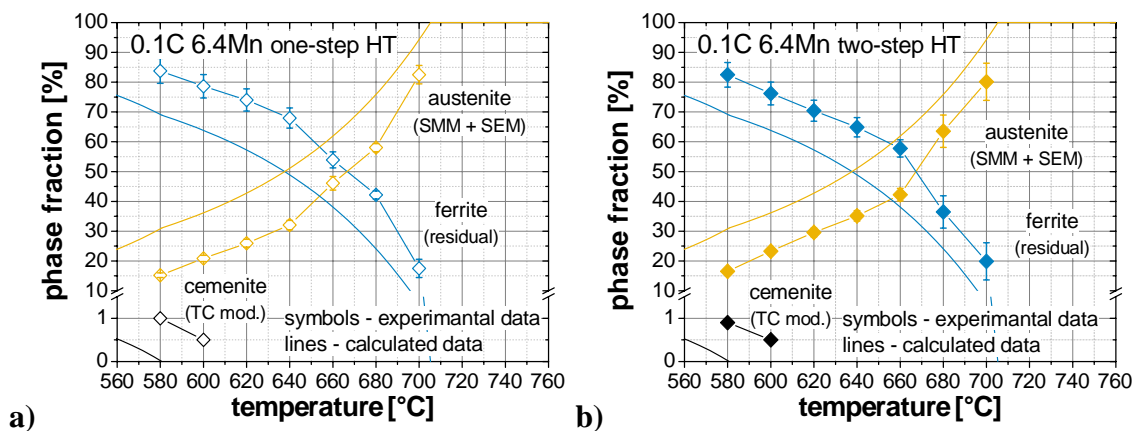


**Figure 6.1:** Comparison of the experimentally determined phase fractions with thermodynamic calculations for a) one-step and b) two-step HT

A further influencing factor that might have considerably increased the deviation between the results of the thermodynamic calculation and the experimental work was the cooling rate. In order to simulate industrial production conditions the cooling rate from  $T_{IA}$  to RT was very slow ( $\sim 0.01$  K/s). It was found that epitaxial growth of ferrite took place during cooling which consequently influenced the amount of retained austenite at RT. The experimental work dealing with this topic focused on the temperature range  $T_{IA} \geq T_{IAmax}$  as for higher temperatures the strongest impact on prolonged cooling time was expected due to accelerated diffusional activity during cooling from high temperatures. **Figure 6.2** presents dilatometric curves of the cooling stage after intercritical annealing at 700 °C for 8 h for two steels with 0.1 wt-% C and 3.5 and 5 wt-% Mn respectively. Both steels exhibited a martensitic

transformation during cooling. With decreasing cooling rate and prolonged cooling time respectively the slope of the dilatometric curves generally flattened. This indicated an increased amount of ferrite in the microstructure. Furthermore, the  $M_s$ -temperature slightly declined which most likely resulted from increased enrichment of C-content in the austenite.

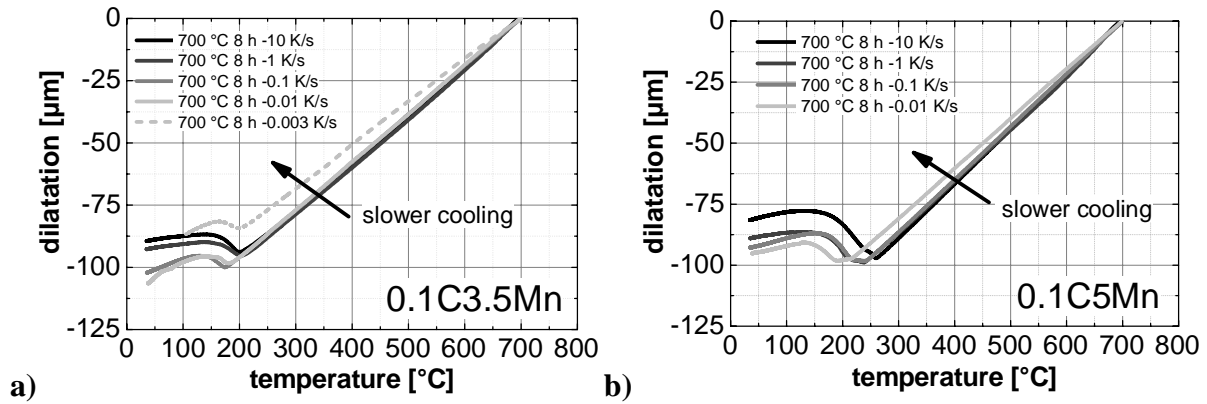


**Figure 6.2:** Dilatometric curves of the cooling phase after intercritical annealing at 700 °C for 8 h of a) 0.1C3.5Mn and b) 0.1C5Mn with various cooling rates [139]

The effect of the cooling rate on the  $M_s$ -temperature as well as retained austenite content is displayed in **Figure 6.3 a)**. For both investigated steels the  $M_s$ -temperature decreased and the retained austenite content increased with slower cooling. The microstructures of 0.1C3.5Mn annealed at  $T_{IA} = 700$  °C are shown in **Figure 6.3 b)** and **c)**. It is obvious that the amount of ferrite strongly increased due to the slow cooling. The results of the investigations on the effect of the cooling rate on the microstructural development of Medium-Mn-steels are presented in detail in K. Steineder *et al.* [139]. When thermodynamic data is used to design alloying concepts for batch annealing cycles the influence of the cooling rate has to be accurately considered.

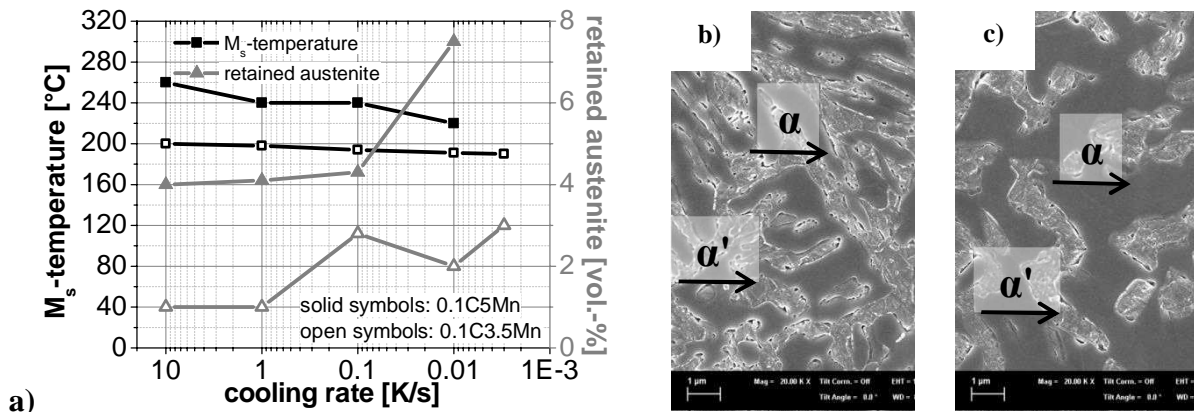


**Figure 6.3:** a) Development of  $M_s$ -temperature and the retained austenite content as a function of the cooling rate b) microstructure of 0.1C3.5Mn after intercritical annealing at  $T_{IA} = 700$  °C cooling rate = 10K/s and c) at  $T_{IA} = 700$  °C cooling rate = 0.01K/s [139]

A further aspect investigated concerning the microstructural development was the influence of the alloying elements C, Mn, Si, Al and Cr on the  $M_s$ -temperature for a variation of steels containing medium Mn-contents (3.5-6.4 wt-% Mn). As there exists no empirical  $M_s$ -formula that relies on data concerning steels with medium Mn-contents a critical review on the applicability of those formulas became necessary. **Figure 6.4 a)** displays the comparison of the experimental data with the  $M_s$ -formula postulated by J. Mahieu *et al.* [79]. The formula

represents a modified version of an empirical formula first published by K. W. Andrews [140] with the introduction of additional alloying element Al. It is commonly applied for TRIP-steels and used in the thermodynamic model for retained austenite prediction for Medium-Mn-steels postulated by S.-J. Lee *et al.* [80]. The comparison of the calculated and experimentally determined data showed an acceptable fit with a mean deviation of 19.2 °C. Further, the experimental data were compared with the original  $M_s$ -formula by K. W. Andrews [140] (**Figure 6.4 b**), which is based on an extensive variety of experimental data containing steels with C-contents between 0.11-0.6 wt-% (mean value 0.35 wt-%) and Mn-contents between 0.04-4.87 wt-% (mean value 0.76 wt-%). The comparison with the experimental data showed that the mean deviation was surprisingly slightly smaller (17.4 °C) than for the formula proposed by J. Mahieu *et al.* [79] although Al-containing steels were also investigated. Naturally for the C-Mn steels the two formulas depicted the same result as the constants for C and Mn do not differ. **Figure 6.4 c**) displays the comparison of the experimental data with the  $M_s$ -formula published by A. E. Nehrenberg [141]. The mean deviation was in this case rather high (51 °C). The  $M_s$ -temperatures, calculated using this formula, were underestimated without exception.

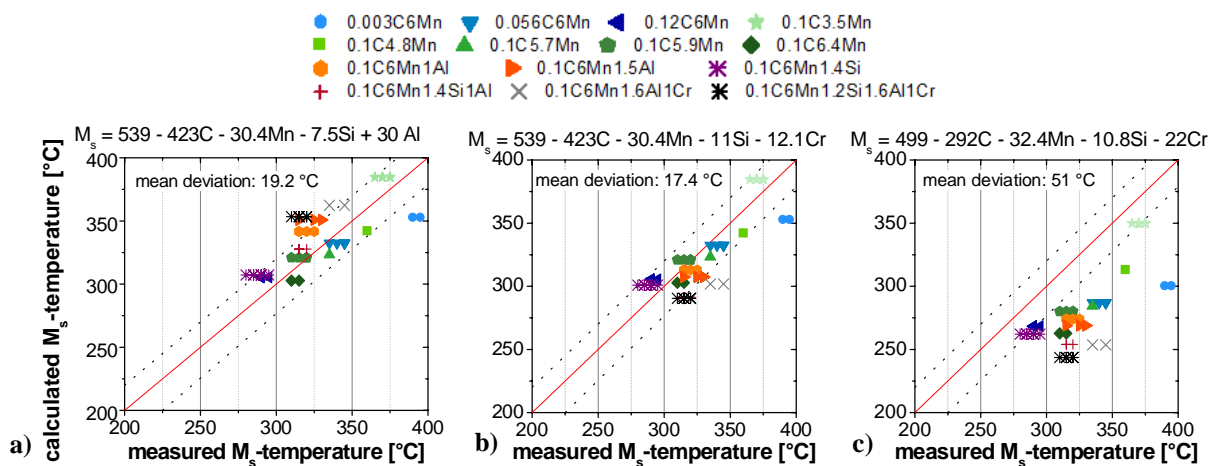


**Figure 6.4:** Comparison of calculated vs. experimental determined  $M_s$ -temperatures for  $M_s$ -formulas proposed by a) J. Mahieu *et al.* [79], b) K. W. Andrews [140] and c) A. E. Nehrenberg [141]

**Figure 6.5** displays the comparison of the experimentally determined  $M_s$ -temperatures with further formulas developed for various alloying systems. While the formula established by W. Steven and A. G. Haynes [142] depicted the best correlation (17 °C) within the investigated formulas, the deviations received by the applications of formulas postulated by R. A. Grange and H. M. Stewart [143] and L. A. Carapella [144] were not satisfying with 40 °C and 70.2 °C respectively.

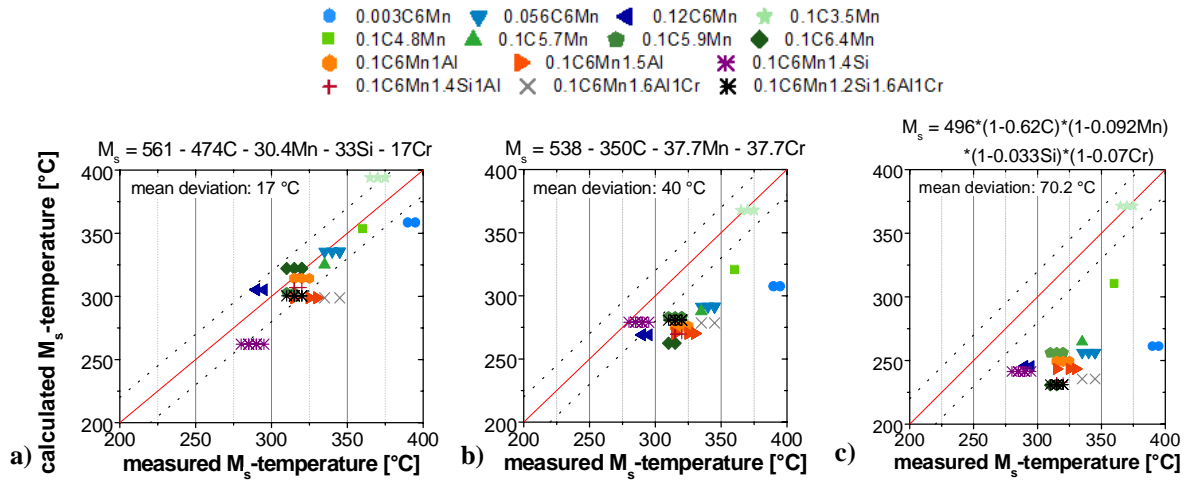


**Figure 6.5:** Comparison of calculated vs. experimental determined  $M_s$ -temperatures for  $M_s$ -formulas proposed by a) W. Steven and A. G. Haynes [142], b) R. A. Grange and H. M. Stewart [143] and c) L. A. Carapella [144]

After detailed analysis of the established  $M_s$ -formulas the experimental data on the Medium-Mn-steels were used to perform a multiple linear regression in order to obtain the best fitting formula. The result is illustrated in **Figure 6.6** and the formula is given by **Equation 6.1**.

$$M_s = 561 - 793C - 28Mn - 14.7Si + 0.5Cr + 16.8Al \tag{6.1}$$

The calculated  $M_s$ -temperatures showed a mean deviation of 7.3 °C which is significantly lower compared to the aforementioned  $M_s$ -formulas. Furthermore, it resulted in an excellent correlation for all the investigated chemical compositions. Comparing the formula regarding the constants representing the influence of the single elements it can be noted that the influence of C significantly increased as well as the impact of Si slightly rose, while the influence of the residual elements (Mn, Cr, Al) was reduced. In conclusion it can be stated that the newly derived formula is to be preferred when used within the range of the investigated chemical compositions or more generally spoken when applied to Medium-Mn-steels.

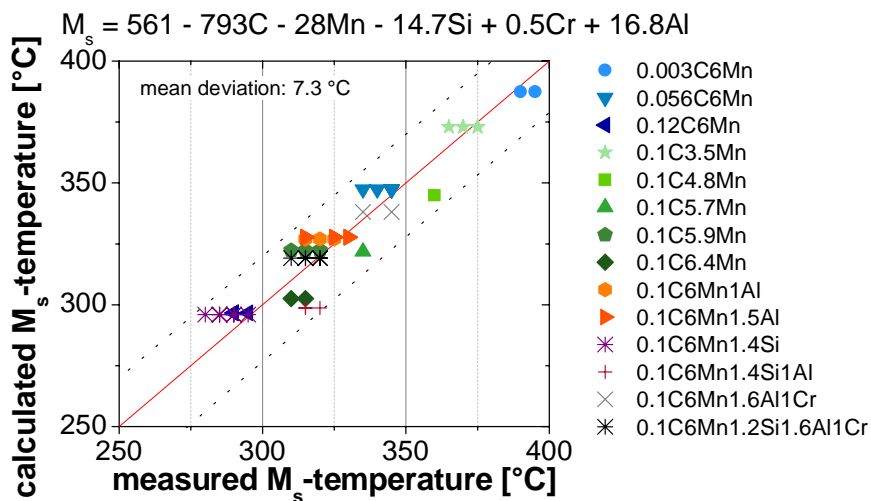


**Figure 6.6:** Comparison of the  $M_s$ -temperatures calculated by the formula obtained by multiple linear regression vs. the experimentally determined  $M_s$ -temperatures

In order to test the applicability of the newly derived formula on the intercritically annealed condition a comparison of the experimentally determined  $M_s$ -temperatures and the calculated



ones are displayed in Figure 6.7. The  $M_s$ -formula by K. W. Andrews [140] was calculated in addition. The chemical composition of the austenite was predicted by Thermo-Calc® calculations. EDX measurements clearly showed (see **Chapter 5.2.1**) that the experimentally determined Mn-content of the retained austenite after IA correlated very well with the thermodynamic simulation until the formation of martensite during cooling. After annealing at high  $T_{IA}$  ( $\geq 660$  °C) the Mn-content was considerably elevated compared to the calculation. Furthermore the precise estimation of the C-content became even more difficult as it was not quantifiable by EDX. Besides these variables the cooling rate has to be considered as well. It is reasonable to expect higher C-contents in the austenite than the calculated ones. During cooling para-equilibrium conditions of a lower  $T_{IA}$  are likely to be established as a detailed study [139] on the influence of the cooling rate clearly showed. Slower cooling resulted in lower  $M_s$ -temperatures. **Figure 6.7** evidently depicts that the calculated temperatures for both applied  $M_s$ -formulas were definitely too high. This was most likely caused by a wrong estimation of the chemical composition due to the aforementioned reasons. Nevertheless, the comparison of the  $M_s$ -formulas with intercritically annealed experimental data shows potential for the further improvement of the model for prediction of the retained austenite content proposed by S.-J. Lee *et al.* [80].

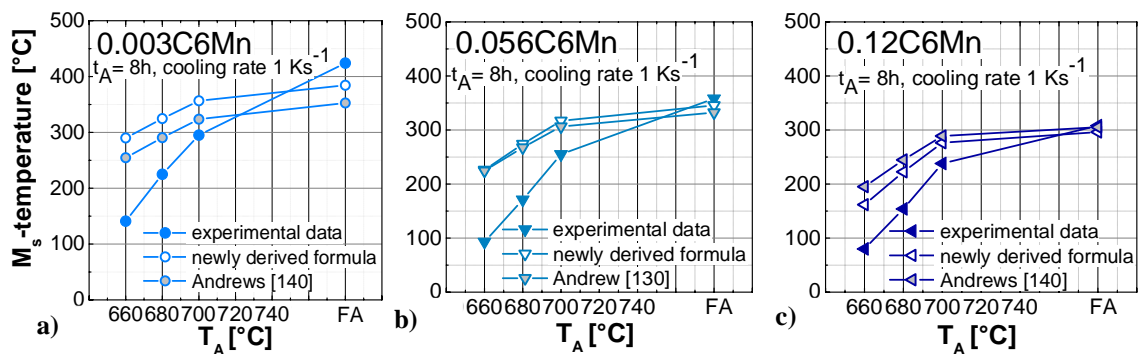


**Figure 6.7:** Comparison of experimentally determined  $M_s$ -temperatures with  $M_s$ -temperatures calculated by the newly established formula and the formula postulated by K. W. Andrews [140] using the chemical composition calculated by Thermo-Calc® a) 0.003C6Mn, b) 0.056C6Mn and c) 0.12C6Mn

**Figure 6.8** exhibits the experimentally determined  $M_s$ -temperatures after IA for the Mn-variation. In general the same trend was found. The calculated  $M_s$ -temperatures determined by the newly derived formula as well as the one postulated by K. W. Andrews [140] were significantly overestimated. For the same reasons as mentioned above, this is most likely due to an improper estimation of the chemical composition of the austenitic phase. Therefore, the expansion of the experimental work towards higher C and Mn-contents as they are existent during IA would be beneficial.



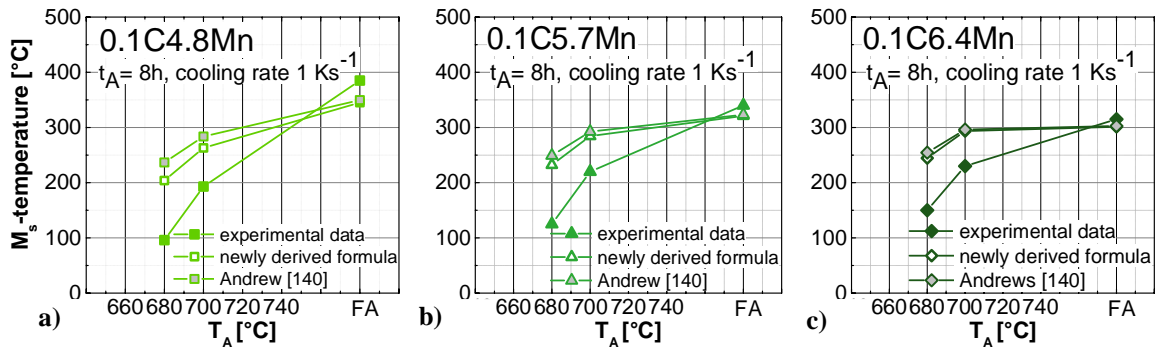


**Figure 6.8:** Comparison of experimentally determined  $M_s$ -temperatures with  $M_s$ -temperatures calculated by the newly established formula and the formula postulated by K. W. Andrews [140] using the chemical composition calculated by Thermo-Calc® a) 0.1C4.8Mn, b) 0.1C5.7Mn and c) 0.1C6.4Mn

**Figure 6.9** shows the retained austenite model proposed by S.-J. Lee *et al.* [80] compared to the experimentally determined retained austenite contents after IA for 8 h and cooling at 0.01 K/s. The experimental data exhibited the predicted maxima but were shifted to higher temperatures and the maximum retained austenite amounts were higher compared to model calculations. Thus, the newly derived  $M_s$ -formula was applied within the model (**Figure 6.9**). This led to an improvement of the model prediction especially pronounced with increasing C-content of the steel. For the steel 0.12C6Mn, the prediction of the  $T_{IAmax}$  as well as the predicted amount could be considerably improved, although a substantial shift of the experimentally determined data to lower  $T_{IA}$  remained. Keeping in mind that this shift was also observed at the determination of the phase fractions (see **Figure 6.1**) it can be assumed that equilibrium conditions were most probably not fully established and the applied cooling rate further influenced the results. This deviation cannot be diminished by improving the  $M_s$ -formula.

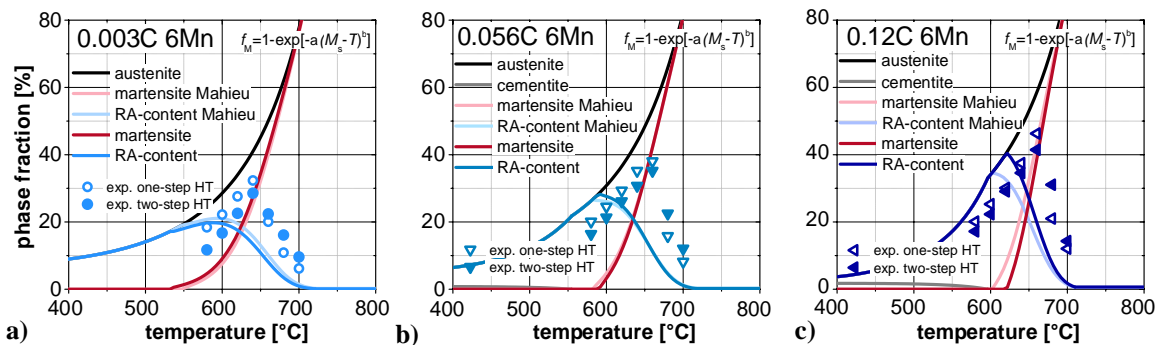


**Figure 6.9:** Retained austenite model proposed by S.-J. Lee *et al.* [80] compared with experimentally determined retained austenite content and application of experimentally determined  $M_s$ -formula for the chemical composition of a) 0.03C6Mn, b) 0.056C6Mn and c) 0.12C6Mn

The comparison of the experimental results of the Mn-variation with the retained austenite model is depicted in **Figure 6.10**. The same correlations as for the C-variation were found. The experimental data were shifted to higher temperatures and higher amounts of retained austenite. Hence, the newly derived  $M_s$ -formula was incorporated and a substantial improvement of the model could be observed for all three steels.

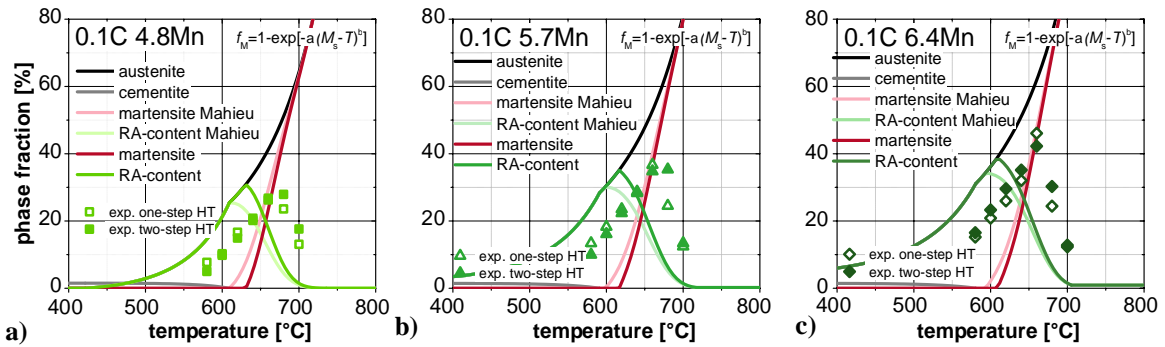


**Figure 6.10:** Retained austenite model proposed by S.-J. Lee *et al.* [80] compared with experimentally determined retained austenite content and application of experimentally determined  $M_s$ -formula for the chemical composition of **a)** 0.1C4.8Mn, **b)** 0.1C5.7Mn and **c)** 0.1C6.4Mn

In order to further develop the  $M_s$ -formula concerning its future application for Medium-Mn-steels the examination of an extended chemical spectrum of steels would be beneficial. Especially regarding the improved prediction of retained austenite under intercritically annealed conditions, where thermodynamic simulation as well as EDX measurement have shown a high enrichment in C and Mn, this would become necessary. Therefore, the examination of alloys with the nominal chemical composition of the intercritical austenite condition would be necessary. Nevertheless a substantial improvement of the model could be already achieved by incorporation of the newly derived  $M_s$ -formula to the models proposed by S.-J. Lee *et al.* [80]. Beside the  $M_s$ -temperature the model relies on two further empirically determined constants  $\alpha_c$  and  $\beta_c$ , which are as well dependent on the chemical composition (see **Equation 3.6** and **3.7**). Both constants are incorporated into the Koistinen-Marburger equation (**Equation 3.4**) and take into account that higher C as well as Mn-contents result into a retardation of the martensite transformation. Since the constants were determined based on Medium-Mn steels a further adaption seems not to be necessary. However, in order to limit the shift of the experimental data to higher temperatures the accuracy of the model would benefit of an incorporation of the cooling rate from  $T_{IA}$  to RT (respecting the epitaxial growth of ferrite as shown in [139]).

As this work highlights the influence of C and Mn as well as the HT on the mechanical properties of Medium-Mn-steels the following section concentrates on the microstructural development depending on these crucial aspects. The microstructure fundamentally determines the resulting mechanical properties. Therefore its thorough analysis is a prerequisite to understand the mechanical behavior of a steel. Furthermore, this in-depth understanding of the microstructure becomes necessary in terms of steel design in order to guarantee required mechanical response. In **Figure 6.11 a)** the influence of C (higher C-content indicated by blue arrow) on the phase fractions at  $T_{IA}$  is shown schematically. An increasing C-content effectively narrowed the intercritical region by decreasing the  $A_{c3}$ -temperature and significantly increasing the  $A_{c1}$ -temperature. Therefore, the slope of the ferrite to austenite formation increased. The cementite dissolution was substantially shifted to higher temperatures with a higher C-content. This was confirmed by thermodynamic modelling as well as SEM investigations. **Figure 6.11 b)** displays the effects of C on the final microstructure at RT. The main consequence of an increased C-content was the extensive increase in retained austenite. The literature review revealed that about 30 vol.-% of retained austenite are necessary to achieve the targeted mechanical properties  $UTS \cdot TE \geq$

30.000 MPa%. Hence, the stabilization of austenite becomes a crucial factor to accomplish it. The increase in C proved to be effective in order to achieve this aimed amount of retained austenite. An increased C-content also shifted the  $T_{IAmax}$ , the temperature where the highest amount of retained austenite was stabilized to RT, to higher temperatures. This can be linked to the increased  $A_{c1}$ -temperature as well as the postponement of the martensite formation during cooling to higher  $T_{IA}$ . The increased amount of C strongly decreased the  $M_s$ -temperature after intercritical annealing (see **Figure 6.7**). Hence, a higher amount of intercritical austenite, which is naturally present at higher temperatures, can be stabilized. This resulted in a shift of the martensite formation during cooling to higher  $T_{IA}$ . The temperature range of the retained austenite significantly reduced with increasing C-content.

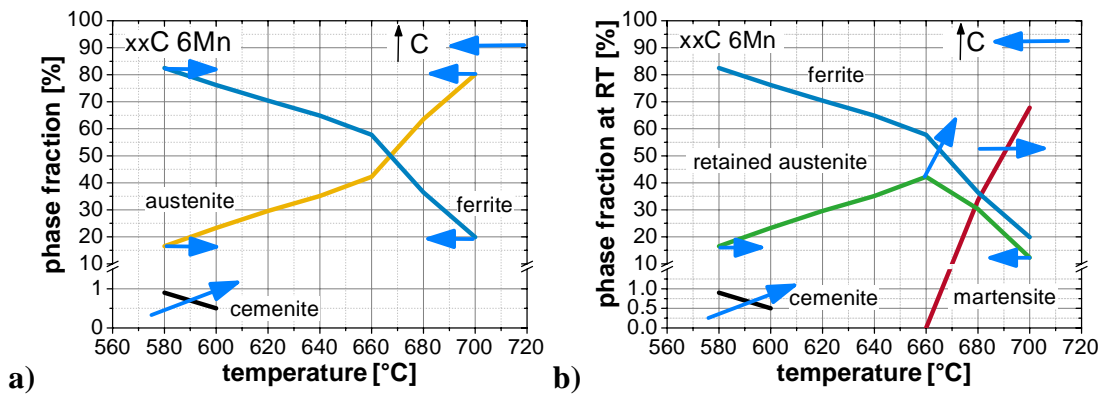


**Figure 6.11:** Phase fraction diagram displaying the schematic influence of the C-content at a)  $T_{IA}$  and b) RT

The influence of Mn on the phase fractions is given in **Figure 6.12**. Dilatometric testing as well as thermodynamic modelling have shown that an increased Mn-content decreased the  $A_{c1}$ - and the  $A_{c3}$ -temperature. This means that at constant  $T_{IA}$  a higher Mn-containing steel consists of an increased amount of intercritically formed austenite. The dissolution of cementite was also shifted to lower temperatures. At RT higher Mn-content substantially increased the amount of retained austenite. Similar to the effect of C this can be explained by the decline of the  $M_s$ -temperature with increasing Mn-content. The higher the steel's nominal Mn-content the more effective is the suppression of the martensite formation below RT. In contrast to the effect of C, higher Mn-contents decreased the  $T_{IAmax}$ . That can be clearly linked to the decreasing  $A_{c1}$ - and the  $A_{c3}$ -temperatures as well as the decrease of the cementite dissolution temperature.

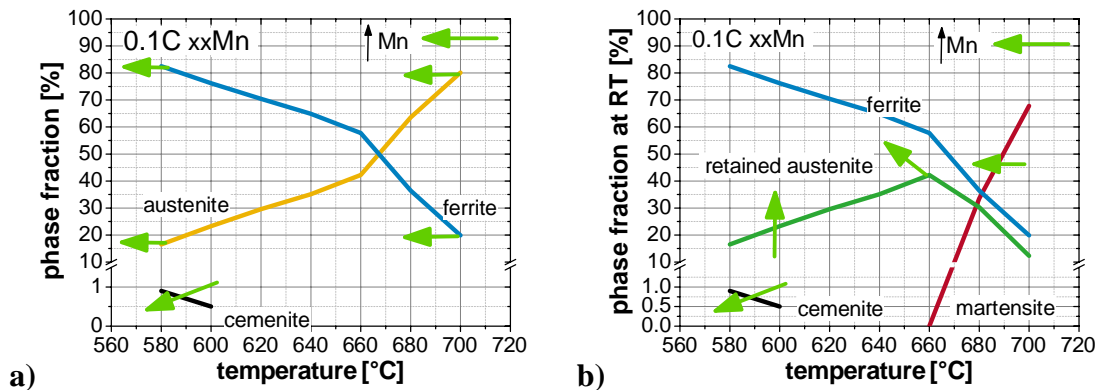


**Figure 6.12:** Phase fraction diagram displaying the schematic influence of the Mn-content at a)  $T_{IA}$  and b) RT

Both elements, C and Mn, are known as strong austenite stabilizers. C and Mn proved to effectively increase the maximal amount of retained austenite at RT, which is necessary to obtain the targeted mechanical properties. In order to offer a stable production Mn is beneficial as it does not diminish the intercritical annealing region.

The effects related to the second influencing factor investigated in this work, namely HT, are presented in **Figure 6.13**. The black arrows indicate the impact of the applied two-step HT compared to the one-step HT. During annealing at  $T_{IA}$  no significant trend concerning the amount of intercritically formed austenite could be found depending on the applied HT schedule. Concerning the cementite formation the two-step HT resulted in a decreasing dissolution temperature. The reason was most probably the different cementite morphology. Subsequent a more in-depth analysis regarding the cementite dissolution is given in **Figure 6.14**. **Figure 6.13 b)** displays the influence of the applied HT on the resulting microstructure at RT. The two-step HT resulted in slightly lower maximal values of retained austenite. However, for  $T_{IA} \geq T_{IAmax}$  more austenite could be stabilized after two-step HT. As dilatometric testing revealed (see **Figure 5.40** and **Figure 5.41**)  $M_s$ -temperatures differed depending on the applied HT schedule. The  $M_s$ -temperature after one-step HT was significantly lower, which would suggest a higher resulting fraction of retained austenite at RT. By thorough examination of the curves a slight deviation of the linear cooling curve at significantly higher temperatures was detected for the one-step HT. According to the temperature range this indicates a strongly decelerated martensitic or at higher temperatures even bainitic transformation that started at elevated temperatures. As a result the two-step HT microstructure contained more retained austenite after annealing at higher  $T_{IA}$  as less martensite was formed during cooling. A possible explanation for this difference in the transformation behavior could be a difference in the austenite grain size according to the HT schedule. Grain size of the two-step HT microstructure has been proven to be considerably lower (see **Figure 5.50**) than after one-step HT. This result is consistent with the findings of H. Luo *et al.* [145]. Various studies have shown the effect of decreasing  $M_s$ -temperature with decreasing grain size [60,61], which can give an explanation for the increased amount of retained austenite after two-step HT at  $T_{IA} \geq T_{IAmax}$ .

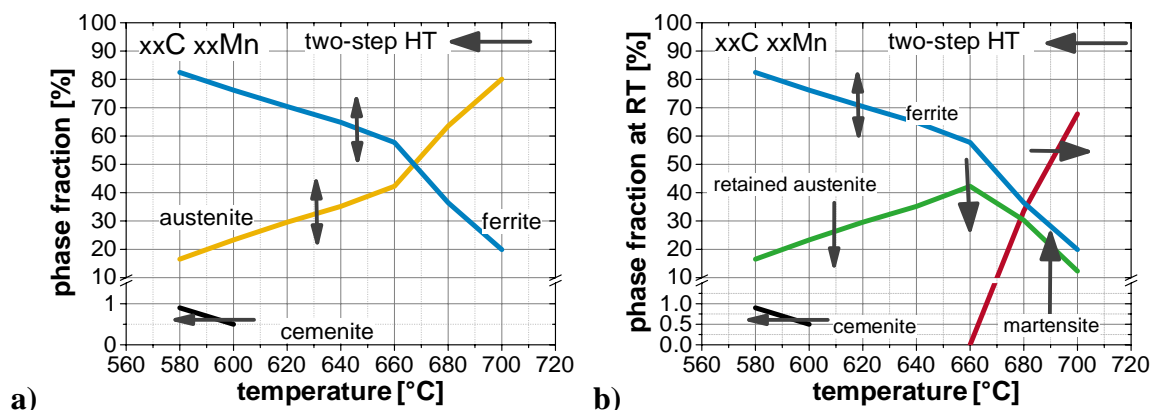


**Figure 6.13:** Phase fraction diagram displaying the schematic influence of one-step vs. two-step HT at a)  $T_{IA}$  and b) RT

A further difference concerning the influence of the HT schedule on the microstructural development is the resulting morphology of the respective phases. As shown in **Figure 5.51 a)** besides the grain size one-step and two-step heat treated austenite resulted in

significantly different morphologies expressed by the circularity. But also ferrite, cementite and partly also martensite clearly appeared different in shape depending on the HT. The one-step HT resulted in an entirely globular shaped microstructure, whereas the microstructural constituents after two-step HT showed to be majorly lath-like shaped. Except for the austenite, which appeared mostly lath-like but with a considerable amount of 22 area-%  $\pm$  7.5 of globular shape. These findings are in agreement with the work of A. Arlazarov *et al.* [42], where exactly this morphology difference is explained in detail. Basically the globular shape is stemming from recrystallization, while the lath-like shaped is handed down from the martensite structure. The mechanisms of the microstructural evolution are described in **Chapter 3.2**. The above mentioned differences in cementite morphology are displayed in detail in **Figure 6.14**. TEM micrographs revealed the different shape and size of the cementite. While after one-step HT the cementite was globular and significantly larger, the cementite after two-step HT was rod-like and very small. The difference in shape and size can be explained by the HT schedule. The globular cementite most likely stems from the annealing of the hot rolled sheet material prior to cold rolling. The rod-shaped cementite of the two-step HT is related to the tempering of the martensitic microstructure established after FA (first step of two-step HT) during intercritical annealing at  $T_{IA}$ . The triaxial alignment ( $120^\circ$ ) of the cementite shown in **Figure 6.14 c)** supports this explanation. Due to the considerably smaller size the cementite rods are more likely to dissolve at a lower  $T_{IA}$  as displayed in **Figure 6.13**.

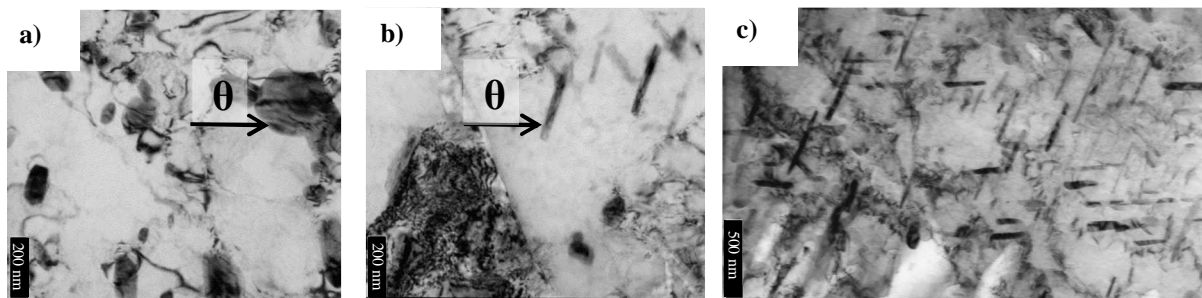


**Figure 6.14:** 0.1C5.9Mn - TEM micrographs revealing cementite morphology  $T_{IA} = 580^\circ\text{C}$  after **a)** one-step HT, **b)** two-step HT and **c)** two-step HT overview (triaxial alignment)

In **Chapter 5.2.1** a detailed examination of the texture development for one-step and two-step HT was presented. After one-step HT, for the ferrite as well as for the austenite pronounced fiber textures were found. The ferrite displayed a pronounced  $\gamma$ -fiber  $\langle 111 \rangle \parallel \text{ND}$ , which is known as a typically rolling texture in bcc materials (e.g. steel), but also comprises important recrystallization components. [136] Furthermore, the  $\gamma$ -fiber is typically pursued for optimum deep drawing behavior of IF steels. [146, 147] Two-step HT significantly reduced the  $\gamma$ -fiber texture components. **Figure 6.15** shows the ODF of the ferritic phase along with the production process. After hot rolling the ferritic grains displayed no preferred orientation. As opposed to this, the heavily cold worked ferrite after cold rolling was substantially orientated. It could clearly be seen that the strong  $\gamma$ -fiber ( $\Phi = 55^\circ$ ,  $\varphi_1 = 0-90^\circ$ ,  $\varphi_2 = 45^\circ$ ), which was observed for all one-step heat treated samples, was introduced by the cold rolling process. Even by recrystallization of the ferrite this texture component did not disappear (see **Figure 5.46**). However, as **Figure 6.15 c)** indicates that after a FA the  $\gamma$ -fiber component could be substantially reduced. This was shown by the strongly decreasing intensities of the texture component after FA.



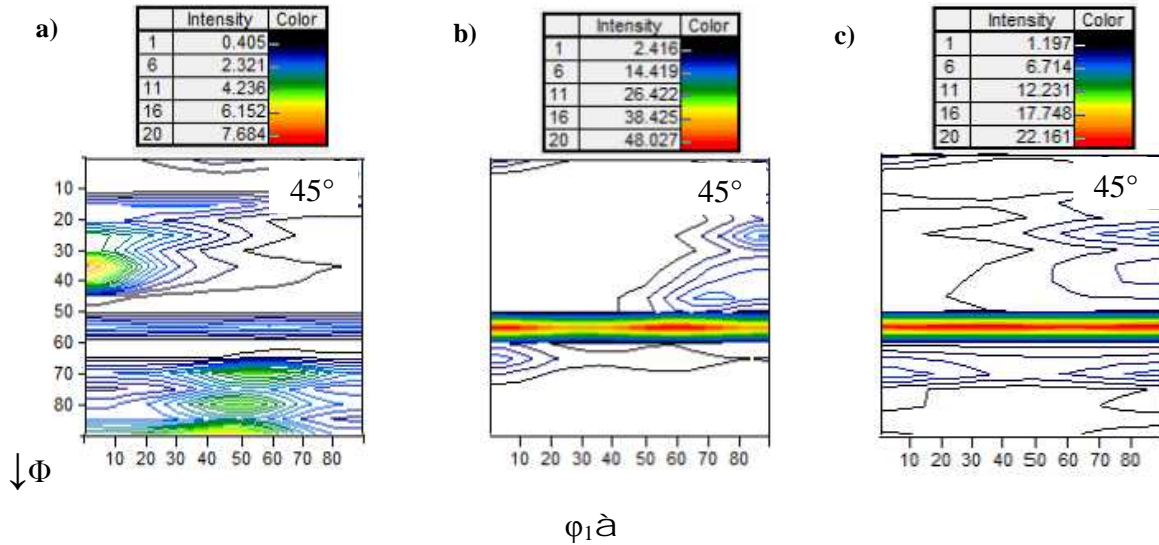


**Figure 6.15:** ODF of the ferritic phase after a) hot rolling, b) cold rolling and c) full austenitization ( $\phi_2 = 45^\circ$ )

As no austenite was present after cold and hot rolling respectively there were no ODFs available. Nevertheless, it seems reasonable to argue that the pronounced  $\alpha$ -fiber component observed with the one-step heat treated austenite resulted from the severe texturing of the ferrite. Given that the austenite forms during IA in the presence of ferrite, it can be assumed that the crystal growth of the austenite is characterized by orientation relationships between the ferritic matrix and the fresh austenite. Thus, if the matrix exhibits a preferred orientation the phase growing next to it should exhibit one too.

**Main conclusions** found concerning the **microstructural development:**

- The microstructural development showed to be strongly dependent on the applied  $T_{IA}$  as the intercritical amount of austenite and its chemical composition were directly altered by the  $T_{IA}$ .
- In general an increasing Mn-content decreased the  $A_{c1}$ - and  $A_{c3}$ -temperatures while C mainly decreased the temperature difference between  $A_{c1}$ - and  $A_{c3}$ -temperature. Both elements substantially increased the amount of retained austenite.
- The influence of the HT schedule on the microstructural development was systematically investigated. One-step and two-step HT resulted in similar fractions of cementite, ferrite, austenite and martensite after annealing at the same  $T_{IA}$  but appeared to be different concerning their grain size and morphology. Concerning the resulting retained austenite optimum, two-step HT broadened the retained austenite peak by decreasing the  $M_s$ -temperature most probably *via* a smaller grain size.
- The newly established  $M_s$ -formula, valid for Mn-contents from 3.5 to 6.4 wt-%, significantly improved the thermodynamic modelling of the retained austenite content at RT.
- One-step HT showed a strong fiber texture of the microstructure stemming from the cold rolling process. The full austenitization during two-step HT could strongly reduce the preferred orientation.

## 6.2 Mechanical properties

It is a matter of fact that the mechanical properties result from the obtained microstructure. Therefore, this chapter gives detailed information about the structure-property relationship in the investigated Medium-Mn-steels. As shown in **Figure 5.54** to **Figure 5.56** the fractions of ferrite, austenite and martensite as well as their chemical composition were strongly influenced by the  $T_{IA}$ . Consequently, the mechanical properties are equally strongly related to the applied  $T_{IA}$ .

The strength of a single phase material is determined by solid solution, density of dislocations, grains size and precipitates. As the microstructure of Medium-Mn-steels consists of several constituents the mechanical behavior of different phases has to be taken into account. For multiphase steels it is generally accepted that the yielding of the softest phase has the dominant effect on YS. [148] **Figure 6.16 a)** gives a schematic overview of the development of YS and the corresponding microstructure as it was found for all investigated steels. Increasing  $T_{IA}$  resulted in a constantly decreasing YS down to a minimum value. This decline was certainly linked to the strong decreasing strength of the ferrite due to the increasing grain size and the decreasing solute solution hardening by Mn, as shown in **Figure 5.50** and **Figure 5.54**. Moreover, recovery and recrystallization of the cold-worked ferrite as well as tempering of the martensite stemming from FA decreased YS even further. [149]

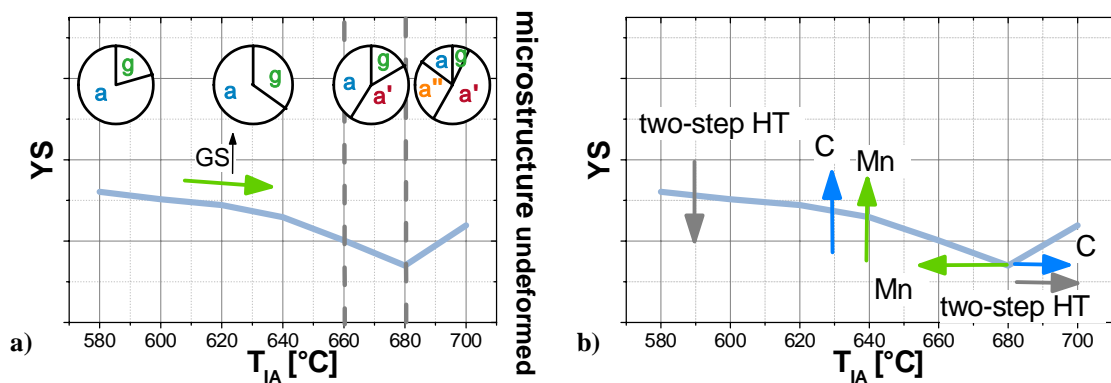


**Figure 6.16:** Schematic illustration of the influence of the a) microstructural composition and grain size (GS) and b) the applied HT and the C-/Mn- content on the YS ( $\gamma$  = austenite,  $\alpha$  = ferrite,  $\alpha'$  = martensite,  $\alpha''$  = tempered martensite)

The decreasing strength of the ferrite is one effect that lowered YS. A further aspect is the existence of an increasing amount of retained austenite with declining stability (see **Chapter 5.2.4**). Therefore, some of the retained austenite is supposed to transform into martensite by elastic stresses so-called stress-assisted transformation (during yielding). The presence of hard martensite in a soft ferritic matrix, which comes along with a considerable volume expansion during its transformation, results in internal stresses [150,151,152] and an increased amount of dislocations in the ferrite [150], which consequently leads the ferrite to yield at a lower amount of external stresses. This behavior of decreasing YS with decreasing stability of the austenite is well known from TRIP-steels. [153,154] Annealing at  $T_{IA}$  of 660 or 680 °C, depending on the alloy's chemical compositions, resulted in fresh athermal martensite that formed during cooling (compare **Figure 5.5** and **Figure 5.7**). This martensite, present in the undeformed microstructure, decreases YS similar to the martensite formed during yielding. This effect is commonly observed for DP-steels. [150,152,155] A. M.

Sarosiek and W. S. Owen [150] showed that the YS of DP-steels is considerably lower than that of a ferritic reference specimen. Furthermore, **Figure 6.16 a)** shows that after annealing at higher  $T_{IA}$  the YS increases again. This can be explained by the self-tempering of the athermal martensite during cooling. The chemical enrichment of the austenite significantly decreased with higher  $T_{IA}$  and therefore the  $M_s$ -temperature rose (compare **Figure 5.40** and **Figure 5.41**). Due to the elevated temperatures during martensite formation and the slow cooling after intercritical annealing (0.01 K/s) the fresh martensite self-tempered. This can be clearly seen in the micrographs in **Figure 5.17**, **Figure 5.21** and **Figure 5.43**. This significantly decreases the internal stresses [151] and therefore resulted in an increase of YS.

**Figure 6.16 b)** illustrates the main impacts of C and Mn as well as of the applied HT on YS. C and Mn increased YS of all investigated steels by solid solution. As YS exhibited a minimum for all steels, a correlation with the chemical composition could be found. An increased C-content shifted the minimum to higher  $T_{IA}$ . As described above the minimum in YS resulted from the impact of fresh martensite. Due to the interaction of altering  $A_c$ - and  $M_s$ -temperatures, the minimal YS appeared at higher  $T_{IA}$  with higher C-content of the steel. The impact of Mn was opposed to that of C. Increasing the Mn-content decreased the  $A_c$ -temperatures and caused the minima of YS to appear at lower  $T_{IA}$ . The HT also affected the minimal YS. Applying the two-step HT caused the  $T_{IA}$  at which the minimum appeared to increase. This was most probably due to the increased amount of formed martensite during cooling for one-step HT due to slightly elevated  $M_s$ -temperatures (compare **Figure 6.13**).

At the lower range of applied  $T_{IA}$ , the two-step heat treated microstructure displayed slightly lower YS than the one-step heat treated. This was rather unexpected as the two-step HT resulted in a smaller ECD of the grains. EDX analysis did not show a considerable difference in Mn-content of the respective phases. Moreover, differences in C-content were also not expected. However, the microstructure strongly differed concerning the thermal history. Hence, the microstructure resulting from two-step HT annealed at low  $T_{IA}$  possessed a rather high dislocation density stemming from initially martensitic microstructure after full austenitization, which was depleted with higher  $T_{IA}$  as tempering of the martensite (see TEM investigations in **Figure 5.44** and **Figure 5.45**) proceeded. The heavily cold-worked initial microstructure at one-step HT underwent recrystallization and resulted in rather equiaxed dislocation free ferrite grains. So neither grains size, chemistry nor dislocations density can explain the difference in YS between the two HT schedules. Based on this, it is not possible to give a valid explanation for this correlation and further research would be necessary to understand the mechanisms influencing YS.

For modern multiphase AHSS the simple rule of mixtures proposed by Mileko [156] (**Equation 6.2** and **6.3**) has shown to be sufficiently effective to describe the UTS and UE.

$$\bar{\sigma} = \sigma_{\alpha} \cdot f_{\alpha} + \sigma_{\beta} \cdot f_{\beta}. \quad 6.2$$

$$\bar{\varepsilon} = \varepsilon_{\alpha} \cdot f_{\alpha} + \varepsilon_{\beta} \cdot f_{\beta}. \quad 6.3$$

Here,  $\bar{\sigma}$ ,  $\sigma_{\alpha}$  and  $\sigma_{\beta}$  are the strength of the composite, of constituent  $\alpha$  and constituent  $\beta$ ,  $\bar{\varepsilon}$ ,  $\varepsilon_{\alpha}$  and  $\varepsilon_{\beta}$  are the elongation of the composite, of constituent  $\alpha$  and constituent  $\beta$ ,  $f_{\alpha}$  and  $f_{\beta}$  are the volume fraction of the respective phases.



**Figure 6.17** illustrates the resulting stress-strain behavior of the composite by applying **Equation 6.2** and **6.3**. It is supposed that both constituents  $\alpha$  and  $\beta$  fit the power-law **Equation 6.4**.

$$\sigma_{true} = k \cdot \varepsilon_{true}^n \tag{6.4}$$

Here,  $\sigma_{true}$  is the true stress,  $k$  is a material constant,  $\varepsilon_{true}$  is the true strain and  $n$  is the work hardening coefficient.

Furthermore, the assumption is made that interfacial bonding is sufficient enough for the composite to reach the Considère instability criterion (**Equation 3.1**). Moreover, it is assumed that the material is isotropic and no residual stresses are present. [157]

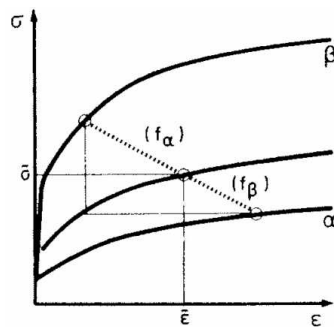


**Figure 6.17:** Resulting stress and strain distribution between two phases [158]

The evolution of UTS and the schematic illustration of the corresponding microstructure are displayed in **Figure 6.18 a)**. For all investigated steels, UTS constantly increased with increasing  $T_{IA}$ . Linking this to the microstructure it could be found that with increasing  $T_{IA}$  the amount of hard phases *e.g.*: austenite and martensite increased. Taking into account the deformed microstructure during tensile testing the amount of hard phases rose even more. Due to the TRIP-effect the majority of the retained austenite was transforming into hard C and Mn enriched martensite while straining. Applying the rule of mixture in such a case, this concluded in a rise of UTS. For TRIP-steels similar correlations between increasing amount of retained austenite and an increasing UTS are stated. [56,153,154] The effect of increasing grain size, which lowers UTS, was too small to reverse this trend. **Figure 6.18 b)** illustrates the effects of increased C- and Mn-content. Both elements increased the strength of each microstructural constituent and therefore the overall UTS. The application of the two different HT schedules did not significantly influence the UTS.

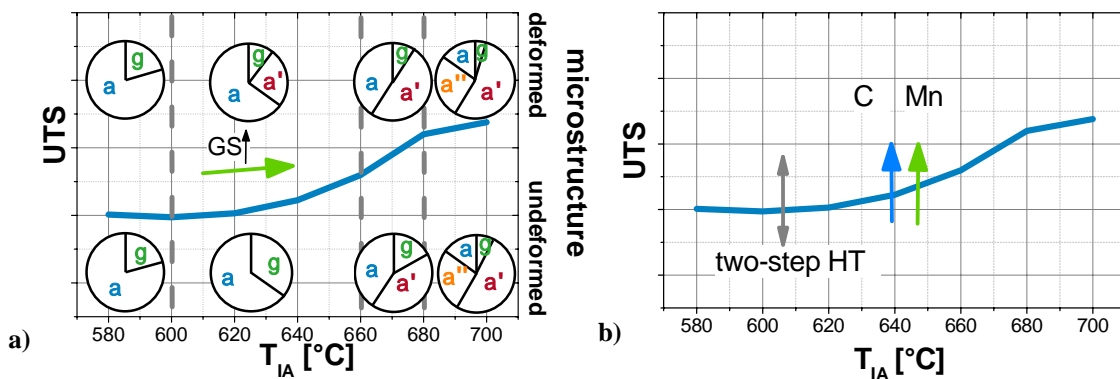


**Figure 6.18:** Schematic illustration of the influence of the **a)** microstructural composition and grain size (GS) and **b)** the applied HT and the C-/Mn- content on the UTS ( $\gamma$  = austenite,  $\alpha$  = ferrite,  $\alpha'$  = martensite,  $\alpha''$  = tempered martensite)

The development of the elongation (both UE and TE) as function of the  $T_{IA}$  is represented in **Figure 6.19**. The general trend showed a maximal elongation appearing at  $T_{IA}$  between 620 and 640 °C. The influence of the microstructure is displayed in **Figure 6.19 a)** illustrating the undeformed and deformed microstructure. At low  $T_{IA}$  the microstructure consisted of a ferritic matrix and a very stable austenite. The strain partitioning between those two phases can be considered as moderate and therefore the strain hardenability was limited. Increasing the temperature to intermediate  $T_{IA}$  maximal elongations were achieved. The microstructure consisted of ferrite and austenite that transformed continuously by strain-induced martensitic transformation and thereby distinctly increased the work hardening behavior. Hence, necking was delayed and high uniform and consequently also high total elongations could be obtained. By further increasing the  $T_{IA}$  more retained austenite was stabilized and finally martensite formed upon cooling. Although the strain hardenability further increased, the elongation declined. In order to obtain high elongations a moderate and continuous work hardening behavior is necessary, which was also reported from other TRIP-assisted steel grades. [51,65,120] At high  $T_{IA}$  the work hardening was concentrated at small elongations which resulted in high UTS but the achieved elongations remained moderate.

**Figure 6.19 b)** shows schematically the improvement of the elongation by increasing the C- and Mn-content. This is clearly linked to an increased amount as well as the enhanced stability of the retained austenite (see **Figure 5.35** and **Figure 5.36**). The two-step HT increased and shifted the maximal elongations to higher  $T_{IA}$  compared to the one-step HT. The explanation for that is given in detail in **Chapter 6.4**.

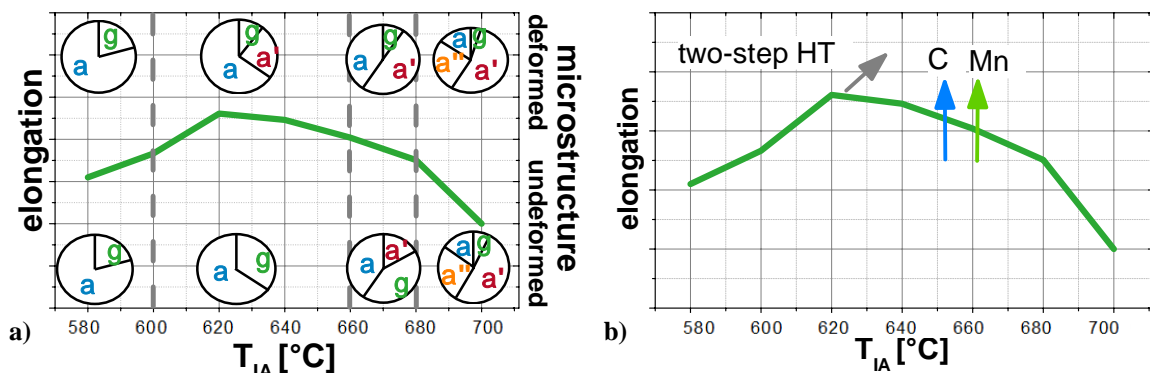


**Figure 6.19:** Schematic illustration of the influence of **a)** the microstructural composition and grain size (GS) and **b)** the applied HT and the C-/Mn- content on the elongation ( $\gamma$  = austenite,  $\alpha$  = ferrite,  $\alpha'$  = martensite,  $\alpha''$  = tempered martensite)

**Figure 6.20** displays the product of UTS\*TE as a function of the  $T_{IA}$  for the C-variation. Clearly a maximum could be found at  $T_{IA}$  between 600 to 640 °C, slightly shifting towards higher  $T_{IA}$  with increasing C-content. In general, the UTS\*TE was improved by increased C-content and two-step HT. The two-step HT enhanced the properties especially at higher  $T_{IA}$  and shifted the maxima to higher  $T_{IA}$ . As a result, the highest combination of UTS\*TE was obtained by 0.12C6Mn and two-step HT.

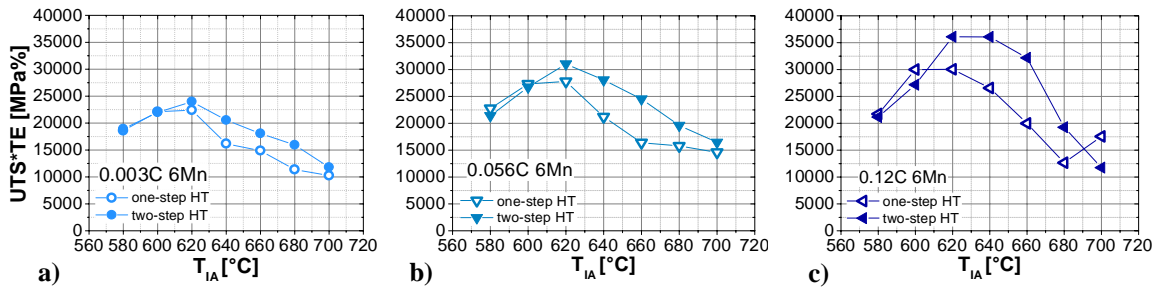


Figure 6.20: UTS\*TE as a function of  $T_{IA}$  for a) 0.003C6Mn, b) 0.056C6Mn and c) 0.12C6Mn

The influence of Mn on the mechanical properties UTS and TE is presented in Figure 6.21. Similar to the effect of C an increased Mn-content improved the maximum product of UTS\*TE. The  $T_{IA}$ , where this maximum was obtained, decreased with a higher Mn-content due to the lowered  $A_c$ -temperatures. In accordance to the results of the C-variation, the two-step HT pushed the maximum UTS\*TE to higher values and higher  $T_{IA}$ .

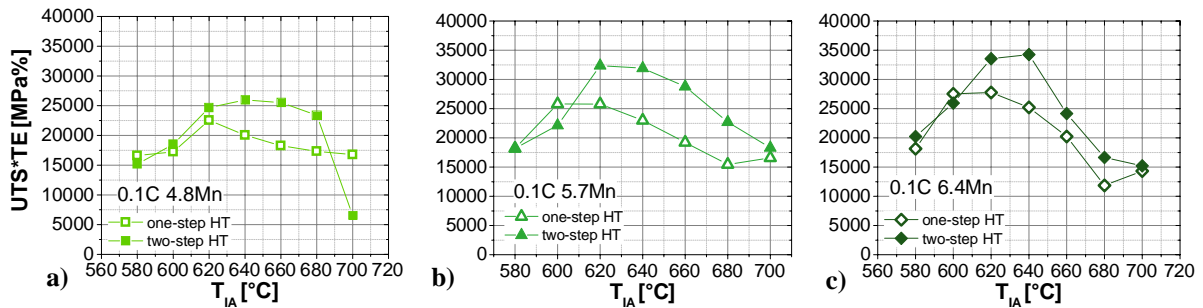


Figure 6.21: UTS\*TE as a function of  $T_{IA}$  for a) 0.1C4.8Mn, b) 0.1C5.7Mn and c) 0.1C6.4Mn

Figure 6.22 shows the comparison of the experimentally determined mechanical properties obtained in the course of the present study with values reported in literature. Generally, the published data showed good correlation with the findings in this study. The only publications that reported values with a better balance out of UTS and TE was reported by M. J. Merwin [16] and W. Cao *et al.* [26] where higher alloyed chemical compositions (0.1C7.1Mn and 0.2C5Mn) were studied and R. L. Miller [24] and J. Shi *et al.* [27] who worked with shorter annealing times (1 h and 2 h). These short annealing times have proven to have a positive effect on the mechanical properties. [24,25,27] This is most probably related to the lower grain size of the austenite and therefore its enhanced stability.

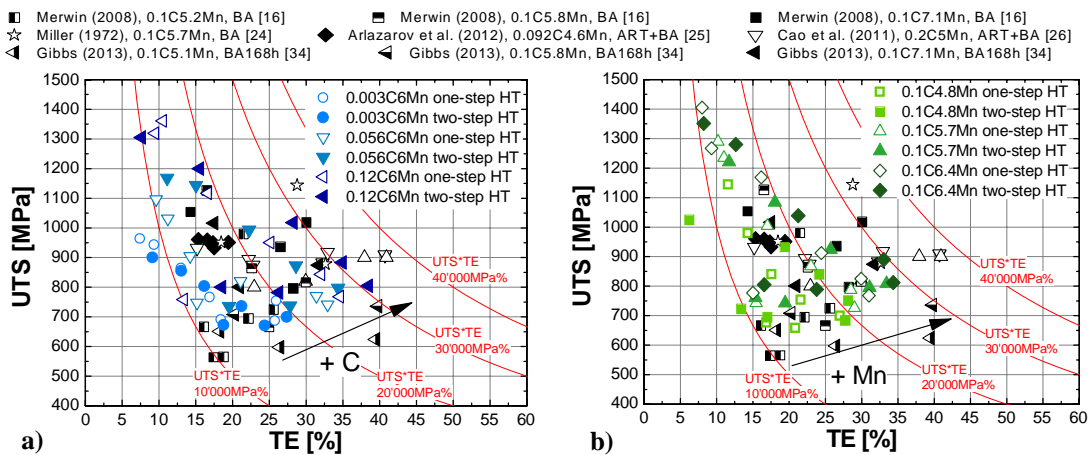
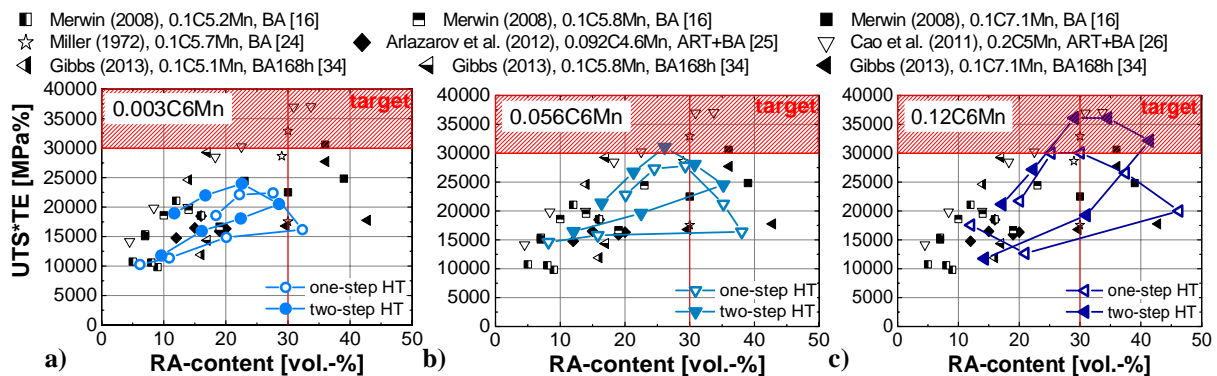


Figure 6.22: Comparison of the experimentally determined mechanical properties UTS vs. TE (normalized to a gauge length of 80 mm) with values reported in literature for a) C-variation 6 wt-% Mn and b) Mn-variation, 0.1 wt-% C

However, not only the achieved mechanical properties are compared to the literature values but also the published retained austenite contents vs. the UTS\*TE. As suggested by D.K. Matlock and J.G. Speer [41] about 30 vol.-% of ideally stabilized retained austenite are necessary to achieve  $UTS*TE \geq 30.000 \text{ MPa}\%$ . As shown in **Chapter 3.2**, a review of the published retained austenite values in literature supported this prediction as well as the experimentally determined retained austenite values presented in **Figure 6.23**. It is clearly shown that not only the amount of retained austenite determined the UTS\*TE but also its stability. For all three steels, there existed an optimally stabilized retained austenite fraction which enabled to achieve an optimum of mechanical properties. Retained austenite fractions, that were exceeding this optimum value, were not capable of increasing the UTS\*TE and thus, the mechanical properties of the steel were strongly deteriorated. This finding corroborates the results from previous work concerning the structure-properties relationship of Medium-Mn steels. [16,25,34] With increasing C-content the maximal amount of stabilized retained austenite at RT constantly increased. The targeted mechanical values of  $UTS*TE \geq 30.000 \text{ MPa}\%$  could be achieved by the steel 0.56C6Mn after two-step HT and for 0.12C6Mn with both HT schedules. In order to obtain this aimed property combination more than 30 vol.-% of retained austenite were necessary as predicted by D. K. Matlock and J. G. Speer [41]. It could be observed that the two-step HT generally obtained higher UTS\*TE containing the same amount of retained austenite.



**Figure 6.23:** UTS\*TE as a function of retained austenite content for a) 0.003C6Mn, b) 0.056C6Mn and c) 0.12C6Mn compared to values found in literature

The same trends were found for the Mn-variation (**Figure 6.24**). For all three steels existed an optimal amount of retained austenite, which resulted in the best product of UTS\*TE. Higher fractions of retained austenite led to a decline of the combination of mechanical properties. The desired mechanical properties of 30.000 MPa% could be achieved only after two-step HT by the steels 0.1C5.7Mn and 0.1C6.4Mn. The two-step HT proved again to affect the mechanical properties positively. By its application better mechanical properties with the same amount of retained austenite could be obtained. As for the steel grades with varying C-content more than 30 vol.-% of retained austenite showed to be prerequisite to gain the desired mechanical properties. [41]

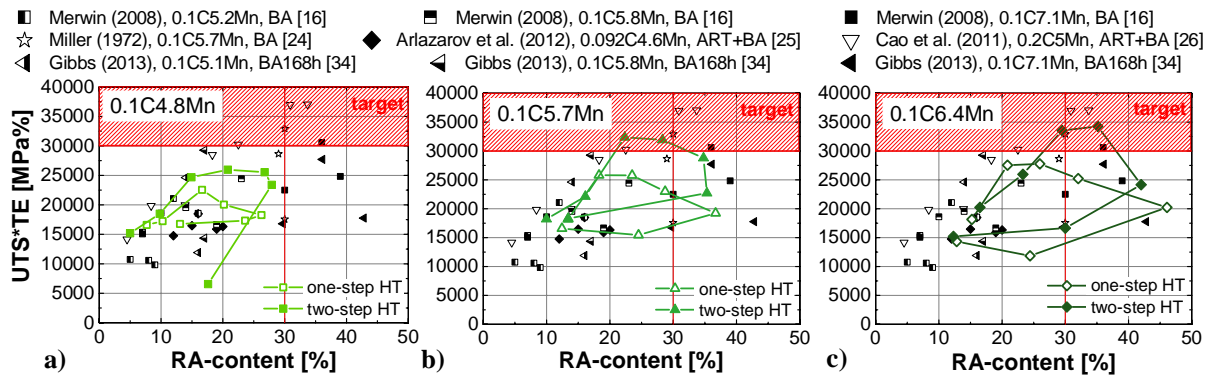


**Figure 6.24:** UTS\*TE as a function of retained austenite content for a) 0.1C4.8Mn, b) 0.1C5.7Mn and c) 0.1C6.4Mn compared to values found in literature

As the group of Medium-Mn-steels represents a new generation of AHSS the comparison of the mechanical properties with those of commercially available 1<sup>st</sup> generation AHSS is essential. **Figure 6.25** displays typical engineering stress-strain curves of an industrially produced DP-, CP- and TRIP-steel with a guaranteed UTS of 800 MPa according to [159] compared to a 0.1C6.4Mn Medium-Mn-steel two-step HT with a UTS exceeding 800 MPa. It is important to mention that the tensile specimen geometry of the 1<sup>st</sup> generation AHSS differed in the gauge length (80 instead of 25 mm). Therefore, the mechanical behavior after necking cannot be compared.

As shown in **Figure 6.25 a)** and **b)** the highest YS was displayed by the CP- and the Medium-Mn-steel grade. Both exhibited YS of about 670 MPa, while the DP- and the TRIP-steel yielded at substantially lower stresses of 515 MPa and 510 MPa respectively. Therefore, the work hardening behavior of the DP- and the TRIP-steel was considerably more pronounced in order to result at UTS 800 MPa. DP-steels with a ferritic-martensitic microstructure are known for high work hardening rates especially at the beginning of straining. [3,160] TRIP-steels offer a similar ratio of YS to UTS, but due to the TRIP-effect the work hardening takes place over a larger strain range, resulting in improved UE. [161,162] Interestingly the Medium-Mn-steel grade, which contains an even larger fraction of metastable austenite transforming into martensite, showed a much higher ratio of YS to UTS. This can most likely be explained by the high stability of retained austenite provided by Medium-Mn-steels with optimal  $k_p$ -values for two-step HT between 10 and 50 compared to  $k_p$ -values published for TRIP-steels of 20 – 388 reported in [76]. For more detailed information see **Chapter 6.4**.

Hence, the Medium-Mn-steel grade resulted in the highest UE and also TE. Further UTS-FS (fracture strength), indicator for the postuniform behavior, is comparatively displayed in **Figure 6.25 b)**. The best value is shown by the CP-steel, which is developed for forming operations with localized deformation *e.g.*: bending. The Medium-Mn-steels exhibited a UTS-FS comparable with the DP-steel, which can be considered as an acceptable standard. The TRIP-steel exhibited the poorest values for UTS-FS. More detailed information on this topic is given in **Chapter 6.5**. By comparing different aspects of the mechanical behavior of Medium-Mn-steels to 1<sup>st</sup> generation AHSS, at constant strength level, significantly improved elongations could be achieved as a consequence of acceptable work hardening and postuniform behavior.



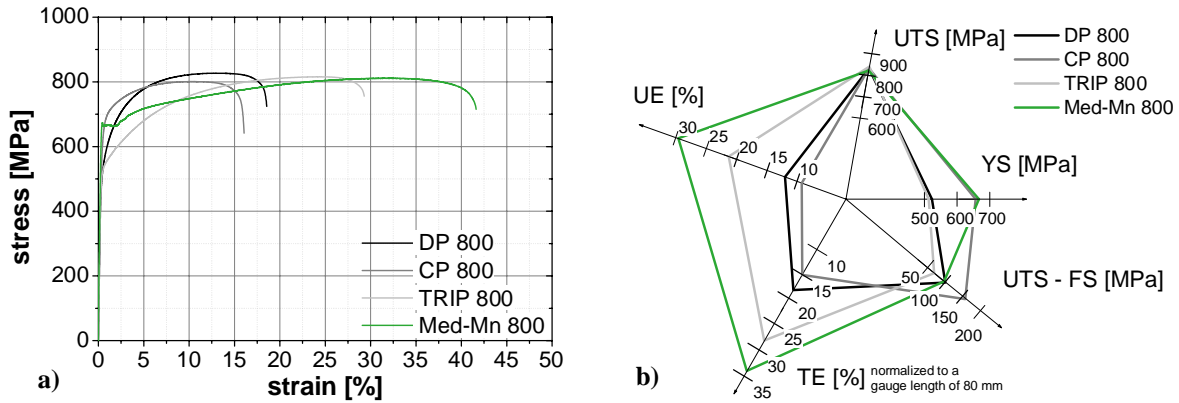


**Figure 6.25:** a) Engineering stress-strain curves of a selected Medium-Mn-steel compared to 1<sup>st</sup> generation AHSS with a tensile stress of 800 MPa and b) comparative diagram of mechanical values of the respective steel grades within the specifications given in [159]

In order to gain an overview of the mechanical properties of all investigated Medium-Mn-chemical compositions compared to 1<sup>st</sup> generation AHSS **Figure 6.26** displays TE (converted to a gauge length of 80 mm) vs. UTS. On the one hand it can be clearly noted that especially the steels 0.12C6Mn and 0.1C6.4Mn could significantly improve the achievable elongations compared to conventional TRIP-steels. On the other hand it becomes obvious that the low C-containing steel 0.003C6Mn as well as the lowest Mn-containing steel 0.1C4.8Mn could not exceed the mechanical properties of 1<sup>st</sup> generation AHSS in terms of UTS vs. TE.

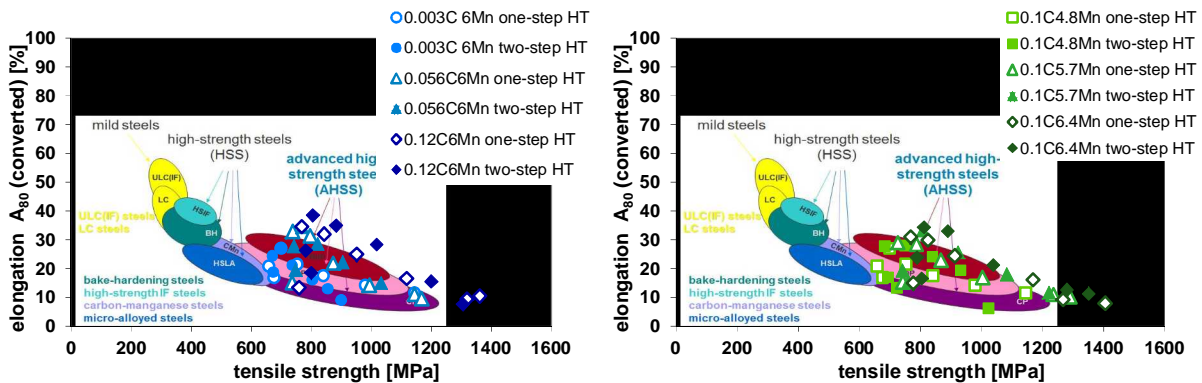


**Figure 6.26:** Comparison of the experimentally determined mechanical properties UTS vs. TE (normalized to a gauge length of 80 mm) with typical values of 1<sup>st</sup> generation AHSS a) C-variation (6 wt-% Mn) and b) Mn-variation (0.1 wt-% C)

**Main conclusions** found concerning the **mechanical behavior:**

- The mechanical behavior is controlled by the microstructure. Therefore, the mechanical properties were strongly influenced by T<sub>IA</sub>. An optimal T<sub>IA</sub> existed for each chemical composition, where maximum UTS\*TE could be achieved.
- In general higher T<sub>IA</sub> led to lower YS (up to minimum at high T<sub>IA</sub>) and increasing UTS. For maximum TE an optimal temperature between 600 and 640 °C depending on the chemical composition was found. It was possible to describe and explain the development of the mechanical properties with existing models known from 1<sup>st</sup> generation AHS multiphase steels (e.g. YS determined by softest phase [148], rule of mixture [156], TRIP-effect [153])

- Mechanical properties of C-Mn alloying concepts with Medium-Mn contents, suitable for a batch annealing route, were published several times in the past. [16,24-28] M. J. Merwin [16] and P. J. Gibbs [28] even presented different Mn-variations and the effect on the mechanical properties. However, this study systematically investigated the effect of varying C- and Mn-content on the mechanical properties and correlated this to the microstructural evolution. Therefore, the influence of altering  $T_{IA}$  as well as the influence of the microstructural evolution during deformation was considered. Both elements showed to substantially increased the achievable  $UTS*TE$ .
- Further the influence of two HT schedules (one-step and two-step) proposed in literature [25,26,46] was displayed and compared precisely for the first time. It was found out, that two-step HT significantly improved of  $UTS*TE$  and significantly shifted the optimal TIA to higher temperatures.
- Compared to 1<sup>st</sup> generation AHSS [159] especially the steels 0.12C6Mn and 0.1C6.4Mn could substantially enhance the achieved  $UTS*TE$ .



### 6.3 Yielding behavior

This chapter engages in detail with the topic of the different yielding behavior of one-step and two-step HT as well as the strong dependency of the YPE on the applied  $T_{IA}$  as shown in **Chapter 5.1.3** and **5.2.3**. The first strong influencing factor on the YPE was found to be the  $T_{IA}$ . With increase of  $T_{IA}$  a strong decrease of the YPE was observed. Secondly, the one-step HT resulted in significantly higher YPE than the two-step HT for all investigated steels. The C-content on the other hand was found to have no evident influence. An increase in the Mn-content showed a slightly increasing tendency on the YPE at constant  $T_{IA}$ . Furthermore the lack of work hardening combined with high TE at low  $T_{IA}$  (not fulfilling the Considère instability criterion) after one-step HT seems to be related to the yielding mode and therefore is also discussed here.

Recently the issue of discontinuous yielding in Medium-Mn steels has been discussed controversially in literature. J. Han *et al.* [46] investigated a 0.05C9Mn steel annealed after hot and cold rolling respectively. Subsequently a one-step annealing (620 °C, 600 s) was applied. The hot rolled material with an initial undeformed martensitic microstructure formed a fine-grained lath-like ferritic/austenitic microstructure which yielded continuously (no YPE could be observed). On the contrary, the cold rolled microstructure resulted in a recovered globular shaped microstructure due to the deformed martensite prior to the intercritical annealing. During tensile testing this material revealed pronounced YPE and limited work hardening. The results of the comparison of hot and cold rolled material are comparable to the differences found between one-step and two-step HT conducted in this work. J. Han *et al.* [46] claimed that the differences in yielding can be explained by the different mechanical properties of the microstructural constituents of ferrite and austenite. For the hot rolled and intercritically annealed material a low Mn-concentration as well as a rather high dislocation density due to inactive recovery was found in the ferrite. The austenite had a low dislocation density and high C- and Mn-concentration. Therefore, the yield strengths of ferrite and austenite were assumed to be similar and this resulted in a continuous yielding. For the cold rolled and intercritically annealed specimens both the recovered ferrite and the intercritically formed austenite exhibited a low dislocation density. Concerning the chemical enrichment in C and Mn the austenite showed substantial higher contents than the ferrite. Thus, according to the argumentation, the ferrite yielded at considerably lower stresses and resulted in discontinuous yielding. Comparing this with the yielding behavior of DP-steels which consist of two phases that strongly differ concerning their mechanical properties and yield continuously, the given explanation for discontinuous yielding for Medium-Mn does not seem to be correct. The work of H. Luo *et al.* [145] concentrated on the differences between the yielding behavior of one-step and two-step HT for  $t_{IA}$  of 10 min. Just like the findings in this work, their study showed that one-step heat treated specimen showed extensive YPE while the two-step HT resulted in comparably low YPE. It is argued that, as the yielding takes place in the soft ferrite, the mechanisms causing the YPE are determined by the plastic deformation of the ferrite. The one-step HT resulted in a generally coarser microstructure than the two-step HT which is contradictory to the well documented phenomena in ferritic or pearlitic steels that smaller grains cause higher YPE. [97,98] Thus, a different mechanism was presented to give a satisfactory explanation. It is stated that the one-step HT microstructure inherited a relatively large number of carbides which at low  $T_{IA}$  were only partially dissolved and

therefore continuously release C atoms into the surrounding ferrite. As the solubility of C in ferrite at  $T_{IA}$  is higher than at RT, rapid quenching resulted in a supersaturated ferrite. The two-step HT with the initial martensitic microstructure and the smaller grain size offered improved partitioning conditions for the C from the martensite to the intercritically formed austenite. It is concluded that after one-step HT more C was available to form Cottrell atmospheres in the ferrite grains resulting in larger YPE. This work showed basically the same results regarding the YPE but under slightly different conditions. Cooling was performed very slowly and the  $t_{IA}$  was significantly increased which offered much better conditions for C partitioning. Nevertheless one-step HT resulted in higher YPE. Therefore, the given explanation of C supersaturated ferrite at RT seems to be unlikely as well. Just recently J. Han *et al.* [163] published further work dealing with YPE in Medium-Mn-steels and presented an interesting approach explaining the phenomenon in a different way. A double HT was applied consisting of two IA-steps. The first step was conducted at a  $T_{IA} > T_{IAmax}$  that provoked martensite to form during cooling. After this HT step the microstructure consisted of globular ferrite and martensite. The size of the resulting globular ferrite was modified by applying different holding times. The  $T_{IA}$  for the second step was selected such as the athermal martensite decomposed into lath-like ferrite and retained austenite. By varying the holding time (4-22 h) during the first step the grain size of the globular ferrite was considerably altered from a diameter of less than 1 to about 2  $\mu\text{m}$ . The ferrite grain size was found to play a crucial role in causing YPE. When the ferrite grows larger than a critical value the YPE disappeared. Furthermore, J. Han *et al.* [163] found that the YPE was attributed to localized deformation by Lüders band formation.

In order to confirm the correlation between localized deformation and YPE, additional tensile tests were performed and the temperature was monitored simultaneously with an infrared (IR)-camera. Thus, it was possible to track localized deformation by the local development of heat in the specimens represented by an increase of the measured intensity which indicates a rise in the temperature of the sample given by **Equation 6.5**.

$$I = \varepsilon_E \sigma_B T^4. \quad 6.5$$

Here,  $I$  is the intensity,  $\varepsilon_E$  is the emission coefficient,  $\sigma_B$  represents the Stefan-Boltzman constant and  $T$  the absolute temperature.

**Figure 6.27 a)** shows the stress as a function of the testing time for 0.1C6.4Mn one-step HT annealed at 580 °C. As observed in previous measurements the specimen exhibited no work hardening. This stress *vs.* time is correlated with the intensities measured by the IR-camera displayed in **Figure 6.27 b) - g)** in a color scale from blue (low intensity) to red/white (high intensity). The thermographic recordings were scaled individually in order to display the important features of each time frame. Additionally, six measuring points (MP) were selected along the longitudinal axis of the tensile specimen to track heat maxima. The intensity development along these MPs is additionally presented in **Figure 6.27 a)**. By this analysis it became obvious, as displayed in **Figure 6.27 b)**, that two temperature maxima (red) formed at the upper and the lower end of the specimen after about 83 s simultaneously to the yielding of the material. The intensity maximum at MP 6 disappeared very quickly after its formation while the band at MP 1 (**Figure 6.27 c)**) intensified and started to move upwards through the tensile sample. This can be identified by the shift of the maximum from MP 1 to 4 (**Figure**

6.27 d and e). As shown in **Figure 6.27 f)**, at a testing time of about 300 s the band changed its direction or a new band that moved towards the lower end formed. This cannot be clearly distinguished from the obtained data. Finally at  $t = 350,68$  s the specimen fractured (**Figure 6.27 g)** near MP 4 which was accompanied with a strong increase in the measured intensity. The IR-camera revealed that the specimen annealed at  $T_{IA} = 580$  °C one-step HT deformed exclusively by localized deformation until failure of the material. The velocity of the first band  $v_b$  (measured at the highest intensity), that traversed the sample, was determined with 0.142 mm/s. By substituting the velocity of the band  $v_b$  in **Equation 3.11** ( $v_c = 0.025$  mm/s,  $n_L = 1$ ) a YPE of about 17.6% resulted. This correlated with the experimentally determined YPE of about 15 % at rupture (indicated by the massive increase in intensity). The tensile behavior can be described as Type II (discontinuous yielding, Lüders band formation, rupture during propagation of the band) by the categorization made by N. Tsuchida *et al.* [96].

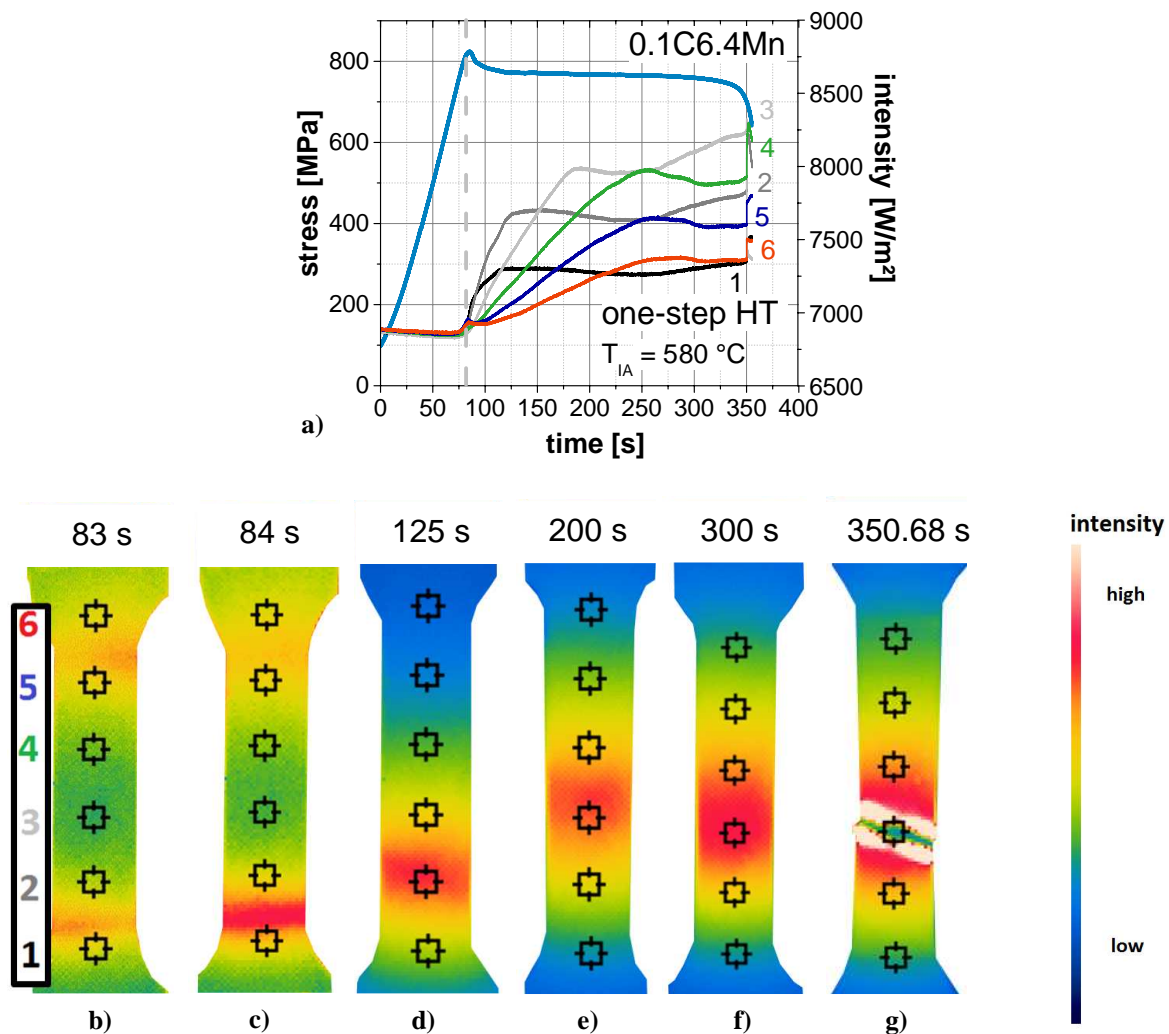


**Figure 6.27:** 0.1C6.4Mn – One-step HT  $T_{IA} = 580$ °C a) stress/intensities by IR vs. time diagram and IR-image recorded at b) 83 s, c) 84 s, d) 125 s, e) 200 s, f) 300 s and g) 350.68 s (colors of the intensities correspond to the numbers next to the measuring points)

Two-step heat treated samples annealed at  $T_{IA} = 580$  °C presented a different tensile behavior with a moderate YPE followed by slight but existing work hardening response (**Figure 6.28 a)** inlay). **Figure 6.28 a)** displays the region of the YPE of the sample in detail. By monitoring the development of the intensities of the single MPs, it can be noted that around a

testing time of 75 s a band formed at the upper end at MP 5 and moved to the lower grip of the tensile machine (**Figure 6.28 b** and **c**). The formation of the band correlated with the yielding of the material. The velocity of the band  $v_b$  was determined with 0.85 mm/s which is considerable higher than for the band observed in the one-step heat treated sample. Here, the comparison of the calculated YPE by **Equation 3.11** of 2.9 % again correlates very well with the experimentally determined YPE of 2.5 %. Finally as the band reached the lower end of the gauge length the intensities started to rise all together homogenously with similar slope. This correlated with the end of YPE and the onset of work hardening. **Figure 6.28 d**) shows that the heat distribution during the homogenous deformation after YPE was not totally even due to the heat conduction to the non-deformed cold grips. These parts attained the lowest temperature and in turn a heterogeneous heat distribution was introduced. The middle of the testing sample had the highest temperature represented by the highest intensity. Thereby, it was indicated that homogenous deformation by dislocation motion took place throughout the whole specimen. The IR-images presented in **Figure 6.28 b) – c)**, which clearly showed the movement of the band and the subsequent homogenous temperature development support this assumption. The stress-strain behavior can be associated with Type III (discontinuous yielding, Lüders deformation, subsequent work hardening) according to N. Tsuchida *et al.* [96].

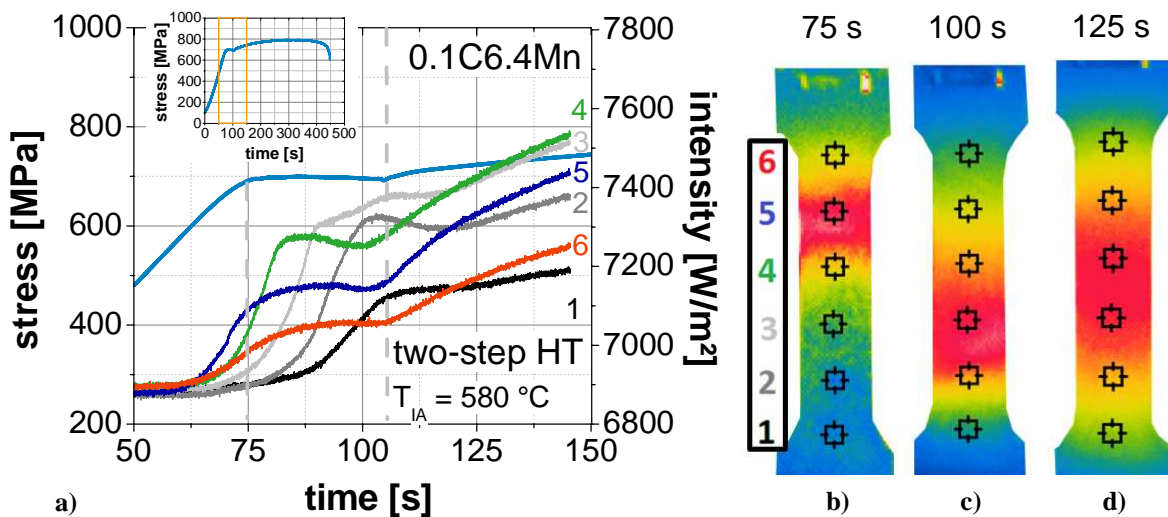


**Figure 6.28:** 0.1C6.4Mn – Two-step HT  $T_{IA} = 580^{\circ}\text{C}$  a) stress/intensities by IR vs. time diagram and IR-image recorded at b) 75 s, c) 100 s and d) 125 s (colors of the intensities correspond to the numbers next to the measuring points)

The results of the investigation of a one-step heat treated sample annealed at  $T_{IA} = 640\text{ }^{\circ}\text{C}$  are depicted in **Figure 6.29**. The material exhibited YPE followed by a substantial work hardening. During YPE a similar behavior of the measured intensities as for the prior presented specimen could be observed. A clear intensity maximum initiated right after yielding, which moved from the upper to the lower end of the sample. **Figure 6.29 b)** presents this maximum as a banded structure across the sample width. At around  $t = 125\text{ s}$  the formation of a second band near MP 3 can be observed in the development of the intensities as well as records of the IR-camera (**Figure 6.29 a** and **c**). At around  $t = 150\text{ s}$  both bands disappeared and the sample started to deform homogenously (**Figure 6.29 d**). Caused by the fact that more than one band moved through the specimen at the same time the applied

method to determine the velocity of the band could not be used. The tensile behavior corresponds to Type III according to [96].

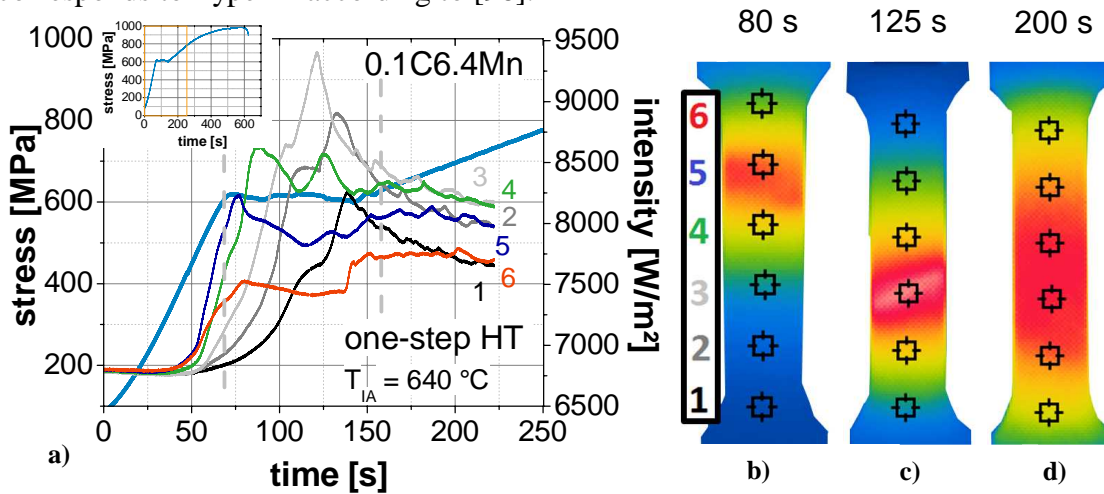


**Figure 6.29:** 0.1C6.4Mn – One-step HT  $T_{IA} = 640^\circ\text{C}$  a) stress/intensities by IR vs. time diagram and IR-image recorded at b) 80 s, c) 125 s and d) 200 s (colors of the intensities correspond to the numbers next to the measuring points)

A similar behavior was found for the two-step HT  $T_{IA} = 640^\circ\text{C}$ . The material first formed out a yield point plateau followed by a considerable work hardening response. The intensities developed a significant maximum that correlates with a band having the highest temperature near MP 4 at  $t = 89$  as displayed in **Figure 6.30 b**). The band moved towards the lower end of the specimen (**Figure 6.30 c**). The increase in intensity of MP 5 at about  $t = 125$  s (**Figure 6.30 a**) implied the formation of a second band that traversed the sample upwards, but it could not be clearly detected by the IR-images. Nevertheless **Figure 6.30 d**) shows that correlating with the end of the YPE the sample started to deform homogenously. As for the one-step heat treated sample presented above, the velocity of the bands could not be properly determined by the existing method caused by the simultaneous existence of two Lüders bands. The stress-strain behavior can be categorized as Type III behavior according to [96].

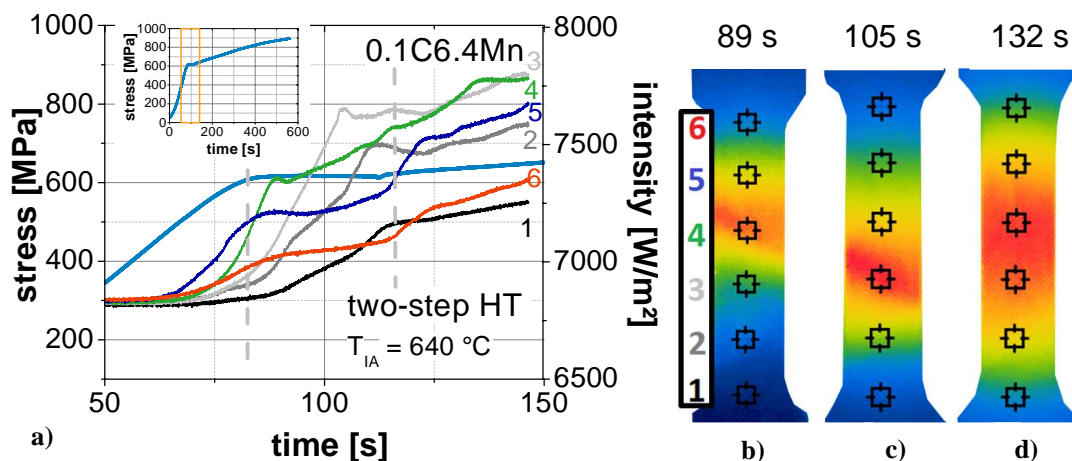


**Figure 6.30:** 0.1C6.4Mn – Two-step HT  $T_{IA} = 640^\circ\text{C}$  a) stress/intensities by IR vs. time diagram and IR-image recorded at b) 89 s, c) 105 s and d) 132 s (colors of the intensities correspond to the numbers next to the measuring points)



An entirely different behavior was shown by the specimens annealed at  $T_{IA} = 680\text{ °C}$ . After annealing at this temperature no YPE could be observed as displayed in **Figure 6.31 a)**. Here, the measured intensities rose constantly for all MPs. The MPs near the grips (MP 1 and 6) were the coldest due to the heat conduction to the colder areas (gripping head, grips). Hence, the MPs in the middle of the gauge length were the hottest spots. Opposed to the samples displaying YPE no localized maximum developed across the width of the sample. This could also be observed in **Figure 6.31 b) – d)** where no bands could be detected across the tensile sample. The stress-strain behavior could be described as Type IV (continuous yielding, no YPE, work hardening) according to [96].

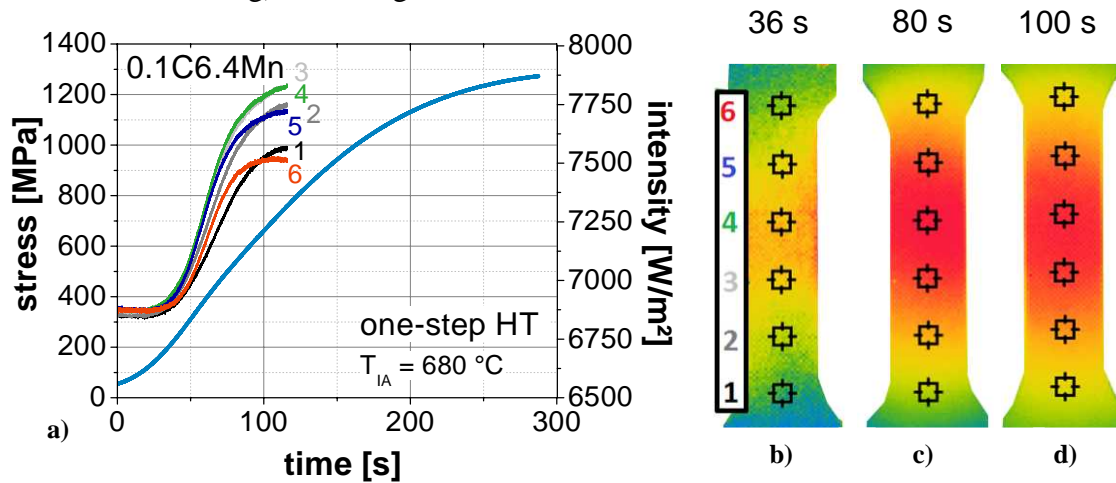


**Figure 6.31:** 0.1C6.4Mn – One-step HT  $T_{IA} = 680\text{ °C}$  a) stress/intensities by IR vs. time diagram and IR-image recorded at b) 36 s, c) 80 s and d) 100 s (colors of the intensities correspond to the numbers next to the measuring points)

The same behavior was found for the two-step HT annealed at  $T_{IA} = 680\text{ °C}$ . **Figure 6.32 a)** depicts the stress as a function of the testing time. The sample showed no YPE. The intensities measured for each single MP rose constantly without any local maximum. The deformation and heat development was homogenously distributed throughout the whole tensile sample (**Figure 6.32 b - c)**. The stress-strain behavior correlated with Type IV according to [96].

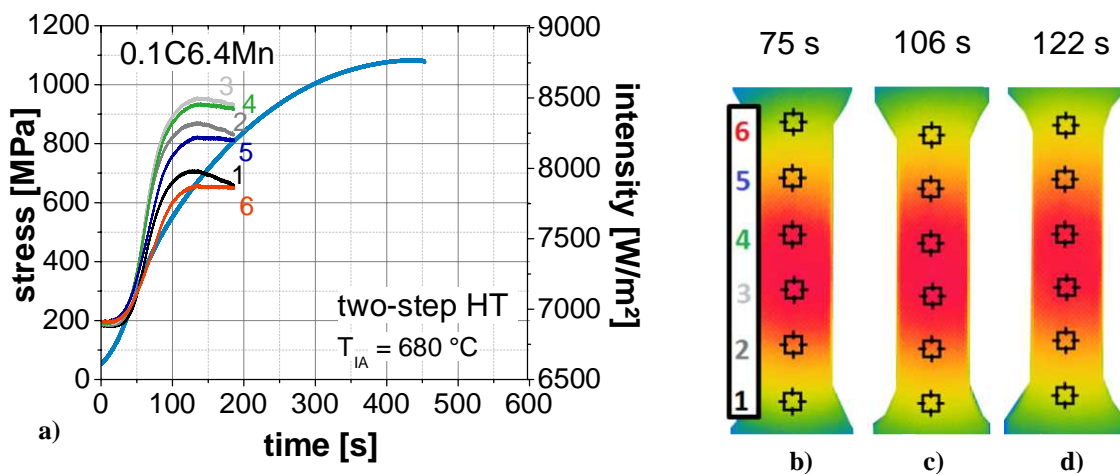


**Figure 6.32:** 0.1C6.4Mn – Two-step HT  $T_{IA} = 680\text{ °C}$  a) stress/intensities by IR vs. time diagram and IR-image recorded at b) 75 s, c) 106 s and d) 122 s (colors of the intensities correspond to the numbers next to the measuring points)

The examination of the heat development during tensile testing *via* IR-camera revealed clearly that low  $T_{IA}$  and one-step HT supported localized deformation by Lüders bands. With increasing  $T_{IA}$  the heterogenous deformation was limited and modified to a homogenous distribution with increasing strain. For microstructures consisting of martensite in the undeformed state no YPE and Lüders band formation was observed. With increasing  $T_{IA}$  the stress-strain behavior transitioned from Type II to Type IV according to the classification made by N. Tsuchida *et al.* [96]. This change in the deformation behavior is associated with a larger grain size.

The further interesting contribution to the topic of YPE was made by E. Emadoddin *et al.* [106] where a correlation between the YPE and the retained austenite in conventional TRIP-steels was made. E. Emadoddin *et al.* [106] found that an increased amount of retained austenite decreased YPE. H. Luo *et al.* [145] further developed this approach for Medium-Mn-steels concluding that not the amount of retained austenite is essential but the amount of intercritically formed austenite. Applying this relationship on the variety of chemical compositions investigated in this work **Figure 6.33** shows that it is essential to distinguish between one-step and two-step HT. The correlation between YPE and intercritically formed austenite was rather low with  $R^2_{one-step} = 0.24$  and  $R^2_{two-step} = 0.2$  respectively over the whole range of chemical compositions. However, comparing each steel isolated the relationship between YPE and fraction of intercritical austenite was considerably more significant ( $R^2$  values right next to the material notation in the legend). The steels exhibited  $R^2$  between 0.24 and 0.997. It can be stated that within one steel grade the relationship between YPE and fraction of intercritically formed austenite was found to be highly significant.

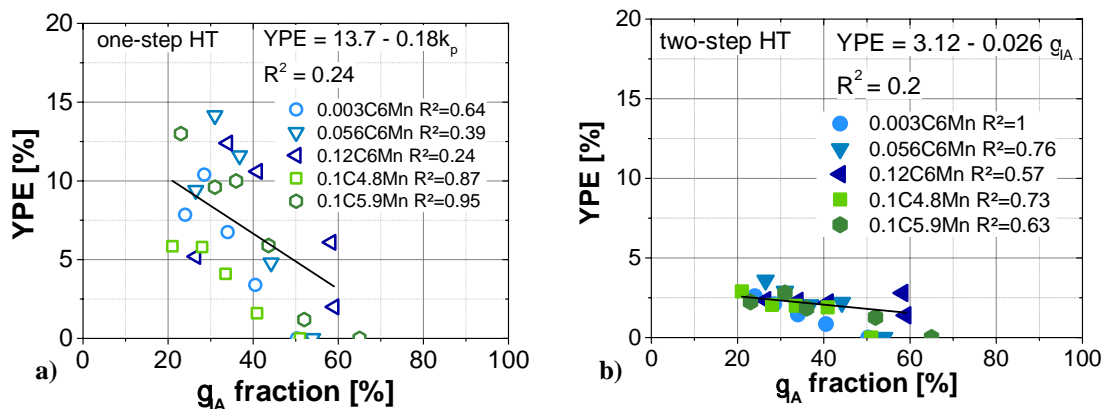


**Figure 6.33:** YPE as a function of the intercritically formed austenite (data taken from TC) for **a)** one-step and **b)** two-step HT

As the amount of intercritical austenite within the same steel is strongly connected to the retained austenite stability (chemical stabilization) it was inevitable to prove whether a correlation between retained austenite stability and YPE existed. Furthermore, J. H. Ryu *et al.* [164] described that a decreasing retained austenite stability strongly suppresses YPE. This seems to be reasonable as Lüders deformation is usually associated with immobile dislocations, commonly explained by the pinning of dislocations by interstitials. The undeformed microstructure of one-step HT specimen was found to have very low dislocation density (see **Figure 5.44**). Furthermore, UFG materials are known to have a low capacity of accommodating dislocations. At the low range of investigated  $T_{IA}$  grain sizes were within the



range of UFG materials ( $< 1 \mu\text{m}$ ). Therefore, the lack of dislocations in the microstructure could have a similar effect on YPE as immobile dislocations pinned by interstitial atoms. The dislocation movement is hindered and heterogeneous deformation is therefore initiated. As soon as the retained austenite transforms into martensite however a massive introduction of dislocations into the microstructure takes place and prevents local deformation by work hardening of this respective area.

In order to confirm this theory the relation between the  $k_p$ -value, which has proven to be a reliable parameter for the retained austenite stability, and the YPE was investigated and displayed in **Figure 6.34** for the C-variation. A linear correlation between the YPE and  $k_p$ -values is supposed. The results confirmed that a higher stability of the retained austenite (lower  $k_p$ -values) resulted in a higher YPE. As observed before, the one-step HT and the two-step HT did not show the same linear function for this relationship. Meaning that a one-step and a two-step heat treated microstructure with equally stabilized retained austenite did not result in the same YPE. The one-step HT led to a significantly higher YPE.

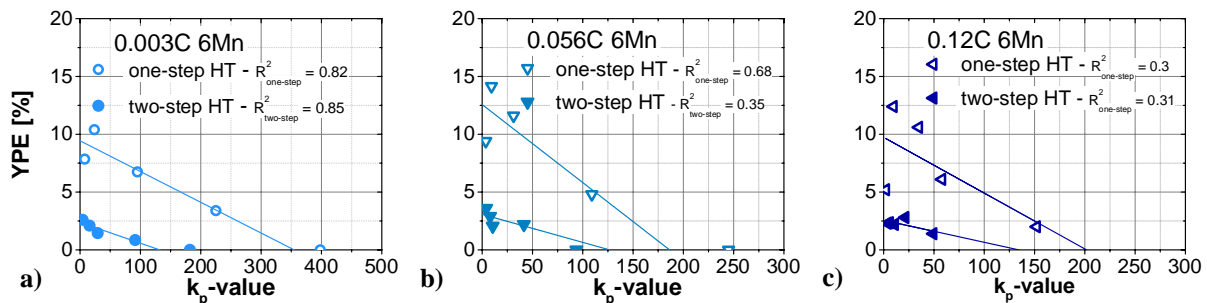


**Figure 6.34:** YPE as a function of  $k_p$ -value for one-step and two-step HT for a) 0.003C6Mn, b) 0.056C6Mn and c) 0.12C6Mn

The same correlation can be seen for the Mn-variation (**Figure 6.34**). According to the findings of the C-variation, linear correlations between YPE and  $k_p$ -values were used to describe the relation. Again a strong dependency on the applied HT schedule was found.

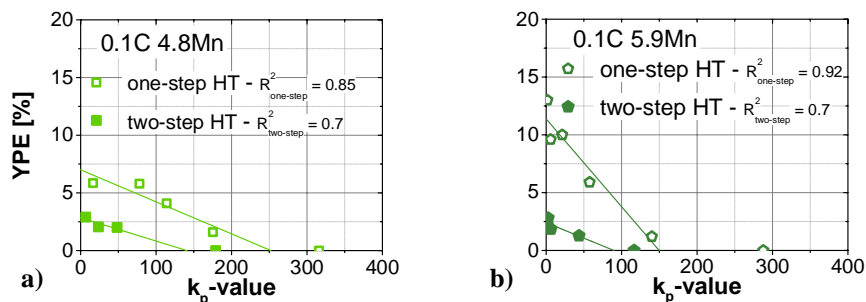


**Figure 6.35:** YPE as a function of  $k_p$ -value for one-step and two-step HT for a) 0.1C4.8Mn and b) 0.1C5.9Mn

Therefore, the YPE as a function of the  $k_p$ -values for the applied HT is presented in **Figure 6.36** for all investigated steels. Independently of the chemical composition significantly higher correlations ( $R^2_{\text{one-step}} = 0.61$  and  $R^2_{\text{two-step}} = 0.54$ ) of the YPE and the  $k_p$ -values could be found than for the correlation with the amount of intercritical austenite. For both HT schedules higher retained austenite stability resulted in a higher YPE following the linear function depicted in **Figure 6.36**. Furthermore, a critical value for  $k_p$  was determined, where no more discontinuous yielding could be observed. For one-step HT this critical value  $k_{pc \text{ one-step}}$  was found to be 220, while for two-step HT the  $k_{pc \text{ two-step}}$  was determined at 127.

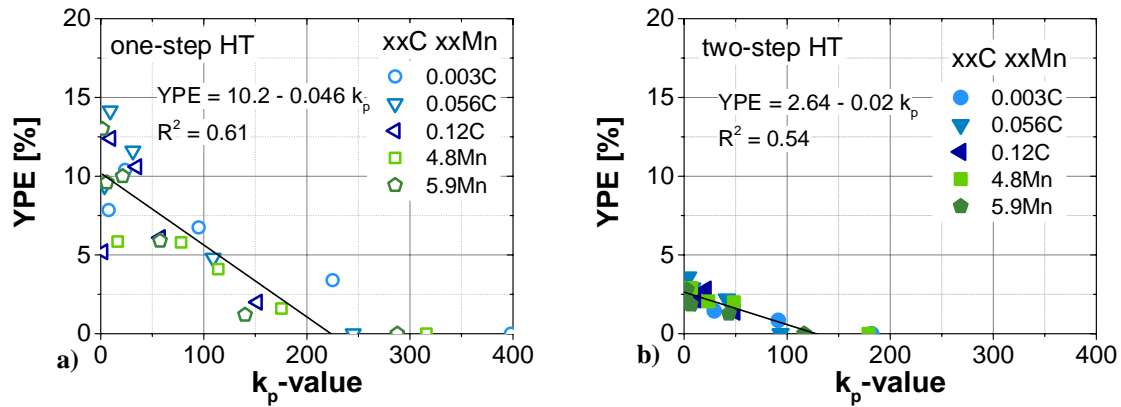


**Figure 6.36:** YPE as a function of  $k_p$ -value for **a)** one-step and **b)** two-step HT

This analysis clearly showed the high importance of the retained austenite stability on the yielding behavior. It also revealed the strong differences in yielding stemming from the HT schedule. The microstructures provoked by the different HT schedules clearly differentiated in grain size, morphology and texture.

To clarify the role of texture, tensile specimens longitudinal and transversal to the rolling direction were used to study the development of the YPE. A thorough investigation of the texture evolution depending on the HT schedule revealed that the one-step HT exhibited a ferrite with a strong  $\gamma$ -fiber texture ( $\langle 111 \rangle \parallel \text{ND}$ ) and a stable austenite with a  $\alpha$ -fiber texture ( $\langle 110 \rangle \parallel \text{ND}$ ) stemming from the cold rolling process, while the grain orientation after FA was evidently more randomized (see **Chapter 5.2.1**). **Figure 6.37 a)** shows the strong influence of the testing direction on the mechanical properties of one-step heat treated specimen at  $T_{\text{IA}} = 580 \text{ }^\circ\text{C}$ . The microstructure consisted of ferrite and stable retained austenite. The transversal specimen showed considerably higher YS compared to the longitudinal ones accompanied by a high LYS-UYS. Subsequently the specimen started to deform by Lüders deformation and fractured at about 5 % of TE. This behavior strongly deviated from the longitudinal direction where the Lüders deformation proceeded and resulted in TE of about 15 % without significant work hardening. The mechanical behavior of the transversal specimen corresponded well with that reported for single phase UFG materials with very limited elongations. [93,96] Comparing the mechanical behavior of the two-step HT in **Figure 6.37 b)** substantial differences can be found. As the material is evidently more isotropic the influence of the testing direction is minimal. Slightly lower YS, lower UYS-LYS and smaller YPE were found for the transversal direction. This investigation clearly revealed that the texture stemming from the cold rolling process strongly promoted the propagation of the Lüders band.

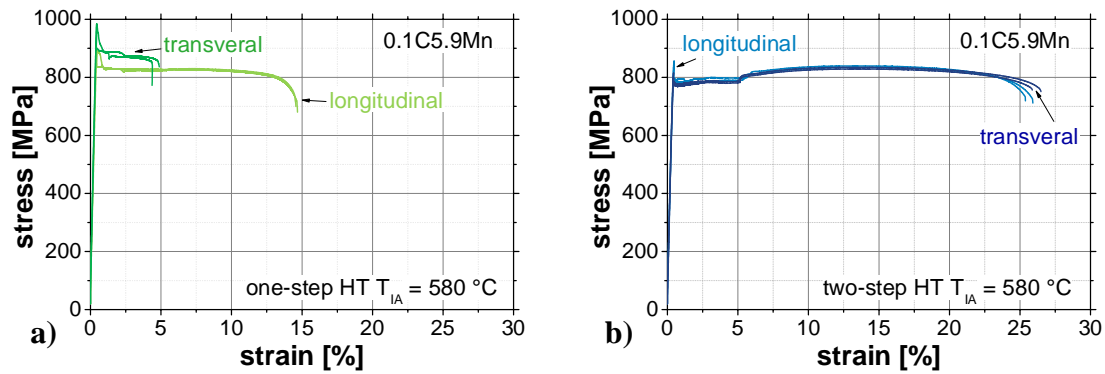


**Figure 6.37:** Engineering stress-strain curves of **a)** one-step and **b)** two-step HT of longitudinal and transversal specimen ( $T_{IA} = 580\text{ °C}$ )

A different correlation between longitudinal and transversal direction was observed when the  $T_{IA}$  was increased to a temperature where pronounced austenite to martensite transformation was ongoing during deformation. For one-step HT **Figure 6.38 a)** depicts that the differences between longitudinal and transversal direction substantially decreased compared to  $T_{IA} = 580\text{ °C}$ . The YS and the UYS-LYS were again significantly higher for the transversal specimen. But opposed to  $T_{IA} = 580\text{ °C}$ , where the TRIP-effect was not active, the specimen started to deform locally until it finally work hardened and deformed homogeneously. At this  $T_{IA}$  even higher YPE could be observed for the transversal than in longitudinal direction. UTS and TE were similar for both tested directions. The decreasing difference in mechanical behavior could be linked to the slightly weaker texture but also to a great extent to the influence of the TRIP-effect. By detailed study of the interrupted tensile tests in **Chapter 5.2.4** it appeared that for this  $T_{IA}$  of  $620\text{ °C}$  martensite formation occurred stress-induced or during YPE. This might have reduced the strong influence of the texture as noted at  $T_{IA} = 580\text{ °C}$ . For two-step HT at  $T_{IA} = 640\text{ °C}$  the mechanical properties were rather similar for specimens longitudinal and transversal to the rolling direction. The microstructure neither exhibited a strong texture nor stable retained austenite.

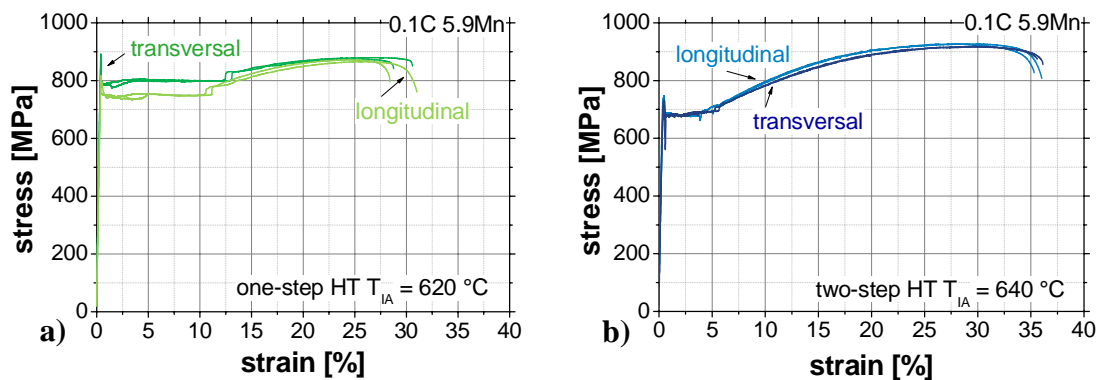


**Figure 6.38:** Engineering stress-strain curves of **a)** one-step HT ( $T_{IA} = 620\text{ °C}$ ) and **b)** two-step HT ( $T_{IA} = 640\text{ °C}$ ) of longitudinal and transversal specimen

The investigation of the anisotropy revealed a strong influence of the texture on the yielding of Medium-Mn-steels. After one-step HT, duplex microstructures with a ferritic matrix (pronounced  $\gamma$ -fiber) and mechanically stable retained austenite ( $\alpha$ -fiber texture) highly promoted Lüders band propagation in longitudinal testing direction (TE up to 15%), while in transversal direction the YPE and TE was considerably reduced. The evidently more

randomized orientation of the two-step heat treated microstructure showed a substantially lower dependency on the testing direction concerning the yielding as well as the remaining mechanical properties as UTS and TE. The impact of texture on the mechanical properties and the YPE decreased with increasing  $T_{IA}$  and the accompanying decreasing retained austenite stability. The different behavior in yielding between one-step and two-step HT on the other hand still remained. Hence, there must be an additional factor influencing the yielding behavior.

An apparent difference in the microstructural characteristics obtained by the different HT cycles was evidently the morphology and the grain size of the respective constituents. Both values were analyzed in detail for the retained austenite *via* quantitative metallography (see **Figure 5.50** and **Figure 5.53**). These differences can likewise be found concerning the ferrite. Microstructural constituents formed during one-step HT had generally a larger grain size and a globular shaped morphology while the two-step heat treated microstructure resulted in smaller ECD and a lath-like morphology. As YPE is associated with small grain sizes [97,98] it seems to be inconsistent that the larger grains of the one-step HT provoked higher YPE.

In order to increase the understanding of the deformation processes going on in one-step and two-step annealed specimens, TEM investigations on deformed samples were performed. Therefore, samples annealed at  $T_{IA} = 580\text{ °C}$  were selected, as this low temperature resulted in the highest differences in the yielding behavior depending on the HT. **Figure 6.39 a)** presents the deformed one-step HT microstructure after 12 % deformation annealed at  $T_{IA} = 580\text{ °C}$ . It can be stated that no significant increase in dislocation density or a significant deformation cell formation could be observed. This is remarkable for a deformation of 12 % and suggests that the investigated area was not deformed at all due to localized deformation which potentially had not approached the present area or that a different deformation mechanisms not relying on dislocation motion as e.g.: grain boundary sliding was responsible for the deformation. Normally this deformation mechanism is associated with creep and does only appear at high homological temperatures [165,166]. For UFG materials, however grain boundary sliding is also considered as deformation mechanism at RT. [92] On the other hand a significant increase in dislocation density as well as cell formation could be observed for the lath-like microstructure of the two-step HT (**Figure 6.39 b)**.

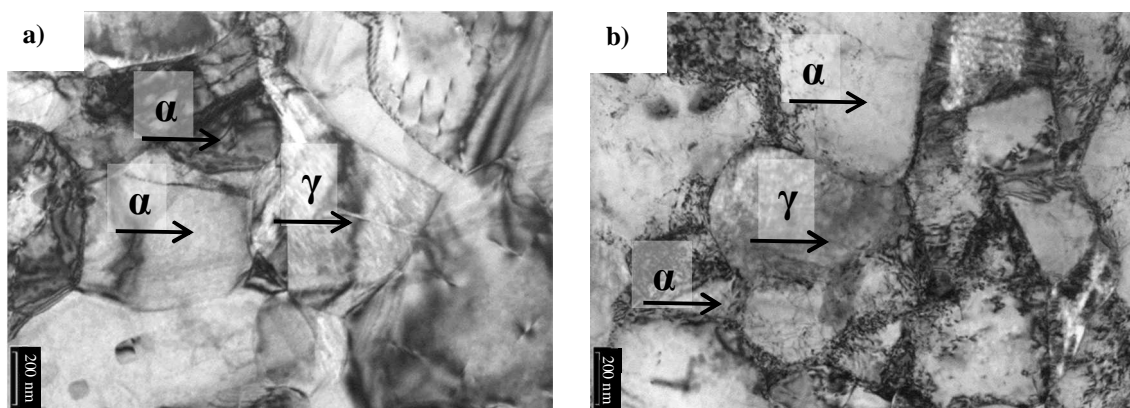


**Figure 6.39:** TEM investigations of a) one-step and b) two-step HT after 12% of deformation ( $T_{IA} = 580\text{ °C}$ )

The results of the TEM investigations combined with the results of the observation obtained by IR-analysis and the texture measurements led to a model which is schematically illustrated

in **Figure 6.40**. It was reported in several studies that small grains are geometrically incapable of accommodating deformation cells and therefore work hardening is limited. [89,90,167] A limited work hardening capacity propagates the formation of localized deformation as for example Lüders bands. [99] This seems to be conflicting with the results obtained in this work. The one-step HT samples with larger grain size showed extensive Lüders deformation and no deformation cell formation in TEM. But when keeping in mind that the grains after both HT schedules especially at low  $T_{IA}$  were extremely fine the importance of the different morphology as well as texture has to be considered. As **Figure 6.40** displays, the lath-like microstructure may be smaller if the area of the grains is compared but the morphology inherits a strongly elongated direction which as shown by TEM is likely to be capable of accommodating deformation cells or at least a higher dislocation density. Due to the weak texture of the two-step heat treated material, the probability of grains oriented in a way so that deformation cells can appear, is high. On the contrary, for one-step HT microstructure there existed exclusively small, globular and highly textured grains, which were not able to accommodate deformations cells due to their size. For this small grain sizes the absorption of dislocation by grain boundaries is very likely and thereby restricts work hardening. All this factors hinder deformation by homogenous dislocation motion and promote Lüders band formation. The IR-analysis showed that tensile samples that have a very stable retained austenite and small globular grains (low  $T_{IA}$ ) deform entirely *via* localized deformation by Lüders band propagation until fracture.

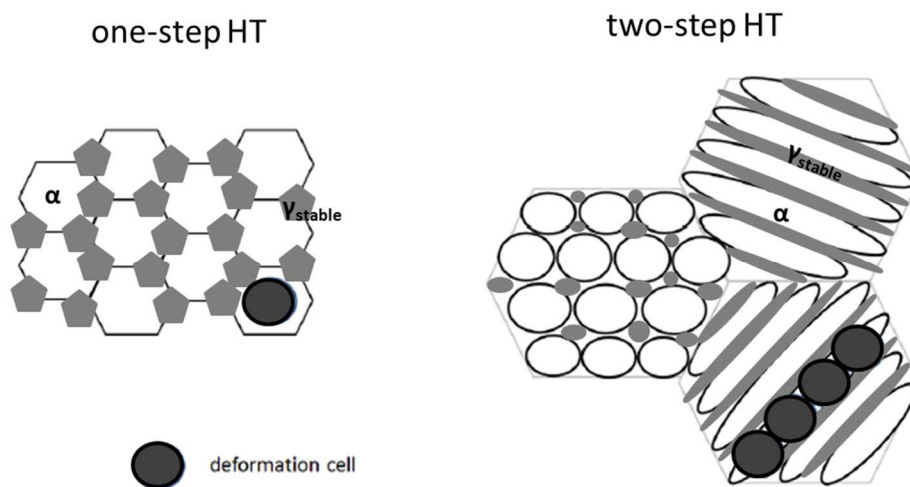


**Figure 6.40:** Schematic illustration of the microstructure after one-step and two-step annealing ( $\alpha$  = ferrite,  $\gamma_{stable}$  = highly stabilized retained austenite) with the formation of deformation cells

In addition, it has to be mentioned that the formation of martensite during deformation or cooling from  $T_{IA}$  to RT also had a strong effect on the YPE. As soon as martensite formed the YPE was strongly reduced. It is reasonable to assume that the hard martensite increased the work hardening behavior and therefore prevented the formation of Lüders bands.

Compared to conventional 1<sup>st</sup> generation AHSS the undeformed microstructure of Medium-Mn-steels has a significant lower density of dislocations. Conventional TRIP-steels contain, besides ferrite and austenite, a considerable amount of ferritic bainite, which is characterized by an enhanced dislocation density. Furthermore, deformation induced austenite to martensite

transformation occurs inducing a number of fresh dislocations in the microstructure. DP- and CP-steels consist of martensite and bainite respectively. Both phases introduce dislocations and an inhomogeneous hardness distribution to the microstructure. Therefore, these steels yield continuously and uniformly. Furthermore, the grain size of Medium-Mn-steels is remarkably smaller compared to 1<sup>st</sup> generation AHSS.

**Main conclusions** found concerning the **yielding behavior**:

- The YPE stemmed from localized deformation by Lüders bands propagation. Low  $T_{IA}$  and one-step HT supported this heterogeneous deformation. The systematic difference between one-step and two-step HT concerning the YPE for various steels and  $T_{IA}$  is shown. This clearly expands the knowledge on this area compared with former studies on this topic [46,145,163].
- A decreasing retained austenite stability ( $k_p$ -value) resulted in a decrease of YPE, as the work hardening is stimulated by strain-induced martensitic transformation. Correlating retained austenite stability and YPE was shown for conventional TRIP-steels [164] before but was not tested for Medium-Mn steels. Furthermore, the highly significant relation between the  $k_p$ -value and the YPE is newly established and can be used to compare different chemical compositions. Moreover, for each HT schedule a critical value for  $k_p$  was determined, where discontinuous yielding disappeared. For one-step HT the  $k_{c \text{ one-step}}$  was at 220, while for two-step HT the  $k_{pc \text{ two-step}}$  was found to be 127.
- Considering the same retained austenite stability, one-step HT exhibited substantial larger YPE than two-step HT. This adds a new aspect towards the understanding of the different yielding behavior after one-step and two-step HT.
- The strong texture of the ferrite ( $\gamma$ -fiber) and the austenite ( $\alpha$ -fiber) observed with the one-step HT promoted the deformation by Lüders propagation in a duplex microstructure consisting of ferrite and stable austenite in specimens longitudinal to the rolling direction. Testing in transversal direction showed only limited elongation and behavior that is commonly known for UFG single phase ferritic steels. The anisotropic behavior of the Lüders band propagation and the strong texture of the microstructure were not studied in any former published work.
- The morphology of the ferrite grains had a large influence on the YPE – despite the smaller ECD the lath-like grains formed after two-step HT allowed a higher accommodation of dislocations than the globular grains of the one-step HT. Therefore, the work hardening was enhanced and YPE was significantly reduced.
- In contrast to 1<sup>st</sup> generation AHSS, which yield continuously, the dislocation density in Medium-Mn-steels after HT was found to be very low as the microstructure consists of recrystallized ferrite, strongly tempered martensite and freshly formed austenite respectively. Furthermore, the grain sizes in Medium-Mn-steels were extremely small. This resulted in a very limited number of dislocations, which were restricted in their mobility.

## 6.4 Work hardening behavior

The work hardening behavior of a material is a crucial factor as it strongly influences the achievable mechanical properties. As a metallic material is deformed, fresh dislocations are generated which, as a result, accumulate and interact with each other. Thus, the dislocation motion is hindered and the stress required for further deformation increases. Considering once more the Considère instability criterion (**Equation 3.1**) it becomes obvious that in order to improve the mechanical properties the work hardening capacity plays an important role. One way to increase the work hardening in single phase materials is to decrease the grain size. As described in **Chapter 3.4** this effect is limited to grain size regimes  $> 30$  nm. [87,88] Further decrease in grain size affects the ability of grains to accommodate dislocations, increases the probability of annihilation of dislocations by grain boundaries and therefore limits their motion and interaction. [86,89,100,101] Another effective way to increase the work hardening behavior besides grain refinement is the introduction of a second phase. The development of DP-steels showed that a dual-phase microstructure consisting of soft ferrite and hard martensite, results in excellent mechanical properties due to high work hardening. Geometrically necessary dislocations are introduced in the microstructure in order to assure a joint plastic deformation of both phases. [168] Furthermore, the important role of metastable retained austenite transforming into martensite on the work hardening behavior was early discovered and described. [50,169,170] The transformation into martensite provides a localized work hardening effect which delays the onset of necking and improves the elongation. If the transformation of austenite into martensite takes place continuously over a large strain regime the TRIP-effect can positively contribute to increasing UE. Hence, the stability of the retained austenite against transformation induced by deformation is a crucial factor in terms of adequate work hardening. In this work a detailed examination of the work-hardening behavior combined with the investigation of the microstructural evolution have therefore been executed.

The variation of  $T_{IA}$  was found to alter the work hardening behavior of Medium-Mn-steels considerably. As displayed in **Figure 5.66** higher  $T_{IA}$  led to increased work hardening. The one-step HT annealed at a  $T_{IA} = 580$  °C resulted in a stress-strain behavior that did not fulfill the Considère instability criterion. It was shown in **Chapter 6.3** that this sample only deformed localized by Lüders band propagation. Hence, the analysis was not valid for this kind of deformation and an UE did not exist for this type of stress-strain behavior (Type II according to [96]). In this chapter, it will be shown that an optimum of work hardening exists in order to achieve maximum UE.

In order to correlate the work hardening behavior with the microstructural constituents present after annealing at the respective  $T_{IA}$ , phase fraction diagrams before and after deformation were exemplarily determined for the steel 0.1C5.9Mn (**Figure 6.41**). The phase fraction diagram revealed that after annealing at low  $T_{IA}$  the retained austenite was too stable to transform into martensite. As the initial microstructure consisted of UFG ferrite and austenite the work hardening capacity was rather low. Increasing the  $T_{IA}$ , the amount of transformed austenite steadily rose. The highest amount of transformed austenite ( $\sim 30$  vol.-%) was found for  $T_{IA} = 660$  °C where the maximal fraction of austenite was retained to RT. At  $T_{IA} \geq 680$  °C athermal martensite additionally increased the amount of martensite after deformation.



However, due to the decreasing amount of  $\gamma \rightarrow \alpha'$  transformation and a steadily more homogenous hardness distribution caused by a dominant martensite fraction, the work hardening became limited again.

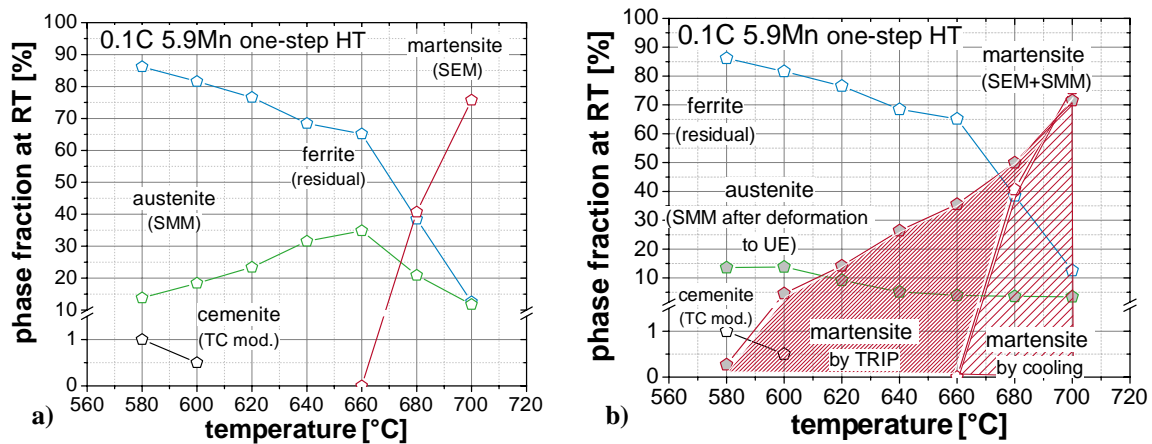
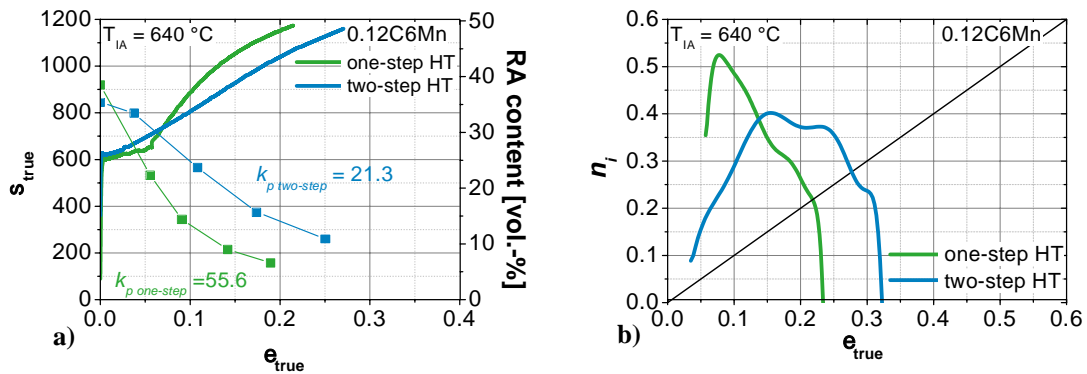


Figure 6.41: 0.1C5.9Mn - Phase fraction diagram a) undeformed and b) after deformation to UE for one-step HT

The phase fraction diagrams after one-step and two-step HT (see **Figure 5.55** and **Figure 5.57**) did not reveal any significant differences between each other but the work hardening behavior as well as the mechanical properties (see **Figure 6.20** and **Figure 6.21**) differed considerably. Concerning the work hardening the two-step HT showed a more moderate behavior that finally resulted in higher elongations which increased the product of UTS\*TE. As outlined before, the strain-induced martensitic transformation has quite a strong impact on the work hardening behavior. As shown in detail in **Chapter 5.2.4**, the two-step HT resulted in considerably more stable austenite than the one-step HT indicated by lower  $k_p$ -values. **Figure 6.42 a)** presents typical stress-strain curves for 0.12C6Mn annealed at 640 °C after one-step and two-step annealing. The two-step annealing exhibited substantially higher UE and TE. Corresponding to the tensile curves the development of the retained austenite content for both HT schedules is displayed. Starting from a similar initial value of  $V_{\gamma 0one-step} = 38$  vol.-% and  $V_{\gamma 0two-step} = 35$  vol.-% the austenite of the one-step heat treated sample transformed at evidently smaller strains compared to the two-step HT. This different  $\gamma \rightarrow \alpha'$  transformation behavior was also reflected in the resulting  $n_i$ -values shown in **Figure 6.42 b)**. The trend for the one-step HT depicted a very early maxima at  $\epsilon_{true} < 0.1$  and deteriorated quite quickly afterwards. Comparing this to the transformation of the austenite it can be seen that about two thirds of the austenite were already transformed to martensite at this strain. The main potential of the TRIP-effect was already exploited at this stage. The trend of the  $n_i$ -value showed to be different for the two-step HT. The  $n_i$ -value increased steadily to a maximum at  $\epsilon_{true} \sim 0.15$ . Not even half of the retained austenite has transformed to martensite up to this strain. Therefore, opposed to the one-step HT the  $n_i$ -value decreases moderately and results in an evidently higher uniform elongation to 0.27 compared to 0.22. These differences in the retained austenite stability and the resulting work hardening behavior and mechanical properties could be found for all the investigated steels and T<sub>IA</sub>. The specimen shown in detail in **Figure 6.42** can be considered as a typical example.



**Figure 6.42:** 0.12C6Mn - a) True stress-strain curve and corresponding retained austenite content and b)  $n_i$ -value as function of  $\epsilon_{true}$  for one-step and two-step HT

Evidently there is a difference in the retained austenite stability after one-step and two-step HT. As explained elaborately in **Chapter 3.3**, there are numerous influencing factors on the retained austenite stability. In order to understand the difference between one-step and two-step HT these factors are reviewed individually in the following section.

The most important influencing factor is the chemical stabilization of the retained austenite. Several chemical elements increase the stability of the retained austenite at RT. Thereby, C is well known to have the strongest impact followed by Mn in conventional TRIP-steels. [68,171] In Medium-Mn steels Mn is supposed to play a major role in stabilizing the retained austenite. Therefore, the Mn-content in the retained austenite and the ferrite was measured by EDX in SEM and is presented in **Figure 5.54** for the steels 0.1C4.8Mn and 0.1C6.4Mn. On the one hand, the measurements clearly revealed a highly Mn-enriched austenite (up to 12 wt.-% Mn at low  $T_{IA}$ ) and a Mn-depleted ferrite (average about 3 wt.-% Mn). On the other hand, no significant differences between the one-step and the two-step HT could be found by this analysis. However, it has to be mentioned at this point that it was not possible to quantify the Mn-content within the lath-like retained austenite of the two-step HT caused by its small size. The EDX mapping conducted during TEM investigations displayed in **Figure 6.43** showed the distribution of Mn within the microstructure in more detail but did not allow any exact quantification. Nevertheless the difference in the Mn-content between ferrite and austenite was evident (yellow = high Mn-content, black = low Mn-content). In **Figure 6.43 b)** it appeared as if some austenite grains were containing higher Mn-contents compared to other ones. Due to the additional thickness information obtained by TEM this interpretation was not permissible as the interaction volume might contain information of two phases.

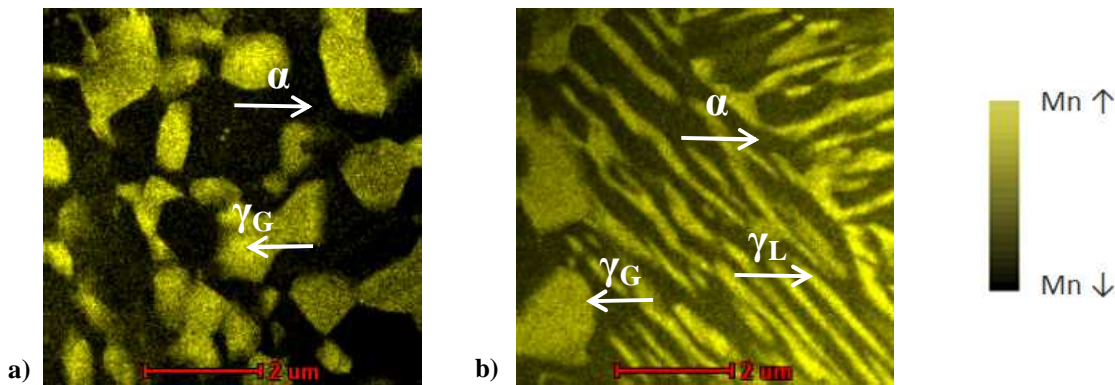


**Figure 6.43:** Mn-distribution in a) one-step HT ( $T_{IA}=620$  °C) and b) two-step HT ( $T_{IA}=640$  °C) by EDX in TEM

**Figure 6.43** shows the Mn distribution obtained by microprobe investigation. Clearly the lateral resolution was not high enough to distinguish between single grains and so it was not possible to differentiate between globular and lath-like austenite. Nevertheless, a heterogeneous Mn distribution within the microstructure could be observed consistent with the EDX analysis. For the two-step heat treated specimen the microscopic substructure appeared finer. Furthermore, no highly banded areas with differentiating Mn-content could be observed.

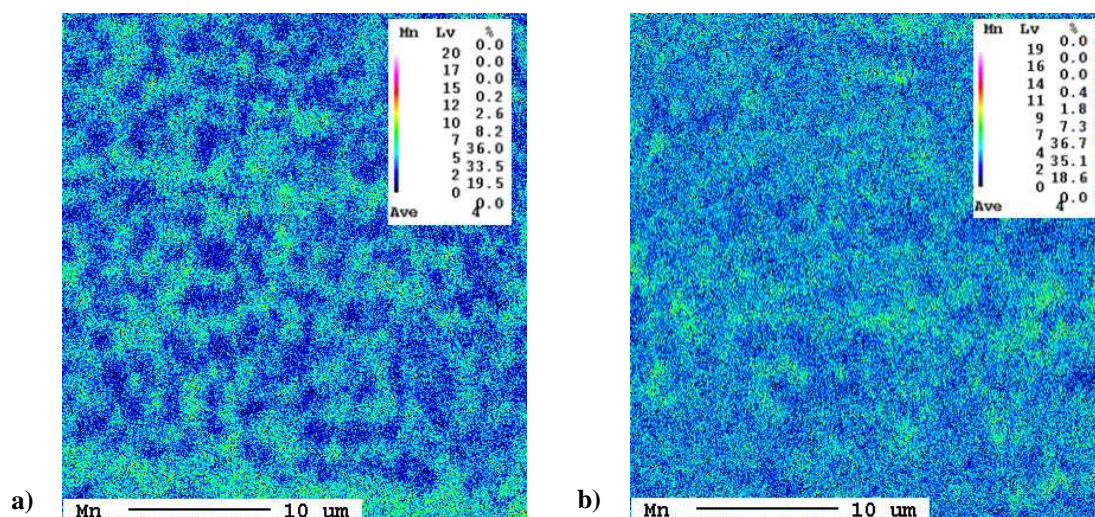


**Figure 6.44:** Mn-distribution in **a)** one-step HT ( $T_{IA}=620\text{ }^{\circ}\text{C}$ ) and **b)** two-step HT ( $T_{IA}=640\text{ }^{\circ}\text{C}$ ) obtained by microprobe analysis

To sum up the results on determining the differences in the chemical composition of one-step and two-step heat treated retained austenite, it was shown to be difficult to precisely analyze the Mn-content in the lath-like austenite. However, the investigations on the globular austenite did not reveal any chemical differences regarding the Mn-content of the austenitic phase. Furthermore, the determined Mn-contents measured by EDX matched with the equilibrium contents calculated by Thermo-Calc<sup>®</sup> (see **Figure 5.54**) it is not reasonable to assume that the lath-like austenite contains even higher Mn-contents. As the Mn-content reached its equilibrium concentration it is presumed that the C-content as well achieved the equilibrium state. This implies that the C-content for one-step and two-step HT respectively should be alike. Hence, it is supposed that regarding the chemical composition no difference between the one-step and the two-step HT existed.

The second important influencing factor on the stability of the retained austenite is the mechanical stabilization *via* grain size and morphology. In several studies it has been shown that smaller austenite grains are more stable against martensite transformation induced by deformation. [60-63] Concerning the morphology just recently investigations on conventional TRIP-steels revealed that a lath-like retained austenite exhibited higher stability compared to globular shaped austenite. [65] Studies on the retained austenite grain size and morphology (see **Figure 5.50** and **Figure 5.51**) clearly depicted substantially smaller and elongated austenite grains for the two-step HT. Both features indicate a higher stability of the austenite stemming from the two-step HT. Concerning the grain size, the difference between the one-step and two-step HT considerably increased with higher  $T_{IA}$ . This fact suggests a high impact of the grain size on the retained austenite stability as the differences in  $k_p$ -values became

evidently more pronounced at higher  $T_{IA}$  as well. The investigations on the morphology of the retained austenite showed that the difference in shape existed up to high  $T_{IA}$  and therefore the lath-like type additionally increased the stability of the two-step heat treated austenite grains.

Furthermore, the strength of the surrounding matrix plays a decisive role on influencing the stability of the retained austenite. A hard matrix can shield the austenite while a soft matrix transfers the applied stresses to the austenite which then transforms more easily. [64-69] No detailed investigation on the strength of the surrounding matrix was made but as it exhibited similar features as the austenite concerning the grain size and morphology, higher strength of the matrix stemming from two-step HT can be assumed. Further at  $T_{IA} = 580$  °C TEM investigations showed a higher dislocation density for the ferritic matrix (tempered martensite) of the two-step HT than for the globular almost dislocation free ferrite of the one-step HT. Although with increasing  $T_{IA}$  this difference disappeared.

Prior studies have noted that the texture influences the stability of the retained austenite. The {200} planes of the austenite orientated with their normal plane parallel to the loading direction were found to have the lowest stability. [68,70] In order to investigate this influencing factor on the retained austenite stability it would be necessary to observe the texture evolution of the microstructure during deformation. This topic was however not included in this study it can only be stated that the one-step HT microstructure which showed austenite with a preferred orientation ( $\alpha$ -fiber component  $\langle 110 \rangle \parallel ND$ ) could be potentially influenced by a destabilizing or even stabilizing effect of texture. For the two-step HT no pronounced texture was found. Therefore it is unlikely that the texture of the austenite plays a significant role in its stabilization unless a substantial texturing would be introduced by deformation. Here, it has to be mentioned that the influence of texture on the stabilization of retained austenite is rather small compared to the influence of the chemical composition, grain size *etc.* [71]

Concluding from all the investigations carried out to determine the differences in retained austenite stability after applying different HT schedules, it can be stated that the mechanical stabilization *via* grain size and morphology of the retained austenite as well as the differences in the strength of the surrounding matrix were identified as the main factors for the increased stability of the retained austenite after two-step HT. This contributed to improved elongations and finally resulted in higher UTS\*TE.

Improved mechanical properties could also be gained by higher alloying in C and Mn-content. As explained in detail in **Chapter 6.1** several factors, such as higher strength of the respective phases, contribute to enhanced mechanical properties. Besides those factors, higher C- and Mn-contents increased the ability of stabilizing the retained austenite chemically. As shown in **Figure 6.45 a)** by comparing the engineering stress-strain curves of steels with altering C-content containing a similar fraction of  $V_{\gamma 0} = 30 \pm 2$  vol.-%, not only higher UTS but also strongly increased TE could be obtained by the steel with the highest C-content. The analysis of the  $n_i$ -value as a function of the  $\epsilon_{true}$  (**Figure 6.45 b)** revealed that the work hardening behavior was substantially altered depending on the chemical composition. While the steel 0.003C6Mn showed a maximum in the  $n_i$ -value at a very low strain, with increasing C-content this maximum was shifted towards larger strains. The increase in the  $n_i$ -value was more moderate and did not exploit at small strains for higher C-contents. Basically this means that



for an increasing amount of C a higher amount of retained austenite could be ideally stabilized.

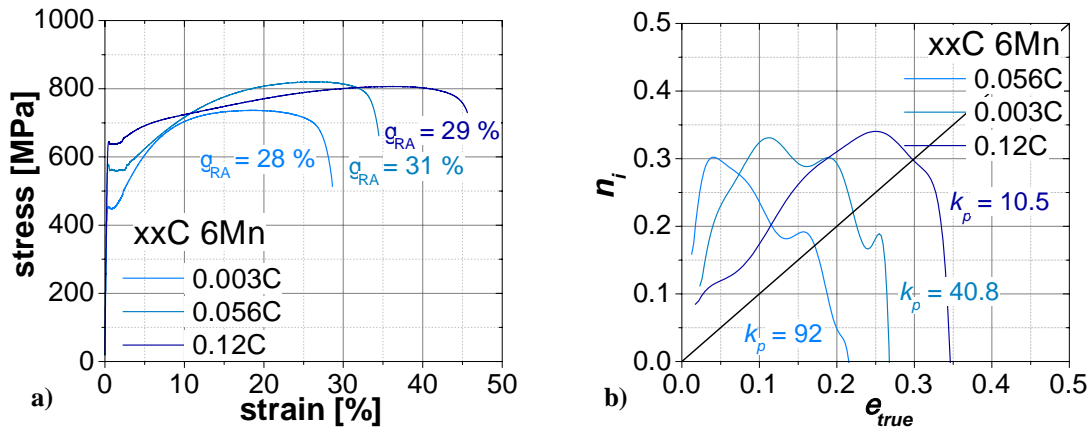


**Figure 6.45:** a) Engineering stress-strain curves for specimen with  $V_{\gamma 0} = 30 \pm 2$  vol.-% and b)  $n_i$  as function of the  $\epsilon_{true}$

This correlation is demonstrated by displaying the  $k_p$ -value as a function of the retained austenite content in **Figure 6.46**. It is evident that for steels with a higher C-content a lower  $k_p$ -value for the same amount of retained austenite was determined. For example for all three steels of the C-variation up to 30 vol.-% of austenite could be retained to RT. Depending on the available C-content and also the applied HT schedule, the  $k_p$ -value varied between 10 and 225. Hence, improved mechanical properties could be obtained due to a higher amount of ideally stabilized retained austenite content with increased C-content.

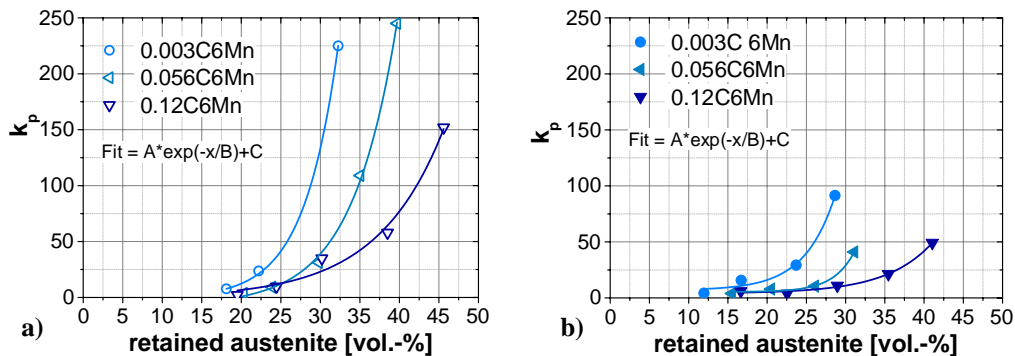


**Figure 6.46:**  $k_p$ -value as a function of the retained austenite content (until maximum value) for a) one-step HT and b) two-step HT (C-variation)

The same analysis was conducted with varying Mn-content (**Figure 6.47**). A similar impact of Mn on the stabilization of the retained austenite could be found. The higher the available Mn-content the higher was the amount of ideally stabilized retained austenite.

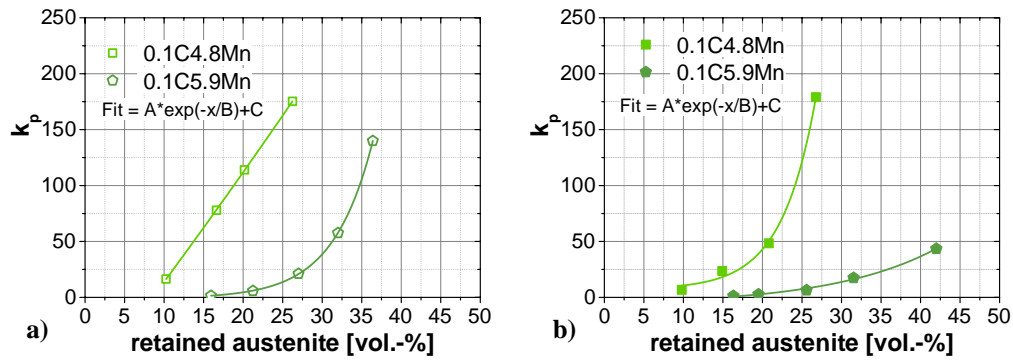


**Figure 6.47:**  $k_p$ -value as a function of the retained austenite content (until maximum value) for **a)** one-step HT and **b)** two-step HT (Mn-variation)

In order to determine whether there is an optimal  $k_p$ -value to obtain the best mechanical properties for all investigated steels, the product of UTS\*TE is displayed as a function of the  $k_p$ -value in **Figure 6.48**. It can be seen that for all investigated steels a maximum of UTS\*TE exists at rather small  $k_p$ -values. For the one-step HT in **Figure 6.48 a)** these optimal values varied between a rather wide range of 5 and 80. There seems to be a trend, that higher C and Mn-contents shift the best properties to smaller  $k_p$ -values. The same trend was observed for the two-step HT (**Figure 6.48 b)**. In this case the optimum values were obtained for  $k_p$ -values between 10 and 50. It was hard to determine if there was a different optimum for each steel and for the respective HT or if the differences were stemming from the selection of the  $T_{IA}$  as mechanical properties were very sensitive to this parameter. Comparing the optimal  $k_p$ -values for Medium-Mn-steels (between 5-80) with those found for conventional TRIP-steels (between 20-388) [76] the retained austenite stability of Medium-Mn-steels seemed to be generally higher (lower  $k_p$ -values).

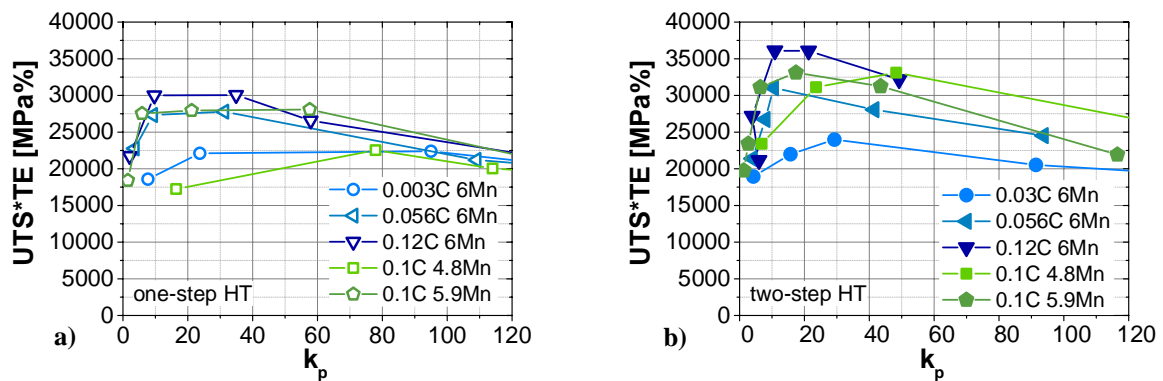


**Figure 6.48:** UTS\*TE as a function of the  $k_p$ -value for **a)** one-step HT and **b)** two-step HT

An important step in order to validate the work hardening behavior of Medium-Mn-steels is the comparison with selected different steel grades. **Figure 6.49** presents the  $n_i$ -value for typical DP-, CP- and TRIP-steels of the 1<sup>st</sup> generation AHSS compared with a Medium-Mn-steel (0.1C6.4Mn two-step HT  $T_{IA} = 640$  °C) all exhibiting a UTS of 800 MPa. The  $n_i$ -value of the DP-steel increased very rapidly to a maximum at small strains. The work hardening potential was exploited very fast as a high hardness difference between soft ferritic matrix and hard martensite inclusions was already present in the initial microstructure. The CP-steel on the other hand showed a very limited work hardening potential over the whole deformation. Several local maxima in the  $n_i$ -value were developed and the  $n_i$ -value increased steadily until

necking. Both steel grades showed low UE of 9 and 12.5 % respectively. The two steel grades containing metastable austenite, the TRIP-steel and the Medium-Mn-steel, both showed a steadily increasing  $n_i$ -value which resulted in a maximum value right before the onset of necking. However, for the Medium-Mn-steel the development of the  $n_i$ -value was even more moderate at small strains and for  $\epsilon_{true} < 0.15$  the  $n_i$ -value of the Medium-Mn-steel was even smaller than for the TRIP-steel. This indicates the very high stability of the present retained austenite. Finally the Medium-Mn-steel achieved a considerably higher UE of about 27 % compared of a UE of 22 % for the TRIP-steel.

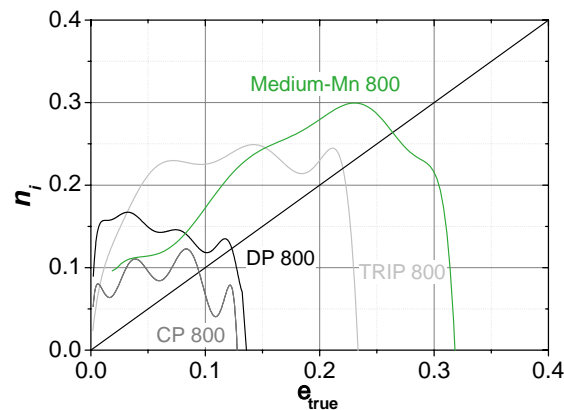


**Figure 6.49:** Incremental  $n$ -value of a selected Medium-Mn-steel compared to 1<sup>st</sup> generation AHSS with a tensile strength of 800 MPa within the specifications given in [159]

#### Main conclusions found concerning the work hardening behavior:

- In order to obtain a maximal UE an optimized work hardening behavior with a  $n_i$ -value that steadily increases over a large strain regime is necessary. [120]
- The results of this study showed that in general the  $n_i$ -value was increased by a coarser microstructure, higher hardness differences within the microstructure and a decreasing retained austenite stability.
- The retained austenite after two-step HT was found to be more stable against transformation into martensite during deformation than after the one-step HT. The main reasons were found to be the smaller grain size and elongated morphology of the austenite as well as the estimated higher strength of the surrounding matrix. This resulted in improved mechanical properties after two-step HT. Studies on conventional TRIP-steels [65] also suggested that lath-like retained austenite is mechanically more stabilized than globular-shaped one. However, the varying retained austenite stability in Medium-Mn steels due to the applied HT and the resulting differences in morphologies have not been investigated before.
- Higher C and Mn-contents of the steel enabled to ideally stabilize higher amounts of retained austenite which resulted in improved mechanical properties. It was clearly shown, that in contrast to conventional TRIP-steels the chemical stabilization was provided to a great extent by Mn-enrichment in the austenite and C was not necessarily required.
- Comparing the work hardening behavior of Medium-Mn-steels with 1<sup>st</sup> generation AHSS steels it appeared to be considerably improved due to a large amount of appropriately stabilized retained austenite.



## 6.5 Damage behavior

The behavior of a material after the onset of necking is a crucial factor for deformation processes with localized deformation *e.g.* bending operations or crash performance. The materials ability of resisting to failure is highly influenced by its microstructure. In **Chapter 3.5** the damage behavior of multiphase steels is described in detail. The most important influencing factors are the homogeneity *e.g.* segregations, the grain size [118,123] and the material's microstructural hardness distribution [109-111]. The latter is a characteristic of multiphase steels as this material group consists of several microstructural constituents with different mechanical properties. When mechanically loaded the individual phases respond differently. For example ferrite deforms at considerably lower stresses than martensite and starts to strain earlier. Therefore, the strain partitioning within the material is not homogenous. Studies [109-111] showed that a more uniform hardness distribution postpones the void formation and subsequent failure of the material. As Medium-Mn-steels are considered to be applied in complex automotive components, the material's response to localized deformation is clearly of great interest. Therefore, the thickness strain  $\varepsilon_3$ , a value that correlates with the reduction of area  $Z$ , the macroscopic and microscopic fracture mode as well as the void appearance was carefully studied.

The thickness strain  $\varepsilon_3$  was determined by measuring the thickness of the fracture surface of the tensile specimen. The  $\varepsilon_3$ -value is a figure highly influenced by the postuniform behavior as it represents the highest deformation the materials sustained prior to fracturing. **Figure 6.50** shows the typical development of  $\varepsilon_3$ -value as a function of  $T_{IA}$ . With increasing  $T_{IA}$  it constantly decreased until it reached a minimum value. Typically this minimum was reached at  $T_{IA} = 680$  °C. Annealing at higher  $T_{IA}$  resulted in a substantial increase of this value. The corresponding microstructural development is schematically shown in **Figure 6.50 a)**. By increasing the  $T_{IA}$  a rising amount of austenite formed and was stabilized to RT. Thermodynamic calculations and EDX measurements showed that with increasing  $T_{IA}$  and thereby increasing amount of retained austenite the C- and Mn-content of the austenite decreased. This suggests that the hardness of the austenite decreases with increasing  $T_{IA}$ , a result which stands in clear contradiction of the development of the  $\varepsilon_3$ -value. A decreasing hardness of the austenite would lead to a decreasing hardness difference between the ferrite and the austenite and therefore the  $\varepsilon_3$ -value is expected to increase. Thus, it was necessary to include the deformed microstructure into consideration. This study showed that the retained austenite stability was strongly depending on the  $T_{IA}$ . With decreasing chemical and mechanical stabilization at higher  $T_{IA}$  the retained austenite stability was strongly reduced. This implies that an increasing amount of austenite in the initial undeformed microstructure transformed into hard martensite. As soon as this fact was considered the decrease of the  $\varepsilon_3$ -value with higher  $T_{IA}$  became apparent. The higher  $T_{IA}$  the harder martensite was formed during the deformation and the hardness distribution became more heterogeneous. As a result, the  $\varepsilon_3$ -value was reduced. By further increase of  $T_{IA}$  the intercritically formed austenite was less chemically enriched. As a consequence martensite formed during cooling to RT. Hence, the initial microstructure contained martensite. The minimum  $\varepsilon_3$ -value was reached when the initial microstructure was made up of around one third of ferrite, austenite and martensite respectively. In this constitution the hardness distribution within the microstructure was

extremely heterogeneous. Furthermore, the existing austenite has extremely low stability and transformed into martensite upon straining very quickly.

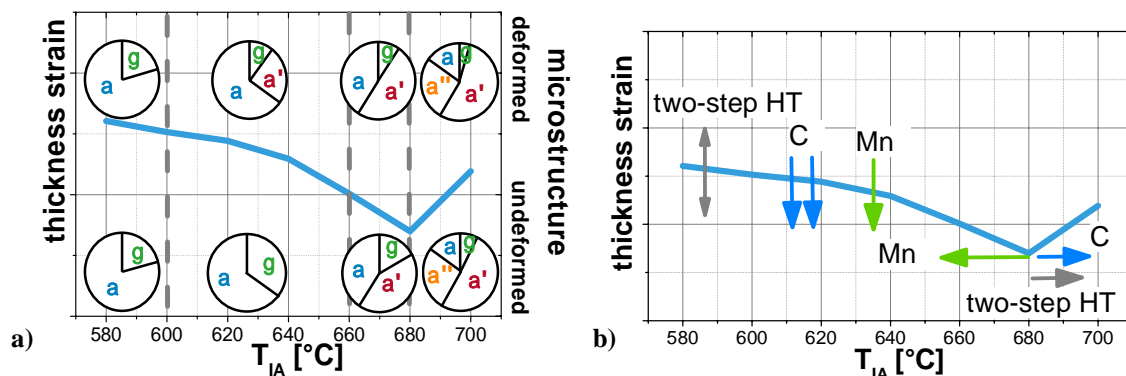


**Figure 6.50:** Schematic illustration of the influence of the a) microstructural composition and b) the applied HT and the C-/Mn-content on the thickness strain  $\epsilon_3$  ( $\gamma$  = austenite,  $\alpha$  = ferrite,  $\alpha'$  = martensite,  $\alpha''$  = tempered martensite)

Interestingly, annealing at very high  $T_{IA}$  (~ 80 vol.-% intercritical austenite) the  $\epsilon_3$ -value increased again. The reason is shown in **Figure 6.51**, which displays the microstructure after annealing at 680 and 700 °C respectively. For 0.1C6.4Mn annealing at 680 °C resulted in hard fresh martensite started to form around 150 °C. Annealing at  $T_{IA} = 700$  °C increased the  $M_s$ -temperature to 230 °C and the athermal martensite was tempered during the slow cooling. This was clearly indicated by the triaxial aligned cementite precipitates displayed in **Figure 6.51 c) and d)**. The tempered martensite has a lower hardness than the fresh martensite and the hardness difference was therefore reduced. Finally, the multiphase characteristics were significantly reduced as the microstructure mainly consisted of fresh and tempered martensite. Both these influencing factors affected the  $\epsilon_3$ -value to rise.

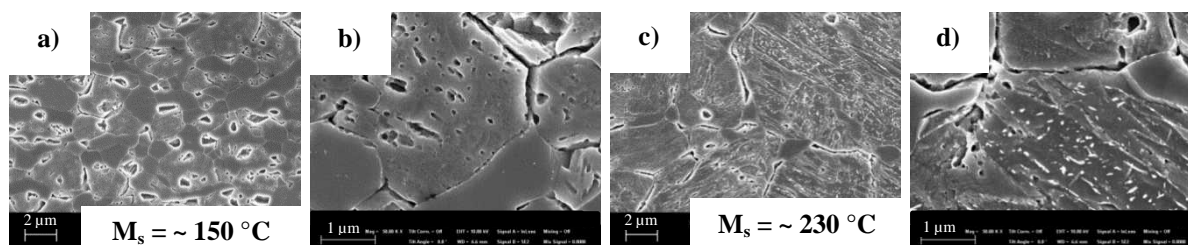


**Figure 6.51:** 0.1C6.4Mn – SEM – Microstructural development after annealing at  $T_{IA}$  of a) and b) 680 °C, c) and d) 700 °C

The influence of the C- and Mn-content as well as the applied HT is presented in **Figure 6.50 b)**. The most important factor of those three was clearly found to be the C-content. Within the investigated C-content of 0.003 and 0.12 wt-% the  $\epsilon_3$ -value varied substantially. The effect of C was most strongly pronounced at the minimum of  $\epsilon_3$ -value. The  $\epsilon_3$ -value for the low C-content was 5-10 times higher than for the highest C-containing steel (see **Figure 5.37**). The influence of the Mn-content was significantly smaller. The reason for this is given in **Figure 5.22**, where the mechanical properties of fully martensitic microstructures of the six investigated chemical compositions are displayed. By far the highest impact on the strength of the martensite has the C-content, while the effect of Mn is clearly detectable but rather small compared to the C-content. The appearance of the minimum was slightly altered by the Mn-content. Mn shifted the  $A_{c3}$ -temperature to lower temperatures and therefore the amount of intercritically formed austenite changed. Thus, higher Mn-content decreased the  $T_{IA}$  where the

minimum appeared. The C-content as well as the two-step HT had a very small impact on this temperature but in contrary to the Mn tended to increase the  $T_{IA}$ , where the minimum existed. Concerning the applied HT schedule no clear trend could be found. The results after applying one-step and two-step HT were rather similar except for the shift of the minimum to higher  $T_{IA}$ .

**Figure 6.52** displays nano-hardness testing of single microstructural constituents of a TRIP-steel. The load-depth curves clearly show the different depth of indentation (**Figure 6.52 b**), while in **Figure 6.52 a**) the resulting hardness values are presented. It can be noted that the hardness decreases in the sequence martensite, austenite, bainite and ferrite. [129] Thereby the aforementioned conclusions are further assured.

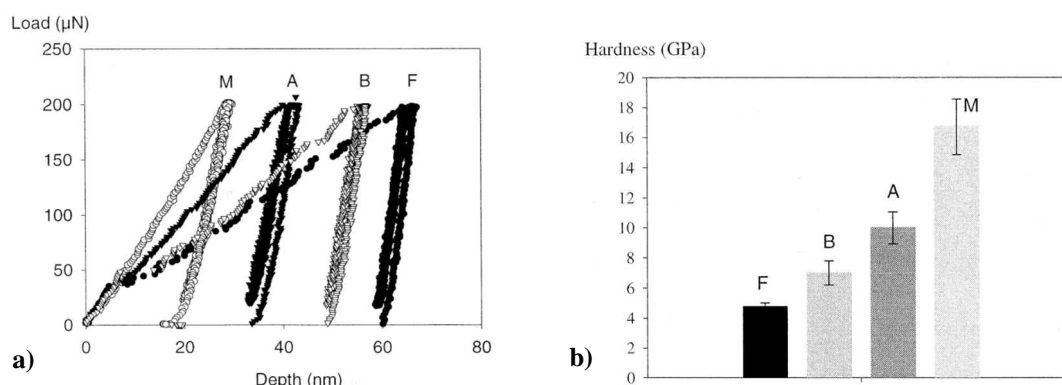


**Figure 6.52:** a) Typical load-depth curves and b) average nano-hardness of respective phases (F – ferrite, B – bainite, A – austenite, M – martensite) in a TRIP-steel [129]

Other useful indicators for the postuniform behavior of a material are the macroscopic and microscopic fracture behavior as well as the void appearance. **Figure 6.53** shows the correlation between these qualitative features and the thickness strain  $\epsilon_3$ . Concerning the macroscopic fracture appearance a transition from a classic cup-cone fracture to the formation of one large shear lip could be observed with decreasing thickness strain. At the lowest measured thickness strain the fracture surface was dominated by brittle fracture. The microscopic fracture indicated the alteration of the  $\epsilon_3$ -value as well. At  $T_{IA}$  where high thickness strain  $\epsilon_3$  was measured (low  $T_{IA}$  – fine structured, high  $T_{IA}$  – coarse structured) combs dominated the fracture appearance. At the minimum  $\epsilon_3$ -value the fracture showed, besides combs, a large amount of smooth, brittle areas. The investigations concerning the initiation sites and appearance of voids revealed that the general knowledge on void formation of multiphase steels [113,117,118,121] can also be applied on Medium-Mn-steels. At low  $T_{IA}$ , where the microstructure contained cementite, the voids formed at the interface of the matrix to the precipitates. With the introduction of the TRIP-effect, and thereby of considerable amounts of martensite into the deformed microstructure, the voids were found at the interfaces ferrite/martensite and martensite/martensite corresponding to TRIP-steels. [122]. Further increase of the  $T_{IA}$  and the formation of athermal martensite, led to martensite cracking and resulted in penny-shaped voids comparable to the behavior of DP-steels. [118] The decrease in martensite hardness due to auto-tempering and the resulting more evenly distributed hardness had a substantial influence on the void appearance. They appeared again at the interface martensite/martensite but were considerably larger than the voids found after annealing at lower  $T_{IA}$ . In conclusion, it can be stated that the results concerning the postuniform and damage behavior provided a clear overall picture. It was found that the

stability of retained austenite and the presence of hard athermal martensite played the most important role governing the overall damage behavior of Medium-Mn-steel. Finally it should be stated that concerning the application of one-step or two-step HT no significant differences in the damage behavior could be detected.

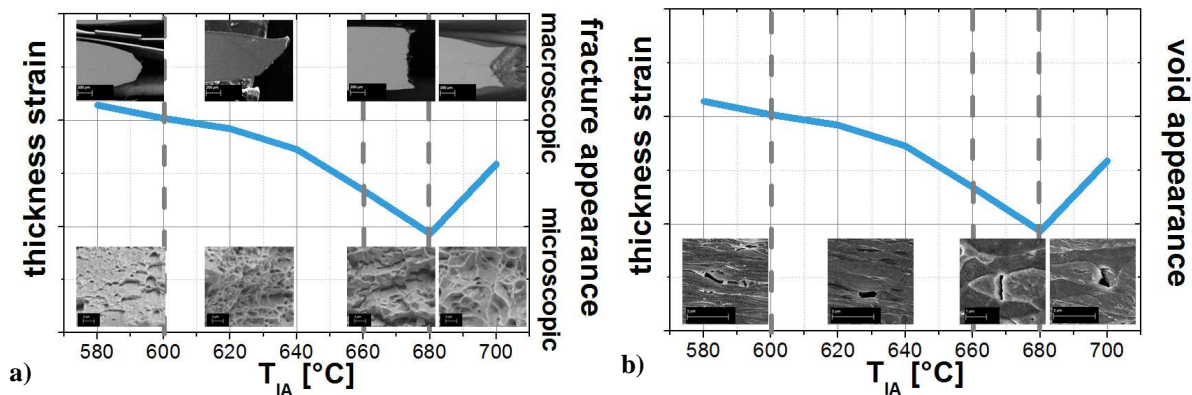


**Figure 6.53:** Development of the thickness strain  $\epsilon_3$  as a function of the  $T_{IA}$  with the corresponding a) macroscopic and microscopic fracture and b) void appearance

According to studies by J. Datsko and C. Yang [126] and T. Nakagawa, and K. Yoshida [127] the thickness strain  $\epsilon_3$  and the reduction of area  $Z$  respectively correspond with the bending behavior and the achievable hole expansion ratio (HER). Both are important characteristics regarding the manufacturing of complex automotive components. Hence, it is of high interest if the targeted mechanical properties obtained by tensile testing met excellent postuniform figures. Therefore, **Figure 6.54** and **Figure 6.55** display the development of  $UTS \cdot TE$  and the thickness strain  $\epsilon_3$  both as a function of  $T_{IA}$ . By comparing these two different material properties it can be noted that at  $T_{IA}$ , where the  $UTS \cdot TE$  reached a maximum (orange rectangle), the thickness strain showed very high values (45-70 %). This is a very promising result towards industrial application. **Figure 6.54** shows the development of the C-variation for one-step HT. Taking the thickness strain  $\epsilon_3$  to the consideration of desired mechanical properties it becomes obvious that a higher C-content clearly improved the mechanical properties concerning  $UTS \cdot TE$  but regarding the postuniform behavior the addition of C had a negative effect. Keeping this fact in mind the use of C should be well-considered in the light of industrial application.

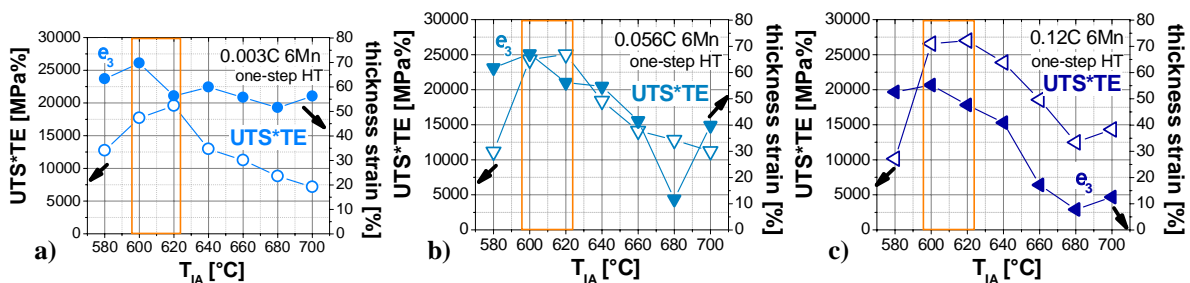


**Figure 6.54:** Development of  $UTS \cdot TE$  and thickness strain  $\epsilon_3$  as a function of  $T_{IA}$  for a) 0.003C6Mn, b) 0.056C6Mn and c) 0.12C6Mn (one-step HT)

Mn, on the other hand, does not show such a detrimental impact on the thickness strain  $\epsilon_3$ , while similar to C enhancing  $UTS \cdot TE$  (**Figure 6.55**). Thus, Mn is the preferential alloying element in order to improve  $UTS \cdot TE$ , while maintaining a rather high level of damage resistance and a good postuniform deformation behavior. It strongly increased the retained

austenite stability but had a considerably smaller impact on the hardness of the forming martensite by final cooling and *via* TRIP-effect respectively compared to C. However, from an economical point of view the increase of C is preferred to the use of Mn, as it is much cheaper concerning the alloying cost. Therefore, the advantages and disadvantages of both alloying elements must be properly considered by the design of the final composition suitable for industrial application.

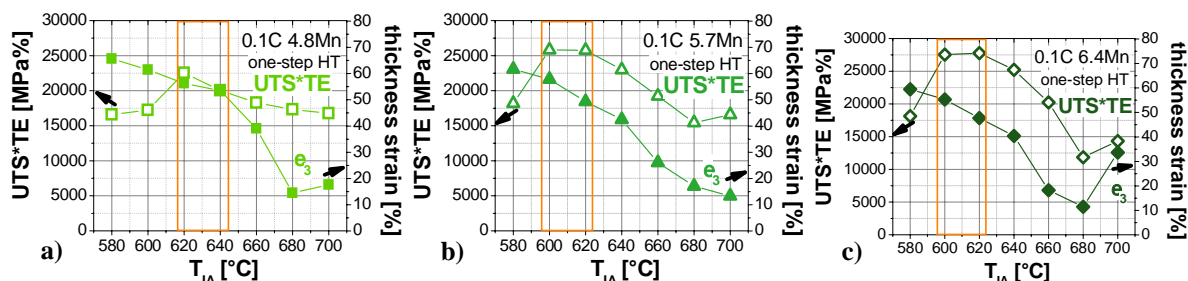


**Figure 6.55:** Development of UTS\*TE and thickness strain  $\epsilon_3$  as a function of  $T_{IA}$  for **a)** 0.1C4.8Mn, **b)** 0.1C5.7Mn and **c)** 0.1C6.4Mn (one-step HT)

### Main conclusions found concerning the damage behavior:

- The investigation of the damage behavior adds a new aspect to the current state of the research of Medium-M steels as up to now no studies on this field have been published.
- The postuniform behavior characterized by the thickness strain  $\epsilon_3$  was strongly influenced by the microstructure and therefore differed substantially with altering  $T_{IA}$ . For all investigated steels, the thickness strain  $\epsilon_3$  was highest at the lower range of investigated  $T_{IA}$ .
- Generally a homogenous hardness distribution is preferential with respect to a favorable damage response. This was also observed with other multiphase steels as DP-, CP- or TRIP-steels. [113,117,118,121] Therefore, pronounced TRIP-effect and the formation of hard athermal martensite decreased the thickness strain and led to brittle macroscopic and microscopic fracture behavior.
- Voids initiated favorably at the interface ferrite/cementite or at the interface of ferrite with TRIP-assisted or athermal martensite. Eventually martensite cracking also appeared.
- Concerning the influence of C and Mn on the fracture behavior, it was found that C strongly declined the thickness strain  $\epsilon_3$ , while the impact of Mn was rather moderate. This is remarkable that low C-contents result in interesting tensile properties combined with an excellent damage behavior. The applied HT schedule showed no significant influence on the postuniform behavior.
- As the thickness strain is known to be representative for bending behavior and hole expansion ratio it is important for industrial application to find a respectable good postuniform performance correlating with the UTS\*TE optimum.

## 7. Summary and Conclusions

The alloying concept of Medium-Mn-steels has been proposed as promising candidate to achieve the targeted properties for 3<sup>rd</sup> generation advanced high strength steels. Production lines *via* batch and continuous annealing have been suggested and interesting mechanical properties were published. This steel group has been developed in order to combine high strength with extraordinary formability to enable the manufacturing of complex automotive body parts that meet the requirements of light weight constructions and state-of-the-art safety requirements.

The present work was designed to determine the influence of the C- and Mn-content and the applied heat treatment schedule on the mechanical properties of Medium-Mn-steels produced by a batch annealing route. Therefore, the C-content was varied between 0.003 and 0.12 wt-% and the Mn-content between 4.8 and 6.4 wt-%. The study on the heat treatment included the influence of an altering intercritical annealing temperature as well as of two different heat treatment schedules. In general, an intercritical annealing, simulating a batch process, was applied (one-step HT). In addition, the effect of a prior full austenitization (two-step HT) was also investigated.

First, the development of the microstructure depending on the intercritical annealing temperature was studied precisely by dilatometry and electron microscopy. It was found that with increasing intercritical annealing temperature the retained austenite content increased up to a maximum. Higher annealing temperatures provoked martensite formation during cooling to RT. This could be supported by thermodynamic calculations and the application of a model for the prediction of the retained austenite content. By establishing a new empirical  $M_s$ -formula for steels with Mn-contents  $\geq 3.5$  wt-% the model could be substantially improved.

Tensile testing of the six different steels revealed that with increasing C- and Mn-content the UTS\*TE was steadily improved. Higher amounts of retained austenite could be stabilized to RT and the strength level of the respective phases increased by solid solution of C and Mn. Moreover, the application of the two-step HT schedule resulted in a further improvement of the UTS\*TE.

Particular attention was paid to the phenomena of extensive yield point elongation. It was found that the characteristic ultra-fine grained microstructure substantially promoted the localized deformation of the material. Therefore, low intercritical annealing temperatures and especially the morphology after one-step HT encouraged large yield point elongations. In order to overcome this potential drawback, the introduction of metastable retained austenite as well as the application of two-step HT, is highly recommended. A correlation to the chemical composition of the steel could not be established.

As the microstructure consists of up to 40 vol.-% of retained austenite, its stability has proven to be a determining factor for the resulting mechanical properties. Therefore, the retained austenite stability against transformation into martensite was precisely studied by interrupted tensile testing. The higher the C- and Mn-content of the steel, the more austenite could be ideally stabilized and thus it could contribute to the improvement of the mechanical properties. Furthermore, it was found that the grain size and morphology of the austenite and the matrix resulting from the two-step HT, significantly enhanced the stability of the retained austenite.

Excellent crash and bendability properties are highly attributed to a material's postuniform behavior and damage response. Hence, these characteristics were precisely investigated by determining the thickness strain after fracture and the macroscopic and microscopic fracture and void appearance. The stability of retained austenite and the presence of hard athermal martensite were determined to play the most important role governing the overall damage behavior. The introduction of martensite caused a strong heterogeneous hardness distribution on a microscopic level, which is detrimental to the targeted damage response. Thus, an increasing C-content, which determines the martensite hardness, strongly declined the postuniform deformation. Fortunately, the best mechanical properties featured satisfactory damage characteristics.

Essentially the most important conclusions can be summarized as follows:

- The steel group of Medium-Mn-steels (C-Mn concepts) can be considered as a promising candidate for future applications in cold-rolled sheet materials as the targeted mechanical properties of  $UTS*TE \geq 30.000 \text{ MPa}\%$  could be achieved. In order to obtain these attributes, C-contents  $\geq 0.056 \text{ wt}\%$  at a constant Mn-content of 6 wt-% and Mn-contents  $\geq 5.7 \text{ wt}\%$  at a constant C-content of 0.1 wt-%, were necessary.
- The influence of C can be considered as highly beneficial concerning the achieved mechanical properties in terms of  $UTS*TE$ . By increasing the C-content more retained austenite could be ideally stabilized and resulted in a moderate work hardening rate over a large strain range. On the other hand, concerning the damage behavior C had proven to be harmful. Furthermore, an increased C-content reduced the intercritical temperature region what in turn diminished the production window.
- Similar to the C-content an increase in Mn improved the mechanical properties concerning  $UTS*TE$ . The retained austenite stability could be substantially increased which enhanced the mechanical properties. On the one hand, opposed to the C-content the influence of Mn on the damage behavior was rather moderate and is therefore to be preferred. On the other hand, the alloying costs increase considerably by extended use of Mn.
- The microstructural constituents at room temperature were substantially altered by changing the intercritical annealing temperature. Therefore, this temperature considerably influenced the resulting mechanical properties.
- Concerning the application of the two-step HT several favored characteristics were featured such as improved  $UTS*TE$ , enlarged production window, decreased yield point elongation and enhanced retained austenite stability. Similar to using an increased amount of Mn, an additional heat treatment step results in higher costs of the final product. Nevertheless, from the abovementioned benefits highlighted in this study it is highly recommended to produce Medium-Mn-steels *via* the introduced two-step HT route.



## 8. Outlook

This thesis provides a broad laboratory scale screening of main factors (C, Mn, intercritical annealing, two-step HT) influencing the mechanical properties of Medium-Mn-steels. Many important conclusions for the industrial production can be drawn from this research work. Nevertheless, the next step towards application has to be an industrial scale production in order to spot potential challenges and also to test laboratory scale developed strategies to overcome certain problems as for example applying two-step HT to reduce pronounced yield point elongation. Furthermore, industrial scale manufacturing would provide material to extensively investigate up to now neglected properties such as weldability, coatability and technological trials concerning formability.

One important step towards industrial production will be to ensure a stable production window during intercritical annealing. Therefore, additional alloying elements e.g.: Si or Al or the important influencing factor of the intercritical holding time should be investigated by laboratory scale testing. Simultaneously, technological ways should be explored to improve the accuracy of the time-temperature regime during production.

Concerning the thermodynamic calculations, further improvement of the model is necessary to improve the accuracy of the predictions. Hence, additional work on the development of the  $M_s$ -formula to higher C- and Mn-contents as well as the integration of e.g.: cooling rate or grain size is recommended.

The current findings add substantially to the understanding of the controversially discussed topic of yield point elongation in Medium-Mn-steels. Nevertheless, in order to confirm the given theory on localized deformation additional TEM investigations are required. A further aspect to this topic would be to thoroughly investigate the role of the texture and free C-content on yield point elongation.

The aspect of retained austenite and the resulting work hardening rate was studied in great detail. But even here, unanswered questions remained as for example the determination of the exact chemical composition of the lath-like austenite could not be detected experimentally by the applied testing methods or the determination of the matrix strength was not conducted by for example nano-indentation.

Concerning the damage behavior the most important question is, if the transferability of the assumptions made, keep up in the case of application e.g.: a crash or hole expansion experiment. As mentioned above in order to clarify this question industrially produced material would be highly beneficial.

## 9. References

- [1] International Council of Clean Transportation, “EU CO<sub>2</sub> standards for passenger cars and light-commercial vehicles,” pp.1–9, 2014.
- [2] McKinsey&Company, “Lightweight, heavy impact,” 2014.
- [3] M. S. Rashid, “Dual Phase Steels,” *Annu. Rev. Mater. Sci.*, vol. 11, pp.245–266, 1981.
- [4] G. R. Speich, V. A. Demarest, and R. L. Miller, “Formation of austenite during intercritical annealing of dual-phase steels,” *Metall. Trans. A.*, vol. 12A, pp.1419–1428, 1981.
- [5] J. Becker, E. Hornbogen, and P. Stratmann, “Dualphasen-Gefüge,” *Int. J. Mater. Res.*, vol. 71, pp.27–31, 1980.
- [6] O. Matsumura, Y. Sakuma, and H. Takechi, “Trip and its kinetic aspects in austempered 0.4C-1.5Si-0.8Mn steel,” *Scr. Metall.*, vol. 21, no. 10, pp.1301–1306, 1987.
- [7] T. Hebesberger, A. Pichler, C. Walch, M. Blaimschein, and K. Spiradek-Hahn, Cold-rolled complex-phase steels: AHSS material with remarkable properties, in: *Int. Conf. Steels Cars Trucks*, Wiesbaden, 2005: pp. 57–64.
- [8] O. Grässel, G. Frommeyer, C. Derder, and H. Hofmann, “Phase Transformations and Mechanical Properties of Fe-Mn-Si-Al TRIP-Steels,” *Le J. Phys. IV.*, vol. 07, no. C5, pp.383–388, 1997.
- [9] G. Frommeyer, U. Brüx, and P. Neumann, “Supra-Ductile and High-Strength Manganese-TRIP / TWIP Steels for High Energy Absorption Purposes,” *ISIJ Int.*, vol. 43, no. 3, pp.438–446, 2003.
- [10] S. Allain, J. P. Chateau, O. Bouaziz, S. Migot, and N. Guelton, “Correlations between the calculated stacking fault energy and the plasticity mechanisms in Fe-Mn-C alloys,” *Mater. Sci. Eng. A.*, vol. 387-389, no. 1-2, pp.158–162, 2004.
- [11] S. Hofer, M. Hartl, G. Schestak, R. Schneider, E. Arenholz, and L. Samek, “Comparison of Austenitic High-Mn-Steels with Different Mn- and C-Contents Regarding their Processing Properties,” *Berg- Und Hüttenmännische Monatshefte.*, vol. 156, pp.99–104, 2011.
- [12] S. Hofer, K. Steineder, R. Schneider, M. Hartl, E. Arenholz, and L. Samek, Effect of annealing parameters on microstructure and mechanical properties of phosphorus alloyed 16%Mn-TWIP steel, in: *Int. Symp. New Dev. AHSS*, Vail, 2013: pp. 105–112
- [13] D. K. Matlock, J. G. Speer, E. De Moor, and P. J. Gibbs, “Recent Developments in Advanced High Strength Sheet Steels for Automotive Applications: an Overview,” *Jestech.*, vol. 15, no. 1, pp.1–12, 2012.
- [14] G. Davies, *Materials for Automobile Bodies*, Elsevier Science, 2012.
- [15] M. J. Merwin, “Low-Carbon Manganese TRIP Steels,” *Mater. Sci. Forum.*, vol. 539-543, pp.4327–4332, 2007.
- [16] M. J. Merwin, “Microstructure and properties of cold rolled and annealed low-carbon manganese TRIP steels,” *Iron Steel Technol.*, vol. 5, no. 10, pp.66–84, 2008.
- [17] K. Sugimoto, T. Iida, J. Sakaguchi, and T. Kashima, “Retained Austenite Characteristics and Tensile Properties in a,” *ISIJ Int.*, vol. 40, no. 9, pp.902–908, 2000.
- [18] H. K. D. H. Bhadeshia, and D. V. Edmonds, “Bainite in silicon steels: new composition–property approach Part 2,” *Met. Sci.*, vol. 17, no. 9, pp.420–425, 1983.
- [19] F. G. Caballero, M. J. Santofimia, C. García-Mateo, J. Chao, and C. G. de Andrés, “Theoretical design and advanced microstructure in super high strength steels,” *Mater. Des.*, vol. 30, no. 6, pp.2077–2083, 2009.
- [20] C. Garcia-Mateo, F. G. Caballero, and H. K. D. H. Bhadeshia, “Acceleration of Low-temperature Bainite,” *ISIJ Int.*, vol. 43, no. 11, pp.1821–1825, 2003.
- [21] E. De Moor, J. G. Speer, D. K. Matlock, J.-H. Kwak, and S.-B. Lee, “Quenching and Partitioning of CMnSi Steels Containing Elevated Manganese Levels,” *Steel Res. Int.*, vol. 83, no. 4, pp.322–327, 2012.
- [22] J. G. Speer, E. De Moor, K. O. Findley, D. K. Matlock, B. C. De Cooman, and D. V. Edmonds, “Analysis of Microstructure Evolution in Quenching and Partitioning Automotive Sheet Steel,” *Metall. Mater. Trans. A.*, vol. 42, no. 12, pp.3591–3601, 2011.
- [23] E. De Moor, P.J. Gibbs, J.G. Speer, and D.K. Matlock, “Strategies for third-generation advanced high-strength steel development,” *AIST Trans.*, vol. 7, no. 3, pp.133–144, 2010.
- [24] R. L. Miller, “Ultrafine-grained microstructures and mechanical properties of alloy steels,” *Metall. Trans.*, vol. 3, pp.905–912, 1972.

- 
- [25] A. Arlazarov, M. Gouné, O. Bouaziz, A. Hazotte, G. Petitgrand, and P. Barges, "Evolution of microstructure and mechanical properties of medium Mn steels during double annealing," *Mater. Sci. Eng. A.*, vol. 542, pp.31–39, 2012.
- [26] W. Cao, J. Shi, C. Wang, L. Xu, M. Wang, and H. Dong, Work hardening behavior of ultrafine grained duplex medium-Mn steels annealed by ART, HMnS 2011.pdf, in: 1st Int. Conf. High Manganese Steel, Seoul, 2011.
- [27] J. Shi, W. Cao, C. Wang, C. Wang, L. Xu, M. Wang, and H. Dong, Lab experiments toward industry trials: Microstructure and Performance of Medium-Mn Steels, in: 1st Int. Conf. High Manganese Steel, Seoul, 2011.
- [28] P. J. Gibbs, Design Considerations for the third Generation Advanced High Strength Steel, PhD-thesis, Colorado School of Mines, 2013.
- [29] D.-W. Suh, S.-J. Park, T.-H. Lee, C.-S. Oh, and S.-J. Kim, "Influence of Al on the Microstructural Evolution and Mechanical Behavior of Low-Carbon, Manganese Transformation-Induced-Plasticity Steel," *Metall. Mater. Trans. A.*, vol. 41, no. 2, pp.397–408, 2010.
- [30] D. W. Suh, J. H. Ryu, M. S. Joo, and H. K. D. H. Bhadeshia, Influence of C and Mn concentration of Mn TRIP steel, in: 4th Int. Conf. Thermomechanical Process. Steels, Sheffield, 2012.
- [31] N. Fonstein, H. J. Jun, O. Yakubovsky, R. Song, and N. Pottore, Evolution of Advanced High Strength Steel (AHSS) to Meet Automotive Challenges, in: Int. Symp. New Dev. AHSS, Vail, 2013.
- [32] S. Lee, K. Lee, and B. C. De Cooman, "Ultra Fine-grained 6wt% Manganese TRIP steel," *Mater. Sci. Forum.*, vol. 654-656, pp.286–289, 2010.
- [33] H. F. Xu, J. Zhao, W. Q. Cao, J. Shi, C. Y. Wang, C. Wang, J. Li., and H. Dong, "Heat treatment effects on the microstructure and mechanical properties of a medium manganese steel (0.2C–5Mn)," *Mater. Sci. Eng. A.*, vol. 532, pp.435–442, 2012.
- [34] P. J. Gibbs, E. De Moor, M. J. Merwin, B. Clausen, J. G. Speer, and D. K. Matlock, "Austenite Stability Effects on Tensile Behavior of Manganese-Enriched-Austenite Transformation-Induced Plasticity Steel," *Metall. Mater. Trans. A.*, vol. 42, no. 12, pp.3691–3702, 2011.
- [35] X. Zhao, Y. Shen, L. Qiu, X. Sun, and L. Zuo, "Effects of Intercritical Annealing Temperature on Mechanical Properties of Fe-7.9Mn-0.14Si-0.05Al-0.07C Steel," *Materials (Basel).*, vol. 7, no. 12, pp.7891–7906, 2014.
- [36] T. Furukawa, H. Huang, and O. Matsumura, "Effects of carbon content on mechanical properties of 5%Mn steels exhibiting transformation induced plasticity," *Mater. Sci. Technol.*, vol. 10, pp.964–969, 1994.
- [37] H. J. Jun, O. Yakubovsky, and N. Fonstein, On stability of retained austenite in medium Mn TRIP steels, in: 1st Int. Conf. High Manganese Steel, Seoul, 2011.
- [38] D. W. Suh, J. H. Ryu, M. S. Joo, H. S. Yang, K. Lee, and H. K. D. H. Bhadeshia, "Medium-Alloy Manganese-Rich Transformation-Induced Plasticity Steels," *Metall. Mater. Trans. A.*, vol. 44, no. 1, pp.286–293, 2013.
- [39] S. Lee, and B. C. De Cooman, "Tensile Behavior of Intercritically Annealed Ultra-Fine Grained 8% Mn Multi-Phase Steel," *Steel Res. Int.*, vol. 86, no. 10, pp.1170–1178, 2015.
- [40] H. Aydin, E. Essadiqi, I.-H. Jung, and S. Yue, Effect of microstructure on the mechanical properties of third generation Advanced High Strength Steels, in: 1st Int. Conf. High Manganese Steel, Seoul, 2011.
- [41] D. K. Matlock, and J. G. Speer, Third Generation of AHSS: Microstructure Design Concepts, in: A. Haldar, S. Suwas, D. Bhattacharjee (Eds.), *Microstructure and Texture in Steels*, Springer, 2009: pp. 185–205.
- [42] A. Arlazarov, M. Gouné, O. Bouaziz, A. Hazotte, and F. Kegel, "Effect of Intercritical Annealing Time on Microstructure and Mechanical Behavior of Advanced Medium Mn Steels," *Mater. Sci. Forum.*, vol. 706-709, pp.2693–2698, 2012.
- [43] S. Lee, S.-J. Lee, and B.C. De Cooman, "Austenite stability of ultrafine-grained transformation-induced plasticity steel with Mn partitioning," *Scr. Mater.*, vol. 65, pp.225–228, 2011.
- [44] J. Lis, and A. K. Lis, "Austenite formation during intercritical annealing," *J. Achiev. Mater. Manuf. Eng.*, vol. 29, no. 1, pp.83–90, 2008.

- 
- [45] C. Wang, J. Shi, C. Y. Wang, W. J. Hui, and M. Q. Wang, "Development of Ultrafine Lamellar Ferrite and Austenite Duplex Structure in 0.2C5Mn Steel during ART-annealing," *ISIJ Int.*, vol. 51, no. 4, pp.651–656, 2011.
- [46] J. Han, S.-J. Lee, J.-G. Jung, and Y.-K. Lee, "The effects of the initial martensite microstructure on the microstructure and tensile properties of intercritically annealed Fe–9Mn–0.05C steel," *Acta Mater.*, vol. 78, pp.369–377, 2014.
- [47] R. Schneider, M. Rahofer, K. Steineder, L. Samek, C. Commenda, and E. Arenholz, "Metallographische Untersuchung von Medium-Mn-Stählen," *Spec. Ed. Pract. Metallogr.* 46, Leoben, 2014: pp. 77–82
- [48] G. E. Totten, and M. A. H. Howes, *Steel Heat Treatment Handbook*, Marcel Dekker, Inc., New York, 1997
- [49] J. Volkmuth, "Werkstoff- und Wärmebehandlungsauswahl für Wälzlager," *Spec.Antriebstechnik.*, no. 2, pp.66–71, 2001.
- [50] V. F. Zackay, E. R. Parker, D. Fahr, and R. Busch, "The enhancement of ductility in high strength steels," *Trans. ASM.*, vol. 60, pp.252–259, 1967.
- [51] K. Sugimoto, N. Usui, M. Kobayashi, and S. Hashimoto, "Effects of Volume Fraction and Stability of TRIP-aided of Retained Austenite on Ductility Dual-phase Steels," *ISIJ Int.*, vol. 32, no. 12, pp.1311–1318, 1992.
- [52] S. Chatterjee, *Transformations in TRIP-assisted Steels: Microstructure and Properties*, PhD-thesis, University of Chambridge, 2006.
- [53] G. B. Olson, and M. Cohen, "A mechanism for the strain-induced nucleation of martensitic transformations," *J. Less Common Met.*, vol. 28, no. 1, pp.107–118, 1972.
- [54] F. Lecroisey, and A. Pineau, "Martensitic transformations induced by plastic deformation in the Fe-Ni-Cr-C system," *Metall. Trans. A.*, vol. 3A, no. 2, pp.391–400, 1972.
- [55] P. L. Mangonon, and G. Thomas, "The martensite phases in 304 stainless steel," *Metall. Trans. B.*, vol. 1, no. 6, pp.1577–1586, 1970.
- [56] B. C. De Cooman, "Structure-properties relationship in TRIP steels containing carbide-free bainite," *Curr. Opin. Solid State Mater. Sci.*, vol. 8, no. 3-4, pp.285–303, 2004.
- [57] H. Schumann, "Umwandlung in austenitischen Mangan-Kohlenstoff-Stählen," *Neue Hütte.*, vol. 17, no. 10, pp.605–609, 1972.
- [58] P. J. Jacques, F. Delannay, and J. Ladrière, "On the influence of interactions between phases on the mechanical stability of retained austenite in transformation-induced plasticity multiphase steels," *Metall. Mater. Trans. A.*, vol. 32, no. 11, pp.2759–2768, 2001.
- [59] S. Zaefferer, J. Ohlert, and W. Bleck, "A study of microstructure, transformation mechanisms and correlation between microstructure and mechanical properties of a low alloyed TRIP steel," *Acta Mater.*, vol. 52, no. 9, pp.2765–2778, 2004.
- [60] A. García-Junceda, C. Capdevila, F. G. Caballero, and C. G. de Andrés, "Dependence of martensite start temperature on fine austenite grain size," *Scr. Mater.*, vol. 58, no. 2, pp.134–137, 2008.
- [61] E. Jimenez-Melero, N. H. van Dijk, L. Zhao, J. Sietsma, S. E. Offerman, J. P. Wright, and S. van der Zwaag, "Martensitic transformation of individual grains in low-alloyed TRIP steels," *Scr. Mater.*, vol. 56, no. 5, pp.421–424, 2007.
- [62] M. Brandt, and G. B. Olson, *Iron Steelmak.*, vol. 20, pp.55–60, 1995.
- [63] J. Wang, and S. van der Zwaag, "Stabilization Mechanisms of Retained Austenite in Transformation-Induced Plasticity Steel," *Metall. Mater. Trans. A.*, vol. 32A, pp.1527–1539, 2001.
- [64] K. Sugimoto, M. Misu, M. Kobayashi, and H. Shirasawa, "Effects of 2<sup>nd</sup> Phase Morphology on Retained Austenite Morphology and Tensile Properties in a Trip-Aided Dual-Phase Steel Sheet," *ISIJ Int.*, vol. 33, no. 7, pp.775–782, 1993.
- [65] J. Chiang, B. Lawrence, J. D. Boyd, and K. Pilkey, "Effect of microstructure on retained austenite stability and work hardening of TRIP steels," *Mater. Sci. Eng. A.*, vol. 528, no. 13-14, pp.4516–4521, 2011.
- [66] I. B. Timokhina, P. D. Hodgson, and E. V. Pereloma, "Effect of microstructure on the stability of retained austenite in transformation-induced-plasticity steels," *Metall. Mater. Trans. A.*, vol. 35A, no. 8, pp.2331–2341, 2004.

- 
- [67] P. J. Jacques, Q. Furnémont, F. Lani, T. Pardoën, and F. Delannay, "Multiscale mechanics of TRIP-assisted multiphase steels: I. Characterization and mechanical testing," *Acta Mater.*, vol. 55, no. 11, pp.3681–3693, 2007.
- [68] R. Blondé, E. Jimenez-Melero, L. Zhao, J. P. Wright, E. Brück, S. van der Zwaag, and N. H. van Dijk., "High-energy X-ray diffraction study on the temperature-dependent mechanical stability of retained austenite in low-alloyed TRIP steels," *Acta Mater.*, vol. 60, no. 2, pp.565–577, 2012.
- [69] S. Cheng, X. L. Wang, Z. Feng, B. Clausen, H. Choo, and P. K. Liaw, "Probing the characteristic deformation behaviors of transformation-induced plasticity steels," *Metall. Mater. Trans. A Phys. Metall. Mater. Sci.*, vol. 39, no. 13, pp.3105–3112, 2008.
- [70] K. Asoo, Y. Tomota, S. Harjo, and Y. Okitsu, "Tensile Behavior of a TRIP-aided Ultra-fine Grained Steel Studied by Neutron Diffraction," *ISIJ Int.*, vol. 51, no. 1, pp.145–150, 2011.
- [71] D. De Knijf, C. Föjler, L. A. I. Kestens, and R. Petrov, "Factors influencing the austenite stability during tensile testing of Quenching and Partitioning steel determined via in-situ Electron Backscatter Diffraction," *Mater. Sci. Eng. A.*, vol. 638, pp.219–227, 2015.
- [72] K.-I. Sugimoto, M. Kobayashi, and S.-I. Hashimoto, "Ductility and strain-induced transformation in a high-strength transformation-induced plasticity-aided dual-phase steel," *Metall. Trans. A.*, vol. 23A, no. 11, pp.3085–3091, 1992.
- [73] G. B. Olson, and M. Cohen, "Kinetics of strain-induced martensitic nucleation," *Metall. Trans. A.*, vol. 6A, no. 4, pp.791–795, 1975.
- [74] D. C. Ludwigson, and J. A. Berger, *J. Iron Steel Inst.*, pp.63–69, 1969.
- [75] L. Samek, E. De Moor, J. Penning, and B. C. De Cooman, "Influence of alloying elements on the kinetics of strain-induced martensitic nucleation in low-alloy, multiphase high-strength steels," *Metall. Mater. Trans. A.*, vol. 37A, no. 1, pp.109–124, 2006.
- [76] D. Krizan, and B. C. De Cooman, "Mechanical properties of TRIP steel microalloyed with Ti," *Metall. Mater. Trans. A.*, vol. 45A, no. 8, pp.3481–3492, 2014.
- [77] E. De Moor, D. K. Matlock, J. G. Speer, and M. J. Merwin, "Austenite stabilization through manganese enrichment," *Scr. Mater.*, vol. 64, no. 2, pp.185–188, 2011.
- [78] D. P. Koistinen, and R. E. Marburger, "A general equation austenite-martensite transformation in pure iron-carbon alloys and plain carbon steels," *Acta Metall.*, vol. 7, pp.59–60, 1959.
- [79] J. Mahieu, B. C. De Cooman, and J. Maki, "Phase transformation and mechanical properties of Si-free CMnAl transformation-induced plasticity-aided steel," *Metall. Mater. Trans. A.*, vol. 33A, no. 8, pp.2573–2580, 2002.
- [80] S.-J. Lee, S. Lee, and B. C. De Cooman, "Martensite transformation of sub-micron retained austenite in ultra-fine grained manganese transformation-induced plasticity steel," *Int. J. Mater. Res.*, vol. 104, no. 5, pp.423–429, 2013.
- [81] M. Umemoto, and W. S. Owen, "Effects of austenitizing temperature and austenite grain size on the formation of athermal martensite in an iron-nickel and an iron-nickel-carbon alloy," *Metall. Trans.*, vol. 5, no. 9, pp.2041–2046, 1974.
- [82] J. R. C. Guimarães, and A. Saavedra, "The mean size of plate martensite: influence of austenite grain size, partitioning, and transformation heterogeneity," *Metall. Trans. A.*, vol. 16, no. 3, pp.329–336, 1985.
- [83] W. B. Morrison, "The effect of grain size on the stress-strain relationship in low-carbon steel," *Trans. ASM.*, vol. 59, pp.824–46, 1966.
- [84] H. Conrad, "Grain size dependence of the plastic deformation kinetics in Cu," *Mater. Sci. Eng. A.*, vol. 341, no. 1-2, pp.216–228, 2003.
- [85] H. Conrad, and K. Jung, "Effect of grain size from millimeters to nanometers on the flow stress and deformation kinetics of Ag," *Mater. Sci. Eng. A.*, vol. 391, no. 1-2, pp.272–284, 2005.
- [86] C. E. Carlton, and P. J. Ferreira, "What is behind the inverse Hall-Petch effect in nanocrystalline materials?," *Acta Mater.*, vol. 55, no. 11, pp.3749–3756, 2007.
- [87] A. H. Chokshi, A. Rosen, J. Karch, and H. Gleiter, "On the validity of the Hall-Petch relationship in nanocrystalline materials," *Scr. Metall.*, vol. 23, pp.1679–1684, 1989
- [88] K. S. Kumar, S. Suresh, M. F. Chisholm, J. A. Horton, and P. Wang, "Deformation of electrodeposited nanocrystalline nickel," *Acta Mater.*, vol. 51, pp.387–405, 2003.

- 
- [89] E. Ma, "Instabilities and ductility of nanocrystalline and ultrafine-grained metals," *Scr. Mater.*, vol. 49, no. 7, pp.663–668, 2003.
- [90] C. C. Koch, "Optimization of strength and ductility in nanocrystalline and ultrafine grained metals," *Scr. Mater.*, vol. 49, no. 7, pp.657–662, 2003.
- [91] Y. M. Wang, and E. Ma, "Three strategies to achieve uniform tensile deformation in a nanostructured metal," *Acta Mater.*, vol. 52, no. 6, pp.1699–1709, 2004.
- [92] R. A. Masumura, P. M. Hazzledine, and C. S. Pande, "Yield stress of fine grained materials," *Acta Mater.*, vol. 46, no. 13, pp.4527–4534, 1998.
- [93] Y. Tomota, A. Narui, and N. Tsuchida, "Tensile behavior of fine-grained steels," *ISIJ Int.*, vol. 48, no. 8, pp.1107–1113, 2008.
- [94] C. Y. Yu, P. W. Kao, and C. P. Chang, "Transition of tensile deformation behaviors in ultrafine-grained aluminum," *Acta Mater.*, vol. 53, no. 15, pp.4019–4028, 2005.
- [95] N. Tsuji, Y. Ito, Y. Saito, and Y. Minamino, "Strength and ductility of ultrafine grained aluminum and iron produced by ARB and annealing," *Scr. Mater.*, vol. 47, no. 12, pp.893–899, 2002.
- [96] N. Tsuchida, H. Masuda, Y. Harada, K. Fukaura, Y. Tomota, and K. Nagai, "Effect of ferrite grain size on tensile deformation behavior of a ferrite-cementite low carbon steel," *Mater. Sci. Eng. A.*, vol. 488, no. 1-2, pp.446–452, 2008.
- [97] J. F. Butler, "Lüders front propagation in low carbon steels," *J. Mech. Phys. Solids.*, vol. 10, no. 4, pp.313–318, 1962.
- [98] N. Tsuchida, Y. Tomota, K. Nagai, and K. Fukaura, "A simple relationship between Lüders elongation and work-hardening rate at lower yield stress," *Scr. Mater.*, vol. 54, no. 1, pp.57–60, 2006.
- [99] B. Jaoul, and D. Gonzalez, "Deformation plastique de monocristaux de fer," *J. Mech. Phys. Solids.*, vol. 9, pp.16–38, 1961.
- [100] A. A. Nazarov, A. E. Romanov, and R. Z. Valiev, "Incorporation model for the spreading of extrinsic grain boundary dislocations," *Scr. Metall. Mater.*, vol. 24, no. 10, pp.1929–1934, 1990.
- [101] K.-T. Park, and D. H. Shin, "Microstructural interpretation of negligible strain-hardening behavior of submicrometer-grained low-carbon steel during tensile deformation," *Metall. Mater. Trans. A.*, vol. 33, no. 3, pp.705–707, 2002.
- [102] A. Vinogradov, "Mechanical Properties of Ultrafine-Grained Metals: New Challenges and Perspectives," *Adv. Eng. Mater.*, vol. 17, no. 12, pp.1710–1722, 2015.
- [103] R. Z. Valiev, and T. G. Langdon, "Principles of equal-channel angular pressing as a processing tool for grain refinement," *Prog. Mater. Sci.*, vol. 51, no. 7, pp.881–981, 2006.
- [104] F. Dalla Torre, R. Lapovok, J. Sandlin, P. F. Thomson, C. H. J. Davies, and E. V. Pereloma, "Microstructures and properties of copper processed by equal channel angular extrusion for 1–16 passes," *Acta Mater.*, vol. 52, no. 16, pp.4819–4832, 2004.
- [105] Y. H. Zhao, X. Z. Liao, S. Cheng, E. Ma, and Y. T. Zhu, "Simultaneously Increasing the Ductility and Strength of Nanostructured Alloys," *Adv. Mater.*, vol. 18, no. 17, pp.2280–2283, 2006.
- [106] E. Emadoddin, A. Akbarzadeh, and G. H. Daneshi, "Correlation between Luder strain and retained austenite in TRIP-assisted cold rolled steel sheets," *Mater. Sci. Eng. A.*, vol. 447, no. 1-2, pp.174–179, 2007.
- [107] R. D. K. Misra, S. Nayak, S. A. Mali, J. S. Shah, M. C. Somani, and L. P. Karjalainen, "Microstructure and Deformation Behavior of Phase-Reversion-Induced Nanograined/Ultrafine-Grained Austenitic Stainless Steel," *Metall. Mater. Trans. A.*, vol. 40, no. 10, pp.2498–2509, 2009.
- [108] P. F. Thomason, *Ductile fracture of Metals*, Pergamon Press, Oxford, 1990.
- [109] A. Karellova, C. Krempaszky, E. Werner, T. Hebesberger, and A. Pichler, Influence of edge condition on the hole expansion property of dual-phase and complex-phase steels, in: *Mater. Sci. Technol.*, Detroit, 2007.
- [110] F. Hisker, R. Thiessen, and T. Heller, "Influence of Microstructure on Damage in Advanced High Strength Steels," *Mater. Sci. Forum.*, vol. 706-709, pp.925–930, 2012.
- [111] M. Kapp, T. Hebesberger, and O. Kolednik, The Deformation Behaviour of Multiphase Steels on the Microscale, in: *2nd Int. Symp. Steel Sci.*, Kyoto, 2009: pp. 1–4.
- [112] X. Sun, K. S. Choi, W. N. Liu, and M. A. Khaleel, "Predicting failure modes and ductility of dual phase steels using plastic strain localization," *Int. J. Plast.*, vol. 25, no. 10, pp.1888–1909, 2009.

- 
- [113] M. Kapp, T. Hebesberger, and O. Kolednik, "A micro-level strain analysis of a high-strength dual-phase steel," *Int. J. Mater. Res.*, vol. 102, no. 6, pp.687–691, 2011.
- [114] E. Y. Kim, H. S. Yang, S. H. Han, J. H. Kwak, and S. H. Choi, "Effect of initial microstructure on strain-stress partitioning and void formation in DP980 steel during uniaxial tension," *Met. Mater. Int.*, vol. 18, no. 4, pp.573–582, 2012.
- [115] J. Kang, Y. Ososkov, J. D. Embury, and D. S. Wilkinson, "Digital image correlation studies for microscopic strain distribution and damage in dual phase steels," *Scr. Mater.*, vol. 56, no. 11, pp.999–1002, 2007.
- [116] P. Uggowither, and H.-P. Stüwe, "Plastizität von ferritisch-martensitischen Zweiphasenstählen," *Zeitschrift Fuer Met. Res. Adv. Tech.*, vol. 73, no. 5, pp.277–285, 1982.
- [117] A. H. Nakagawa, and G. Thomas, "Microstructure-mechanical property relationships of dual-phase steel wire," *Metall. Trans. A.*, vol. 16, no. 5, pp.831–840, 1985.
- [118] Q. Lai, O. Bouaziz, M. Gouné, A. Perlade, Y. Bréchet, and T. Pardoen, "Microstructure refinement of dual-phase steels with 3.5wt% Mn: Influence on plastic and fracture behavior," *Mater. Sci. Eng. A.*, vol. 638, pp.78–89, 2015.
- [119] K. Park, M. Nishiyama, N. Nakada, T. Tsuchiyama, and S. Takaki, "Effect of the martensite distribution on the strain hardening and ductile fracture behaviors in dual-phase steel," *Mater. Sci. Eng. A.*, vol. 604, pp.135–141, 2014.
- [120] F. Spenger, T. Hebesberger, A. Pichler, C. Kremaszky, and E. Werner, AHSS Steel Grades: Strain Hardening and Damage as Material Design Criteria, in: *Int. Conf. New Dev. Adv. High-Strength Sheet Steels*, Orlando, 2008: pp. 39–51.
- [121] G. Lacroix, T. Pardoen, and P. J. Jacques, "The fracture toughness of TRIP-assisted multiphase steels," *Acta Mater.*, vol. 56, no. 15, pp.3900–3913, 2008.
- [122] P. J. Jacques, Q. Furnemont, T. Pardoen, and F. Delannay, "On the role of martensitic transformation on damage and cracking resistance in TRIP-assisted multiphase steels," *Acta Mater.*, vol. 49, pp.139–152, 2001.
- [123] H. Mohrbacher, Advanced Metallurgical Concepts for DP Steels With Improved Formability and Damage Resistance, in: *Int. Symp. New Dev. Adv. High Strength Sheet Steels*, Vail, 2013: pp.319–329
- [124] S. Kalpakjian, and S. Schmid, *Manufacturing Processes for Engineering Materials*, 5<sup>th</sup> ed., Prentice Hall, 2008.
- [125] ASM Handbook Committee, *ASM Handbook Vol. 8 Mechanical Testing and Evaluation*, ASM International, Materials Park, 2000.
- [126] J. Datsko, and C. Yang, "Correlation of bendability of materials with their tensile properties," *Trans. ASME, Ser. B J. Eng. Ind.*, vol. 82, no. 4, pp.309–314, 1960.
- [127] T. Nakagawa, and K. Yoshida, "Improvement in the Deformability of Sheared Edge of Steel Sheets," *Suppl. Trans. ISIJ.*, vol. 11, pp.813–818, 1971.
- [128] J. Angeli, A. C. Kneissl, and E. Füreder, "Ätztechniken für die Phasencharakterisierung von niedriglegierten, hochfesten Mehrphasenstählen," *Pract. Metallogr.*, vol. 10, pp.489–504, 2006.
- [129] Q. Furnémont, M. Kempf, P. J. Jacques, M. Göken, and F. Delannay, "On the measurement of the nanohardness of the constitutive phases of TRIP-assisted multiphase steels," *Mater. Sci. Eng. A.*, vol. 328, no. 1-2, pp.26–32, 2002.
- [130] Technical Report: Vatron GmbH, Restaustenit Magnetjoch - Neue Erkenntnisse und Möglichkeiten, 2009.
- [131] L. Zhao, N. H. van Dijk, E. Brück, J. Sietsma, and S. van der Zwaag, "Magnetic and X-ray diffraction measurements for the determination of retained austenite in TRIP steels," *Mater. Sci. Eng. A.*, vol. 313, no. 1-2, pp.145–152, 2001.
- [132] Technical Report: voestalpine Steel Division GmbH, Probenkatalog - Mikrozugprobe, 2010.
- [133] V. Randle, and O. Engler, *Introduction to Texture Analysis*, Taylor&Francis Ltd, London, 2000.
- [134] S. Suwas, and R. K. Ray, *Representation of Texture*, in: *Crystallogr. Texture Mater.*, Springer-Verlag, London, 2014: pp. 11–38.
- [135] P. Gilormini, "The theory of rate sensitive pencil glide application to rolling texture," *Acta Metall.*, vol. 37, no. 7, pp.2093–2101, 1989.



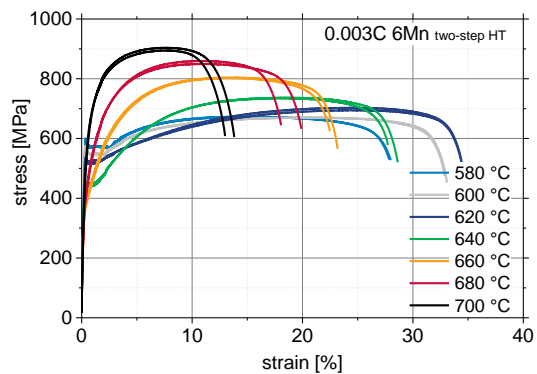
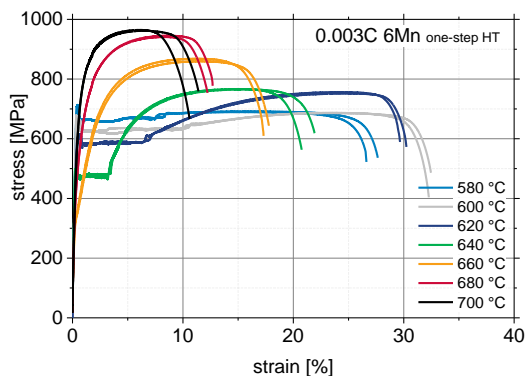
- 
- [136] D. Raabe, and K. Lücke, "Texture and microstructure of hot rolled steel," *Scr. Metall.*, vol. 26, no. 2, pp.1221–1226, 1992.
- [137] D. Raabe, "Textures of strip cast and hot rolled ferritic and austenitic stainless steel," *Mater. Sci. Technol.*, vol. 11, pp.461–468, 1995.
- [138] J. Hirsch, and K. Lücke, "Overview no. 76: mechanism of deformation and development of rolling textures in polycrystalline fcc metals - I. Description of rolling texture development in homogeneous CuZn alloys," *Acta Metall.*, vol. 36, no. 11, pp.2863–2882, 1988.
- [139] K. Steineder, R. Schneider, D. Krizan, C. Béal, and C. Sommitsch, "Comparative Investigation of Phase Transformation Behavior as a Function of Annealing Temperature and Cooling Rate of Two Medium-Mn Steels," *Steel Res. Int.*, vol. 86, no. 10, pp.1179–1186, 2015.
- [140] K. W. Andrews, "Empirical Formulae for the Calculation of Some Transformation Temperatures," *J. Iron Steel Inst.*, vol. 203, no. 7, pp.721–727, 1965.
- [141] A. E. Nehrenberg, *Trans. ASM.*, vol. 45, pp.77–95, 1953.
- [142] W. Steven, and A. G. Haynes, "The Temperature of Formation of Martensite and Bainite in Low-alloy Steel," *J. Iron Steel Inst.*, vol. 183, pp.349–359, 1956.
- [143] R. A. Grange, and H. M. Stewart, "The Temperature Range of Martensite Formation," *Trans. AIME.*, vol. 167, pp.467–490, 1946.
- [144] L. A. Carapella, "Computing A<sub>11</sub> or M<sub>s</sub> (Transformation Temperature on Quenching) from Analysis," *Met. Prog.*, vol. 46, pp.108, 1944.
- [145] H. Luo, H. Dong, and M. Huang, "Effect of intercritical annealing on the Lüders strains of medium Mn transformation-induced plasticity steels," *Mater. Des.*, vol. 83, pp.42–48, 2015.
- [146] M. Hölscher, D. Raabe, and K. Lücke, "Relationship between rolling textures and shear textures in f.c.c. and b.c.c. metals," *Acta Met. Mater.*, vol. 42, no. 3, pp.879–886, 1994.
- [147] B. Hutchinson, "Development and control of annealing textures in low-carbon steels," *Int. Met. Rev.*, vol. 29, no. 1, pp.25–42, 1984.
- [148] A. Bag, K. K. Ray, and E. S. Dwarakadasa, "Influence of martensite content and morphology on tensile and impact properties of high-martensite dual-phase steels," *Metall. Mater. Trans. A.*, vol. 30, no. 5, pp.1193–1202, 1999.
- [149] C. H. Young, and H. K. D. H. Bhadeshia, "Strength of mixtures of bainite and martensite," *Mater. Sci. Technol.*, vol. 10, no. 3, pp.209–214, 1994.
- [150] A. M. Sarosiek, and W. S. Owen, "On the importance of extrinsic transformation accommodation hardening in Dual-phase steels," *Scr. Metall.*, vol. 17, no. 2, pp.227–231, 1983.
- [151] T. Waterschoot, *Fundamentals of Aging in Multiphase Ferrous Alloys: Static Strain Aging and Tempering in Dual Phase Steels*, PhD-thesis, Ghent University, 2003.
- [152] M. Erdogan, and R. Priestner, "Effect of epitaxial ferrite on yielding and plastic flow in dual phase steel in tension and compression," *Mater. Sci. Technol.*, vol. 15, pp.1273–1284, 1999
- [153] A. Pichler, S. Taint, H. Pauli, H. Mildner, J. Szinyur, M. Blaimschein, et al., Processing and properties of cold-rolled TRIP steels, in: 43rd Mech. Work. Steel Process. Conf. Proc., Charlotte, 2001: pp. 411–434.
- [154] A. Pichler, S. Taint, T. Hebesberger, P. Stiaszny, and E. A. Werner, "Processing of thin sheet multiphase steel grades," *Steel Res. Int.*, vol. 78, no. 3, pp.216–223, 2007.
- [155] R.G. Davies, "The Deformation Behavior of a Vanadium-Strengthened Dual Phase Steel," *Metall. Mater. Trans. A.*, vol. 9A, pp.41–52, 1978.
- [156] S. T. Mileiko, "The tensile strength and ductility of continuous fiber composites," *J. Mater. Sci.*, vol. 4, no. 11, pp.974–977, 1969.
- [157] D. A. Korzekwa, R. D. Lawson, D. K. Matlock, and G. Krauss, "A consideration of models describing the strength and ductility of dual-phase steels," *Scr. Metall.*, vol. 14, pp.1023–1028, 1980.
- [158] I. Tamura, Y. Tomota, and M. Ozawa, Strength and Ductility of Iron-Nickel-Carbon Alloys Composed of Austenite and Martensite with Various Strength, in: 3rd Int. Conf. Strength Met. Alloy., Cambridge, 1973: pp. 611–615.
- [159] Technical data sheet, „Cold-rolled steel strip,“ voestalpine Stahl GmbH, 2016
- [160] R. Kuziak, R. Kawalla, and S. Waengler, "Advanced high strength steels for automotive industry," *Arch. Civ. Mech. Eng.*, vol. 8, no. 2, pp.103–117, 2008.

- 
- [161] S. Curtze, V. Kuokkala, M. Hokka, and P. Peura, "Deformation behavior of TRIP and DP steels in tension at different temperatures over a wide range of strain rates," *Mater. Sci. Eng. A.*, vol. 507, pp.124–131, 2009.
- [162] H. Huh, S.-B. Kim, J.-H. Song, and J.-H. Lim, "Dynamic tensile characteristics of TRIP-type and DP-type steel sheets for an auto-body," *Int. J. Mater. Sci.*, vol. 50, pp.918–931, 2008.
- [163] J. Han, S.-H. Kang, S.-J. Lee, and Y.-K. Lee, "Fabrication of bimodal-grained Al-free medium Mn steel by double intercritical annealing and its tensile properties," *J. Alloys Compd.*, vol. 681, pp.580–588, 2016.
- [164] J. H. Ryu, J. I. Kim, H. S. Kim, C.-S. Oh, H. K. D. H. Bhadeshia, and D.-W. Suh, "Austenite stability and heterogeneous deformation in fine-grained transformation-induced plasticity-assisted steel," *Scr. Mater.*, vol. 68, no. 12, pp.933–936, 2013.
- [165] R. L. Bell, and T. G. Langdon, "An Investigation of Grain-Boundary Sliding during Creep," *J. Mater. Sci.*, vol. 2, pp.313–323, 1967.
- [166] R. Raj, and M. F. Ashby, "On Grain Boundary Sliding and Diffusional Creep," *Metall. Trans.*, vol. 2, pp.1113–1127, 1971.
- [167] S. Lee, S.-J. Lee, and B. C. De Cooman, "Work hardening behavior of ultrafine-grained Mn transformation-induced plasticity steel," *Acta Mater.*, vol. 59, no. 20, pp.7546–7553, 2011.
- [168] M. F. Ashby, "The deformation of plastically non-homogeneous materials," *Philos. Mag.*, vol. 21, no. 170, pp.399–424, 1970.
- [169] A. R. Marder, Factors Affecting the Ductility of Dual Phase Alloys, in: A.T. Davenport (Ed.), *Trans. AIME*, New York, 1977: p. 87.
- [170] T. Furukawa, H. Morikawa, H. Takechi, and K. Koyama, Structure and Properties of Dual-Phase Steels, in: R.A. Kot, J.W. Morris (Eds.), *Trans. AIME*, New York, 1979: p. 281.
- [171] N. H. van Dijk, A. Butt, L. Zhao, J. Sietsma, S. E. Offerman, J. P. Wright, et al., "Thermal stability of retained austenite in TRIP steels studied by synchrotron X-ray diffraction during cooling," *Acta Mater.*, vol. 53, no. 20, pp.5439–5447, 2005.

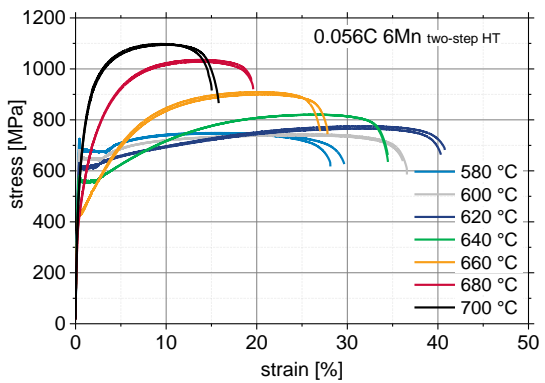
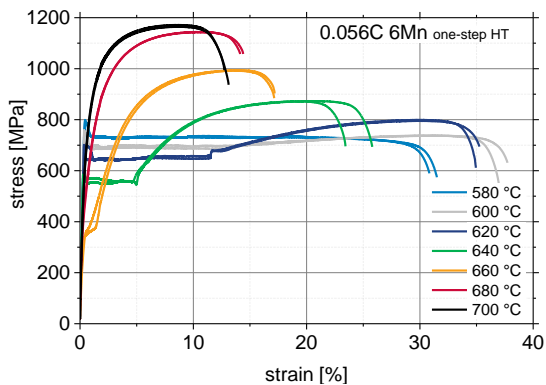
## 10. Appendix

### 10.1 Mechanical properties and retained austenite

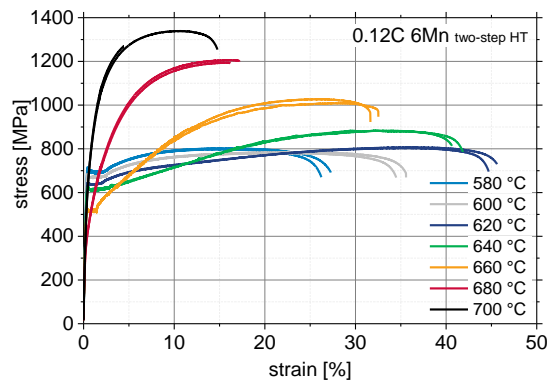
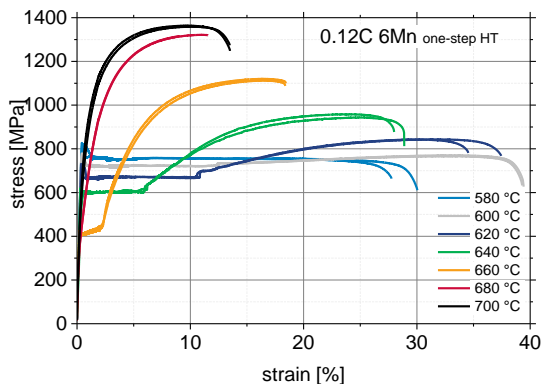
0.003C6Mn									
sample	HT	T <sub>IA</sub> [°C]	YS [MPa]	UTS [MPa]	UE [%]	TE [%]	ε <sub>3</sub> [%]	YPE [%]	RA [vol.-%]
U6141449_P1	one-step	580	706	692	15.1	27.4	60.6	8.3	18.4
U6141449_P2	one-step	580	681	690	14.1	26.4	66.0	7.5	
U6141431_P1	one-step	600	635	687	23.1	32.1	72.1	10.4	22.2
U6141431_P2	one-step	600	667	687	22.6	32.3	67.4	10	
U6141450_P1	one-step	620	587	756	24.1	29.4	53.4	6.8	27.6
U6141450_P2	one-step	620	606	751	24.4	30.0	59.2	7	
U6141433_P1	one-step	640	491	765	15.4	21.7	58.4	3.4	32.3
U6141433_P2	one-step	640	478	767	14.6	20.5	61.5	3.2	
U6141434_P1	one-step	660	346	868	11	17	54.9	0	20.1
U6141434_P2	one-step	660	342	860	11.2	17.4	56.5	0	
U6141437_P1	one-step	680	485	942	8	11.8	55.5	0	10.9
U6141437_P2	one-step	680	471	945	8.2	12.3	47.6	0	
U6141436_P1	one-step	700	634	962	6.1	11.0	54.2	0	6.2
U6141436_P2	one-step	700	593	964	5.8	10.3	58.2	0	
U7140208_P1	two-step	580	576	672	14.2	28	70.0	2.9	11.7
U7140208_P2	two-step	580	576	673	14.9	28.3	69.8	2.9	
U7140175_P1	two-step	600	557	670	20.4	32.7	68.8	2.1	16.7
U7140175_P2	two-step	600	549	670	20.7	32.9	69.1	2.2	
U7140176_P1	two-step	620	532	703	24.1	34.2	68.1	1.4	22.6
U7140176_P2	two-step	620	520	694	24.4	34.4	66.7	1.4	
U7140177_P1	two-step	640	453	737	18.4	28.4	64.4	0.7	28.6
U7140177_P2	two-step	640	446	735	18.1	27.4	61.3	0.6	
U7140178_P1	two-step	660	381	804	13.5	22.9	58.0	0	22.4
U7140178_P2	two-step	660	379	803	13.1	22.1	61.8	0	
U7140179_P1	two-step	680	423	850	10.4	19.6	57.1	0	16.1
U7140179_P2	two-step	680	402	859	10.6	17.7	56.8	0	
U7140180_P1	two-step	700	523	903	7.3	13.5	59.8	0	9.6
U7140180_P2	two-step	700	541	895	7.4	12.7	59.8	0	



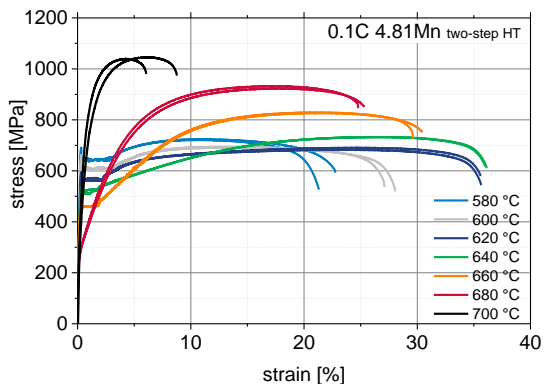
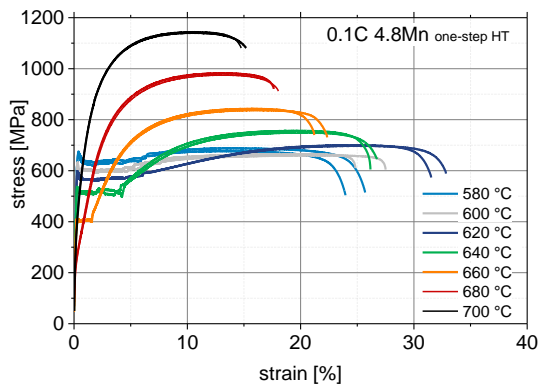
0.056C6Mn									
sample	HT	T <sub>1A</sub> [°C]	YS [MPa]	UTS [MPa]	UE [%]	TE [%]	ε <sub>3</sub> [%]	YPE [%]	RA [vol.-%]
U6141479_P1	one-step	580	788	735	5.5	31.3	55.8	2.8	20.1
U6141479_P2	one-step	580	744	737	10.5	30.6	67.8	9.4	
U6141485_P1	one-step	600	742	737	31.5	37.4	64.4	13.7	24.5
U6141485_P2	one-step	600	698	738	30.6	36.7	69.9	15	
U6141486_P1	one-step	620	651	799	29.8	34.7	55.6	11.5	29.3
U6141486_P2	one-step	620	652	796	29.9	35.0	56.8	11.5	
U6141487_P1	one-step	640	576	873	20.5	25.5	54.1	5	35.2
U6141487_P2	one-step	640	559	872	18.8	23.1	55.4	4.6	
U6141488_P1	one-step	660	339	994	13.7	16.7	40.6	0.3	38
U6141488_P2	one-step	660	360	993	12.7	16.3	42.7	1.5	
U6141489_P1	one-step	680	481	1144	10	13.7	12.0	0	15.8
U6141489_P2	one-step	680	461	1144	10.1	13.9	11.5	0	
U6141490_P1	one-step	700	648	1164	8.2	12.3	38.7	0	8.2
U6141490_P2	one-step	700	638	1172	8.4	12.7	40.9	0	
U7140222_P1	two-step	580	676	749	15.3	29.4	57.0	3.2	16.4
U7140222_P2	two-step	580	685	747	15.5	27.8	58.4	3.2	
U7140215_P1	two-step	600	653	744	23.7	36.3	62.4	3	21.3
U7140215_P2	two-step	600	648	740	24.5	35.8	59.5	3	
U7140216_P1	two-step	620	627	775	31.6	40.5	54.4	2.9	26.1
U7140216_P2	two-step	620	616	766	31.7	40.1	56.5	2.9	
U7140217_P1	two-step	640	577	821	25.9	34.2	53.6	2.1	30.7
U7140217_P2	two-step	640	569	821	26.3	34.2	55.9	2.1	
U7140218_P1	two-step	660	423	909	19.9	26.7	51.6	0.5	35.2
U7140218_P2	two-step	660	430	901	20.2	27.5	50.7	0.5	
U7140219_P1	two-step	680	432	1028	13.1	19.1	39.8	0	22.5
U7140219_P2	two-step	680	424	1035	13.4	18.9	38.3	0	
U7140220_P1	two-step	700	564	1098	9.0	14.6	46.0	0	12.1
U7140220_P2	two-step	700	555	1096	9.7	15.4	46.6	0	



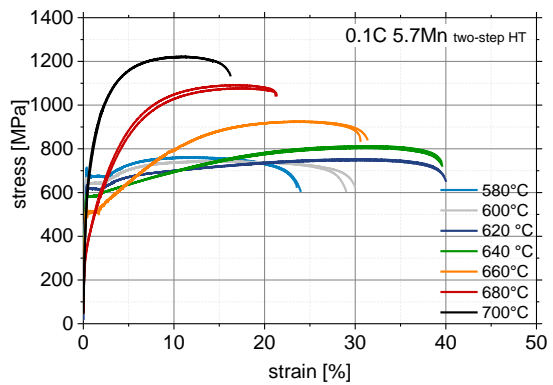
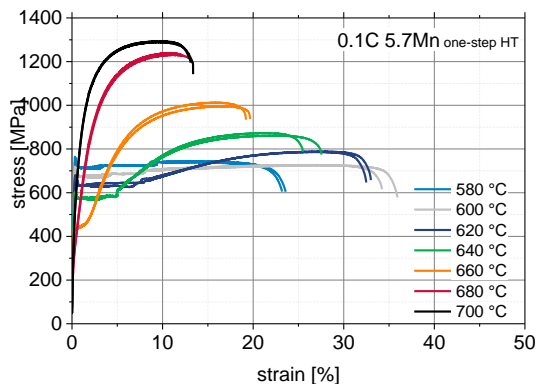
0.12C6Mn									
sample	HT	T <sub>IA</sub> [°C]	YS [MPa]	UTS [MPa]	UE [%]	TE [%]	ε <sub>3</sub> [%]	YPE [%]	RA [vol.-%]
U6141507_P1	one-step	580	814	758	6.3	29.8	56.2	3.8	20.1
U6141507_P2	one-step	580	786	759	6.6	27.5	49.0	3.3	
U6141499_P1	one-step	600	771	766	32.5	39	55.6	12.4	25.3
U6141499_P2	one-step	600	772	771	32.6	39.1	54.9	12.4	
U6141500_P1	one-step	620	673	843	29.4	34.2	45.9	10.8	30.1
U6141500_P2	one-step	620	700	843	31.4	37.1	49.5	10.4	
U6141501_P1	one-step	640	600	943	24.4	28.3	39.8	6.2	37.5
U6141501_P2	one-step	640	605	958	23.3	27.6	42.0	5.9	
U6141502_P1	one-step	660	405	1121	15.9	17.9	17.7	2.2	46.3
U6141502_P2	one-step	660	406	1112	16.2	17.9	16.6	2.2	
U6141503_P1	one-step	680	456	1322	10.4	10.8	9.7	0	21
U6141503_P2	one-step	680	446	1316	8.4	8.4	5.9	0	
U6141504_P1	one-step	700	717	1363	9.1	12.9	12.7	0	12.1
U6141504_P2	one-step	700	618	1359	9.8	12.9	12.4	0	
U7140259_P1	two-step	580	700	802	15.4	27	55.6	2.2	17.2
U7140259_P2	two-step	580	690	798	14.5	25.9	54.8	2.2	
U7140250_P1	two-step	600	677	780	22	34.2	50.7	2.2	22.3
U7140250_P2	two-step	600	672	785	22.9	35.3	44.8	2.2	
U7140251_P1	two-step	620	645	807	35.9	45.3	37.7	2.9	29.1
U7140251_P2	two-step	620	632	803	35.3	44.4	55.5	2.9	
U7140252_P1	two-step	640	624	883	31.8	41.5	46.3	1.5	34.6
U7140252_P2	two-step	640	623	883	32.7	40.2	44.4	1.5	
U7140253_P1	two-step	660	511	1027	25.5	31.2	35.3	0	41.5
U7140253_P2	two-step	660	525	1009	28	32	20.8	0	
U7140254_P1	two-step	680	409	1194	15.2	15.5	10.2	0	31.1
U7140254_P2	two-step	680	394	1206	15.4	16.6	10.4	0	
U7140255_P1	two-step	700	655	1339	10.1	14.1	11.9	0	14.3
U7140255_P2	two-step	700	620	1271	3.9	3.9	4.8	0	



0.1C4.8Mn									
sample	HT	T <sub>IA</sub> [°C]	YS [MPa]	UTS [MPa]	UE [%]	TE [%]	ε <sub>3</sub> [%]	YPE [%]	RA [vol.-%]
U6140076_P1	one-step	580	629	676	13.5	23.9	64.9	3.2	7.7
U6140076_P2	one-step	580	656	677	13.4	25.2	66.4	1.7	
U6140073_P1	one-step	600	600	666	20.5	28.1	62.3	6.1	10.3
U6140073_P2	one-step	600	612	656	16.4	24.3	61.4	2	
U6140074_P1	one-step	620	570	698	24.9	32.9	54.3	3.1	16.6
U6140074_P2	one-step	620	588	700	24.5	31.6	55.5	2.5	
U6140075_P1	one-step	640	513	757	19	26.3	53.5	4.1	20.2
U6140075_P2	one-step	640	523	750	19.6	26.9	53.4	4.2	
U6140077_P1	one-step	660	398	843	15.5	21.2	41.3	1.6	26.3
U6140077_P2	one-step	660	408	838	16.2	22.3	36.8	1.6	
U6140078_P1	one-step	680	278	976	12.9	17.9	15.7	0	23.6
U6140078_P2	one-step	680	281	982	12.6	17.5	15	0	
U6140079_P1	one-step	700	477	1141	10.6	14.8	18.1	0	13.1
U6140079_P2	one-step	700	478	1146	10.1	14.5	18.9	0	
U7140107_P1	two-step	580	649	716	9.2	20.5	57.5	3.3	5
U7140107_P2	two-step	580	655	731	10.7	21.5	57.1	0.9	
U7140066_P1	two-step	600	600	695	12.4	25.7	62.4	2.7	9.8
U7140066_P2	two-step	600	604	692	12.8	27.6	61.9	2.4	
U7140105_P1	two-step	620	559	683	23.7	36.3	60.6	1.9	14.9
U7140105_P2	two-step	620	563	684	24.2	35.9	58	1.5	
U7140106_P1	two-step	640	541	754	24.8	34.7	48.4	1.8	20.8
U7140106_P2	two-step	640	536	747	25.5	34.5	50.9	2	
U7140108_P1	two-step	660	463	840	21.6	30.1	39.3	5.5	26.8
U7140108_P2	two-step	660	462	840	21.1	30.7	31.2	5.2	
U7140109_P1	two-step	680	301	932	16.7	24.5	30.2	0	27.9
U7140109_P2	two-step	680	297	932	16.9	25.7	33.3	0	
U7140067_P1	two-step	700	428	984	4.3	4.6	18.2	0	17.6
U7140067_P2	two-step	700	409	1066	8.1	8.2	14	0	

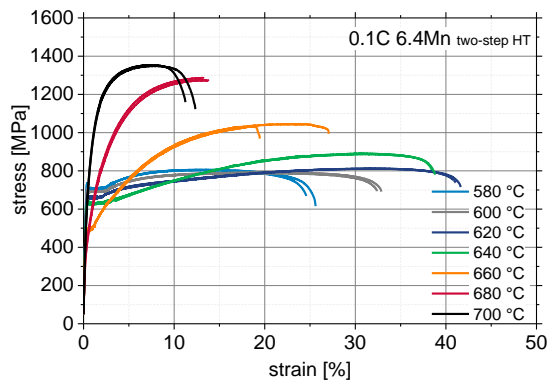
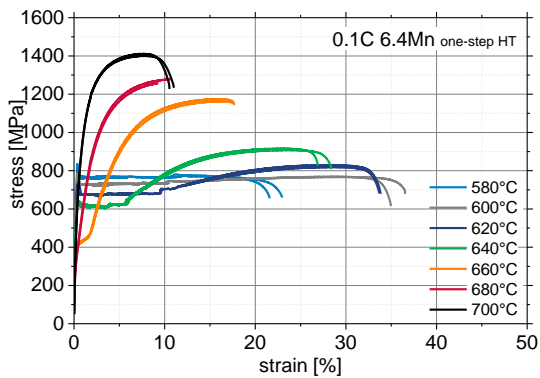


<b>0.1C5.7Mn</b>									
<b>sample</b>	<b>HT</b>	<b>T<sub>IA</sub></b> [°C]	<b>YS</b> [MPa]	<b>UTS</b> [MPa]	<b>UE</b> [%]	<b>TE</b> [%]	<b>ε<sub>3</sub></b> [%]	<b>YPE</b> [%]	<b>RA</b> [vol.-%]
U6140112_P1	one-step	580	717	745	13.5	23.8	60.8	8.5	13.4
U6140112_P2	one-step	580	737	740	9.3	25.2	62.5	9.3	
U6140109_P1	one-step	600	677	727	25.6	34.8	57.4	7.3	18.8
U6140109_P2	one-step	600	709	725	26.8	36.3	58.3	8	
U6140110_P1	one-step	620	639	788	26.6	33	49.6	7.3	23.5
U6140110_P2	one-step	620	666	787	26.5	32.5	48.6	6.95	
U6140111_P1	one-step	640	593	873	20.8	25.4	45.8	4.9	28.7
U6140111_P2	one-step	640	590	862	22	27.6	39.1	5	
U6140113_P1	one-step	660	431	1012	15.6	18.9	28.1	1.6	36.7
U6140113_P2	one-step	660	432	996	16.3	19.4	23.3	1.6	
U6140114_P1	one-step	680	362	1231	10.5	13	14.9	0	24.5
U6140114_P2	one-step	680	365	1240	10.2	12	14.2	0	
U6140115_P1	one-step	700	601	1288	8.8	13	17.3	0	12.4
U6140115_P2	one-step	700	613	1293	9.2	12.7	15.2	0	
U7140127_P1	two-step	580	677	762	11.3	24.2	59.3	2.7	10
U7140127_P2	two-step	580	673	759	11.6	23.7	60	2.8	
U7140070_P1	two-step	600	644	743	14.5	29.3	55.7	2.3	16.1
U7140070_P2	two-step	600	644	741	15	30.3	55.9	2.6	
U7140072_P1	two-step	620	633	752	32.4	39.8	52.9	1.85	22.4
U7140072_P2	two-step	620	633	549	32.3	40.1	51.8	1.8	
U7140126_P1	two-step	640	585	812	31.2	39.4	48.4	1.7	28.3
U7140126_P2	two-step	640	589	804	30.1	39.6	45.4	1.85	
U7140128_P1	two-step	660	509	926	23.3	31.4	38.6	0	34.8
U7140128_P2	two-step	660	515	924	23.2	30.9	41	0	
U7140129_P1	two-step	680	344	1077	16.8	21.1	18.4	0	35.3
U7140129_P2	two-step	680	330	1092	16.6	20.8	19.5	0	
U7140071_P1	two-step	700	602	1220	10.3	15.9	15.6	0	13.4
U7140071_P2	two-step	700	630	1222	10.2	14.1	14.2	0	





0.1C6.4Mn									
sample	HT	T <sub>IA</sub> [°C]	YS [MPa]	UTS [MPa]	UE [%]	TE [%]	ε <sub>3</sub> [%]	YPE [%]	RA [vol.-%]
U6140132_P1	one-step	580	793	774	11.8	23.7	59.7	11.8	15.2
U6140132_P2	one-step	580	771	780	10.9	23	59.2	10.9	
U6140127_P1	one-step	600	768	767	29.2	36.8	55.7	10.4	20.9
U6140127_P2	one-step	600	737	769	28.6	34.9	55	10.2	
U6140128_P1	one-step	620	681	819	28.2	33.5	49.5	9.5	26
U6140128_P2	one-step	620	723	830	28.3	33.8	45.9	9.6	
U6140130_P1	one-step	640	628	916	22.8	26.9	39.2	5.75	32
U6140130_P2	one-step	640	641	908	23.4	28.4	41.6	5.6	
U6140133_P1	one-step	660	405	1174	15.5	17.2	19	1.5	46.1
U6140133_P2	one-step	660	415	1164	15.8	17.4	17.4	1.7	
U6140129_P1	one-step	680	373	1257	8.6	8.7	11.4	0	24.4
U6140129_P2	one-step	680	389	1278	10	10	11.5	0	
U6140134_P1	one-step	700	746	1400	7.2	10.4	34.2	0	12.8
U6140134_P2	one-step	700	741	1411	7	10	33.1	0	
U7140152_P1	two-step	580	711	804	12.7	24.6	59.9	2.8	16.5
U7140152_P2	two-step	580	710	806	12.6	25.7	61.2	2.7	
U7140075_P1	two-step	600	694	788	18.8	32.8	50.9	2.65	23.3
U7140075_P2	two-step	600	705	791	20.5	33	50.5	2.75	
U7140150_P1	two-step	620	673	812	31.2	41.6	53.8	2.1	29.5
U7140150_P2	two-step	620	666	812	31.2	41	41.7	2.2	
U7140151_P1	two-step	640	636	891	30.5	38.2	47	3	35.1
U7140151_P2	two-step	640	640	888	30.6	38.8	48.5	2.6	
U7140153_P1	two-step	660	484	1044	22.7	26.7	23	1	42
U7140153_P2	two-step	660	491	1033	18	19.8	19.2	1.2	
U7140154_P1	two-step	680	431	1274	12.6	13.3	13	0	30
U7140154_P2	two-step	680	428	1286	12.4	12.7	13.4	0	
U7140076_P1	two-step	700	719	1350	6.8	11.8	38.3	0	12.3
U7140076_P2	two-step	700	719	1353	6.9	10.7	37.5	0	



## 10.2 Interrupted tensile testing

<b>0.003C6Mn</b>						
<b>T<sub>IA</sub></b> [°C]	<b>HT</b>	<b>strain</b> [%]	<b>RA</b> [vol.-%]	<b>HT</b>	<b>strain</b> [%]	<b>RA</b> [vol.-%]
580	one-step	0.00	18.1	two-step	0.00	12
580	one-step	0.09	17.4	two-step	0.04	12.1
580	one-step	0.12	16.6	two-step	0.06	11.5
580	one-step	0.14	15.5	two-step	0.1	11.8
580	one-step	0.18	13.6	two-step	0.14	11.2
600	one-step	0.00	22.2	two-step	0.00	16.7
600	one-step	0.12	15.8	two-step	0.03	16.1
600	one-step	0.15	13.2	two-step	0.07	15.6
600	one-step	0.18	12.6	two-step	0.15	12.5
600	one-step	0.22	9.7	two-step	0.2	10.8
620	one-step	0.00	21.8	two-step	0.00	23.7
620	one-step	0.08	8.2	two-step	0.02	23.8
620	one-step	0.10	6.9	two-step	0.08	18.4
620	one-step	0.14	5.6	two-step	0.16	13
620	one-step	0.18	4.5	two-step	0.24	8.7
640	one-step	0.00	32.3	two-step	0.00	28.7
640	one-step	0.04	9.1	two-step	0.02	20.6
640	one-step	0.07	5.2	two-step	0.05	14
640	one-step	0.10	3.8	two-step	0.1	9.1
640	one-step	0.14	3.2	two-step	0.18	5.1
660	one-step	0.00	17.3	two-step	0.00	21.4
660	one-step	0.01	8.5	two-step	0.01	14.9
660	one-step	0.04	4.5	two-step	0.04	9.3
660	one-step	0.07	3.1	two-step	0.09	3.9
660	one-step	0.1	2.3	two-step	0.12	4.9

<b>0.056C6Mn</b>						
<b>T<sub>IA</sub></b> [°C]	<b>HT</b>	<b>strain</b> [%]	<b>RA</b> [vol.-%]	<b>HT</b>	<b>strain</b> [%]	<b>RA</b> [vol.-%]
580	one-step	0.00	20.3	two-step	0.00	15.5
580	one-step	0.04	20.3	two-step	0.04	15.6
580	one-step	0.06	19.3	two-step	0.06	15.7
580	one-step	0.1	19.2	two-step	0.10	14.7
580	one-step	0.14	18.3	two-step	0.14	14.3
600	one-step	0.00	23.9	two-step	0.00	20.5
600	one-step	0.16	20.4	two-step	0.02	20.1
600	one-step	0.20	18.1	two-step	0.04	19.9
600	one-step	0.25	16.6	two-step	0.09	17.4
600	one-step	0.30	13.5	two-step	0.18	16.3
620	one-step	0.00	29.8	two-step	0.00	26.1
620	one-step	0.14	17.2	two-step	0.03	25.5

620	one-step	0.18	13.0	two-step	0.08	24.1
620	one-step	0.24	9.5	two-step	0.14	20.3
620	one-step	0.30	8.0	two-step	0.20	16.10
640	one-step	0.00	35.1	two-step	0.00	31.1
640	one-step	0.05	14.9	two-step	0.03	26.8
640	one-step	0.08	10.4	two-step	0.08	19.9
640	one-step	0.14	6.1	two-step	0.16	11.4
640	one-step	0.18	4.4	two-step	0.24	7.6
660	one-step	0.00	39.7	two-step	0.00	32.9
660	one-step	0.02	11.9	two-step	0.01	22.5
660	one-step	0.04	7.9	two-step	0.04	15.3
660	one-step	0.08	4.8	two-step	0.08	10.4
660	one-step	0.12	3.3	two-step	0.20	4.9

<b>0.12C6Mn</b>						
<b>T<sub>IA</sub></b> [°C]	<b>HT</b>	<b>strain</b> [%]	<b>RA</b> [vol.-%]	<b>HT</b>	<b>strain</b> [%]	<b>RA</b> [vol.-%]
580	one-step	0.00	19.5	two-step	0.00	16.7
580	one-step	0.06	19.5	two-step	0.03	16.7
580	one-step	0.1	19.2	two-step	0.06	15.9
580	one-step	0.14	18.3	two-step	0.10	12.6
580	one-step	0.2	17.9	two-step	0.14	14.6
600	one-step	0.00	24.5	two-step	0.00	22.6
600	one-step	0.16	20.5	two-step	0.03	22.6
600	one-step	0.20	18.6	two-step	0.07	22.9
600	one-step	0.25	16.1	two-step	0.12	20.9
600	one-step	0.30	13.5	two-step	0.18	19.0
620	one-step	0.00	30.2	two-step	0.00	29.0
620	one-step	0.12	18.2	two-step	0.03	29.1
620	one-step	0.18	12.5	two-step	0.14	24.0
620	one-step	0.24	9.4	two-step	0.20	29.5
620	one-step	0.30	7.1	two-step	0.34	13.9
640	one-step	0.00	38.5	two-step	0.00	35.5
640	one-step	0.06	22.3	two-step	0.04	33.4
640	one-step	0.1	14.4	two-step	0.12	23.7
640	one-step	0.16	9.0	two-step	0.20	15.7
640	one-step	0.22	6.6	two-step	0.30	10.9
660	one-step	0.00	45.6	two-step	0.00	41.1
660	one-step	0.03	16.2	two-step	0.02	32.9
660	one-step	0.05	10.9	two-step	0.06	23.3
660	one-step	0.1	6.0	two-step	0.14	13.1
660	one-step	0.16	4.0	two-step	0.24	7.1

<b>0.1C4.8Mn</b>						
<b>T<sub>IA</sub></b> [°C]	<b>HT</b>	<b>strain</b> [%]	<b>RA</b> [vol.-%]	<b>HT</b>	<b>strain</b> [%]	<b>RA</b> [vol.-%]
600	one-step	0.00	12.0	two-step	0.00	9.0
600	one-step	0.05	11.3	two-step	0.04	8.5
600	one-step	0.08	11.5	two-step	0.06	8.9
600	one-step	0.12	9.9	two-step	0.08	8.3
600	one-step	0.20	8.4	two-step	0.12	8.5
620	one-step	0.00	13.8	two-step	0.00	15.9
620	one-step	0.03	13.9	two-step	0.03	15.4
620	one-step	0.10	9.3	two-step	0.06	14.7
620	one-step	0.20	5.0	two-step	0.12	12.9
620	one-step	0.28	3.4	two-step	0.24	8.1
640	one-step	0.00	19.9	two-step	0.00	20.0
640	one-step	0.05	10.5	two-step	0.05	17.2
640	one-step	0.08	7.6	two-step	0.10	12.6
640	one-step	0.12	5.8	two-step	0.14	10.1
640	one-step	0.16	4.3	two-step	0.20	6.2
660	one-step	0.00	26.4	two-step	x	x
660	one-step	0.02	12.4	two-step	x	x
660	one-step	0.05	7.4	two-step	x	x
660	one-step	0.10	4.7	two-step	x	x
660	one-step	0.14	3.9	two-step	x	x
680	one-step	0.00	18.7	two-step	0.00	26.6
680	one-step	0.01	10.3	two-step	0.01	18.7
680	one-step	0.03	6.6	two-step	0.04	10.0
680	one-step	0.06	4.0	two-step	0.01	4.7
680	one-step	0.10	2.9	two-step	0.16	3.3

<b>0.1C5.9Mn</b>						
<b>T<sub>IA</sub></b> [°C]	<b>HT</b>	<b>strain</b> [%]	<b>RA</b> [vol.-%]	<b>HT</b>	<b>strain</b> [%]	<b>RA</b> [vol.-%]
600	one-step	0.00	21.2	two-step	0.00	19.5
600	one-step	0.08	21.0	two-step	0.05	18.5
600	one-step	0.12	19.7	two-step	0.07	19.1
600	one-step	0.16	17.8	two-step	0.10	18.2
600	one-step	0.20	16.0	two-step	0.14	18.0
620	one-step	0.00	27.0	two-step	0.00	25.8
620	one-step	0.10	19.9	two-step	0.05	25.5
620	one-step	0.14	17.1	two-step	0.10	23.9
620	one-step	0.20	12.2	two-step	0.14	21.5
620	one-step	0.24	10.6	two-step	0.20	18.3
640	one-step	0.00	32.0	two-step	0.00	31.6
640	one-step	0.07	19.4	two-step	0.05	28.1
640	one-step	0.10	15.0	two-step	0.10	19.7

640	one-step	0.14	9.4	two-step	0.14	18.6
640	one-step	0.20	6.0	two-step	0.20	14.2
660	one-step	0.00	40.3	two-step	0.00	42.2
660	one-step	0.02	18.0	two-step	0.02	32.6
660	one-step	0.06	8.8	two-step	0.07	20.8
660	one-step	0.10	6.0	two-step	0.12	13.7
660	one-step	0.14	4.6	two-step	0.18	9.4
680	one-step	0.00	24.5	two-step	0.00	34.1
680	one-step	0.01	13.2	two-step	0.02	20.7
680	one-step	0.03	7.7	two-step	0.06	10.4
680	one-step	0.05	5.7	two-step	0.10	7.4
680	one-step	0.08	4.1	two-step	0.14	4.9